Universität Zürich

PHYSIK - INSTITUT

www.physik.unizh.ch

Wissenschaftlicher Jahresbericht

April 2001 - März 2002

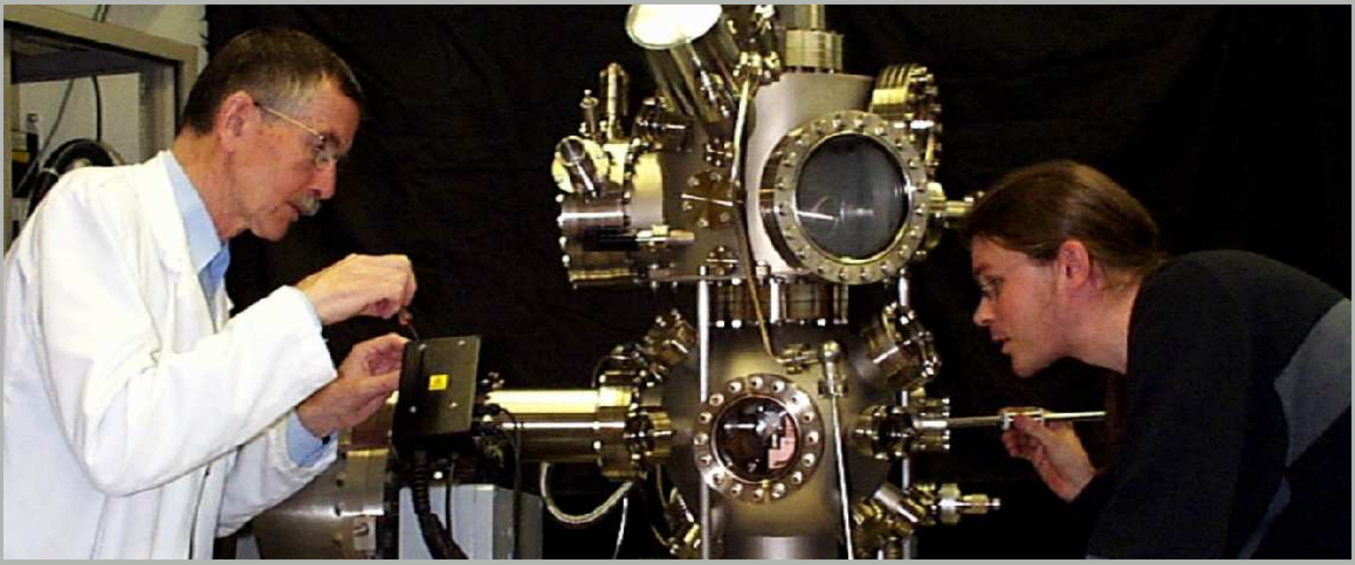

Winterthurerstrasse 190, CH-8057 Zürich/Schweiz

Universität Zürich

PHYSIK - INSTITUT

Wissenschaftlicher Jahresbericht

April 2001 - März 2002

Winterthurerstrasse 190, CH-8057 Zürich/Schweiz www.physik.unizh.ch

The picture on the cover shows Werner Deichmann and Moritz Hoesch working at the COPHEE spectrometer (described in Sec.12.8).

Sekretariat	01 635 5721	secret@physik.unizh.ch
Prof. C. Amsler	01 635 5784 022 767 2914	amsler@cern.ch
Prof. H.-W. Fink	01 635 5801	fink@physik.unizh.ch
Prof. H. Keller	01 635 5748	keller@physik.unizh.ch
Prof. P.F. Meier	01 635 4016	meier@physik.unizh.ch
Prof. J. Osterwalder	01 635 5827	osterwal@physik.unizh.ch
Prof. U.D. Straumann	01 635 5768	strauman@physik.unizh.ch
Prof. P. Truöl	01 635 5777	truoel@physik.unizh.ch

Begleitwort

Dieser Jahresbericht legt Rechenschaft ab über die zwischen April 2001 und März 2002 erreichten Fortschritte der sechs Forschungsgruppen des Physik-Instituts der Universität Zürich in den Schwerpunktsbereichen Physik der kondensierten Materie und Elementarteilchenphysik. Er ist wie üblich in englischer Sprache abgefasst[1], um die Kommunikation innerhalb unserer internationalen Kollaborationen zu erleichtern, und um Teile dieses Berichtes den forschungsfördernden Instanzen und ihren Gutachtern vorlegen zu können.

Einige Punkte gilt es schon hier speziell zu erwähnen.

Die Biophysik-Gruppe von Prof. H.W. Fink konnte im Januar 2002 ihre neuen Labors in einem speziell für empfindliche Experimente mit langsamen, kohärenten Elektronen eingerichteten Gebäude beziehen. Das Holographielabor verfügt über sehr gute Erschütterungsdämpfung und magnetische Abschirmung.

In der Oberflächenphysik (Gruppe von Prof. J. Osterwalder) gilt es die erfolgreiche Inbetriebnahme von zwei neuen Apparaturen zu vermerken. Es kann nun auch die Polarisation der emittierten Photoelektronen gemessen werden. Zudem kann mit durch Streuung an Laserpulsen erzeugten, gepulsten Elektronenstrahlen die zeitliche Entwicklung von Oberflächen verfolgt werden, die dem gleichen Laserpuls ausgesetzt waren.

Der Gruppe Supraleitung und Magnetismus von Prof. H. Keller sah ihre Messungen zum Isotopeneffekt in Hochtemperatursupraleitern durch amerikanische und japanische Kollegen bestätigt. Dies beendet eine lang anhaltende Diskussion, und bedingt, dass neben der Elektron-Elektron-Korrelation auch die Wechselwirkungen zwischen den supraleitenden Ladungsträgern und den Gitterschwingungen (Phononen) bei der Erklärung des Mechanismus der Hochtemperatursupraleitung berücksichtigt werden sollten.

Im gleichen Gebiet gelang Mitarbeitern der Computational Physics Gruppe von Prof. P.F. Meier eine erfolgreiche *ab initio* Berechnung der elektrischen Feldgradienten und Hyperfeinkopplungen im Hochtemperatursupraleiter $YBa_2CU_3O_7$.

Das Athena-Experiment, an dem die Gruppe von Prof. C. Amsler beteiligt ist, kam ihrem Ziel die Zustände von Antiwasserstoff spektroskopisch zu untersuchen, mit der erfolgreichen Speicherung von Antiprotonen in einer Penning Falle näher.

Obwohl sich die Inbetriebnahme des LHC weiter verzögert, lässt die Intensität der Vorbereitungen für die dort geplanten Experimente nicht nach. Prof. U. Straumann's Gruppe arbeitete intensiv am Technical Design Report für den inneren Spurdetektor des speziell für die Aufklärung der Teilchen-Antiteilchen Asymmetrie konzipierten Experiments LHCb.

An Europas einzigem zur Zeit aktiven Beschleuniger- und Speicherring-Komplex HERA am DESY ist die Umbauphase, die zu höheren Wechselwirkungsraten führen sollte, abgeschlossen worden. Parallel dazu sind auch die für die sogenannte HERA II-Phase in Zürich gebauten Detektorteile in den H1-Detektor - an dieser Kollaboration sind die Gruppen von Prof. U. Straumann und P. Truöl beteiligt - eingebaut und in Betrieb genommen worden.

Alle Gruppen können sich in ihrer Arbeit auf den zuverlässigen Service der mechanischen und elektronischen Werkstatt, der anderen technischen Mitarbeiter des Instituts und des Sekretariats verlassen. Ihnen allen gilt unser besonderer Dank. Aus diesem Kreis verlor das Institut 2001 altersbedingt mit Herrn *Bernhard Zaugg* einen Mitarbeiter der Werkstatt, der sowohl umsichtig das zentrale Rohmateriallager der Universität betreute als auch als Fachmann für Schweissarbeiten so sehr geschätzt war, dass man ihn auch aus dem Ruhestand gelegentlich für schwierige Arbeiten zurückholt.

[1] Der Jahresbericht ist auch über das Internet einsehbar: http://www.physik.unizh.ch/jb/

Nachruf Eugen Holzschuh

Mitten aus seiner vielseitigen Forschungs- und Lehrtätigkeit herausgerissen starb am 3.November 2001 Dr. Eugen Holzschuh, Privatdozent für Experimentalphysik und Oberassistent an unserem Institut, im Universitätskrankenhaus Ulm (Deutschland) an einem Herzversagen. Eugen Holzschuh besuchte gerade seinen Heimatort Lonsee (Kreis Ulm), dem er als Mitbesitzer eines alten landwirtschaftlichen Anwesens auch während seiner Zürcher Zeit immer sehr verbunden blieb. Wir haben mit Eugen Holzschuh einen bescheidenen, hilfsbereiten und das intellektuelle Leben immer wieder bereichernden Kollegen verloren, die Physik-Studenten einen beliebten Lehrer, dessen Vorlesungen und Übungen sich durch sorgfältige Vorbereitung und originelle Ansätze auszeichneten, seine Fachkollegen einen kompetenten Redner an internationalen Kongressen und schliesslich seine Heimatgemeinde einen Wahrer traditioneller Werte in ländlicher Arbeit und Kultur.

In Lonsee wurde Eugen Holzschuh am 12. Juni 1949 geboren, und nach dem Besuch der dortigen Grundschule führte ihn sein nicht immer einfacher Weg über eine landwirtschaftliche Lehre, eine Berufsaufbauschule und das Kolping-Gymnasium in Friedrichshafen im Alter von bereits von 25 Jahren an die Universität Konstanz. In Rekordzeit und mit brillanten Noten schloss er dort sein Studium 1978 Experimentalphysik mit dem Diplom ab. In der Gruppe von Prof. Walter Kündig an der Universität Zürich promovierte Eugen Holzschuh 1982 mit Auszeichnung. In diese Gruppe kehrte er dann zunächst als wissenschaftlicher Mitarbeiter und dann als Oberassistent 1984 nach einem Postdocjahr und einer Assistenzprofessur an der University of Michigan in Ann Arbor (USA) zurück. 1993 folgte die Habilitation in Experimentalphysik, die vorgeschlagene Ernennung zum Titularprofessor lehnte er 1999 ab. Das Forschungsspektrum des ebenso geschickten, wie findigen Experimentators Eugen Holzschuh reichte von der Physik der kondensierten Materie über die nukleare Astrophysik bis hin zur Gravitation, immer begleitet von ebenso tiefem wie breitem Verständnis für komplexe mathematische Modelle, die es zur Interpretation der Resultate brauchte. Um nur einige Meilensteine zu nennen: Die Entwicklung einer neuen Methode zum Verfolgen der Spinpräzession von in Halbleitern implantierten Myonen mit hoher Zeitauflösung führte z.B. zur ersten direkten Beobachtung der Hyperfeinübergänge im exotischen Myonium-Atom ohne äusseres Magnetfeld. Die Untersuchung des Betazerfalls von radioaktivem Tritium in einem innovativen Spektrometer widerlegte den Befund eines russischen Experiments einer relativ grossen Masse des Neutrinos, legte eine erst viel später unterschrittene obere Grenze für die Masse dieses einer experimentellen Beobachtung nur schwer zugänglichen Elementarteilchens fest, und half damit auch zu verstehen, warum uns von den in der Sonne bei der Kernfusion erzeugten Neutrini weniger als erwartet erreichen. Zuletzt widmete er seine ganze Aufmerksamkeit und Arbeitskraft dem in diesem Jahresbericht beschriebenen und noch andauernden Forschungsprojekt zur Neubestimmung der Gravitationskonstante.

Zürich, im April 2002
Prof. Dr. Peter Truöl

P. Truöl

Contents

1 Measurement of the Gravitational Constant G

St. Schlamminger and E. Holzschuh[2]

The principle of our experiment is shown in Fig. 1.1. Two cylindrical stainless steel vessels, each filled with 6.75×10^3 kg mercury (labelled field masses), are used to change the weight difference of two test masses. The field masses are hollow cylinders, which can be moved vertically between two positions. The two test masses are copper cylinders coated with a thin gold layer to avoid oxidation. Each has a total mass of 1100 g. Both test masses are suspended by two tungsten wires (0.1 mm diameter) on a device called mass exchanger. This device allows to connect the test masses alternately to the balance. First, the field

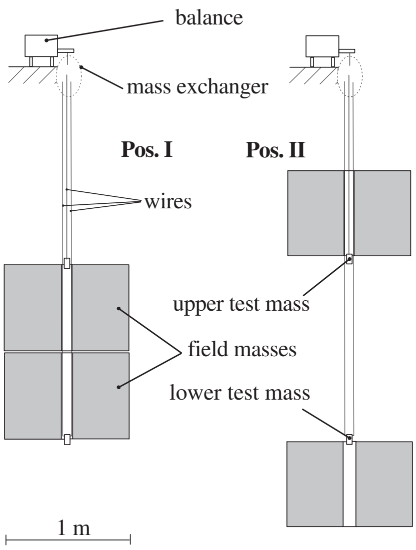

Figure 1.1: *The principle of the experiment. The two field masses are shown in the two positions I and II used for the measurements.*

masses are at position I and the weight of each test mass is determined repeatedly. The weight difference, which we call the signal, is calculated. After a few hours we move the field masses in position II. Again the weight difference is determined. This cycle is repeated throughout the total measurement period (typically a few months). The signal is modulated by the gravitational forces of the two field masses. The gravitational constant G can be calculated from the amplitude of this modulation (approximately 0.8 mg) and the known mass distribution. In order to calibrate the balance two 100 mg standard masses are put on the balance. Together with the precisely known value of the local gravity one can convert the reading of the balance into a force.

The balance, a modified *Mettler-Toledo AT1006*, is a single pan beam balance. The total measuring range is 1.7 g with a resolution of 12.5 ng. To avoid disturbances caused by time delayed relaxation of mechanical stress in flexure strips of the balance, the load on the balance is kept constant during the exchange of the masses. The total load on the balance varies during the interchange by less than 100 mg. The whole weighing is performed in vacuum, to avoid errors due to buoyancy, convection and other gas pressure forces. For reasons of clarity the vacuum system is not shown in Fig. 1.1. A detailed description of our experiment is given in Ref.[1].

In 1998 a preliminary result of our measurements with a total relative uncertainty of 220×10^{-6} has been published[2]. The main problem of this measurement was a possible nonlinear response of the balance. For the required accuracy the calibration weights must

[2]Deceased in the course of this work.

be much larger than our signal amplitude (0.8 mg). Considering a deviation from a strictly linear behaviour of the balance, a significant systematic error may result. To overcome this problem, we developed a method which can be used in situ and simultaneously. It is based on the fact that one only need to relate the average slope of the balance's response as determined by the calibration weights with the slope of the signal amplitude averaged over the calibration interval. This can be accomplished by placing a large number of small auxiliary masses on the balance while measuring G. These masses must be changed in approximately equal steps and over a range from zero to the value of the standard masses. Such a device operating in vacuum and under computer control has been built. It allows us to use two sets of 16 auxiliary masses each. By properly choosing the masses 256 steps are achieved.

A histogram of the signal amplitude is shown in Fig.1.2. The standard deviation of the measurements ranges between 200 ng and 400 ng, depending on the experimental conditions. This includes the noise of the balance and the nonlinearity. By averaging this 256 single measurements it is possible to reduce the effect of the nonlinearity to the ppm level.

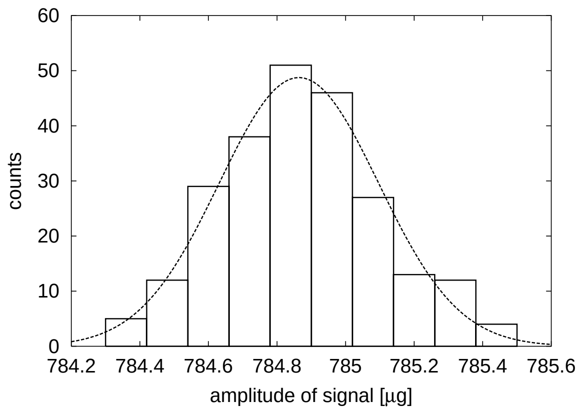

Figure 1.2: *Histogram of the signal amplitude measured over four days. For technical reasons only 237 of 256 possible operating points of the balance were included. The dashed line is a Gaussian distribution.*

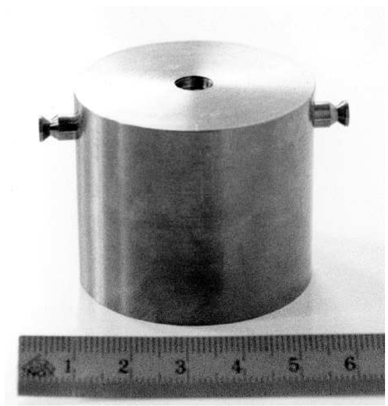

Figure 1.3: *The dimensions of the tantalum test mass are chosen such, that the gravitational quadrupole moment is minimised.*

We finished the measurements with the gold plated copper test masses and finally reached a statistical uncertainty of 7×10^{-6}. The calculation of the systematic uncertainty is still in progress. At present we are working on the mass integration and the estimation of the uncertainties. The integration of the test masses is relatively simple but has so far not been tested experimentally. In order to clarify this point, we install a second set of test masses made from tantalum ($\varrho = 16.6$ g/cm^3) (see Fig. 1.3). The high density allows us to choose a ratio between height and radius of the cylinders, such that the quadrupole moment of the test masses can be neglected.

We hope to have sufficient accurate measurements with the tantalum test masses during 2002. From the combined measurements of the tantalum and the copper test mass, the gravitational constant G will be calculated. This work is supported by the Swiss National Science Foundation and the Dr. Tomalla Foundation.

References

[1] J. Schurr *et al.*, Phys. Lett. A, **248** (1998), 295-308.

[2] F. Nolting, Dissertation, Uni. Zürich 1998.

2 Measurement of the Neutrino Magnetic Moment at the Bugey Nuclear Reactor

C. Amsler, O. Link and T. Speer

in collaboration with:
Institut des Sciences Nucléaires (Grenoble), Université de Neuchâtel, Università di Padova

(MUNU Collaboration)

2.1 Introduction

In the standard model the magnetic moment vanishes for massless neutrinos. Even for massive ν_e with masses in the range observed recently, the standard model predicts magnetic moments much below 10^{-20} μ_B, which are not accessible experimentally. The experimental evidence for a large magnetic moment would mean new physics beyond the standard model. With a finite magnetic moment the spin of a lefthanded neutrino may flip due to the electromagnetic interaction, and the neutrino becomes a “sterile” righthanded state which does not interact, and hence is experimentally invisible. The precession of a magnetic moment in the range $\mu_\nu \sim 10^{-10} - 10^{-12}$ μ_B in the solar magnetic field offers an alternative explanation to the MSW effect for the observed deficit of solar neutrinos.

We measure the magnetic moment of antineutrinos $\overline{\nu}_e$ from a nuclear reactor, using the elastic scattering reaction $\overline{\nu}_e e^- \to \overline{\nu}_e e^-$. This process is very sensitive to the magnetic moment of the $\overline{\nu}_e$ (especially at low neutrino and low electron recoil energies) because it is a purely leptonic and theoretically well understood weak process. A finite neutrino magnetic moment leads to an excess of forward scattered low energy electrons.

A detailed description of the apparatus can be found in Ref. [1, 2] and in previous annual reports. MUNU uses a 1 m^3 time projection chamber (TPC, gaseous CF_4 at 3 bar) surrounded by a tank filled with liquid scintillator to guard against cosmic muons and Compton scattering of low energy γ's. We measure both the angle and the energy of the recoil electron and hence can calculate the neutrino energy. The energy threshold for detecting electrons is typically 300 keV. We also measure simultaneously the signal and the background, since electrons cannot be scattered in the backward hemisphere.

2.2 Data analysis

The experiment works well since the beginning of 2001. We collected neutrino data during 111 days, corresponding to 68 days after deadtime subtraction. We also collected reactor off data during 37 days (24 days after deadtime subtraction). In addition, calibration data were recorded periodically for various triggers. A typical event is shown in Fig.2.1.

The data are being analysed following two different routes. In the first procedure (“visual” tracking, applied by the Neuchâtel group) every potential neutrino event is examined by eye and the scattering angle and recoil energy is determined. We briefly discuss the results from 30 days of neutrino runs with a high offline electron threshold of 700 keV. The lefthand side of Fig.2.2 shows the energy distribution of the recoil electrons for forward emission, i.e. for electrons emitted in the direction opposite to the reactor core. The distribution for backward electrons is also shown. Backward electrons do not stem from neutrino-electron scattering. Assuming that they are isotropically distributed we can subtract the two spectra to obtain the contribution from the signal events (Fig.2.2, right). The spectrum shows the expected

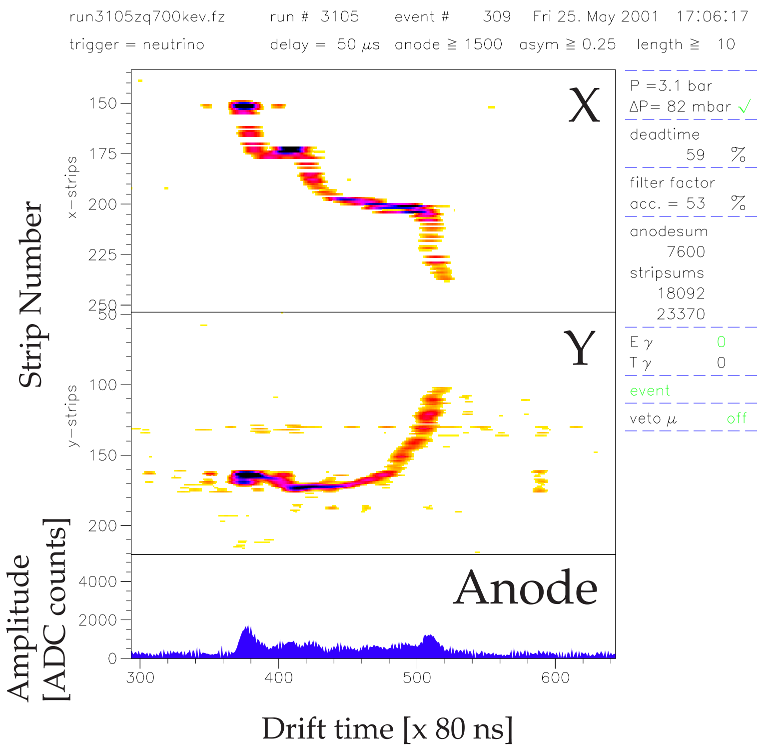

Figure 2.1: *Typical neutrino-electron scattering event visualised in the MUNU TPC. Shown are the x-z and y-z projections and the pulse height measured on the anode (bottom). Note the high ionisation rate of the electron at the end of its track (dark blob).*

shape, rising towards low electron energies. We obtain 95 ± 20 neutrino events for 30 days, while expecting 51 for a vanishing neutrino magnetic moment. We thus observe roughly twice as many events as predicted.

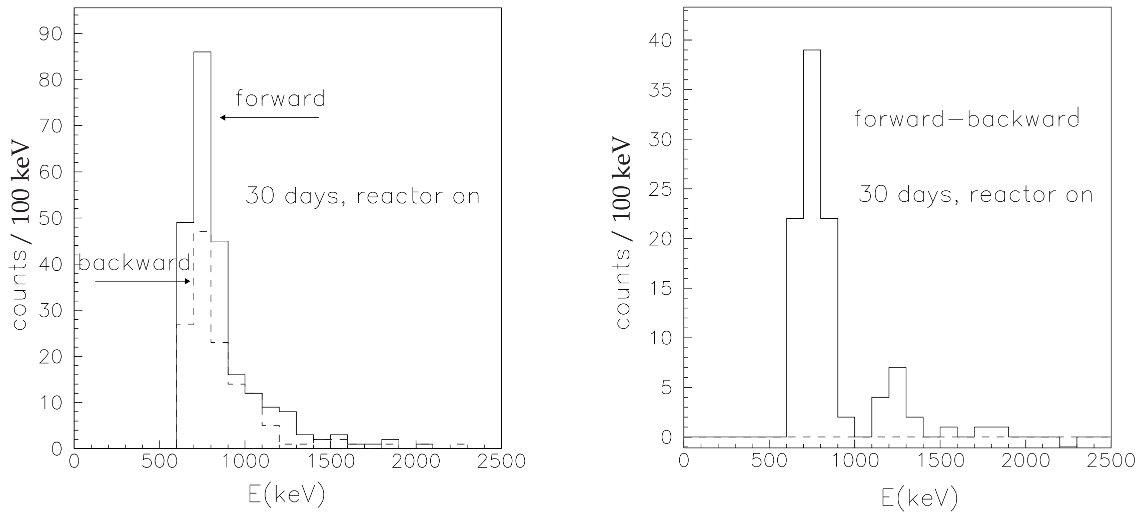

Figure 2.2: *Left: recoil energy distribution of electrons in the TPC for a 30 days run (visual tracking). Right: subtracted plot. The low energy cut is due to the offline threshold cut of 700 keV (the event drop below 700 keV is not sharp because a precise re-calibration of the anode pulse height was performed after the cut).*

In the alternative analysis (followed by the University of Zürich group) events are processed using a pattern recognition program ("automatic tracking"). With the automatic reconstruction program we should be able to analyse larger datasets, e.g. neutrino data with lower electron recoil energies. However, the software needs to be carefully tested and compared to Monte Carlo simulation. In fact, some of the early reconstruction algorithms were inappropriate and we had to rewrite part of the reconstruction software. We now describe in more details the analysis of about 24% of the data using the new automatic reconstruction software[3].

The typical TPC trigger rate of 100 Hz was reduced by the anti-Compton shield (which mostly removed the cosmic muons) to about 0.15 Hz. The size of an event was 600 kB and we collected 1.4 million raw data events on exabyte tapes with reactor ON. The data were first filtered to remove noise on the anode signal and to set a preliminary electron recoil energy threshold of 250 keV. Events with tracks crossing the anode led to fast photomultiplier signals and were removed. The anti-Compton veto was applied with a threshold of 100 keV and a first fiducial volume cut was applied to remove events with signals close to the edge of the TPC, i.e. those with a signal on the first or last $x-y$-strips (which are perpendicular to the axis z of the TPC).

These cuts led to 2.8×10^5 reactor ON events (and to 8.1×10^4 reactor OFF events) to be further processed by the pattern recognition programme. The point with the largest energy deposit (see Fig.2.1) determines the coordinates of the track endpoint (stopping electron). The track is then reconstructed and the vertex (neutrino-electron scattering point) determined independently in the $x-z$ and $y-z$ projections. The vertex position along z has to agree in either projection within a resolution of 1.4 cm determined by Monte Carlo simulation using GEANT. A new fitting procedure was developed to determine the azimuthal angle ϕ of the electron as the previous approach led to computational instabilities. The electron recoil angle (polar angle Θ) is finally determined knowing the position of the reactor core. The $\cos\Theta$ (Fig.2.3) distribution is now in much better agreement with the results from the visual tracking. The events are then written to data summary tapes.

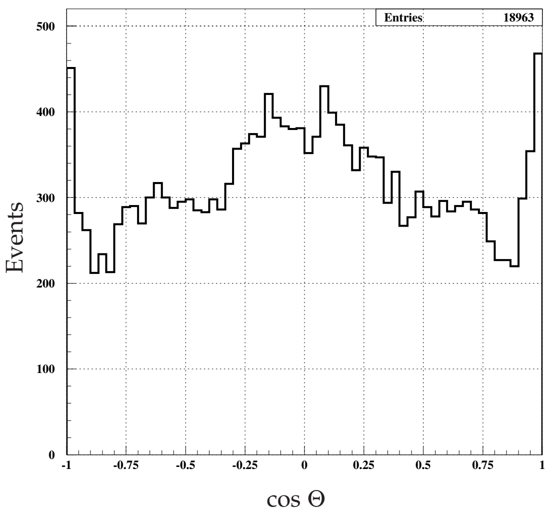

Figure 2.3: *Distribution of* $\cos\Theta$ *of recoil electrons for reactor ON events (not corrected for acceptance). The value* $\cos\Theta = 1$ *corresponds to the direction opposite to the reactor core.*

This reconstruction procedure was applied so far to 30% of the available 2.8×10^5 reactor ON events (and to 56 % of the reactor OFF events). Further cuts were then applied: (i) an electron threshold cut of 500 keV, (ii) a fiducial volume cut of 42 cm around the TPC axis and (iii) a drift time cut ensuring that the track is confined within 40 μs (the maximum drift time of the TPC), (iv) a positive neutrino energy, reconstructed from the recoil angle and recoil energy. We obtained 160.4 $\pm$ 2.8 events/day in the forward hemisphere (hence opposite to the reactor core) and 155.1 $\pm$ 2.8 events/day in the backward hemisphere. This leads to a forward/backward asymmetry A_{FB} of 5.3 $\pm$ 4.0 events/day (the corresponding asymmetry for reactor OFF events is -4.1 $\pm$ 5.0). Figure 2.4 shows A_{FB} as a function of electron energy. The electroweak prediction without contribution from the neutrino magnetic moment is shown as well.

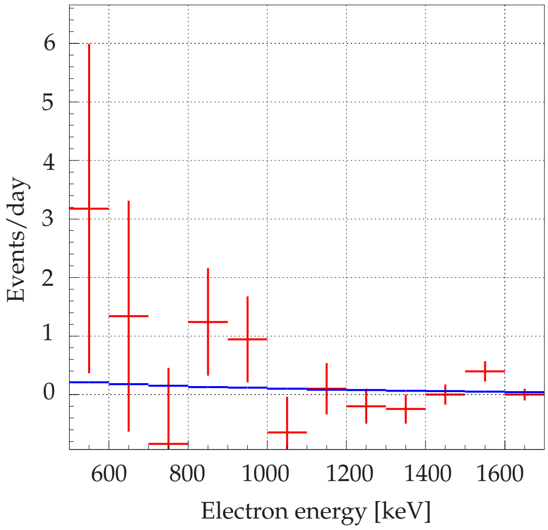

Figure 2.4: *Forward/backward asymmetry A_{FB} as a function of electron energy (crosses). The solid histogram shows the expected electroweak signal assuming a vanishing magnetic moment.*

As for the visual tracking at 700 keV threshold, we find about twice as many events as expected. Of course the statistical significance is not yet sufficient to claim a non-vanishing magnetic moment, but another 75% of the data remain to be processed. We find from these results a preliminary 90% confidence level upper limit of 3 $\times 10^{-10}$ μ_B. Previous laboratory experiments led to upper limits of $\mu_\nu <$ 1.9$\times$ 10^{-10} μ_B [4] and 1.5 $\times$ 10^{-10} μ_B [5]. The astrophysical upper limits, e.g. from SN1987A, are lower by two orders of magnitude but make assumptions, in particular that the neutrino is a Dirac particle. On the other hand, it is interesting to note that a reanalysis of Reines' Savannah data[6] led to a magnetic moment of the size of our upper limit, when taking into account today's improved knowledge of reactor spectra[7].

Data taking for this experiment was completed in autumn 2001. The detector is currently running at 1 bar, and various calibrations are being performed before de-commissioning in 2002.

References

[1] C. Amsler *et al.*, Nucl. Instr. Methods **A 396** (1997) 115.

[2] M. Avenier *et al.*, Nucl. Instr. Methods in Phys. Research (in print).

[3] O. Link, PhD thesis, Universität Zürich, in preparation.

[4] A. I. Derbin *et al.*, JETP Lett. **57** (1993) 768.

[5] J.F. Beacom and P. Vogel, Phys. Rev. Lett. **83** (1999) 5222.

[6] F. Reines, H.S. Gurr and H.W. Sobel, Phys. Rev. Lett. **37** (1976) 315.

[7] P. Vogel and J. Engel, Phys. Rev. **D39** (1989) 3378.

3 Search for μ-e Conversion with SINDRUM II

Andries van der Schaaf

in collaboration with: Willi Bertl, PSI

The measurements discussed here were performed in the year 2000 by: W. Bertl, F. Rosenbaum and N.M. Ryskulov, Paul Scherrer Institute, R. Engfer, E.A. Hermes, G. Kurz, A. van der Schaaf and P. Wintz, Physik-Institut der Universität Zürich, J. Kuth and G. Otter, RWTH Aachen, and T. Kozlowski and I. Zychor, IPJ Swierk.

(SINDRUM II Collaboration)

3.1 Data taking stopped

In the year 2000 SINDRUM II raised the sensitivity to neutrino-less μ-e conversion on heavy targets by two orders of magnitude. In a preliminary analysis [1] no signal was observed and since no further large improvements in sensitivity can be expected the experiment was stopped.

In the past year the two of us left to finish the project have focused on a better understanding of the observed electron distribution which has a dominant contribution from μ^- decay in orbit (MIO). Other sources of electrons, such as radiative muon capture followed by $\gamma \to e^+e^-$ or μ^- decay in flight, have contributions of $O(\%)$ which can be ignored. Once a good description of the observed distributions has been obtained a reliable estimate can be made of the new limit on μ-e conversion on gold.

3.2 High-momentum component of decay electrons from muonic gold

The energy distribution of electrons from the decay of free muons at rest peaks at the kinematic endpoint $m_\mu c^2/2$. In muonic atoms the endpoint is raised to $m_\mu c^2 - B - R$, with B: μ^- binding energy and R: nuclear recoil energy. The energy distribution has been calculated for various cases. We use results for lead [2] correcting for the 0.54 MeV shift in endpoint energy. The resulting spectrum is shown in Fig.3.1.

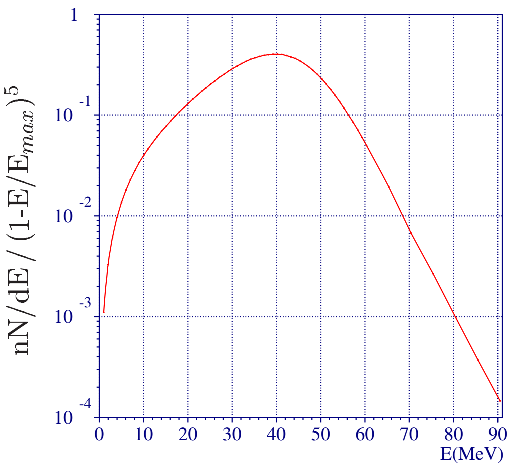

Figure 3.1: *Theoretical energy distribution weighed by 1/(1-E/E$_{max}$)^5 for electrons from the decay of muonic gold. Note the linear energy dependence above 60 MeV resulting from the weighting. The yield per stopped muon drops to* 5.15×10^{-7}, 5.67×10^{-8} *and* 4.36×10^{-9} *for energy thresholds of 70, 75 and 80 MeV, respectively.*

Detailed studies were made of:

- *the number of muon stops*

  The number of muons stopping in the target was measured during the experiment by observing the characteristic muonic gold X-rays penetrating the superconducting coil of the spectrometer (see figures 3.2 and 3.3). The sensitivity of the monitor was determined by simulation and reproduced with an accuracy of 3 % by a calibration using ^{137}Cs and ^{60}Co sources. The number of muons stopping during the live time of the experiment was determined as:

$N_\mu^{stop} = (4.30 \pm 0.3_{stat} \pm 0.3_{sys}) \times 10^{13}$.

- *exact geometry of the spectrometer.*

  Careful adjustments were made of the parameters in the simulation that describe the relative positions of the various detector components and vacuum flanges.

- *position of the two gold tubes used as stopping target* and *the distribution of muon stops over the target.*

  As can be seen from the distributions of Fig. 3.4 the target was off centre by more than a centimetre which has a strong effect on the acceptance of the spectrometer at the low end of the observed energy distribution. Better knowledge of the target geometry also allows a better suppression of backgrounds from cosmic rays and reconstruction errors.

- *variations of the tracking efficiency during data taking.*

  Tracks in the main drift chamber have typically thirty anode hits and roughly half of them have cathode information as well. During the measurements this single-hit cathode efficiency varied within a factor two, however, depending on parameters such as gas quality and chamber high voltage.

- *precision of the tracking detector.*

  The observed position resolution versus drift time was implemented in the event simulation.

- *the efficiency of the Cerenkov end-cap detector.*

  For a correct description of the observed distribution of polar angle it is crucial to account for the angular dependence of the light collection efficiency.

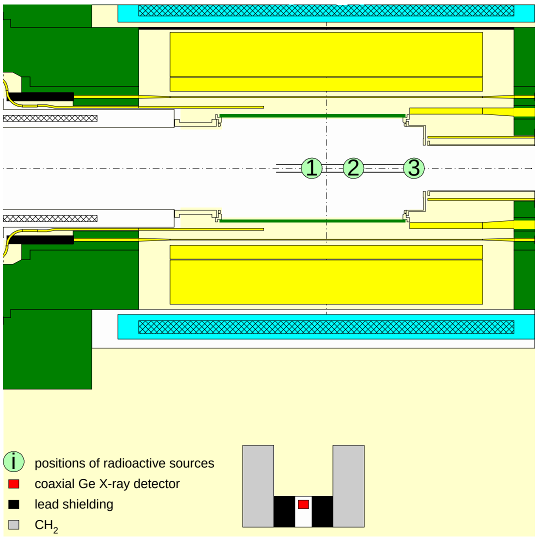

Figure 3.2: *Horizontal cross-section through the spectrometer showing the location of the X-ray monitor.*

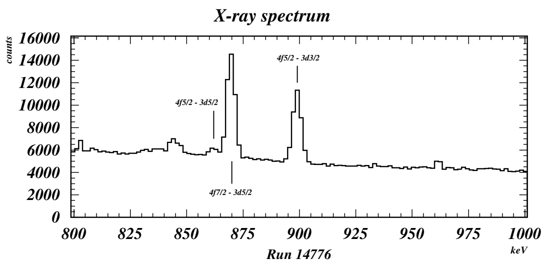

Figure 3.3: *X-ray spectrum accumulated during 3 hours of μe data taking.*

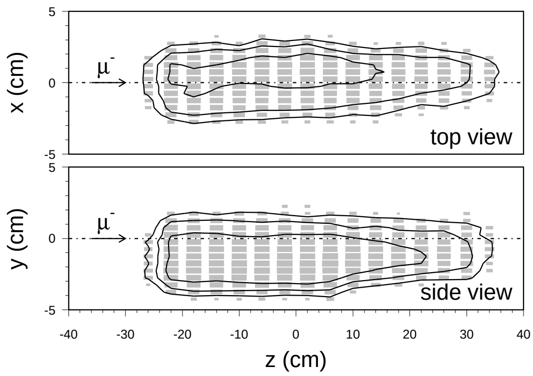

Figure 3.4: *Distributions of the trajectory's point of closest approach to the spectrometer axis. The target consisted of two tubes of 32 cm length each. As can be seen the downstream target had a slightly smaller diameter (38 mm, as compared to 45 mm for the upstream tube).*

- *calibration of the field/current relation.*

  The momentum calibration is done with the endpoint of the *Michel* decay $\mu^+ \to e^+\nu\overline{\nu}$ taken with scaled and reversed spectrometer field. Since there appears to be an offset in the setting of the power supply we measured the scaling factor directly with a Hall probe.

- *the inhomogeneity of the magnetic field*

  The spectrometer field drops by $\approx$ 10% towards the downstream end of the tracking region. Ten years ago the field was precisely mapped and the observed distribution is taken into account in the momentum fit. Recent changes in the downstream mirror plate led to further distortions in the field shape. We determined their effect on the momentum calibration by studying the endpoint of the $\mu^+ \to e^+\nu\overline{\nu}$ decay versus polar angle. Figure 3.5 shows the resulting spectrum, which is in perfect agreement with the expectations from the event simulation.

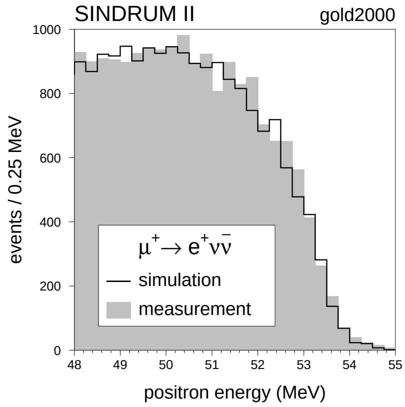

Figure 3.5: *Positron energy distributions for μ^+ beam and scaled spectrometer field.*

Figure 3.6 compares the measured energy and angle distributions with the predictions from the GEANT simulation. The shape of the stop distribution along the target was adjusted. The agreement is quite satisfactory given the 10-20% errors introduced by uncertainties in quantities such as the number of stopped muons, the value of the magnetic field, the shape of the beam profile, the trigger and selection efficiencies. The structure in the φ distribution reflects the shift in the target position. The dip around $\theta = 90^o$ is caused by the endcap requirement. The drop of the event rate towards lower energies is caused by the lower threshold on tranverse momentum resulting from the cylindrical symmetry of the spectrometer. The overall efficiency varies as a function of electron energy: from $\approx$ 1% around 75 MeV where the event rate has its maximum to $\approx$ 10% in the region of interest for μe conversion. As a next step we will focus on that region.

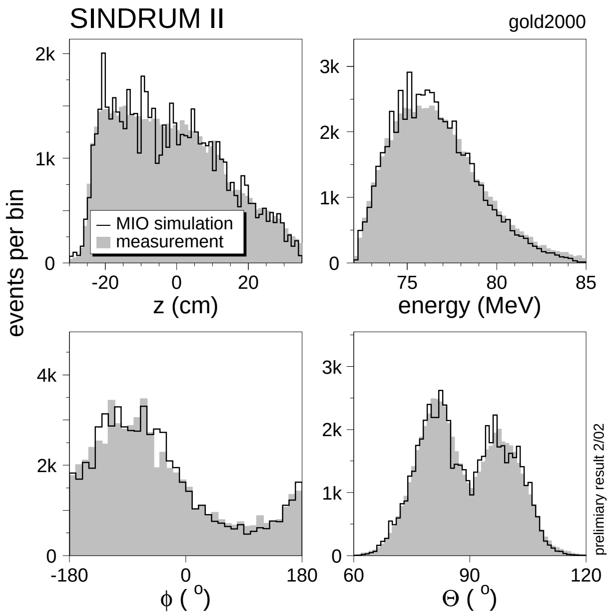

Figure 3.6: *Comparison of measurement and simulation of muon decay in orbit for various kinematic quantities.*

References

[1] SINDRUM II Collab., Annual Report 2000-2001, Physik-Institut, Zurich University.

[2] R. Watanabe *et al.*, Atom. Data and Nucl. Data Tab. **54** (1993), 165.

4 Production and Spectroscopy of Antihydrogen

C. Amsler, A. Glauser, D. Grögler, O. Iannarelli, D. Lindelöf, N. Madsen, H.P. Meyer, H. Pruys, and C. Regenfus

collaboration with:
CERN, MIT, Universities of Aarhus, Brescia, Genoa, Pavia, Rio de Janeiro, Tokyo, Wales

(ATHENA/AD-1 Collaboration).

4.1 Introduction

The physics goal of the ATHENA experiment [1] is a direct comparison of the properties of antihydrogen and hydrogen atoms (for a recent review, see Ref.[2]). The final target is the most precise test of CPT invariance in the lepton and baryon sector. The long lifetime (122 ms) of the metastable (anti-)hydrogen 2S level is associated with a relative natural line width of 5×10^{-16} for the 1S-2S transition, which can be exploited by two-photon laser spectroscopy. In addition, such high precision measurements would give valuable experimental information on the gravitational interaction of antihydrogen, because a change in the 1S-2S transition frequency could also originate from a different redshift of antihydrogen and hydrogen atoms in the gravitational field of the earth. So far, only the existence of antihydrogen was demonstrated experimentally with the production of a few dozens of energetic antihydrogen atoms at LEAR [3] and at FNAL [4].

The current phase 1 of ATHENA is devoted to the formation of large quantities of antihydrogen atoms in Penning traps, with the goal of obtaining large rates ($>$ 1 Hz) at the lowest possible kinetic energy ($<<$ 1 eV). The formation rate depends on the densities of antiproton and positron plasmas, the absolute number of particles, their temperature, and on the trap potentials. The result of these studies will determine the apparatus of phase 2, the laser spectroscopic precision measurements.

The ATHENA apparatus was installed and commissioned in 1999/2000 at one of the three extraction lines of the new Antiproton Decelerator (AD) at CERN. The AD captures 5×10^7 antiprotons at 3.5 GeV/c and decelerates them to 100 MeV/c (5.3 MeV kinetic energy), using stochastic and electron cooling, before extracting the antiproton bunch within 250 ns. Steady improvements by the AD team resulted in an intensity of 3–4×10^7 antiprotons per spill, with a cycle time of 96 seconds. The number of antiprotons per bunch is now exceeding the value given in the design report.

4.2 Experimental setup

The apparatus (Fig.4.1) consists of (i) an antiproton capture trap and a recombination trap, located in a cryogenic vacuum enclosure inside a large bore 3 T solenoid, (ii) a positron accumulator for collecting, cooling and transferring a large number of positrons ($> 10^8$) every 3–5 minutes to the recombination trap, and (iii) a high granularity large solid angle antihydrogen detector. More details on the apparatus are given in previous annual reports.

The incoming antiproton pulse is monitored by a 67 μm thin segmented silicon beam counter. The range of antiprotons with kinetic energy of 5.3 MeV is only about 200 μm in silicon. The amount of material in the beam was carefully optimised to obtain the maximum number of captured antiprotons by introducing a foil with variable tilt angle. The optimum thickness was determined by trapping antiprotons, releasing them after a delay of several

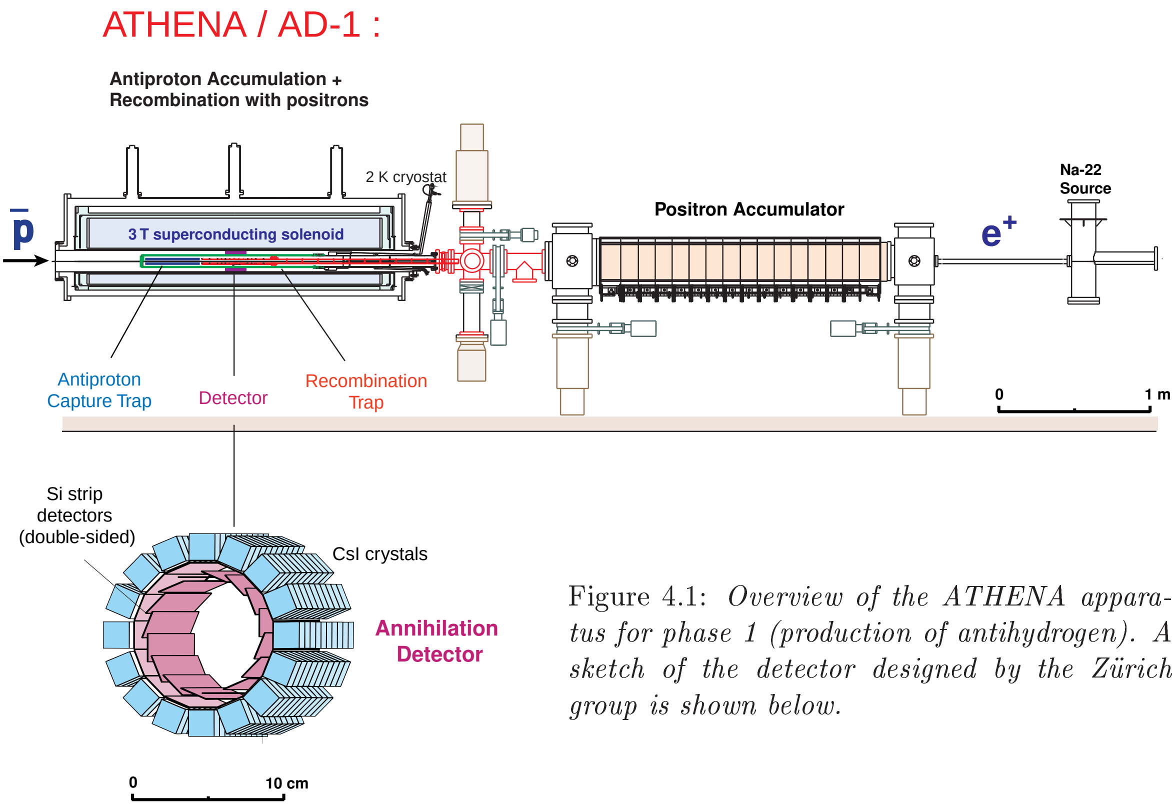

Figure 4.1: *Overview of the ATHENA apparatus for phase 1 (production of antihydrogen). A sketch of the detector designed by the Zürich group is shown below.*

seconds and measuring the number of annihilations. After determination of the optimal value, the tilted foil was removed and 44 μm of aluminium was added to the degrader material at the trap entrance.

The antiproton catching trap consists of cylindrical electrodes of various lengths and radii 1.25 cm made of gold-plated aluminium. Seven electrodes are used to create a harmonic field region in the capture region, three upstream and downstream to shape the electric field during various phases of particle transfer and handling, and two at the ends for applying the high voltage necessary to capture antiprotons. The exit electrode is biased to –10 kV. The entrance electrode (HVL) is quickly lowered to –10 kV, triggered by the signal from an external scintillator monitoring the arrival of antiprotons. We are able to capture about 20'000 antiprotons from a single AD shot of a few 10^7 antiprotons.

Before antiproton injection, a few 10^8 electrons are loaded from an electron source (heated filament). The electron cloud quickly cools down to ambient cryogenic temperature (10 K) by emitting synchrotron radiation. Antiprotons with energies in the keV range are then cooled within 20-30 s by interactions with the cold electrons stored in the central part of the catching trap. The lifetime of cooled antiprotons was measured to exceed ten hours. The high voltage electrodes could then be lowered to capture further $\bar{p}$ and several AD shots were successfully stacked.

Positrons are emitted from a 50 mCi ^{22}Na source. After moderation in solid neon the low energy beam of 7×10^6 positrons/s is guided into a 0.14 T magnetic field. The positrons enter an array of cylindrical electrodes, which have increasing radii and are biased at appropriate electric potentials. They are moderated by inelastic collisions with a nitrogen buffer gas. The size and radial position of the plasma is measured by dumping the positrons on a movable, segmented Faraday cup detector. One of the trapping electrodes is split into six azimuthal segments to compress the plasma by applying a rotating electric field of several hundred

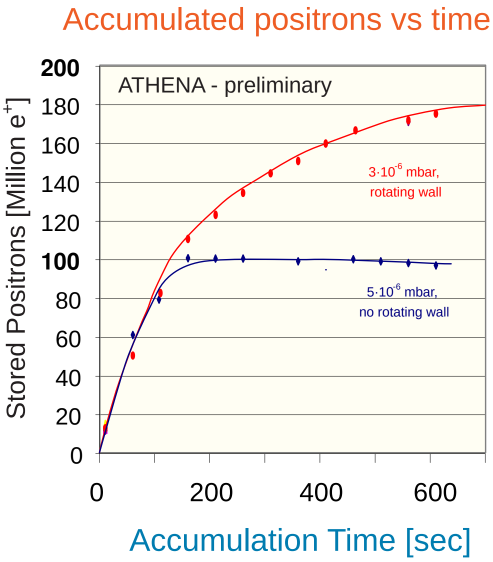

Figure 4.2: *Number of trapped positrons as a function of time, with and without rotating wall compression.*

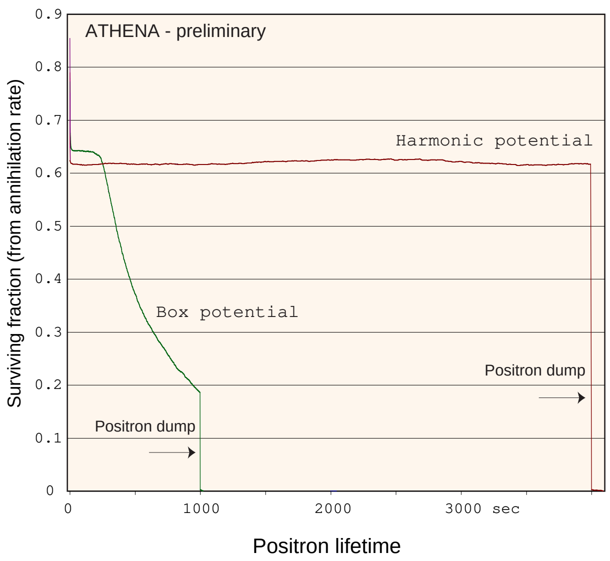

Figure 4.3: *Positron lifetime in the recombination trap, using a box potential or a harmonic trap potential.*

kHz ("rotating wall"). During compression the plasma is cooled by the nitrogen buffer gas. The rotating wall technique reduces the diameter of the positron plasma from 15 to 4 mm. Figure 4.2 shows the number of positrons accumulated as a function of time: $1.7\ \times 10^8$ positrons were accumulated in 450 seconds while without compression this number drops to about 10^8.

Positrons are transferred into the recombination trap by extracting the positron cloud from the accumulator trap: the buffer gas is pumped out and a magnet is turned on (1.2 T in 20 ms). The electrostatic trap is opened and the transfer electrodes are biased to accelerate the positrons towards the recombination trap. The transfer efficiency is measured by shooting the positrons directly on a Faraday cup and by measuring the annihilation signal with a CsI detector. Positrons are routinely transferred with efficiencies exceeding 50 %. The positrons are captured within 1 s in the recombination region, where they cool by synchrotron radiation to the ambient temperature (10 K). Positron lifetimes of several hours have been achieved with a harmonic trap potential (Fig.4.3) and about 25 million trapped and cooled positrons were observed.

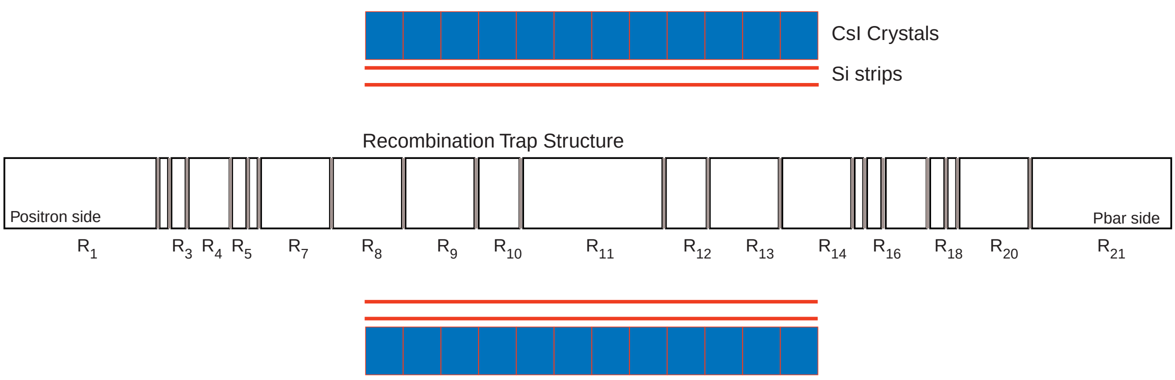

Figure 4.4: *Side view of the recombination trap and the antihydrogen detector.*

The recombination trap (Fig.4.4) consists of 21 cylindrical electrodes with radii 1.25 cm and a total length of 41 cm. With this complicated structure we will be able to cool and compress the positron cloud with the rotating wall technique, store the anitiprotons transferred from the capture trap, overlap the antiproton and positron clouds, and monitor the plasma parameters (density, temperature).

The antihydrogen detector built by the Zürich group is now commissioned and is being used to detect antiproton and positron annihilations with the rest gas or the trap electrodes and to measure the position, size and shape of the plasma. The compact and highly granular detector observes the annihilation products of antiproton and positron annihilations. Since antihydrogen atoms are not confined by the electromagnetic fields of the recombination trap, they propagate freely and annihilate at the electrode surfaces within 1 ms. To maximise the detection efficiency, the detector is installed as close as possible to the recombination trap, inside the vacuum bore of the superconducting solenoid and around the cold nose containing the recombination trap system. Antiproton annihilation produces on average three charged pions and three high energy γ's while positron annihilation produces two 511 keV back-to-back photons (Fig.4.5). The charged pions are detected in two cylindrical layers of 16 double-sided silicon microstrip detectors (8192 channels) at average radii of 3.9 cm and 4.5 cm, respectively. The 511 keV photons from positron annihilation are detected by 16 rows of 12 pure CsI crystals (13 x 17.5 x 17 mm^3) read out by photodiodes. Figure 4.6 shows a photograph of the detector assembly. Details can be found in previous annual reports, diploma works [5] and in Ref.[6].

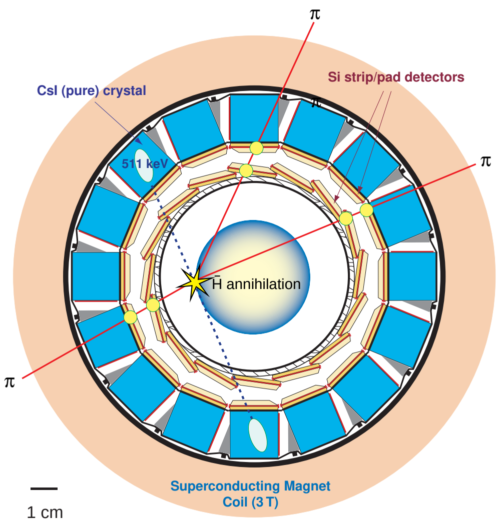

Figure 4.5: *Antihydrogen annihilation detector.*

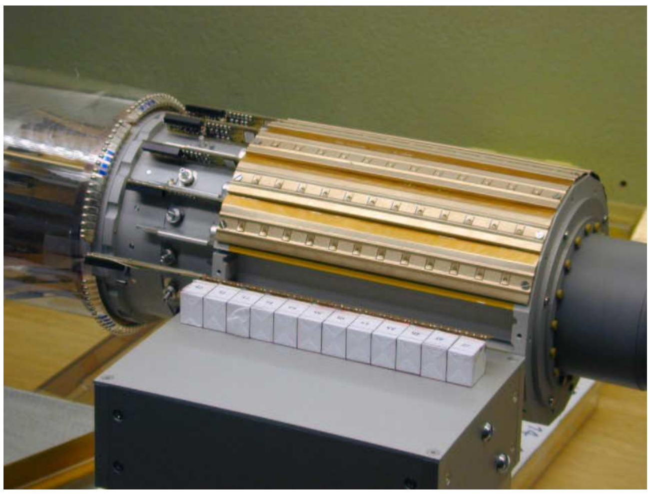

Figure 4.6: *Antihydrogen detector during assembly showing a row of crystals.*

A high granularity of the detector and good resolution on the photon energies are required by background considerations: antiproton annihilating on the electrode surface can fake antihydrogen annihilation, since high energy photons from the annihilation convert e.g. in the magnet coil, creating positrons which annihilate outside the detector region. This background can be suppressed by requiring the two back-to-back 511 keV photons to emerge from the annihilation vertex. The latter is determined from the tracks of the emitted pions and is required to lie at the electrode radius. The resolution on the annihilation vertex is 3 mm (r.m.s).

The detector located inside the cold bore of the magnet is operated at a temperature

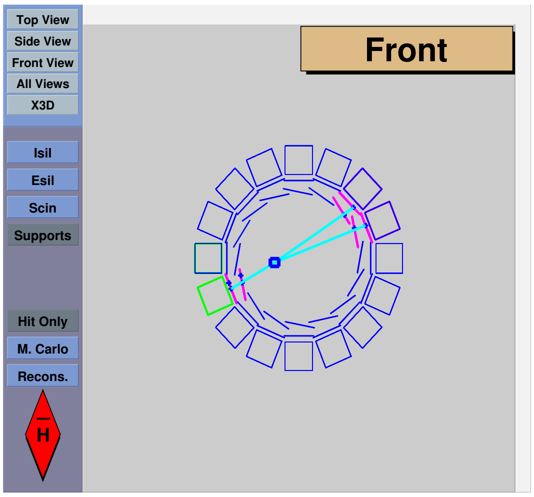

Figure 4.7: *Event display of a 3-prong annihilation event from a trapped antiproton hitting the cylindrical electrode. The hits in the strip detectors and the associated crystals are visible.*

between 77 and 140 K. The performance of pure CsI crystals and photodiodes (light yield and efficiency) were measured at low temperature: the photon yield at 80 K is on average, 30'000 per MeV, as compared to 3'200 per MeV at room temperature. A record value of 50'000 per MeV was reported [6]. The first annihilations from antiprotons in the recombination trap were observed during summer 2001. Figure 4.7 shows a 3-prong annihilation event from a trapped antiproton.

The capability to measure the vertex of antiproton annihilations with rest gas atoms or on trap electrodes is a new tool for (destructive) plasma diagnostics. We can monitor the shape of the antiproton cloud and follow its evolution in time. Figure 4.8 shows the $\bar{p}$ annihilation vertex distribution in the recombination trap in three projections. Annihilations on a trap electrode at a radius of 1.25 cm are visible. Annihilations at smaller radii are due to collisions with rest gas atoms. The resolution of σ= 3–4 mm stems from the unknown track curvatures in the magnetic field (which cannot be measured with two layers of strip detectors) and is fully compatible with expectations.

The transfer, capture and storage of positrons in the recombination trap can be monitored by measuring their annihilations with our CsI crystals. The annihilation signal from one of the 192 crystals is shown in Fig.4.9 and the energy distribution of the 511 keV γ's in Fig.4.10.

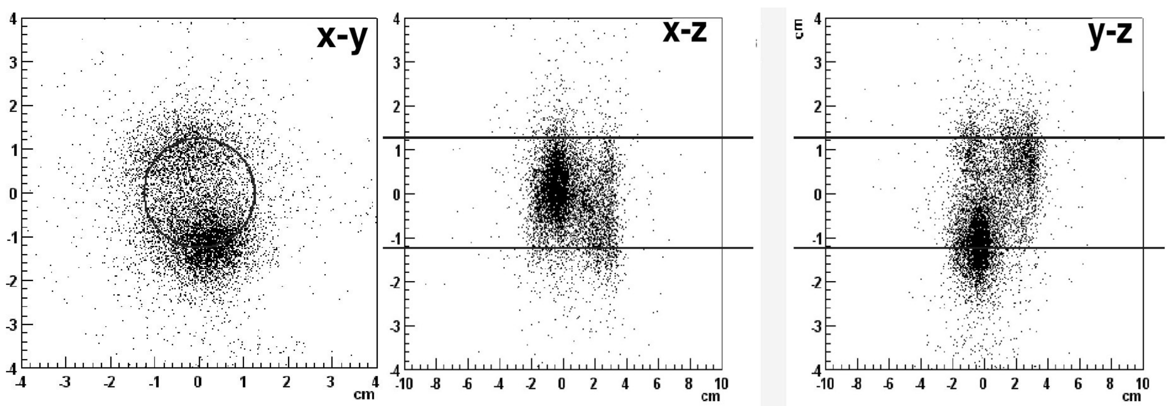

Figure 4.8: *Distribution of the antiproton annihilation vertices in the three projections; the z direction is the along the symmetry axis of the cylindrical trap. The lines show the boundary (wall) of the trap.*

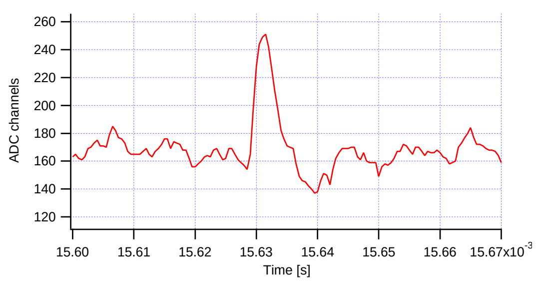

Figure 4.9: *Time signal from a 511 keV photon observed in one of the 192 CsI crystals of the antihydrogen detector surrounding the recombination trap filled with positrons at a temperature of 140 K.*

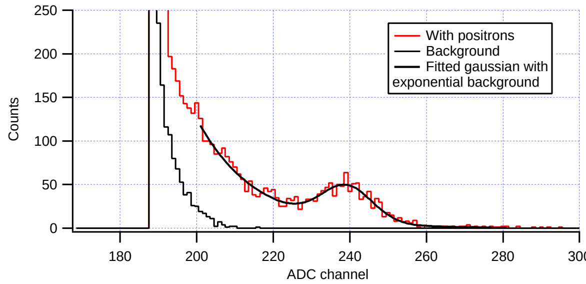

Figure 4.10: *γ-Energy distribution from a CsI crystal when the trap is filled with positrons. Top: spectrum from e^+e^- annihilation, with a clear peak at 511 keV, and a shoulder due to Compton scattered gammas. Bottom: background spectrum.*

The background spectrum is clearly separated from the 511 keV peak and its associated Compton edge.

4.3 Avalanche photodiodes

To reduce costs and also to match the surface of our crystals the photodiodes were manufactured from the same wafers as the silicon strip detectors, with very thin entrance windows to maximise the efficiency for detection of blue light from CsI. However, we discovered during the 2001 runs that the electronic noise from many of the SINTEF photodiodes had increased substantially, reaching unacceptable levels (signal over noise ratio of 5 or less) so that 511 keV photons could not be detected with the good resolution (better than 10% [6]) achieved previously. The problem was traced to oxidation of the electrical contacts to the photodiode (possibly due to the iodine of CsI). Commercially available Hamamatsu pin-photodiodes were found to yield insufficient electron/hole pairs, essentially due to their small size.

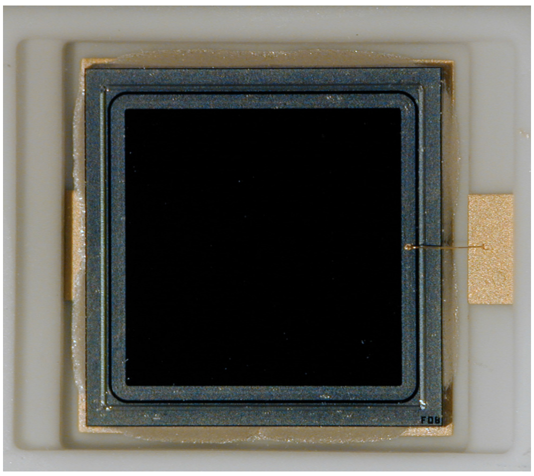

Figure 4.11: *Avalanche photodiode (5 × 5 mm^2) used for the CMS experiment with its epoxy window removed.*

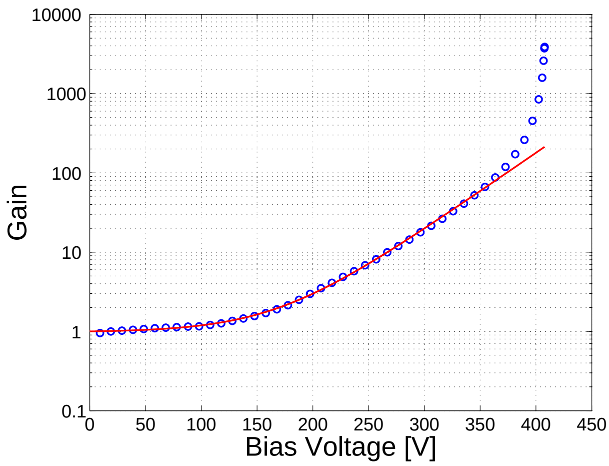

Figure 4.12: *Gain of an avalanche photodiode at room temperature as a function of bias voltage V. The curve is a fit with a function of the form $a + b\exp(cV)$.*

As an alternative solution we tried avalanche photodiodes (APD) which have the advantage of a large gain and hence a much better signal-over-noise ratio. Encouraging tests were performed with spare APD's obtained from the CMS experiment not satisfying their stringent gain requirements. However, we first had to remove the epoxy windows which break at liquid nitrogen temperature. The best stripping agent was found to be sulfuric acid. Figure 4.11 shows a photograph of one of the 300 APD's purchased from CMS (a small batch from their 160'000 supply!). The gain of the APD as a function of bias voltage was measured with a pulsed (blue) light emitting photodiode (Fig.4.12). The plateau at low voltage corresponds to unit gain, the rise is due to the generated avalanche in the diode. The voltage at which multiplication starts depends on temperature. The advantage of APD's for ATHENA is the very low dark current at low temperature, so that the signal can be amplified to very high values (with a gain of 10^4 a signal-over-noise ratio of the same order of magnitude can be reached for 511 keV photons!). The useful gain is however limited by our VA2 preamplifiers. We settled for a gain of 20 (compared to 50 for CMS) corresponding to a signal-over-noise ratio of about 100.

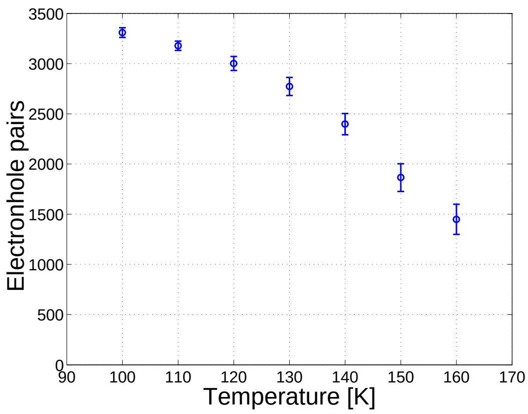

Figure 4.13: *Number of primary electron-hole pairs in the APD per 1 MeV energy loss in CsI, as a function of temperature.*

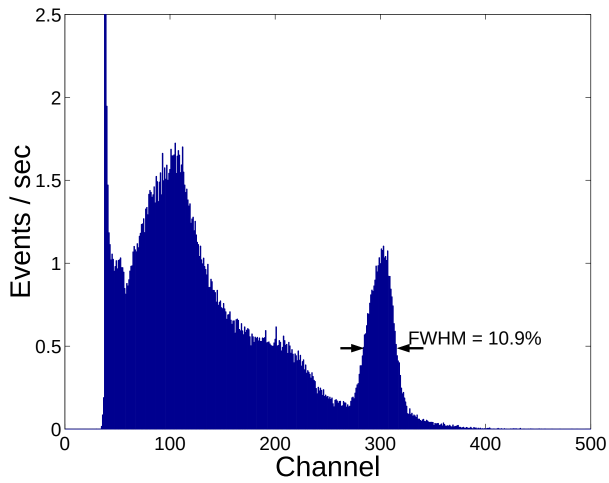

Figure 4.14: ^{137}*CsI spectrum from a CsI crystal coupled to an APD measured at liquid nitrogen temperature. The 662 keV photopeak has a resolution of 10.9 % (FWHM) and the Compton shoulder is clearly visible.*

Figure 4.13 shows the number of electron-hole pairs produced for an energy loss of 1 MeV in the CsI crystals. The typical yield of about 3'000/MeV is much lower than our 30'000 with SINTEF diodes [6]. This is due to the much smaller size of the APD's (5 $\times$ 5 mm^2 compared to 17 $\times$ 13 mm^2) and also to the thin air gap between the diode and the crystal. However, the energy resolution is now determined by the light collection efficiency while noise becomes negligible. The resolution is not significantly worse than that obtained with SINTEF diodes (Fig.4.14).

We also found that APD's were much more sensitive to the blue component of light than to the red one. Therefore the red dye used previously as wavelength shifter to coat the crystals was removed and all SINTEF diodes replaced by APD's for the forthcoming 2002 runs.

4.4 Summary and outlook

To summarise, in 2001 ATHENA demonstrated the trapping, cooling and transfer to the recombination trap of 2×10^4 antiprotons. Several antiproton shots were stacked in the antiproton capture trap where a lifetime of 10 hours was measured. This allows us to reach the target of 10^5 stored and cooled antiprotons. In the positron accumulator we accumulated 1.5×10^8 positrons in five minutes which corresponds to an increase by two orders of magnitude with respect to the previous year. The transfer of 10^8 positrons from the accumulator to the recombination trap was demonstrated. Trapping and cooling led to 2.5×10^7 positrons with a lifetime of several hours. The target of 10^8 stored and cooled positrons is thus within reach.

The main goal for the coming year is to store simultaneously 10^5 antiprotons and 10^8 positrons in the recombination trap. We will search for annihilation of antihydrogen atoms hitting the electrodes using the antihydrogen detector. We will drive the antiprotons through the positron plasma with a frequency which maximises the spontaneous antihydrogen formation rate while keeping the positron temperature as low as possible. Once the production of antihydrogen has been demonstrated we will measure its production rate as a function of plasma density and temperature, number of particles and trap potentials. Based on the $\bar{p}$ and e^+ intensities given above and on theoretical models of spontaneous radiative recombination, we expect the production of about 0.1 to 1 antihydrogen atom per second. Depending on the yield of anti-atoms with very low kinetic energy (<0.05 meV), the optimal setup for a 1S-2S precision experiment will be designed. Meanwhile the Zürich group is involved in the preparation of the laser system, in particular the frequency doubler to produce the 243 nm light inducing the 1S to 2S transition by recoilless two-photon absorption. The year 2002 promises to be very exciting.

References

[1] ATHENA proposal, M.H. Holzscheiter *et al.*, CERN-SPSLC/P302, October 1996, see also http://www.cern.ch/athena/.

[2] M. H. Holzscheiter and M. Charlton, Rep. Prog. Phys. 62, 1 (1999);
see also C. Amsler *et al.*, *Antihydrogen Production and Precision Spectroscopy with ATHENA*, in "The Hydrogen Atom, Precision Physics of Simple Atomic Systems", edited by S.G. Karshenboim *et al.*, Springer Lecture Notes in Physics, Berlin, 2001, p. 469-488.

[3] G. Baur *et al.*, Phys. Lett. B368 (1996) 251.

[4] G. Blanford *et al.*, Phys. Rev. Lett. 80 (1998) 3037.

[5] P. Niederberger, *Untersuchung von CsI-Szintillatoren bei tiefen Temperaturen*, Universität Zürich, 1999;
R. Brunner, *Aufbau und Test eines Microstrip-Detektors für das ATHENA-Experiment*, Universität Zürich, 2000;
D. Grögler, *Temperature Dependence of Pure CsI between 77 K and 165 K and the Performance of Wavelength Shifters*, Universität Zürich, 2000.

[6] C. Amsler *et al.*, N.I.M. **A** 480 (2002) 492.

5 Rare Kaon Decays at Brookhaven AGS

H. Kaspar (visiting scientist), P. Robmann, A. van der Schaaf,
S. Scheu, A. Sher and P. Truöl

The two projects discussed below exploit the unique low-momentum neutral and charged kaon beams available at Brookhaven National Laboratory's Allernating Gradient Synchrotron (AGS). Although BNL E-865 finished data-taking four years ago the analysis of the huge amount of recorded data is still in progress. KOPIO on the other hand is still in its planning phase. The experiment has been approved both by BNL and the U.S. National Science Foundation which reserved major funds for the combined MECO/KOPIO proposal [21]. MECO is a new search for $\mu - e$ conversion down to a sensitivity level of 10^{-16}.

5.1 BNL E-865: a search for lepton flavor violation in K^+ decay.

in collaboration with:
Paul–Scherrer–Institut, CH-5234 Villigen, Brookhaven National Laboratory, Upton, NY-11973, USA, University of New Mexico, Albuquerque, NM-87131, USA, University of Pittsburgh, Pittsburgh, PA-15260, USA, Yale University, New Haven, CT-06511, USA, Institute for Nuclear Research, Academy of Sciences 117 312 Moscow, Russia

While the analysis of the data for the lepton flavor violating decay $K^+ \to \pi^+\mu^+e^-$ ($K_{\pi\mu e}$), the primary goal of experiment E-865 at the Brookhaven AGS [1], is still in progress, the analysis of two further decay channels recorded in parallel has been concluded last year.

5.1.1 $K^+ \to \pi^+\pi^-e^+\nu_e$

The analysis of the $K^+ \to \pi^+\pi^-e^+\nu_e$ (K_{e4}) event sample has been published [2]. As reported already last year we collected more than ten times the number of events for this decay channel than all previous experiments combined. The model independent analysis of these data yielded the momentum dependence of the form factors of the hadronic currents as well as $\pi\pi$ scattering phase shifts. The form factors and phase shifts have served as an important input in the program to determine the couplings of the effective Hamiltonian of chiral QCD perturbation theory (ChPT) at low energies [3]. Furthermore, tight bounds on the value of the quark condensate, the fundamental order parameter of ChPT have been extracted [4]. Based on a suggestion of the authors of Ref. [4] we have slightly extended our analysis for our publication. The phase shifts can be related to the s-wave scattering lengths a_0^0 and a_0^2 for the isospin $I = 0$ and the $I = 2$ channel, respectively, using analyticity via the so-called Roy equations [5]. The values of the scattering lengths are restricted to a band in the a_0^0 versus a_0^2 plane by analyticity[5]:

$$a_0^2 = -0.0849 + 0.232a_0^0 - 0.0865(a_0^0)^2 \quad [\pm 0.0088] \ .$$

The centroid of this band is known in the literature as the *universal curve* [6]. The allowed region reduces considerably, if chiral symmetry constraints are imposed [4]:

$$a_0^2 = -0.0444 + 0.236(a_0^0 - 0.22) - 0.061(a_0^0 - 0.22)^2 - 9.9(a_0^0 - 0.22)^3 \quad [\pm 0.0008] \ .$$

From analyticity alone we obtain the result quoted last year:

$$a_0^0 = 0.228 \pm 0.012(\text{stat.}) \pm 0.003(\text{syst.})^{+0.006}_{-0.012}(\text{theor.}) \ , \tag{5.1}$$

while with the chiral symmetry constraints, we obtain:

$$a_0^0 = 0.216 \pm 0.013(\text{stat.}) \pm 0.004(\text{syst.}) \pm 0.005(\text{theor.}) \ . \qquad (5.2)$$

This value agrees well with the latest ChPT prediction ($a_0^0 = 0.220 \pm 0.005$ [7]).

5.1.2 $K^+ \to \mu^+\nu_\mu e^+e^-$ and $K^+ \to e^+\nu_e e^+e^-$

Radiative kaon decays similar to radiative pion decays, which we investigated at PSI in the past [8, 9], play a special rôle in the ChPT program, because they serve both as an important test and as a source of input parameters for the theory. Compared to the decay modes with real photons $K^+ \to e^+\nu_e\gamma$ ($K_{e2\gamma}$) and $K^+ \to \mu^+\nu_\mu\gamma$ ($K_{\mu2\gamma}$) the decays accompanied by a virtual photon turning into an electron-positron pair $K^+ \to \ell^+\nu_\ell e^+e^-$ (K_{e2ee}, $K_{\mu2ee}$) allow a more detailed investigation into the structure of these decays. Our data [10] constitute a 100- and 150-fold increase in the number of events over previously published samples [11] for K_{e2ee} and $K_{\mu2ee}$, respectively.

K_{e2ee} and $K_{\mu2ee}$ decays are assumed to proceed via exchange of a W^+-boson ($\to \ell^+\nu$) and a photon ($\to e^+e^-$). The decay amplitude[12, 13] includes inner bremsstrahlung (IB), corresponding to the diagrams in Fig.5.1a,b and structure dependent (SD) radiation (Fig.5.1c), parameterised by vector F_V, axial-vector F_A, and R form factors. $K_{e2\gamma}$ and $K_{\mu2\gamma}$ experiments [14] were only sensitive to $|F_V + F_A|$. R has not yet been measured, because it contributes only to decays with an e^+e^--pair. It can, however, be related to the kaon decay constant, $F_K = 160$ MeV, and the charge radius of the kaon $\langle r_K^2\rangle$[12]:

$$R = \frac{1}{3} M_K F_K \langle r_K^2 \rangle \ .$$

The IB contribution is unambiguously determined by F_K. Since this contribution is helicity

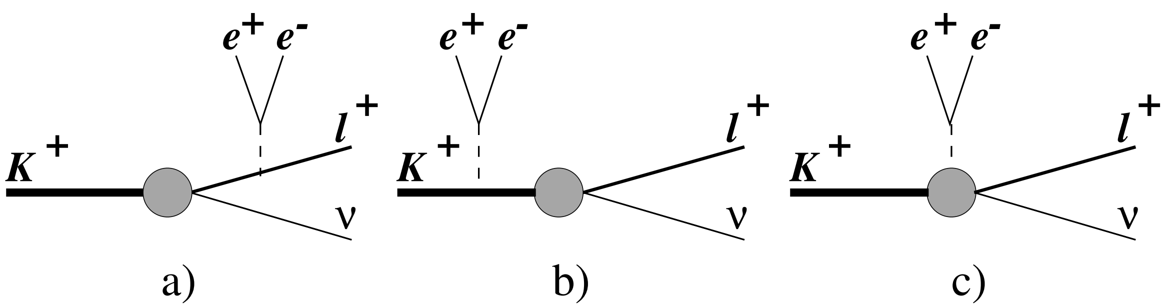

Figure 5.1: $K^+ \to \ell\nu_\ell e^+e^-$ *decay diagrams: a) and b) describe contributions from inner Bremsstrahlung, c) represents the structure dependent contribution.*

suppressed it is negligible in the K_{e2ee} decay whereas it contributes to about 60% of the $K_{\mu2ee}$ branching ratio for invariant masses $m_{ee} > 145$ MeV. An additional 20% comes from the interference between IB and SD amplitudes. This interference makes it possible to determine the signs of all form factors relative to F_K.

The K_{e2ee} and $K_{\mu2ee}$ data were obtained in the 1996 run together with the $K^+ \to \pi^+e^+e^-$ ($K_{\pi ee}$) data [15]. The trigger pre-selected events with three charged tracks, including an e^+e^- pair with high invariant mass m_{ee}. Off-line the K_{e2ee} and $K_{\mu2ee}$ events were selected as those with small missing neutrino mass, m_ν, calculated from the momenta of the identified decay products and the nominal beam momentum, known from $K^+ \to \pi^+\pi^-\pi^+$ decays with an

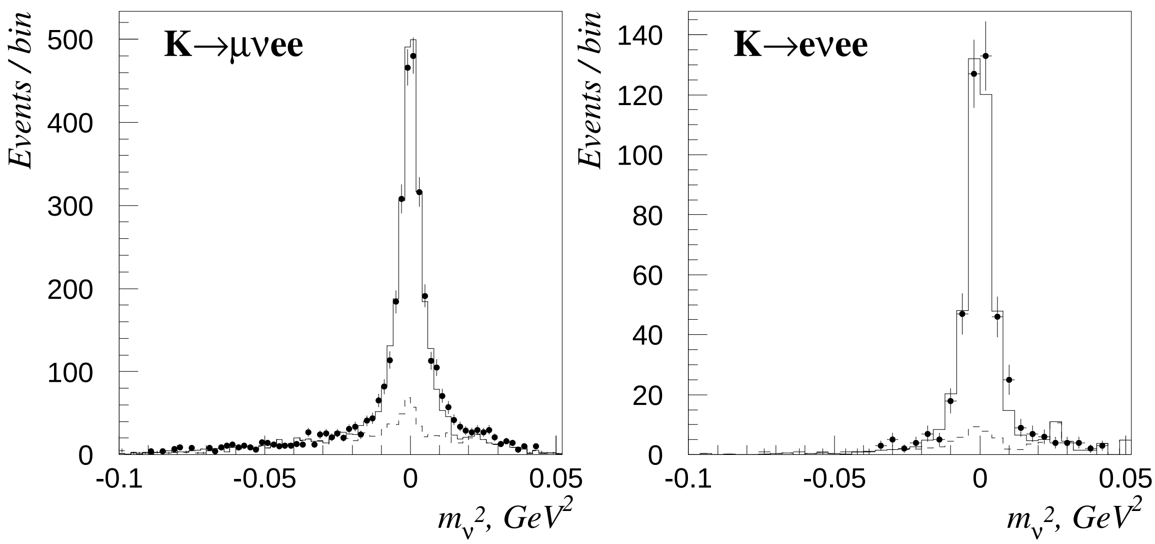

Figure 5.2: *Missing mass distributions for $K_{\mu 2ee}$ and K_{e2ee} decays. Points with error bars correspond to measured data, dashed lines indicate background, and solid lines represent the simulated distributions.*

uncertainty $\sigma_p/p = 1.3\%$ and $\sigma_{\theta x} = \sigma_{\theta y} = 4$ mrad. The m_ν^2 distribution is displayed in Fig.5.2. A cut $|m_\nu^2| < 0.016$ GeV^2 was used to isolate $K_{\ell 2ee}$ decays.

Background in both cases was dominated by accidental tracks accompanying a decay. By selecting events out of time for one of the tracks, we were able to obtain model independent samples of this background. The samples were normalised in the region $m_\nu^2 < -0.03$ GeV^2. The accuracies of normalisation, 8% for $K_{\mu 2ee}$ and 25% for K_{e2ee}, were sufficient for this purpose. To eliminate backgrounds associated with large branching ratio processes, *e.g.* $K \to \pi\pi_D^0$, cuts on the invariant e^+e^- mass > 145 MeV ($K_{\mu 2ee}$) and > 150 MeV (K_{e2ee}) were applied. The remaining background levels were determined from Monte Carlo simulation. The normalisation sample stems from pre-scaled K^+-decays with a π^0 in the final state followed by Dalitz decay $\pi_D^0 \to e^+e^-\gamma$ with a low invariant mass m_{ee}. Table 5.1 summarises the events samples. Using the calculated relative efficiencies for signal and normalisation

Table 5.1: $K_{\ell\nu_\ell e^+e^-}$ *event samples for signal and normalisation.*

Data sample	K_{e2ee}	$K_{\mu 2ee}$
Total	410	2679
Accidentals	35	355
$\pi^+e^+e^-$	5	126
$\pi^+\pi_D^0\pi_D^0$		33
Signal	370	2169

Normalisation sample	K_{e2ee}	$K_{\mu 2ee}$
$e^+\nu_e\pi_D^0$	86000	
$\mu^+\nu_e\pi_D^0$		16200
$\pi^+\pi_D^0$	2300	800
$\pi^+\pi^0\pi_D^0$		3000
Accidentals		400

channels and the number of events in Table 5.1 the following branching ratios were obtained:

$$K_{e2ee}: \quad (2.48 \pm 0.14 \text{ (stat.)} \pm 0.14 \text{ (syst.)}) \times 10^{-8} \quad (m_{ee} > 150 \text{ MeV}) ,$$

$$K_{\mu 2ee}; \quad (7.06 \pm 0.16 \pm \text{ (stat.)} 0.26 \text{ (syst.)}) \times 10^{-8} \quad (m_{ee} > 145 \text{ MeV}) .$$

The event distributions were used to fit the three form factors F_A, F_V and R, assuming that all three depend in the same way on W^2, the effective mass of the $\ell^+\nu_\ell$-pair, and q^2, the effective mass of the photon (e^+e^- pair). For the small mass ranges which are relevant here it suffices to consider only the low lying resonances [12]:

$$F_{V,A,R}^{(q^2,W^2)} = F_{V,A,R} \,/\, [(1-q^2/m_\rho^2)(1-W^2/\tilde{m}^2)] \;,$$

where $m_\rho = 770$ MeV, and $\tilde{m} = m_{K^*} = 892$ MeV for F_V and $\tilde{m} = m_{K_1} = 1270$ MeV for F_A, R. For further details we refer to Ref. [10]. Table 5.2 lists our results, which are in good agreement with both theoretical expectations and previous experimental results, where available.

F_V is related to the so-called axial anomaly: $F_V = \sqrt{2}M_K/8\pi^2 F$ [12], while R can be obtained from the measured kaon charge radius $\langle r_K^2 \rangle = 0.34 \pm 0.05$ fm^2 [16]. If we use our value of R we obtain $\langle r_K^2 \rangle = 0.333 \pm 0.027$ fm^2. The difference with respect to the pion charge radius $\langle r_\pi^2 \rangle = 0.439 \pm 0.008$ fm^2 [17] disagrees with the ChPT $\mathcal{O}(p^4)$ relationship

Table 5.2: *Results for the form factors F_V, F_A, and R (in units of 10^{-3}; errors are ±stat. ± syst. ± model). For comparison to previous experiments and because there exists a correlation between the form factor results the linear combinations $F_V \pm F_A$ are also listed.*

	$K^+ \to \mu^+\nu e^+e^-$	$K^+ \to e^+\nu e^+e^-$	Combined Fit	Expected	
F_V	$124 \pm 19 \pm 13 \pm 4$	$87 \pm 30 \pm 8 \pm 5$	$112 \pm 15 \pm 10 \pm 3$	96	[a]
F_A	$31 \pm 21 \pm 14 \pm 5$	$38 \pm 29 \pm 11 \pm 3$	$35 \pm 14 \pm 13 \pm 3$	48 ± 6	[b]
R	$235 \pm 25 \pm 14 \pm 12$	$227 \pm 20 \pm 10 \pm 8$	$227 \pm 13 \pm 10 \pm 9$	230 ± 34	[c]
$F_V + F_A$	$155 \pm 25 \pm 21 \pm 5$	$125 \pm 38 \pm 12 \pm 3$	$147 \pm 21 \pm 15 \pm 4$	144 ± 9	[14]
$F_V - F_A$	$93 \pm 32 \pm 17 \pm 7$	$50 \pm 44 \pm 15 \pm 7$	$77 \pm 20 \pm 19 \pm 6$	102 ± 74	[14]

[a] Theoretical value from the axial anomaly, see text;

[b] deduced from $\gamma = F_A/F_V = 0.522 \pm 0.050$ measured in a $\pi \to e\nu\gamma$ experiment [8];

[c] calculated from the measured $\langle r_K^2 \rangle$, see text.

$\langle r_\pi^2 \rangle - \langle r_K^2 \rangle = (1/32\pi^2 F^2) \ln (M_K^2/m_\pi^2) = 0.036$ fm^2 [13].

5.1.3 $K^+ \to \pi^+\mu^\pm e^\mp$

The analysis of the final $K_{\pi\mu e}$ run dating from 1998, which is the thesis project of Aleksey Sher, is nearing completion. We expect to improve the sensitivity by at least a factor of three beyond our published limit of 2.8×10^{-11} [18]. Potential accidental background is studied using $K^+ \to \pi^+\pi^-\pi^+$ and $K^+ \to \pi_D^0 X$ calibration data. Background may be caused by combining a charged particle pair from one decay with a third track from another decay. To minimize these, the timing calibrations have been redone combining smaller groups of runs. This leads to an adjustment of the likelihood functions entering the final analysis.

The *blind* analysis philosophy is followed here, i.e. possible signal candidates are only looked for at the very end, after all tools have been established independently. We expect to *open the box* in summer 2002.

5.2 KOPIO: a study of the CP-violating rare decay $K_l^0 \to \pi^0 \nu \overline{\nu}$

in collaboration with:
Brookhaven National Laboratory, University of Cincinatti, INR Moscow, KEK, Kyoto University of Education, Kyoto University, University of New Mexico, INFN University of Perugia, Stony Brook University, Thomas Jefferson National Accelerator Facility, TRIUMF/UBC, University of Virginia, Virginia Polytechnic Institute & State University, and Yale University.

5.2.1 CP-violation in the neutral K system

Since the early sixties it is known that the observed neutral kaon states are asymmetric mixtures of the strangeness eigenstates $K^0 = (d, \overline{s})$ and $\overline{K^0} = (\overline{d}, s)$:

$$\begin{aligned} K_s &= \frac{1}{\sqrt{2(1+\epsilon^2)}}((1+\epsilon)|K^0> + (1-\epsilon)|\overline{K^0}>) \\ K_l &= \frac{1}{\sqrt{2(1+\epsilon^2)}}((1+\epsilon)|K^0> - (1-\epsilon)|\overline{K^0}>) \end{aligned}$$

This so-called *indirect CP-violation* results from the difference in amplitudes for $K^0 \to \overline{K^0}$ and $\overline{K^0} \to K^0$:

$$\epsilon = \frac{<\overline{K^0}|H_{eff}|K^0> - <K^0|H_{eff}|\overline{K^0}>}{2(m_l - m_s) - i(\Gamma_l - \Gamma_s)}$$

Experimentally ($\epsilon = |\epsilon| e^{i\varphi_\epsilon}$):

$$|\epsilon| = (2.25 \pm 0.08) \times 10^{-3} \;, \quad \varphi_\epsilon = (43.5 \pm 0.1)^o \;.$$

An additional source of CP-violation, *direct CP-violation*, is found in a dependence of the amount of CP-violation on a specific final state, i.e. a difference between η_{+-} and η_{00} defined as:

$$\eta_{+-} \equiv \frac{<\pi^+\pi^-|H_{eff}|K_l>}{<\pi^+\pi^-|H_{eff}|K_s>} = \epsilon + \epsilon' \quad \eta_{00} \equiv \frac{<\pi^0\pi^0|H_{eff}|K_l>}{<\pi^0\pi^0|H_{eff}|K_s>} = \epsilon - 2\epsilon'$$

Only recently, after a long series of attempts an unambiguous signal for ϵ' was found [19, 20]. Unfortunately, the theoretical uncertainties in the standard model prediction are so large that the result can not yet be used as a constraint on physics beyond the standard model.

Within the standard model flavor mixing in W exchange is described by the complex 3×3 CKM matrix. Although the model makes no predictions for the values of the various elements the number of free parameters is reduced to four by constraints from unitarity, i.e. three angles and a phase. This is examplified by a very popular parametrization of the CKM matrix which is due to Lincoln Wolfenstein:

$$\begin{pmatrix} V_{ud} & V_{us} & V_{ub} \\ V_{cd} & V_{cs} & V_{cb} \\ V_{td} & V_{ts} & V_{tb} \end{pmatrix} = \begin{pmatrix} 1-\lambda^2/2 & \lambda & A\lambda^3(\rho - i\eta) \\ -\lambda & 1-\lambda^2/2 & A\lambda^2 \\ A\lambda^3(1-\rho-i\eta) & -A\lambda^2 & 1 \end{pmatrix}$$

Empirically $A = O(1)$, $\lambda, \rho, \eta = O(0.1)$. All CP-violating observables are proportional to $A^2\lambda^6\eta$. Constraints on the values of ρ and η are generally correlated, i.e. can be described by hyperbolic and circular regions in the ρ, η plane. Since the standard model makes no predictions for the CKM matrix all that can be done at present is check the consistency of the description, i.e. see whether the various observables can be described by a single set of values. It is very fortunate that we may expect significant improvements in the experimental constraints, both from the K and the B sector, in the next decade so that meaningful tests can be made.

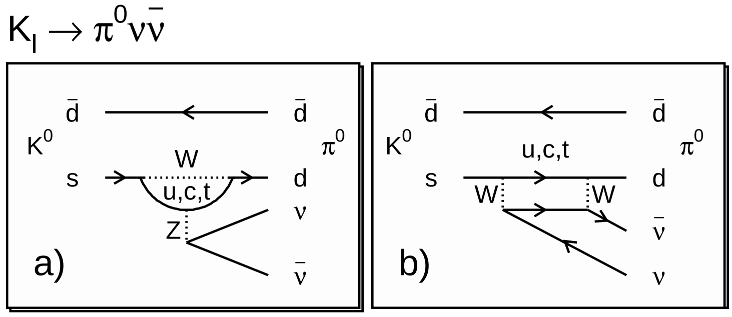

Figure 5.3: *Leading diagrams inducing $K_l^0 \to \pi^0\nu\overline{\nu}$.*

The decay $K_l \to \pi^0\nu\overline{\nu}$ plays a special role in this program. As is illustrated in Fig.5.3 the process has major contributions from penguin and box diagrams with up-type quarks in the intermediate state. Since the transition amplitude scales with the quark mass the top contribution dominates by far and:

$$A(K_l \to \pi^0\nu\overline{\nu}) \propto V_{td}^* V_{ts} - V_{ts}^* V_{td} \propto i\eta \ ,$$

so:

$$B(K_l \to \pi^0\nu\overline{\nu}) \propto \eta^2.$$

The branching ratio is thus a direct measure of η^2 without "background" from CP conservation or indirect CP violation. The price to pay is a very low branching ratio ($\approx 3 \times 10^{-11}$) and a very weak all-neutral event signature. Experimentally only an upper limit was found until now [22], more than four orders of magnitude above the expectation.

The corresponding charged decay mode does not require CP violation but gives a circular constraint around $\rho = 1.3, \eta = 0$:

$$B(K^+ \to \pi^+\nu\overline{\nu}) \propto (\rho - 1.3)^2 + \eta^2.$$

Until recently BNL E-787 found two event candidates [23].

5.2.2 Overview of the KOPIO experiment

Two photons with the invariant mass of a π_0 and nothing else is the signature for a $K_{\pi\nu\nu}$ decay. The KOPIO proposal [21] explains in detail, how this signature is used to isolate this ultrarare decay mode from the background. Here we summarize the basic features.

The most important aspect of the experiment is the use of a low momentum short-pulse K_L^0 beam, whose momentum can be determined event by event via time-of-flight. The observed π^0, reconstructed from the energy, direction and common vertex of the two photons from its decay, can then be transformed into the K_L^0 center-of-mass system, and kinematic constraints can be applied, allowing to distinguish the events of interest from the dominant background source $K_L^0 \to \pi^0\pi^0$. Figure 5.4 shows a sketch of the planned detector.

A 24 GeV primary proton beam from the AGS strikes the production target in 200 ps wide pulses separated by 40 ns. Neutral particles emerging from the target at angles around 48° in the horizontal plane may reach the experiment starting 9 m downstream. Under these conditions the K_L^0 momentum spectrum at the decay region peaks at 650 MeV/c. Vertically the beam is collimated into a narrow band, to limit the beam halo and to provide another vertex reconstruction constraint. 16% of the kaons decay within the 4 m long evacuated decay region, which is surrounded by the π^0 detector and the various charged-particle and photon veto systems. The π^0 detector consists of a highly segmented preradiator followed by an electromagnetic calorimeter. The arrival time, position and angle of each photon is

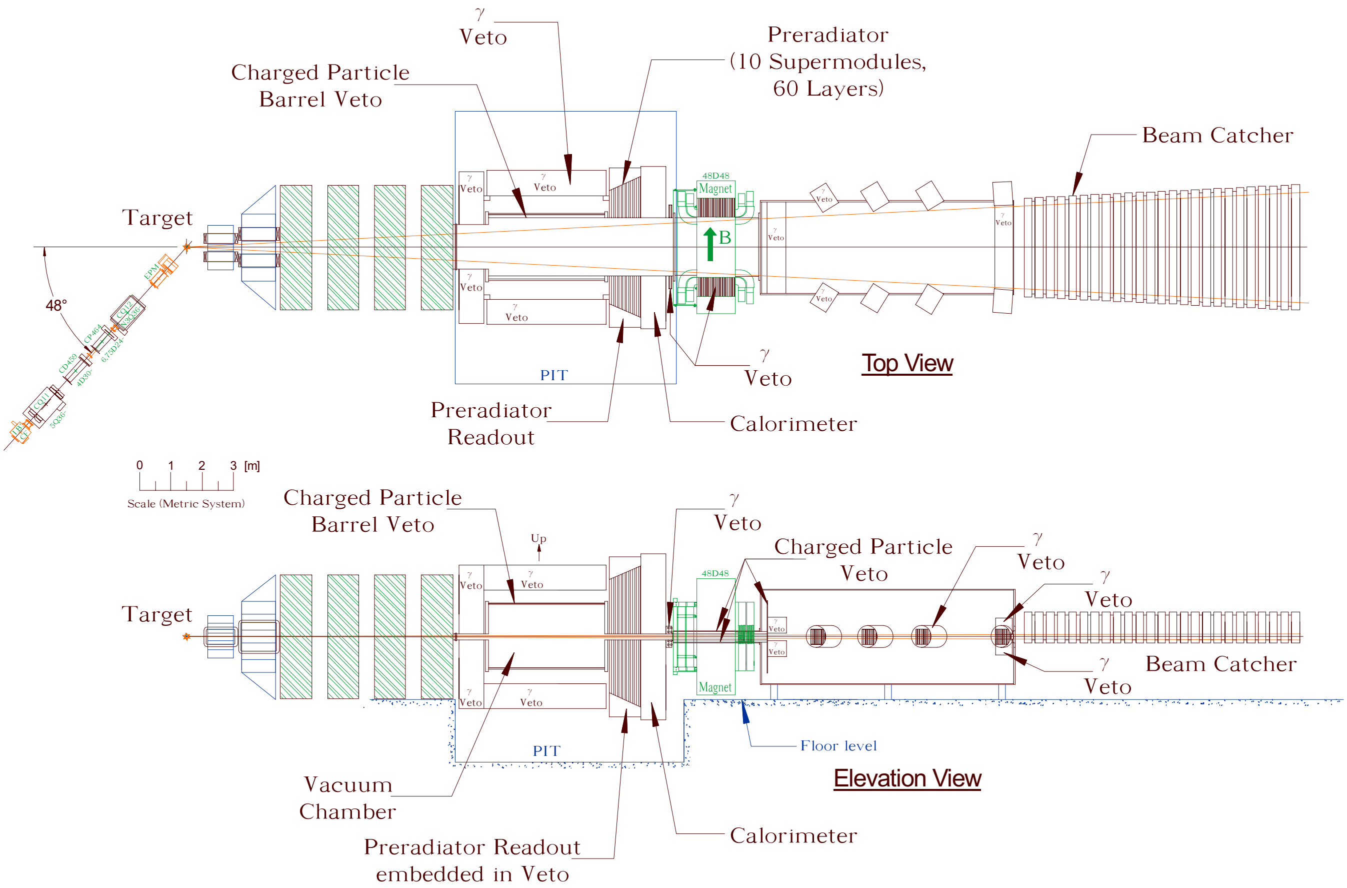

Figure 5.4: *Plan and elevation views of the KOPIO detector.*

determined in the preradiator by recontruction of the trajectories of the initial e^+e^- pairs. The photon energies are determined by combining the signals observed in the preradiator with those from the calorimeter. A resolution of $\sigma_E/E \approx 0.033/\sqrt{E}$ is expected.

The Zurich group took over the responsibility for the charged-particle veto system situated directly around the decay region. In the following we discuss the requirements to this system and some other considerations that should lead to a specific design.

5.2.3 The KOPIO charged particle veto system

The purpose of the charge-particle veto system is the efficient identification of background processes in which an apparent $\pi^0 \to 2\gamma$ decay inside the decay volume is accompanied by charged particle emission. Examples of such background processes are, (i) $K_L \to \pi^+\pi^-\pi^0$, (ii) $K_L \to e^+\pi^-\nu\gamma$ in which the positron creates a second photon through Bremsstrahlung or annihilation in flight, (iii) $K_L \to e^+\pi^-\nu$ again followed by $e^+ \to \gamma$ whereas the π^- creates a photon through $\pi^-p \to \pi^0 n$. In all cases two particles with opposite electrical charge emerge. In all cases the events may also produce signals in other detector elements, like the barrel veto system. Detection efficiencies of 99.99% or better are required to keep these backgrounds below a few events in the final sample.

The charged-particle veto system will consist of two or three layers of plastic scintillator mounted inside the vacuum tank surrounding the decay volume. The detectors will be separated from the high-quality beam vacuum by a thin metallic foil.

5.2.4 Response of plastic scintillator to $\pi^{\pm}$ at 185 - 360 MeV/c

In spring 2001 we measured the response of plastic scintillator to $\pi^{\pm}$, $\mu^{\pm}$ and $e^{\pm}$ at momenta between 185 and 360 MeV/c. The purpose of these studies performed at PSI was twofold, (i) determination of the fundamental limitations to the detection efficiency associated with processes (such as pion absorption or positron annihilation in flight) that result in a partial or complete loss of scintillator signal, and (ii) tests of detector prototypes, in particular of scintillators with embedded wave-length-shifting fibres. For a detailed discussion see Ref.[24].

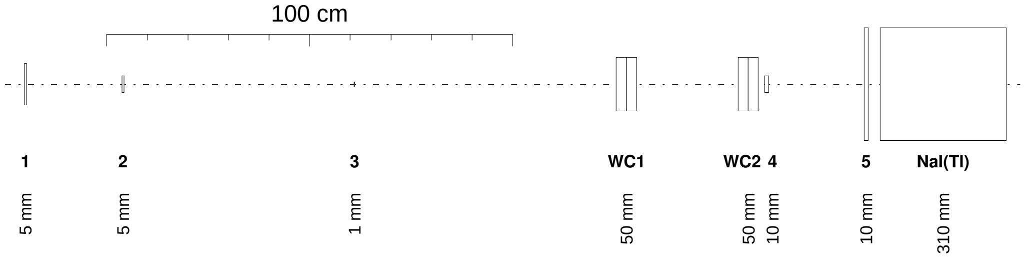

Figure 5.5: *Setup for the study of the response of plastic scintillator to $\pi^{\pm}$, $\mu^{\pm}$ and $e^{\pm}$. 1-5: plastic scintillators; WC1/2: x-y proportional wire chambers (1mm spacing). The values on the bottom denote the thickness of the corresponding detector. The beam enters from the left.*

Figure 5.5 shows the experimental setup which consists of a particle defining telescope (counters 1-3 and $x-y$ multiwire proportional chambers WC1 and WC2) followed by a veto system consisting of two plastic scintillation detectors (4 and 5) and a NaI(Tl) crystal.

Particle identification was done on the basis of time of flight between the production target and detector 2. The resulting samples have purities of 99.9% or better. Events were selected with trajectories pointing both at counter 3 and counter 4. Figure 5.6 shows the corresponding NaI(Tl) energy distributions for $e^{\pm}$ and $\pi^{\pm}$. The muon spectra are very similar to those observed for $e^{\pm}$. Whereas 99% of the electrons and positrons produce signals in

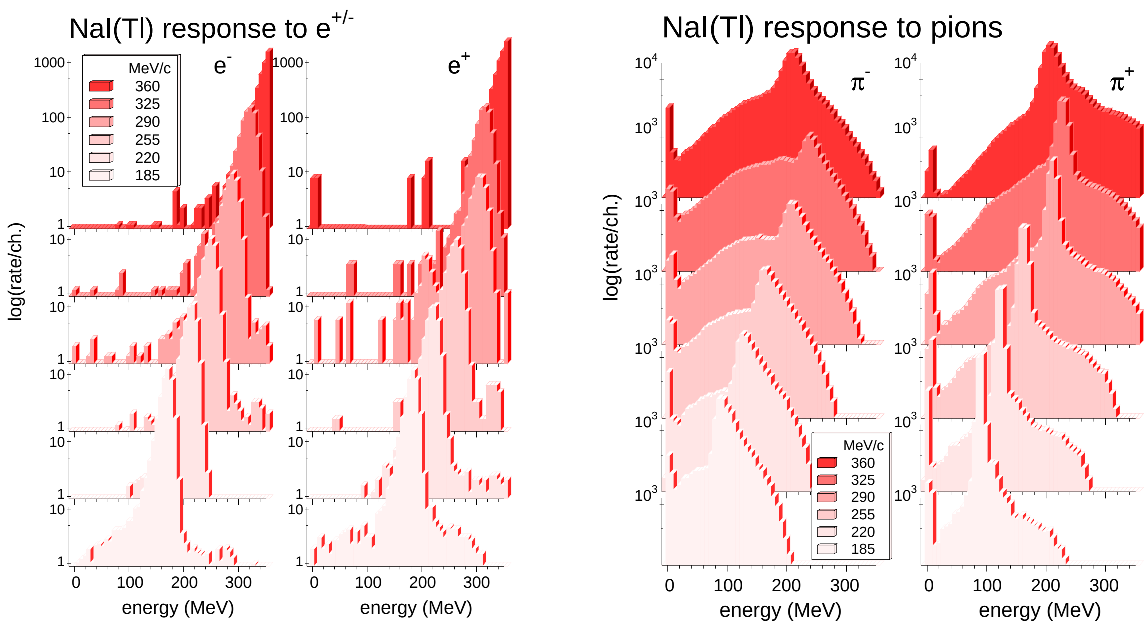

Figure 5.6: *NaI(Tl) response to $e^{\pm}$ and $\pi^{\pm}$ at momenta in the range 185-360 MeV/c. At 360 MeV/c pions may cross the detector resulting in a reduction in energy deposit.*

the full-energy peak with no indication of a pedestal peak, pions may disappear by nuclear

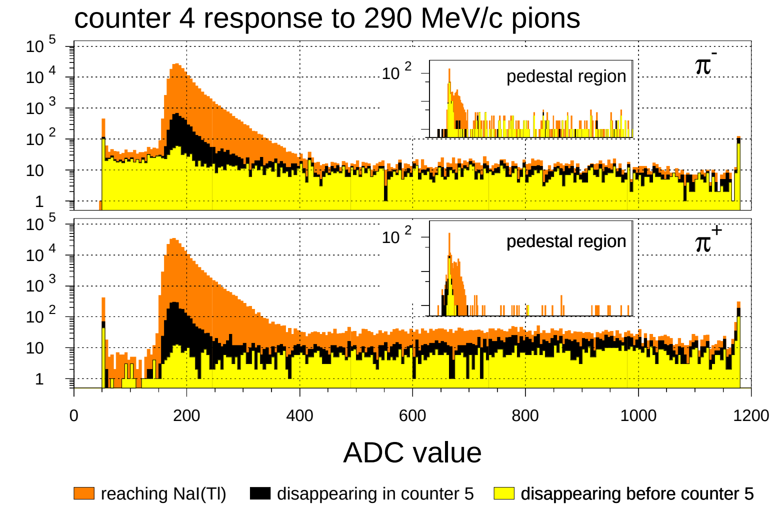

Figure 5.7: *Response of counter 4 to 290 MeV/c $\pi^{\pm}$ for, (i) all events with trajectories pointing at counter 4, (ii) the subset of (i) contained in the NaI(Tl) pedestal peak (see Fig. 5.6), and (iii) the subset of (ii) contained in the pedestal peak of counter 5.*

reactions resulting in a broad continuum. In 1-3% of the cases no signal is seen at all. These events are caused by interactions in counters 4 and 5 (total thickness 15 mm).

Figure 5.7 shows various distributions of the signals produced by 290 MeV/c pions in counter 4. Similar spectra are observed at the other momenta. Events without signals in counter 5 and NaI(Tl) are characterised by flat distributions with a small peak contribution caused by interactions in the dead layer between counters 4 and 5. Note the striking difference between π^+ and π^- in the event rate at the low side of the peak: whereas π^- interactions often lead to neutral final states π^+ is known to produce one or more low-energy protons which result in additional scintillation light. From the observation that the pedestal peak has similar strengths for both polarities one must conclude that these secondary charged particles tend to have relatively short ranges.

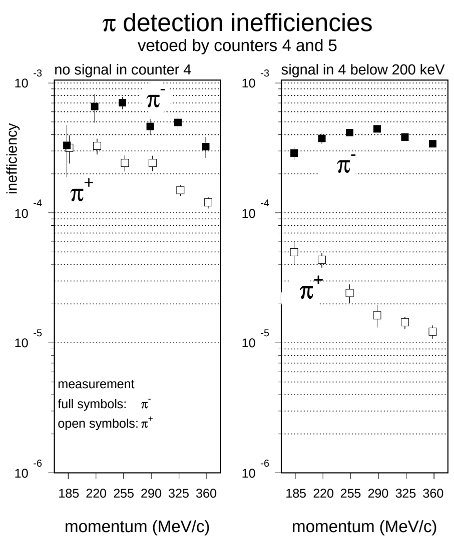

Figure 5.8: *Pion detection inefficiency caused by interactions in WC2 and the wrapping of counter 4 and by a 200 keV detection threshold on the signal in counter 4. Results are shown for the case that counter 5 is used as veto counter too. When also NaI(Tl) is used as veto counter the inefficiencies drop by up to 50%.*

The observed pion detection inefficiencies are plotted against beam momentum in Fig. 5.8. We conclude that detection inefficiencies of $O(10^{-4})$ for momenta around 300 MeV/c could be obtained if (i), the dead layer in front of the veto system (which includes the window separating the detector from the high-vacuum decay region) could be kept below 20 mg/cm^2 and (ii), a detection threshold of $\approx$ 75 keV (corresponding to $\approx$ 0.3 mm scintillator thickness) could be reached. Meeting this performance seems neither trivial nor hopeless. Most critical parameter is the yield of photo-electrons per energy deposit (see Sec. 5.2.5). The detection efficiencies for $e^{\pm}$ and $\mu^{\pm}$ would always be better than for pions. At most momenta we found lower limits only.

5.2.5 Experience with a first detector prototype

At present we plan to equip the charged particle barrel veto with 2-3 detector layers for which two options are considered:

- Scintillator bars with dimensions typically 400 × 50 × 5 mm^3. These detector elements would be coupled through short light guides to miniature photomultipliers mounted inside the vacuum tank. Active elements inside the vacuum tank increase the time required in case of repair. Also care has to be taken to avoid break-through of the photomultiplier high voltage. At the other hand the detector threshold which is the main figure of merit might be significantly lower than for option 2.

- Scintillator tiles with dimensions typically 400 × 100 × 5 mm^3. The scintillation light would be extracted with the help of wave-length-shifting fibres glued in grooves of 1 mm depth and 5-10 mm spacing. The fibres would be coupled to multi-channel hybrid photomultipliers mounted on the outside of the vacuum tank. We have tested this option both in the beam and with cosmic rays. The observed number of photo-electrons (≈ 100 in 10 mm scintillator) is compared with predictions in Fig.5.9.

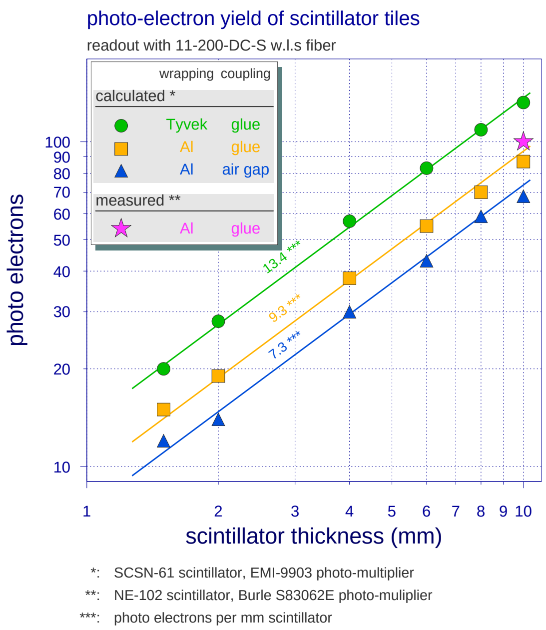

Figure 5.9: *Mean number of photo-electrons for minimum-ionising particles crossing a scintillator tile with embedded wave-length-shifting fibres. Our measured value is compared with predictions for similar configurations by [25].*

The value of ≈ 100 photo-electrons for minimum ionising particles crossing 10 mm of scintillator read out with embedded w.l.s. fibre corresponds to 3 photo-electrons for a 75 keV threshold. The sensitivity of counter 4 which was viewed through a classical fishtail light guide is about 20 times higher and for this reason we intend to make a critical comparison between full-scale prototypes of both types of detector.

References

[1] *A Large Acceptance, High Resolution Detector for Rare K^+-decay Experiments*, R. Appel *et al.*, Nucl. Instr. Meth. **A479** (2002), 340.

[2] *A New Measurement of K^+_{e4} Decay and the s− Wave ππ Scattering Length*, S. Pislak *et al.*, Phys. Rev. Lett. **87** (2001), 221801.

[3] G. Amoros, J. Bijnens, and P. Talavera, Phys. Lett. **B480**,71 (2000); Nucl. Phys. **B595**, 293 (2000); err. **B598**, 665 (2001); ibid. **B602**, 87 (2001).

[4] G. Colangelo, J. Gasser, and H. Leutwyler, Phys. Rev Lett. **86**, 5008 (2001).

[5] B. Ananthanarayan *et al.*, Phys. Rep. **353/4**, 207 (2001).

[6] D. Morgan, and G. Shaw, Nucl. Phys. **B10**, 261 (1969).

[7] G. Colangelo, J. Gasser, and H. Leutwyler, Phys. Lett.**B488**, 261 (2000).

[8] A. Bay *et al.*, Phys. Lett. **B174** (1986), 445.

[9] S. Egli *et al.*, Phys. Lett. **B222** (1989), 533.

[10] *Experimental Study of the Radiative Decays* $K^+ \to \mu^+\nu_\mu e^+e^-$ *and* $K^+ \to e^+\nu_e e^+e^-$, A.A. Poblaguev *et al.*, hep-ex 0204006, submitted to Phys. Rev. Lett. (2002).

[11] A.M. Diamant-Berger *et al.*, Phys. Lett. **62** (1976), 485.

[12] D. Bardin, and E. Ivanov, Sov. J. Part. Nucl. **7** (1976), 485.

[13] J. Bijnens, G. Ecker, and J. Gasser, Nucl. Phys. **396** (1993), 81.

[14] S. Adler *et al.*, Phys. Rev. Lett. **85** (2000), 2256; S. Heintze *et al.*, Nucl. Phys. **149** (1979), 365; K. Heard *et al.*, Phys. Lett. **B55** (1975), 324.

[15] R. Appel *et al.*, Phys. Rev. Lett. **83** (1999), 4482.

[16] S. Amendiola *et al.*, Phys. Lett. **B178** (1986), 435.

[17] S. Amendiola *et al.*, Nucl. Phys. **B277** (1986), 168.

[18] R. Appel *et al.*, Phys. Rev. Lett. **85** (2000), 2450.

[19] A. Lai *et al.*, Eur. J. Phys. **C22** (2001), 231.

[20] A. Alavi-Harati *et al.*, Phys. Rev. Lett. **83** (1999), 22.

[21] *Rare Symmetry Violating Processes*
Joined MECO/KOPIO proposal (1999), `http://pubweb.bnl.gov/people/rsvp`.

[22] A. Alavi-Harati et al., Phys. Rev. **D61** (2000), 072006.

[23] S. Adler *et al.*, E787 Collaboration, Phys. Rev. Lett. **88** (2002), 041803.

[24] H. Kaspar, P. Robmann, A. v.d. Schaaf, S. Scheu, P. Truöl, J. Egger, and M. Blecher, *Measurements on the response of plastic scintillator to charged pions at 185 - 360 MeV/c*, KOPIO techn. note tn027 (2001).

[25] V. Issakov, private communication.

6 Particle Physics at DESY/HERA (H1)

J. Becker, Ilaria Foresti, S. Hengstmann (until 4/01), M. Hildebrandt, N. Keller, J. Kroseberg, Katharina Müller, P. Robmann, F. Sefkow, U. Straumann, P. Truöl, M. Urban, R. Wallny (until 4/01) and Nicole Werner

in collaboration with:
R. Eichler, W. Erdmann, C. Grab, M. Hilgers, B. List, S. Lüders, D. Meer and A. Schöning, Institut für Teilchenphysik der ETH, Zürich, S. Egli, K. Gabathuler, J. Gassner, and R. Horisberger, Paul–Scherrer–Institut, Villigen, and 34 institutes outside Switzerland

(**H1**–Collaboration)

6.1 Electron proton collisions at up to 320 GeV center of mass energy: overall status of the project

Since September 2000 no new data have been collected by the H1-experiment, because even after the conclusion of the long shutdown for the upgrade of the detector and the accelerator in July 2001, no useful collisions have been observed so far. The tuning of the positron and proton accelerators turned out to be more troublesome then expected, as we will report below (Sec.6.2). Consequently, also the status of those H1-components which have undergone an upgrade remains largely untested under realistic, high intensity conditions. However, after conclusion of the major effort, which was undertaken to optimize the calibration and alignment of tracker components (see Sec.6.5) near the end of 2001, finally the first results are emerging from the reprocessed 1999/2000 data ($\mathcal{L} = 91\text{pb}^{-1}$). Despite this most of our publications use data taken before 1999 ($\mathcal{L} = 50\text{pb}^{-1}$). In 18 publications ([1]-[18]) and 21 papers contributed to the 2001 high-energy conferences ([20]-[40]) of the collaboration the following principal areas are covered:

- neutral and charged electroweak current cross sections, proton structure functions and parton densities (extensions into the lower and higher Q^2 regimes, longitudinal structure function and use of radiative events) [4, 5, 11, 20, 24, 25, 26, 37, 43, 44, 47],
- determination of α_s and its scale dependence (structure function analysis, dijets) [2, 4, 43, 44, 47],
- search for states outside the standard model (squarks, ν^*, leptoquarks, single top, odderons) [6, 10, 14, 22, 33, 34, 36],
- photoproduction (inclusive, dijets, $\rho, J/\Psi$, $Q\bar{Q}$) [7, 16, 21, 30, 32, 38, 40],
- parton-fragmentation into multijet final states [1, 2, 3, 8, 15, 16, 31, 40],
- photo- and electroproduction of exclusive final states ($\rho, J/\Psi, \Psi'$) [21, 23, 27, 30],
- production of heavy quark-antiquark states ($Q\bar{Q}$) and of open charm and beauty [12, 13, 46, 38, 39, 41, 42, 45],
- diffractively produced final states (inclusive, D^*, jets, $\rho, J/\Psi, \Psi'$) [3, 13, 17, 18, 21, 23, 28, 29, 30, 31],
- virtual Compton scattering [9].

We will report below on the analyses in the heavy quark sector (sections 6.6.2 and 6.6.4), an area where there is manifest activity of the University of Zürich group (F. Sefkow's habilitation project and theses of J. Kroseberg and I. Foresti), in prompt photon production

(Sec.6.6.3, K. Müller's habilitation project) and also give a brief overview of the general status (Sec.6.6.1). Two Zürich analysis projects which are not discussed in detail concern QED Compton scattering (thesis N. Keller) and high Q^2 data (thesis N. Werner).

Besides the physics analysis the commissioning of our contributions to the upgrade program of the H1-detector occupied most group members (see Sec.6.4).

6.2 Status of the HERA accelerator

At an H1-meeting in February 2002 F. Willeke reported on the progress of the commissioning of the HERA accelerator complex. First collisions were registered by the H1 luminosity detector in September 2001. While collisions at low beam intensities ($I_e = 0.8$ mA (e^+) and $I_p = 12$ mA) have been obtained in December 2001 with a specific luminosity $\mathcal{L}_{spec.} = 1.68 \cdot 10^{30}$ mA^{-2}cm^{-2}s^{-1} (84 % of the design value, three times pre-upgrade average value) and beam spot sizes of $\sigma_x \times \sigma_y \approx 150 \times 50$ μm^2, the synchrotron radiation backgrounds exceeded the values which allow to turn on the detectors at full currents by two orders of magnitude. The beam based alignment procedures near the interaction regions took much longer than originally envisioned, but the new beam lattice and optics are now relatively well understood and the influence of the detector fields (in the absence of compensation coils) is now manageable. The origins of the high synchrotron radiation backgrounds were traced to a magnet aperture 90 m before the interaction region and backscattering from a collimator behind H1 (in positron direction). New shielding masks were inserted between January and March 2002 to protect against this. Furthermore a broken beam tube support in a cold straight section of the proton ring was replaced during this period, which required breaking the vacuum. In April 2002 shortly after the time interval reported here, the commissioning procedures have restarted.

6.3 Status of the H1-detector

Figure 6.1 shows the H1-detector with those elements highlighted, which experienced modification or have been added. In forward direction the existing proton and neutron detectors at 106 m and 60 - 90 m, respectively are supplemented by a very forward proton spectrometer at 200 m, where the scattered proton and the circulating beam are already separated sufficiently. This will increase the acceptance for charmed meson and vector meson production for $|t| \leq 0.5$ GeV^2.

For high Q^2 events the track density in forward direction is quite high. The reconstruction of events in this region has therefore been quite difficult and had to rely primarily on calorimeter response. The former radial drift chamber and transition radiation detector modules in the forward tracker (FTD) have now been replaced by eight planar wire chambers giving greater redundancy and helping to resolve pattern recognition ambiguities. Five new planes of Si detectors were also inserted near the beam pipe to cover small scattering angles. The design is similar to that of the existing backward silicon detector (BST). In combination with the central silicon detector built by ETHZ/PSI/UZH the H1-detector will now have nearly 4π precision Si tracking coverage.

In the low Q^2 backward region new proportional chambers have replaced the backward drift chamber, and the geometry of the time-of-flight scintillators has been adapted to the new beam elements. The latter was also done in forward direction.

The two-layer inner proportional chambers (CIP) and the drift chamber (CIZ) built in Zürich have been replaced by a new five-layer proportional chamber (CIP2000) also built in Zürich. The aim of this change was to improve z-vertex triggering and track reconstruction at the trigger level, as well as the rejection of background events, as we reported last year.

The trigger scheme is based on a projective geometry of the pads along the z-axis, thus requiring a decreasing number of pads with increasing width from the inner to the outer layers. The increased number of readout channels required new readout [48] and trigger electronics [49]. ETHZ is also involved in the development of a fast track trigger derived from central jet chamber information, which will allow online invariant mass reconstruction and hence selective triggering on charm and beauty production enriched samples.

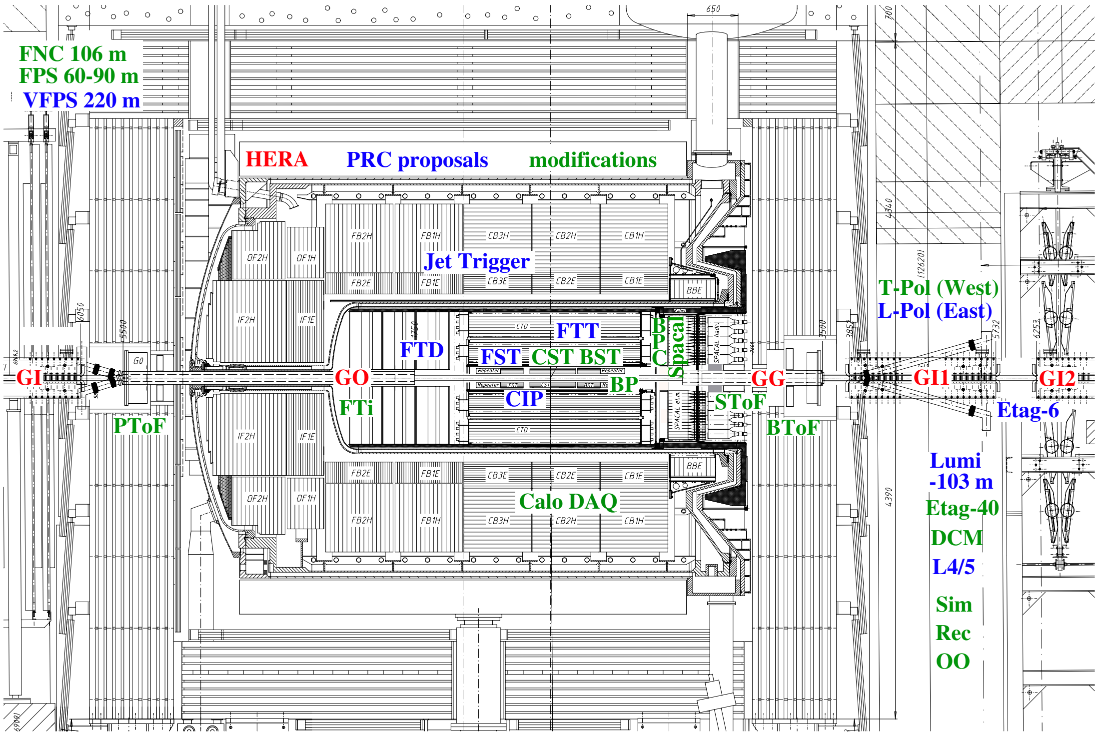

Figure 6.1: *The H1-detector after its 2000/2001 upgrade. New or modified detector elements are marked.*

6.4 Summary of group activities related to the H1-upgrade

The CIP2000 upgrade project is coordinated by the University of Zürich (U. Straumann) with ETH Zürich and University of Heidelberg as partners. The ASIC laboratory in Heidelberg developed the amplifier and readout chip CIPix, and the electronics for trigger and data acquisition is a common Heidelberg and Zürich University effort. ETH Zürich was responsible for all components dealing with the readout of the data at the detector end, and the transport to the electronic trailer via an optical transmission line with drivers and receivers at either end.

At the end of the two year construction period which involved up to five people in the workshops of our institute the CIP was transported to DESY in February 2001 and mounted inside the central tracker of H1. The readout prints and all other necessary supply connections have been mounted in April 2001. Figure 6.2 shows some aspects of the final test procedures in our laboratory in Zürich and of the installation steps in Hamburg.

For the z-vertex trigger the CIP2000 data are multiplexed fourfold and fed to 16 trigger cards, one per ϕ-sector. To cope with the enormous data rate a highly parallel system had to be developed. It is realised in large FPGA's (Altera APEX 20k400) with internal dual ported

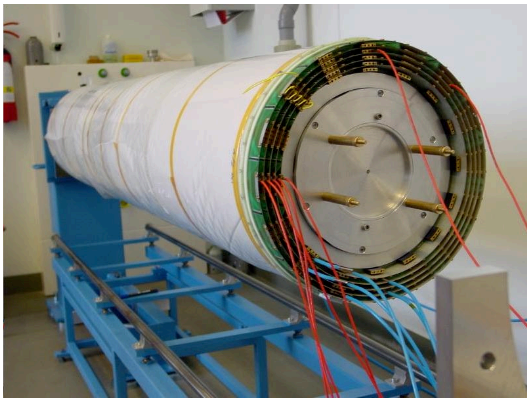

- *CIP2000 after completion in the laboratory in Zürich.*

- *CIP2000 is prepared for insertion into the H1 central tracker.*

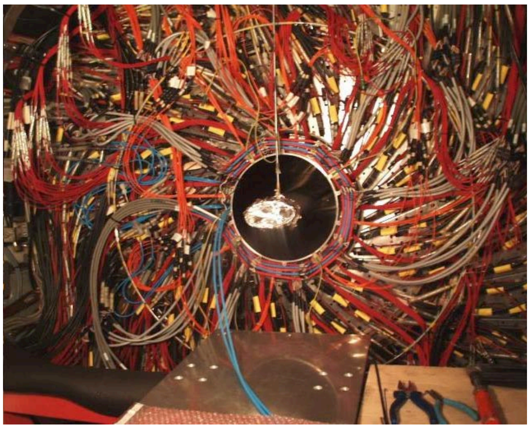

- *The H1 central tracker in its final position within the H1 detector seen from the backward (incoming proton) side with the electronics, gas and cooling lines connected (May 2001).*

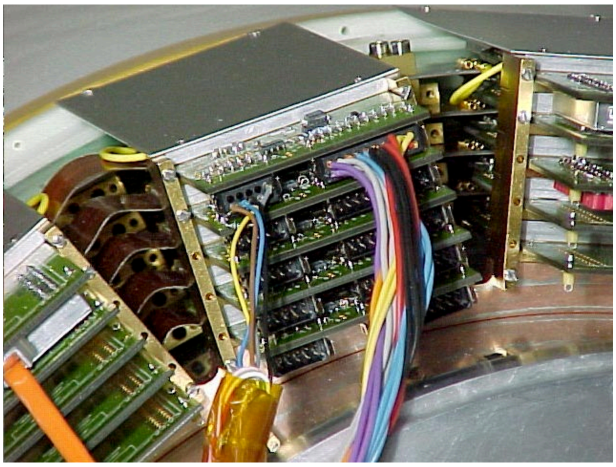

- *On-chamber electronics is being mounted for tests in Zürich.*

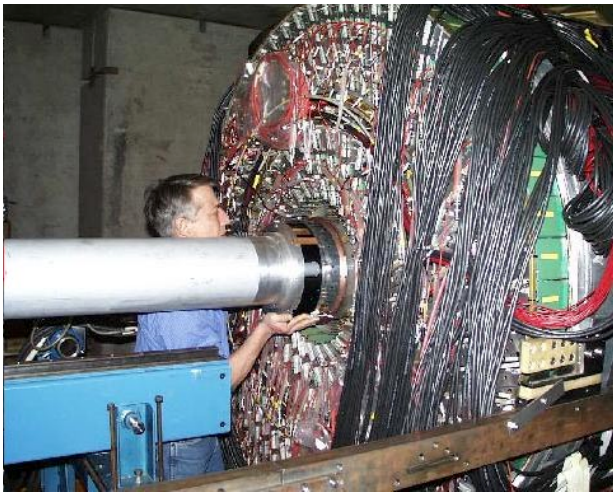

- *CIP2000 is in place.*

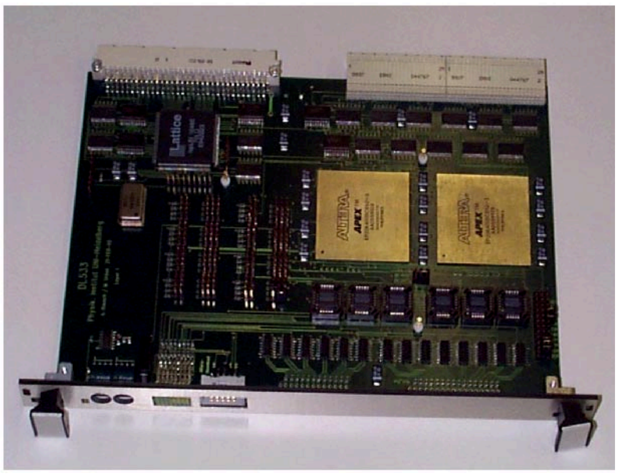

- *A CIP2000 trigger card.*

Figure 6.2: *Some aspects of the test procedures in our laboratory in Zürich and of the installation in Hamburg.*

memory. A trigger card is shown in Figure 6.2. The memory is used as a pipeline for the data of the CIP2000 for 21 bunch crossings while the trigger decision is being made. The latter proceeds in three consecutive steps. First tracks are reconstructed from the hits in the $\approx 10^4$ pads, then a z-vertex histogram is built, and finally a trigger decision is made. The system can cope with inefficient areas of a chamber or missing layers. The stored data are transfered via VME bus to the H1 storage bank systems. Therefore a DAQ system with fast inhomogeneous bus systems was developed. The whole system is now complete and has passed its initial tests successfully. The total data throughput of the system is 108 GBytes/s (!). For the system 25'000 lines of code in a special hardware description language (verilog) had to be written. The design and implementation of this trigger is the thesis project of M. Urban [49]. The development of the CIP2000 data acquisition system is a task included in the thesis project of J. Becker [50], while slow control (i.e. chamber HV and current as well as temperature monitoring and control), and on-line monitoring of the chamber efficiency is part of the thesis project of N. Werner. These different tasks necessary for the full integration of CIP2000 into H1 are being coordinated by M. Hildebrandt. Since the old z-vertex trigger allows to calculate the z-vertex histograms with a certain momentum threshold, it is planned to include it into the system, too. The necessary interface cards necessary are being developed.

In July 2001 first tests with cosmic muons were possible with the H1-detector closed and in beam position. Using the OR-signal, which is available from the 16 pads served by each CIPix readout chip, and a combination of two layers of proportional chambers in each of its 16 ϕ sectors, a cosmic muon trigger was created from the chamber itself. This initial test confirmed the satisfactory chamber performance measurements in the laboratory in Zürich, but also pointed to a variety of problems related to insufficient cooling. The ambient temperature produced by the central jet chamber electronics is so high, that the CIPix reaches temperatures near 50°C with the normal cooling circuit running at 17°C. At these temperatures instabilities in the addressing of some CIPix chips occurred at first, and later a complete loss of their functionality can be observed. A subsequent laboratory test confirmed that at these high temperatures wires bonded to the chips can break, which explains the loss of connection. As a counter measure a separate cooling circuit was installed with an operating temperature of 8°C, which will keep the CIPix temperature below 40°C. However, out of the five chamber layers the outermost two were partly lost before the roots of the problem were discovered. Furthermore three of the 24'000 anode wires are broken, and a few ϕ sectors in the remaining three planes are missing, too. However, the inner three chambers and the trigger derived from them still cover the complete solid angle and can be operated, requiring a coincidence of at least two cathode pads on a track. The whole frontend electronics is presently being rebuilt in such a way, that the bond breaking can no longer occur, and during the next short shutdown a replacement is planned. Furthermore additional cooling lines will then be added to the chamber electronics.

Since August 2001 the data acquisition has been completed, such that each individual pad of the whole chamber can now be read out. Events are correctly stored and displayed, and the readout timing has been adjusted within one bunch crossing to the central data acquisition system. The correct trigger algorithm based on pad information and tracks has been written, and was implemented on the FPGA's and tested. For the fine tuning of course real collisions are awaited. Four trigger elements are foreseen: correct event timing ($T0$), vertex in the interaction region, background from upstream or from downstream of the interaction region. The temperature monitoring is installed and if a limit is exceeded the supply voltages will be automatically switched off.

6.5 Reprocessing for optimal tracking performance

Last year we reported on the collaboration-wide effort to optimize the performance of the H1 tracking system. Using the additional redundancy provided by the central silicon tracker (CST) and new mathematical procedures, the calibration of individual components, as well as their overall consistency has been considerably improved; such that the obtained tracking resolution now corresponds to the design goals. Although this initiative was primarily directed towards achieving optimal vertexing precision which is so crucial for tagging heavy quarks by means of their lifetime signature, momentum and angular resolution benefited as well. As a consequence, the signal quality of invariant mass peaks also improved significantly. To illustrate this, in Figure 6.3 the D^* signal in the "golden" decay mode $D^* \to K\pi\pi$, is shown, as it has been obtained before and after the new reconstruction. Meanwhile all data taken

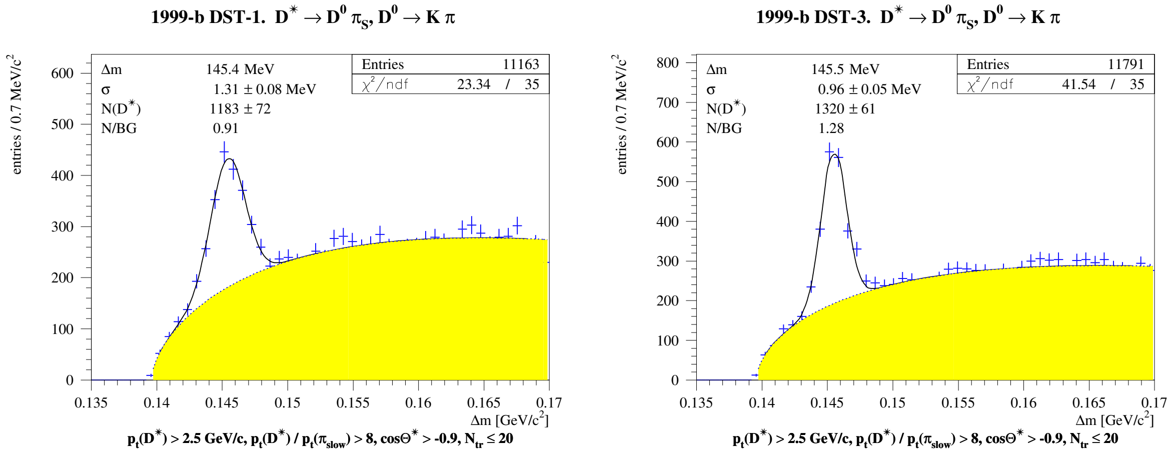

Figure 6.3: *D^* signal in the mass difference distribution $\delta m = m(K\pi\pi) - m(K\pi)$ before and after reprocessing the data with new alignment and calibration.*

from 1997 to 2000 have been reprocessed, and similar improvements are observed for all running periods. With the "Tracking Task Force" thus successfully terminated, F. Sefkow, who led the team for the past 2 years, has switched over to act as new convenor of the Heavy Flavour physics working group in H1, which looks forward to exploiting the potential offered by the improved precision and statistics of the data. In paticular the studies of charm and beauty production depend heavily on the tracking performance, and in this area the largest fraction of the HERA data still waits to be analyzed.

6.6 Results from recent analyses

6.6.1 *ep* collisions at high energies

Progress in our understanding of proton structure in the last few years is closely linked to the improved accuracy and larger kinematic extent of the measurements from the two experiments H1 and ZEUS at the electron- or positron-proton collider HERA. In conjunction with older fixed target muon and neutrino data these new data are used to determine quark and gluon densities within the proton through analysis of their QCD evolution.

To briefly introduce the terminology, we recall that the differential cross section for deep inelastic positron (electron) proton scattering, if only the neutral electromagnetic current (virtual photon (γ) and boson (Z^0) exchange) is considered, takes the following form:

$$\frac{d^2\sigma_{NC}}{dx\ dQ^2} = \frac{2\pi\alpha^2}{xQ^4}\Phi_{\gamma,Z}(x,Q^2) = \frac{2\pi\alpha^2}{xQ^4}\left[Y_+\tilde{F}_2(x,Q^2) \mp Y_- x\tilde{F}_3(x,Q^2) - y^2\tilde{F}_L(x,Q^2)\right] .$$

The *structure function term* $\Phi_{\gamma,Z}(x,Q^2)$ is a linear combination of the dominant $\tilde{F}_2$ structure function, the longitudinal structure function $\tilde{F}_L$, and the $x\tilde{F}_3$ structure function which in the standard model is significant only when Q^2 is sufficiently large to render Z^0 exchange non-negligible. $Q^2 \equiv -t$ is the squared four-momentum transfer of the scattered positron and x the fraction of the proton momentum carried by the struck quark. The variable y is defined as $y = Q^2/xs$, with $\sqrt{s}$ being the total positron-proton center of mass energy. In a Lorentz frame where the proton is at rest, y measures the energy transfer of the positron. The kinematical range covered at HERA is compared with that of fixed target experiments in Fig.6.5. Reaching $Q^2 \approx 10^5$ GeV^2 corresponds to a spatial resolution in the am range.

One of the main goals of the HERA physics program is the determination of the three structure functions. Since both the positron and the final state hadrons marking the path of the struck quark are observed in the detector the kinematical variables can be reconstructed from angle and energy of either positron or hadronic jet or a combination of both. For example in terms of positron quantities one finds

$$y_e = 1 - \frac{E_e(1-\cos\theta_e)}{2E_e^0} , \quad Q_e^2 = \frac{E_{T,e}^2}{1-y_e} , \quad M_e = \sqrt{sx_e} = \sqrt{\frac{Q_e^2}{y_e}} .$$

M_e is the mass of the positron-quark system, $E_{T,e}$ the transverse energy of the positron, $E_e^0 = 27.5$ GeV and θ_e is the polar scattering angle relative to the proton direction. The H1-detector has good positron energy resolution, which favors use of positron variables in particular at high momentum transfers, but important and quite accurate cross checks using the jet quantities are possible, too.

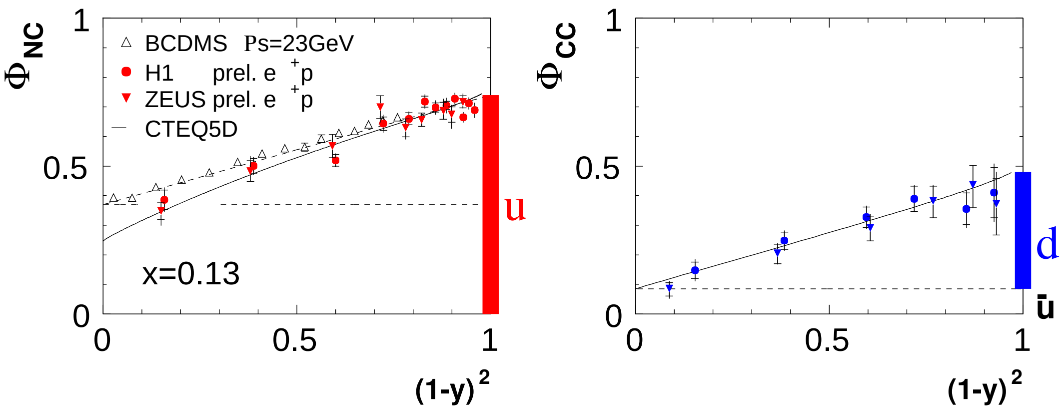

Figure 6.4: *Structure function terms $\Phi_{NC} \equiv \Phi_\gamma$ and $\Phi_{CC} \equiv \Phi_W$ for e^+p scattering at $x = 0.13$ as a function of $(1-y)^2$(taken from [51]).*

For the charged electroweak current mediated by W-boson exchange the cross section takes the form

$$\frac{d^2\sigma_{CC}}{dx\ dQ^2} = \frac{G_F^2}{2\pi x}\left(\frac{M_W^2}{M_W^2+Q^2}\right)^2 \Phi_W(x,Q^2) .$$

In leading order QCD the structure function terms take a particularly instructive form which exhibits the valence (u, d) and sea quark (s, c) densities within the proton

$$\Phi_\gamma = \left(1 + (1-y)^2\right) \left[\frac{4}{9}(u + c + \bar{u} + \bar{c}) + \frac{1}{9}(d + s + \bar{d} + \bar{s})\right]$$

$$\Phi_W = x\left[(\bar{u} + \bar{c}) + (1-y)^2(d+s)\right] \quad (e^+) \quad ; \; \Phi_W = x\left[(u+c) + (1-y)^2(\bar{d} + \bar{s})\right] \quad (e^-) \quad .$$

The valence quark contributions can be identified through their dependence on $(1-y)^2$ equivalent to $\cos^4(\theta^*/2)$, where θ^* is the scattering angle in the eq centre-of-mass system (Fig.6.4).

Figure 6.5 displays the positron proton cross section at high momentum transfer and indicates nicely the electroweak unification scale of $Q^2 \approx 10^4$ GeV^2 (near equality of the charged and neutral current cross sections), and the agreement between the data from the two collider experiments as well as with standard model predictions. The latter agreement holds also for all observables sensitive to signals of beyond the standard model physics. The lower limits (95% confidence) on the quark radius assuming point-like leptons ($f_e \equiv 1$: $R_q < 0.82$ am (10^{-18}m) or common form factors ($f_e = f_q$: $R_q < 0.57$ am) may be cited [52] as just one example for the various exclusion limits set by our data [6, 10, 14, 35, 36, 52].

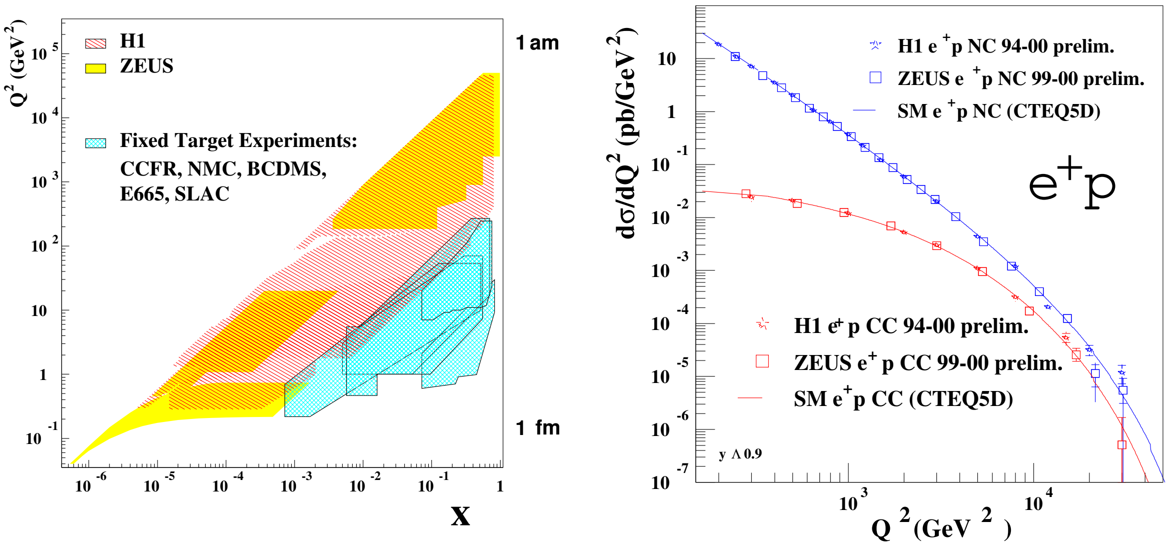

Figure 6.5: *Left: Kinematic reach of deep inelastic scattering experiments in the x versus Q^2 plane [51]. Right: Positron-proton charged and neutral current cross section integrated over all parton momenta x in function of the momentum transfer Q^2. The data come from both HERA collider experiments* [P52] *[51].*

6.6.2 Beauty cross section

Beauty production recently received renewed interest, also due to the new measurements at HERA, which were in the focus of discussions on QCD tests at last year's summer conferences. The results [41, 45, 53] are summarized in Fig. 6.6a.

Thanks to the central silicon tracker H1 is leading the field in this area. The lifetime-based results are unique at HERA and currently being finalized for publication (Thesis J. Kroseberg). Similar discrepancies between data and theory have been observed in $\bar{p}p$ collisions, and more recently, also in two-photon interactions at LEP (for a short review, see [41]). Deep-inelastic ep scattering provides, apart from e^+e^- annihilations, the cleanest environment for

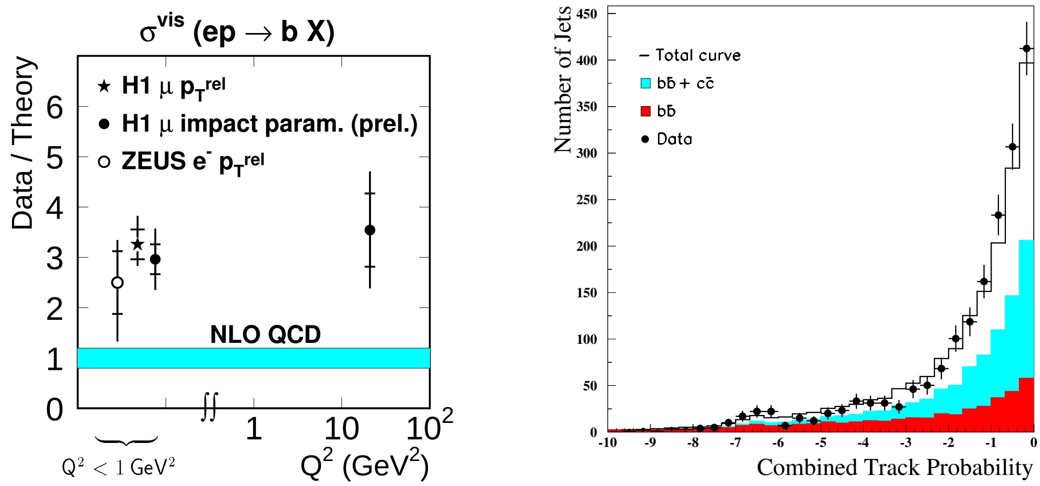

Figure 6.6: *Left: ratio of b production cross sections measured at HERA over theoretical expectation, as a function of Q^2. Right: distributions of a vertex estimator for data and simulated $b\bar{b}$, $c\bar{c}$ and light quark events. Small values indicate the presence of tracks from secondary decay vertices.*

the study of beauty production, since uncertainties associated with hadronic structure are limited to the well-measured proton. Studies of the process at HERA therefore hold the promise to provide clues to resolve this puzzle.

In order to obtain more information on the production dynamics, it is necessary to tag the rarely produced b quarks with highest possible efficiency. Multi-impact parameter methods based on the lifetime signature in inclusive decay modes have been successfully applied at other experiments and hold the promise to bear fruit also at HERA, since the achieved track and vertex resolutions are similar to, e.g., what is available at LEP. The idea is to combine the significances with which extrapolated tracks miss the ep interaction point such that one obtains a probability which quantifies whether an event or a jet originates from one common primary vertex, or contains secondary vertices from heavy quark decays. The discriminating power of an estimator constructed along these lines is illustrated in Fig.6.6b taken from ongoing analysis work (thesis I. Foresti).

We are using here a muon-tagged dijet sample, on which our previous measurements are based, such that the beauty content is under control. This allows the tagging efficiency to be calibrated for a subsequent application of the method to the general case of an unbiased jet selection.

6.6.3 Prompt photon production

Besides deep-inelastic scattering at HERA also reactions of high energy photons with the proton can be studied (γp collisions).

During the last years the research concentrated on the structure of the virtual photon, and on the determination of an effective parton distribution in the photon based on the measurement of di-jet events.

With the large luminosity of 133 pb^{-1} collected in the years 96-00 it is now possible to study the structure of the photon in more detail by analysing events with isolated high energetic photons. Events with a hard photon (prompt photon) instead of a gluon emitted in the hard subprocess depend much less on details of the fragmentation or hadronisation. As a result the systematic error in the determination of the momentum fraction of the partons of the scattering process is reduced considerably.

The cross section of the direct process $q\gamma \rightarrow q\gamma$ where the virtual photon takes part in the scattering process is 197 pb. Relevant for the determination of the photon structure is the resolved process, where a parton from the photon scatters off a parton from the proton. The dominant resolved process $qg \rightarrow q\gamma$ has a cross section of 273 pb, the process $q\bar{q} \rightarrow g\gamma$ is strongly suppressed with a cross section of only 40 pb. The resolved process is further suppressed kinematically, since the scattered photon is pointing in forward direction (direction of the proton beam). In forward direction the identification of the photon is hampered by multiple scattering and conversion due to dead material and particles from the proton remnant.

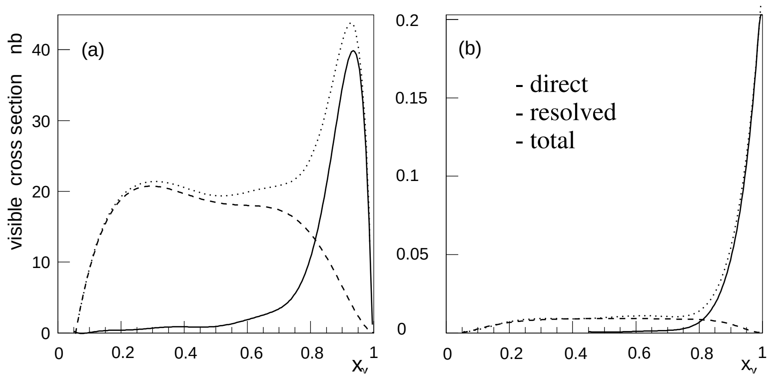

Figure 6.7: *Visible cross section for (a) two jet events and (b) events with prompt photons as a function of x_γ the momentum fraction of the photon carried by the parton. The full line shows the contribution of the direct process, the dashed line from the resolved process and the dotted line the sum of both.*

The disadvantage of this analysis is the low cross section which is suppressed by a factor of the order of $\mathcal{O}(\alpha/\alpha_s)$ with respect to the two jet production (see Fig.6.7). Therefore, the crucial point of the analysis is the identification of background from di-jet production in photoproduction events with high transverse momenta. The particles which mimic a photon candidate are mainly neutral mesons (π^0 or η).

The transverse and longitudinal cluster size is used to suppress these events but is not sufficient to separate signal and background. A further cut on the isolation of the photon, which also reduces higher order processes such as events with a photon radiated off the outgoing quark, has to be applied. It reduces the background to roughly 25% but cuts also significantly into the signal for resolved photons.

Further discrimination of neutral mesons and photons on a statistical basis need a detailed understanding of the shower shapes both in data and in Monte Carlo. The standard Monte Carlo description is not sufficient so it was necessary to start a detailed though time consuming simulation both for the signal and the background contribution. Preliminary results are expected this summer.

6.6.4 Inelastic J/Ψ production

Also in the second branch of heavy flavour physics, in heavy quarkonium production, H1 recently arrived at new, leading results based on large statistics ($\sim 80\,pb^{-1}$), including most recent data. The J/Ψ meson with its clean experimental dilepton signature was originally thought to provide access to the gluon density in the proton in a similar manner as open charm production. However, measurements of charmonium production in $\bar{p}p$ collisions were found in excess of predictions by one to two orders of magnitude and put the validity of the conventional QCD approach into doubt. In the theoretical description, additional production channels were introduced; the requirement that the bound $c\bar{c}$ state produced in the hard perturbative interaction must be left in a color-neutral (*color-singlet* CS) state was given up, *color-octet* (CO) states with net color-charge are in general expected to contribute as well. The Tevatron data can be described in this framework, however at the expense of new non-perturbative degrees of freedom, which describe the transition from the octet states into observable (color-neutral) hadrons. These parameters must be adjusted to experimental data, but are considered to be universal; a hypothesis which must withstand experimental verification.

HERA provides a formidable testing ground for these rather recent developments. The measured p_T spectrum of J/Ψ mesons recorded in photoproduction is compared to theoretical predictions in Fig.6.8. The events have triggered using track information from the CIP and CJC, in coincidence with a muon signal from the J/Ψ decay. The data extend to higher transverse momenta than previous measurements and thus provide a better lever arm to disentangle contributions with different p_T dependences. In fact, the reaction $\gamma p \to J/\Psi X$ is

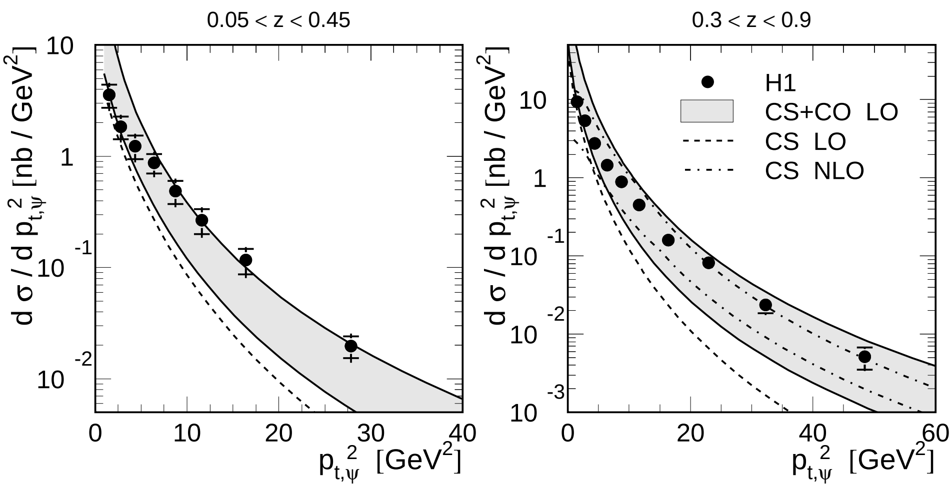

Figure 6.8: *p_T spectra of J/Ψ mesons, measured in photoproduction, compared with QCD predictions. The NLO calculation is not applicable at low values of the inelasticity z, where resolved photon processes become important.*

the only one for which a full next-to-leading order (NLO) computation has been performed, and the comparison shows that while a description including CS and CO contributions is compatible with the data, adding order α_s^2 corrections can change their relative importance considerably. The CO processes also exhibit different variations with photon virtuality Q^2; measurements in DIS therefore provide complementary information. The J/Ψ cross section as a function of Q^2 is displayed in Fig.6.9. The recent QCD calculation, shown for comparison, includes part of the NLO corrections and is expected to be more reliably for virtualities higher than the J/Ψ mass squared. The new data, with extended range and precision, are in fact better described as Q^2 increases. These measurements represent significant constraints to the further development of a unified QCD description of charmonium production in $\bar{p}p$, γp and ep interactions.

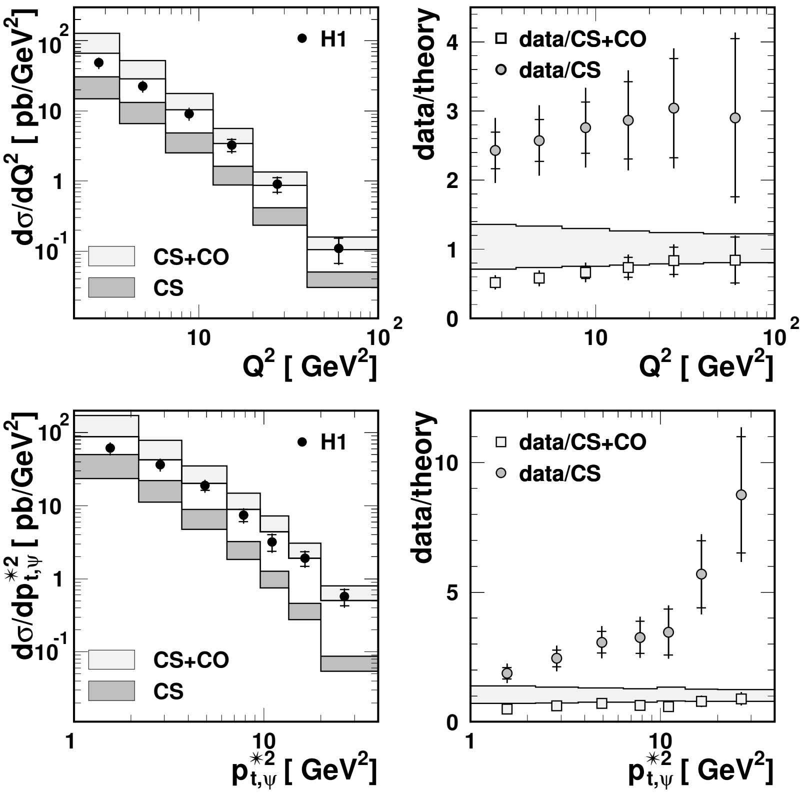

Figure 6.9: *J/Ψ production cross sections, measured in DIS as functions of Q^2 and of p_T^*, the transverse momentum in the hadronic centre-of-mass system, compared with QCD calculations.*

References

[1] *Di-jet Production in Charged and Neutral Current e^+p Interactions at High Q^2*, H1-Coll., C. Adloff *et al.*, Eur. Phys. J. **C19** (2001), 429

[2] *Measurement and QCD Analysis of Jet Cross Sections in Deep-Inelastic Positron-Proton Collisions at $\sqrt{s}$ of 300 GeV*, H1-Coll., C. Adloff *et al.*, Eur. Phys. J. **C19** (2001), 289

[3] *Diffractive Jet-Production in Deep-Inelastic e^+p Collisions at HERA*, H1-Coll., C. Adloff *et al.*, Eur. Phys. J. **C20** (2001), 29

[4] *Deep-Inelastic Inclusive ep Scattering at Low x and a Determination of α_s*, H1-Coll., C. Adloff *et al.*, Eur. Phys. J. **C21** (2001), 33

[5] *Measurement of Neutral and Charged Current Cross Sections in Electron-proton Collisions at High Q^2 at HERA*, H1-Coll., C. Adloff *et al.*, Eur. Phys. J. **C19** (2001), 269

[6] *Searches at HERA for Squarks in R-Parity Violating Supersymmetry*, H1-Coll., C. Adloff *et al.*, Eur. Phys. J. **C20** (2001), 639

[7] *Photoproduction with a Leading Proton at HERA*, H1-Coll., C. Adloff *et al.*, Nuclear Physics **B619** (2001), 3

[8] *Three-Jet Production in Deep-Inelastic Scattering at HERA*, H1-Coll., C. Adloff *et al.*, Phys. Lett. **B515** (2001), 17

[9] *First Measurement of the Cross Section for Deeply Virtual Compton Scattering*, H1-Coll., C. Adloff *et al.*, Phys. Lett. **B517** (2001), 47

[10] *A Search for Leptoquark Bosons in e^-p Collisions at HERA* , H1-Coll., C. Adloff *et al.*, Phys. Lett. **B523** (2001), 234

[11] *On the Rise of the Proton Structure Function F_2 towards Low x* , H1-Coll., C. Adloff *et al.*, Phys. Lett. **B520** (2001), 183

[12] *Measurement of $D^{*\pm}$-Meson Production and F_2^c in Deep-Inelastic Scattering at HERA*, H1-Coll., C. Adloff *et al.*, Phys. Lett. **B528** (2002), 199

[13] *$D^{*\pm}$ Meson Production in Deep-Inelastic Diffractive Interactions at HERA*, H1-Coll., C. Adloff *et al.*, Phys. Lett. **B520** (2001), 191

[14] *Search for Excited Neutrinos at HERA* , H1-Coll., C. Adloff *et al.*, Phys. Lett. **B525** (2002), 9

[15] *Measurement of Dijet Electroproduction at Small Jet Separation*, H1-Coll., C. Adloff *et al.*, Eur. Phys. J. **C** (2002), in print

[16] *Measurement of Dijet Cross Sections in Photoproduction at HERA*, H1-Coll., C. Adloff *et al.*, DESY 01 – 225, hep-ex 0201006, Eur. Phys. J. **C** (2002), in print

[17] *Energy Flow and Rapidity Gaps between Jets in Photoproduction at HERA*, H1-Coll., C. Adloff *et al.*, DESY 02 – 023, hep-ex 0203011, Eur. Phys. J. **C** (2002), in print

[18] *A Measurement of the t Dependence of the Helicity Structure of Diffractive ρ Meson Electroproduction at HERA*, H1-Coll., C. Adloff *et al.*, DESY 02 – 027, hep-ex/0203022, Phys. Lett. **B** (2002), in print

[19] Contr. to Int. Europhysics Conf. on High Energy Physics, Budapest, Hungary (July 2001), and to *Lepton-Photon 01*: XX. Int. Symp. on Lepton and Photon Interactions at High Energies, Rom (July 2001).

[20] *Inclusive Measurement of Deep Inelastic Scattering at High Q^2 in ep Collisions at HERA* (# 741, # 481, [19])

[21] *Diffractive $\Psi(2s)$ Photoproduction at HERA* (# 792, # 486, [19])

[22] *Investigation of Pomeron- and Odderon Induced Photoproduction of Mesons Decaying to Pure Multiphoton Final States at HERA* (# 795, # 488, [19])

[23] *Measurement of Density Matrix Elements for ρ Meson Production at Large $|t|$* (# 796, #489, [19])

[24] *A New Measurement of the Deep Inelastic Scattering Cross Section and of F_L at Low Q^2 and Bjorken-x at HERA* (#799, # 492, [19])

[25] *Measurement of the Proton Structure Function Using Radiative Events at HERA* (# 801, # 493, [19])

[26] *Radiative Charged Current Interactions at HERA* (#804, # 497, [19])

[27] *Diffractive J/Ψ Vector Meson Production at High t at HERA* (# 806, # 499, [19])

[28] *Measurement of the Diffractive Structure Function $F_2^{D(3)}(\beta, Q^2, x_\P$* (#808, # 500, [19])

[29] *Measurement of Semi-inclusive Diffractive Deep-inelastic Scattering with a Leading proton at HERA* (# 809, # 501, [19])

[30] *Photoproduction of ρ Mesons with a Leading Proton* (# 810, # 502, [19])

[31] *Dijet Cross Section in Photoproduction and Deep-inelastic Scattering with a Leading Neutron at HERA* (# 811, # 503, [19])

[32] *The Photoproduction of Protons at HERA* (# 815, # 507, [19])

[33] *Search for Compositeness, Leptoquarks and Large Extra Large Dimensions in eq Contact Interaction at HERA* (#785, # 479, [19])

[34] *Observation of Events with Isolated Leptons and Missing P_T and Comparison to W Production at HERA* (#802, #495, [19])

[35] *A Search for Leptoquark Bosons in ep Collisions at HERA* (#822, # 514, [19])

[36] *Search for Single Top Production in $e^+ - p$ collisions at HERA* (# 824, # 512, [19])

[37] *Inclusive Measurement of Deep Inelastic Scattering at High Q^2 in ep Collisions at HERA* (# 787,# 481, [19])

[38] *Measurement of the Beauty Photoproduction Cross Section* (# 790, # 483, [19])

[39] *Beauty Production in Deep Inelastic Scattering* (# 807, # 484, [19])

[40] *Measurement of Single Inclusive High E_T Jet Cross Sections in Photoproduction at HERA* (# 813, # 505, [19])

[41] *Open beauty production*, F. Sefkow, Proc. Workshop on New Trends in HERA Physics 2001, Ringberg Castle, Tegernsee, Germany (June 2001); hep-ex/0109038.

[42] *Open beauty production at HERA*, J. Kroseberg, hep-ex/0108052, Proc. 9^{th} Int. Workshop on Deep Inelastic Scattering (DIS 2001), Bologna, Italy, 27 Apr - 1 May 2001

[43] *The Gluon Distribution xg and the Strong Coupling Constant α_s from Inclusive DIS data by H1*, R. Wallny, Proc. 9^{th} Int. Workshop on Deep-Inelastic Scattering (DIS2001), Bologna, Italy (May 2001)

[44] *Measurement and QCD Interpretation of the Deep-inelastic ep Scattering Cross Section by H1*, R. Wallny , Proc. Int. Europhysics Conf. on High-Energy Physics (HEP 2001), Budapest, Hungary (July 2001), D. Horvath *et al.* eds., J. High-Energy Phys. Proc. Sect. (*http://jhep.sissa.it/*), PRHEP-hep2001/008

[45] *Heavy Quark Production in Deep-inelastic Scattering*, F. Sefkow, Proc. Int. Europhysics Conf. on High-Energy Physics (HEP 2001), Budapest, Hungary (July 2001), D. Horvath *et al.* eds., J. High-Energy Phys. Proc. Sect. (*http://jhep.sissa.it/*), PRHEP-hep2001/021, hep-ex/0110036.

[46] *Open Heavy Flavour Production at HERA*, J. Kroseberg, Proc. Lake Louise Winter Institute on Fundamental Interactions, Lake Louise, Alberta, Canada (February 2002)

[47] *Deep-Inelastic Inclusive ep Scattering at Low x and a Determination of α_s*, Rainer Wallny, PhD-thesis

[48] *Compact Frontend-Electronics and Bidirectional 3.3 Gbps Optical Datalink for Fast Proportional Chamber Readout*, S. Lüders *et al.* hep-ex 0107064, Nucl. Instr. Meth. **A** (2001), in print

[49] *Das Triggersystem der CIP Kammer bei H1*, Frühjahrstagung DPG, Leipzig (März 2001), available at *https://www.desy.de/ ũrban/ftp/DPG%202002/H1_CIP2k_Triggersystem_DPG2002_140302.zip*

[50] See report given by J. Becker at DESY, November 2001, available at *http://www-h1.desy.de/b̃ecker/Documents/Trigger_Meeting_12_11_01.ps.gz*

[51] M. Erdmann, *Proton and photon structure*, Proc. Int. Symp. on Lepton and Photon Interactions at High Energies, Rome (July 2001), DESY 02 – 013.

[52] *Search for New Physics Phenomena in eq Contact Interactions at HERA*, H1-Coll., C. Adloff *et al.*, in preparation.

[53] C. Adloff *et al.* [H1 Collaboration], Phys. Lett. **B467** (1999) 156, erratum ibid. **B518** (2001) 331; J. Breitweg *et al.* [ZEUS Collaboration], Eur. Phys. J. **C18** (2001) 625.

[54] F. Abe *et al.* [CDF Collaboration], Phys. Rev. Lett. **79** (1997) 572; ibid. 578.

[55] G.T. Bodwin, E. Braaten and G.P. Lepage, Phys. Rev. **D51** (1995) 1125, erratum ibid. **D55** (1995) 5853; E. Braaten and Y.Q. Chen, Phys. Rev. **D54** (1996) 3216; W.E. Caswell and G.P. Lepage, Phys. Lett. **B167** (1986) 437.

[56] *Inelastic Photoproduction of J/Ψ Mesons at HERA*, H1-Coll., C. Adloff *et al.*, in preparation.

[57] *Inelastic Leptoproduction of J/Ψ Mesons at HERA*, H1-Coll., C. Adloff *et al.*, in preparation.

7 Particle Physics at DESY/HERA (HERA-B)

P. Robmann, P. Truöl and T. Walter (until 2/01)

in collaboration with:
the Universities of Heidelberg and Siegen and 31 further institutes from outside Switzerland

(**HERA-B** collaboration)

The difficulties encountered by the HERA machine crew in recommissioning the accelerators have prevented the HERA-B collaboration from taking new data, too. The detector is ready and the planned improvements on the microstrip gas chamber system for the inner tracker (see last years annual report [1]) have been carried out. The experiences gained with this system during design, prototyping, testing and one year of exposure to the beam in 2000 have now been documented and submitted for publication [2].

From a short exploratory run in 2000 it was possible to determine the $b\bar{b}$ production cross section for 920 GeV protons, albeit with rather limited accuracy [3]. Since the first level trigger of HERA-B was not fully operative the proton interaction rate was limited to 5 MHz. The analysis was based on the chain $pA \to b\bar{b}\ X$; $b\bar{b} \to J/\Psi\ Y \to (e^+e^-/\mu^+\mu^-)\ Y$, with b-hadron decays into J/Ψ distinguished from prompt J/Ψ background using the *lifetime tag*, i.e. employing a vertex cut. The prompt $\mu^+\mu^-$ mass spectrum is shown in Fig.7.1. With a

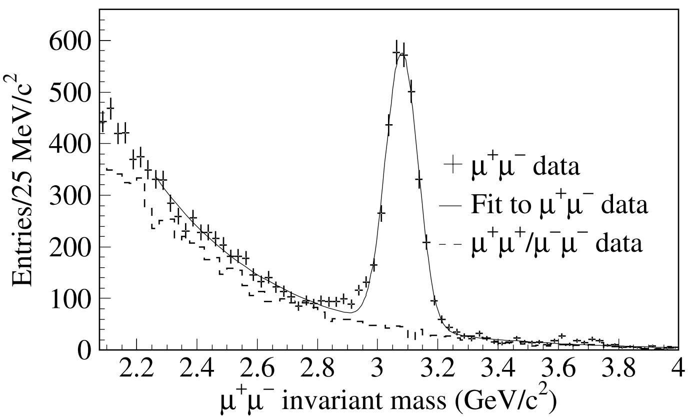

Figure 7.1: *The $\mu^+\mu^-$ invariant mass spectrum, after the J/Ψ selection cuts, observed in a one week exploratory run in 2000.*

decay length resolution of $\sigma(\Delta z) = 715 \pm 24\ \mu$m and a mean decay length of the triggered b-hadrons of about 8 mm, a few events (see Table 7.1) survive a vertex cut of $>$ 5 mm downstream from the wire, on which the interaction occurred. The background from the tails of the vertex distributions can be estimated by looking at the upstream sample, or from a Monte Carlo simulation of the charm contribution. When normalized to the inclusive J/Ψ production cross section measured elsewhere [4], and using the calculated acceptance the cross section listed in Table 7.1 and plotted in Fig.7.2 results. The latest QCD calculations [5, 6] predict cross sections at 920 GeV of $\sigma(b\bar{b}) = 25^{+20}_{-13}$ and 30 ± 13 nb/nucleon, respectively, in favorable agreement with the measured value $\sigma(b\bar{b}) = 32^{+14}_{-12}$ (stat.) ± 7 (syst.) nb/nucleon. This analysis indicates, that the upcoming 2002/3 data taking may also lead to significant tests of potentially refined QCD predictions in the $b\bar{b}$ sector similar to what has been discussed in connection with the H1 ep data elsewhere in this annual report.

Table 7.1: *Parameters entering the calculation of the* $(b\bar{b})$ *cross section.* $\Delta\sigma$ *refers to the restricted kinematic range* $-0.25 < x_F < 0.15$.

		$\mu^+\mu^-$ ch.	e^+e^- ch.
Target	77% C(A=12) + 23% Ti(A=48)		
Beam energy	920 GeV		
pp c.o.m. energy	41.6 GeV		
$\sigma(J/\Psi) \times A^\alpha/A$, α [4]	314 ± 31 nb/nucleon, 0.955(5)		
Prompt J/Ψ		2880 ± 60	5710 ± 380
Detached J/Ψ		$1.9^{+2.2}_{-1.5}$	$8.6^{+3.9}_{-3.2}$
Acceptance $\epsilon_R \cdot \epsilon_B^{\Delta z}$		0.41 ± 0.01	0.44 ± 0.02
Branching ratio $(b\bar{b} \to J/\Psi X)$	0.0232 ± 0.0020		
$\Delta\sigma(b\bar{b})$ (nb/nucleon)		16^{+18}_{-12}	38^{+18}_{-15}
Combined $\Delta\sigma(b\bar{b})$	$30^{+13}_{-11} \pm 6$ (syst.) nb/nucleon		
Combined $\sigma(b\bar{b})$	$32^{+14}_{-12} \pm 7$ (syst.) nb/nucleon		

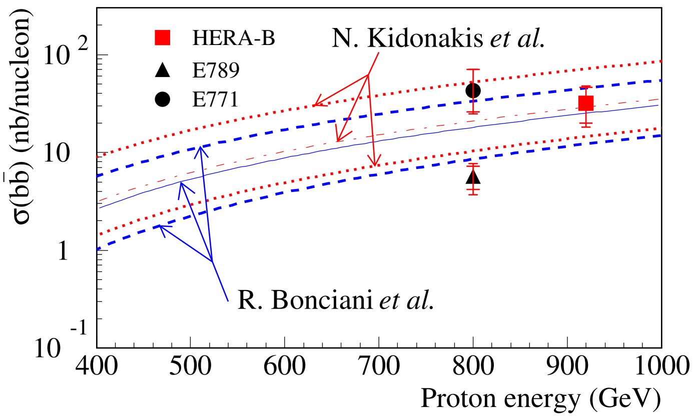

Figure 7.2: *Comparison of the HERA-B (2000)* $b\bar{b}$ *production cross section with other experiments [4] and theoretical predictions of Bonciani et al. [5] and Kidonakis et al. [6]*

References

[1] Physik-Institut, Universität Zürich, Annual Report 2001/2, available at *http://www.physik.unizh.ch/jb/2001*.

[2] *Studies of aging and HV break down problems during development and operation of MSGC and GEM detectors for the inner tracking system of HERA-B*, Y. Bataguria *et al.*, hep-ex/0204022, Nucl. Instr. Meth. **A**, in print.

[3] *Measurement of the* $b\bar{b}$ *production cross section in 920 GeV fixed-target proton-nucleus collisions*, I. Abt *et al*, to be submitted to Eur. Phys. J.**C**.

[4] M.H. Schub *et al.*, Phys. Rev. **D52** (1995), 1307; T. Alexopoulos *et al.*, Phys. Rev. **D55** (1997), 3927.

[5] R. Bonciani *et al.*, Nucl. Phys. **B529** (1998), 424.

[6] N. Kidomakis *el al.*, Phys. Rev. **D64** (2001), 11401.

8 High-precision CP-violation Physics at LHCb

R. Bernet, F. Lehner, M. Needham, P. Sievers, O. Steinkamp, U. Straumann, A. Vollhardt, D. Wyler, M. Ziegler

in collaboration with:
The inner tracking group of LHCb: University of Lausanne; Max Planck Institute, Heidelberg, Germany; University of Santiago de Compostela, Spain; Budker Institute for Nuclear Physics (INP), Novosibirsk, Russia and Ukrainian Academy of Sciences, Kiev, Ukraine.

The full LHCb collaboration consists of 50 institutes from the countries Brazil, China, Finland, France, Germany, Italy, Netherlands, Poland, Romania, Russia, Spain, Switzerland, Ukraine and the United Kingdom.

(LHCb)

8.1 Introduction

LHCb [1] is a dedicated B-physics experiment under development to operate at the LHC at CERN. The main goal of the experiment is a precise determination of many different CP violating amplitudes and the study of rare decays of B mesons. It will use a moderate luminosity of $2-5\times10^{32}\mathrm{cm}^{-2}\mathrm{s}^{-1}$ and will be fully operational at the startup of the collider. Since the production of b quarks at LHC is strongly peaked towards small polar angles with respect to the beam axis, the LHCb detector is layed out as a single-arm forward spectrometer, with an acceptance coverage of up to 300 mrad in the bending plane of the dipole magnet. In the design of the experiment, special attention has been given to the precise reconstruction of primary and secondary vertices (vertex detector VELO), to efficient particle identification over a wide momentum range, from 1 to 100 GeV/c (two RICH detectors), and to efficient triggering of B meson decays.

The efficient and precise reconstruction of the trajectories of charged particles and their momenta is one of the most challenging tasks in LHCb. A magnetic spectrometer consisting of a 4 Tm dipole magnet and nine planar tracking stations has been designed for this purpose. Each of these stations has four detection layers. In two layers the detector elements are oriented vertically. In the other two they are rotated by a small stereo angle, clockwise and counter-clockwise. This layout provides precise coordinate information in the horizontal plane, which is the bending plane of the magnet, and sufficient spatial information for pattern recognition in the vertical plane. The largest tracking station extends over a sensitive area of about $4.5\times6.5\,\mathrm{m}^2$. In Monte-Carlo studies, an average momentum resolution of 0.39% is obtained, which is dominated by multiple scattering for momenta up to 100 GeV/c.

Each tracking station employs two different detector technologies. Charged particle densities can be as high as $10^6\mathrm{cm}^{-2}\mathrm{s}^{-1}$ in the innermost region near to the beam pipe, but fall off rapidly with increasing distance from the beam axis. The largest part of the sensitive area of each tracking station will be covered with a straw drift tube detector. However, close to the beam pipe particle densities are prohibitively high for the use of this detector technology. This region will be covered with a silicon strip detector, the Inner Tracker.

The charged particle flux in the LHCb spectrometer is dominated by electrons and positrons from gamma conversions in the material of beam pipe and detector, and by pions from the primary vertex. The expected charged particle rates thus translate to a moderate 1-MeV neutron equivalent fluence of $5\times10^{13}\,\mathrm{cm}^{-2}$ after 10 years of operation in the hottest region of the detector, although the integrated radiation dose can be as high as 20 Mrad after 10 years.

8.2 Detector layout

The size and shape of the Inner Tracker are determined by the requirement of occupancies which should not exceed 15% in the straw tracker, while minimising the area covered by the expensive silicon technology. Our studies lead to the layout [2] illustrated in Fig. 8.1, in which the Inner Tracker covers a cross-shaped area around the beam pipe.

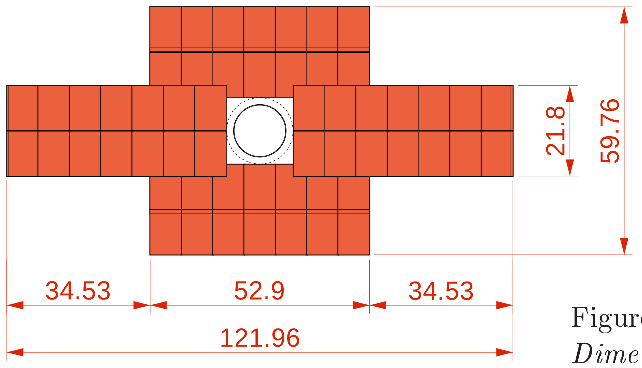

Figure 8.1: *Layout of an Inner Tracker station. Dimensions are in cm.*

Each Inner Tracker station consists of four detector boxes, above, below and to both sides of the beam pipe. Each of these boxes contains four detection layers (strips vertical, +/-5° stereo angle, vertical) and each detection layer consists of seven or eight staggered ladders of silicon sensors. The ladders are either 11 or 22 cm long, assembled from one or two silicon sensors, and are read out at one end. The four detection layers are enclosed in a common, light tight and thermally and electrically insulating housing. The complete Inner Tracker, consisting of nine stations, employs 36 detector boxes and about 1500 silicon sensors and covers a sensitive area of about 14 m^2.

An important design aim in the development of the Inner Tracker was to devise a modular and uniform system. In the current layout, each detector box can be operated as a standalone unit, and the full Inner Tracker can be produced using only one type of silicon sensor, two types of ladders, and three types of detector boxes.

8.3 Silicon sensors

The momentum resolution of the LHCb tracking system being dominated by multiple scattering, a moderate spatial resolution of about 80 μm is sufficient for the Inner Tracker. This suggests the use of sensors with a large read-out pitch of typically 240 μm. Simulation studies show that at this pitch occupancies are below a few percent everywhere. Sensors should be as thin as possible in order to minimise the multiple scattering of particles in the detector material. On the other hand, the LHC bunch-crossing frequency of 40 MHz forces the use of fast front-end electronics, with a shaping time of the order of 25 ns, in order to avoid overlapping events from consecutive bunch crossings. The combined requirements of fast read-out electronics, thin sensors and long read-out strips, limit the attainable signal-to-noise performance of the detector. The sensor strip geometry has to be carefully chosen in order to optimise this performance.

First prototype sensors [3] were designed and produced in single-sided p^+n technology from 300 μm thick 4" wafers by the company SPA Detector, Kiev. The sensors had 64 read-out strips of 66.6 mm length, and the strip pitch was $p = 240\,\mu$m. Implant widths w corresponding to $w/p = 0.2$, 0.25 and 0.3, were implemented on three different groups of strips. The read-out strips were AC coupled and biased through polysilicon resistors. The characterisation of these sensors in a laboratory setup in Zürich (P. Sievers) showed a typical depletion voltage of about 50–70 V and a total strip capacitance of 1.3–1.6 pF / cm depending on implant width. Unfortunately, all sensors exhibited rather low break-down voltages of typically 100–130 V.

Several silicon ladders were assembled from these sensors and tested in laboratory setups in Zürich and Heidelberg, and in test beams at CERN. Ladders used either one or three silicon sensors, the latter resulting in a total read-out strip length of 20 cm. A first beam test [4], using 9 GeV/c charged pions at the T7 facility, was performed using the HELIX read-out chip [5]. The shortest shaping time of the HELIX of about 70 ns (FWHM) is too long for LHCb, but its noise performance is quite similar to that expected for the final LHCb read-out chip (see Sec. 8.4). A beam telescope assembled from HERA-B vertex-detector counters [6] allowed a precise reconstruction of the track impact point in the test ladder and a determination of the collected charge, the signal-to-noise performance and the particle detection efficiency, as function of the track position in between the read-out strips.

The spatial resolution of the test ladders was measured to be of the order of 50 μm. However, the analysis of the data, by P. Sievers, also demonstrated a significant charge loss in the inter-strip region that, for the 20 cm long ladder at fastest shaping, resulted in a sizeable efficiency loss. As illustrated in figures 8.2 and 8.3, the efficiency loss was more pronounced for smaller values of w/p and decreased with increasing bias voltage. We interpret this as the result of a local region of low electric field in between the strips. Charge carriers generated in this region drift very slowly and are either trapped or arrive too late at the read-out strip. An effort to simulate this effect is ongoing. If this interpretation is correct, it should be possible to suppress the charge loss by significantly over-biasing the silicon sensor. Unfortunately, the low break-down voltage of the prototype sensors did not allow to test this hypothesis.

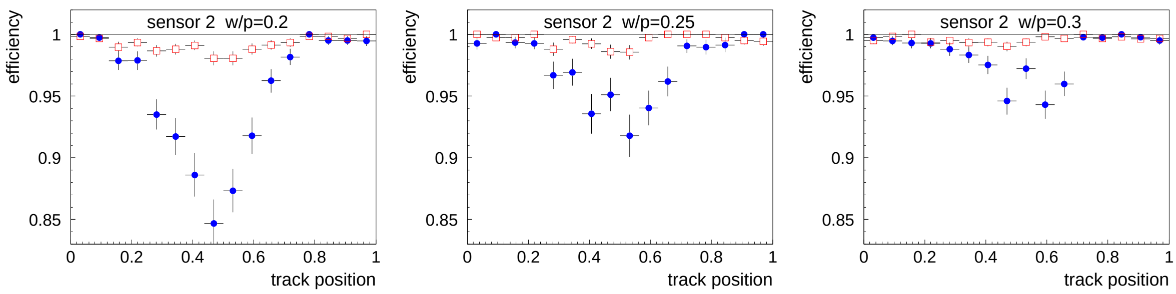

Figure 8.2: *Efficiency of 20 cm long ladder as function of the track position in between strips for w/p=0.2, 0.25, 0.3. The bias voltage was 90 V. Crosses are for shortest, open squares for a longer shaping time (about 120 ns FWHM) of the HELIX read-out amplifier.*

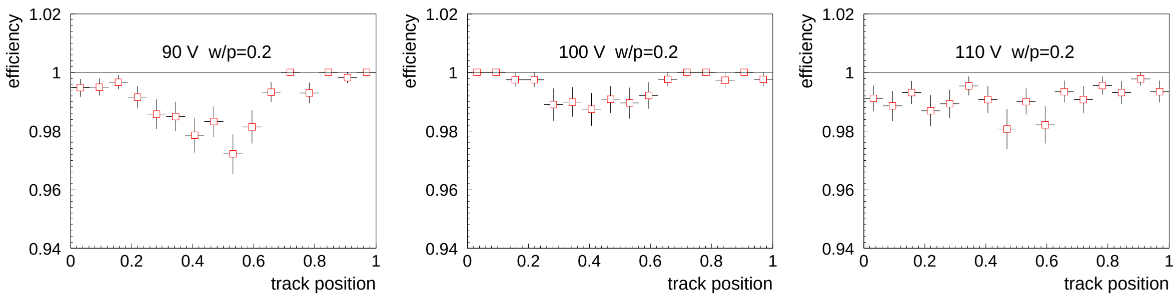

Figure 8.3: *Efficiency of 20 cm long ladder as function of the track position in between strips for w/p=0.2, for bias voltages of 90 V, 100 V and 110 V. Measurements were done with a 120 ns shaping time of the HELIX read-out amplifier.*

A second generation of prototype sensors have been produced by Hamamatsu in single-sided p^+n technology from 320 μm thick 6" wafers, according to specifications by F. Lehner and O. Steinkamp. They have the same overall dimensions as is foreseen for the final detectors, 110 mm long and 78 mm wide, and contain 352 read-out strips with five different strip geometries, namely two strip pitches (198 μm and 237.5 μm) and w/p values between 0.25 and 0.35. Read-out strips are AC coupled and biased through polysilicon resistors. These sensors are currently being characterised in the laboratory and have been biased up to more than 300 V without breakdown. As a next step, they will be assembled to ladders in Zürich and tested in a beam at CERN end of May 2002. The results of this test will provide the basis for the decision on the final strip geometry for the Inner Tracker.

8.4 Front-End electronics

A radiation hard read-out chip in 0.25 μm CMOS technology, called BEETLE [7], is being custom developed in Heidelberg for the LHCb vertex detector and Inner Tracker. It provides a 128-channel preamplifier, and a 168 cells deep analog pipeline that matches the latency of the LHCb L0-trigger. The chip operates at a sampling rate of 40 MHz, and four analog output ports allow to read out the 32-fold multiplexed signals within 900 ns.

The analog output signals of the BEETLE will be transmitted via 10 m long low-mass copper cables to service boxes located on the frames of the tracking station. Here, the signals will be digitised by 8-bit FADCs and fed via 32-bit serializer chips (CERN GOL) and 12-channel VCSEL optical converters into parallel optical cables that will transmit the digitised data at a rate of 19.2 Gbit / s per 12-fibre cable over a distance of about 100 m to the LHCb counting room. A prototype data link is currently being assembled by A. Vollhardt in Zürich.

A first working version of the full read-out chip, the BEETLE v1.1, was connected to Inner Tracker prototype sensors and operated successfully in a beam of 120 GeV/c muons at the CERN–X7 facility in October 2001 [8]. The Zürich group was strongly involved in all phases of this test. Two test ladders were assembled, using one respectively three prototype sensors produced by SPA Detector, Kiev, and read out with two BEETLE chips each. Although the setup did not allow new insights into the S/N performance of the ladders, the chip operated reliably throughout the test. BEETLE v1.1 chips were also exposed to a total ionising dose irradiation at the CERN X-ray facility and showed full functionality up to an integrated dose of 45 Mrad, with only minimal deterioration of the analog performance. The BEETLE v1.1 chip will also be used in a test of the new full-size prototype sensors from Hamamatsu. Beam time at the X7 facility is scheduled for May 2002.

A new version of the read-out chip, the BEETLE v1.2, will be submitted in April 2002. Major improvements for this new version will be the use of SEU-resistent logics and the implementation of a further optimised front end.

The front end has to provide a fast pulse shape and at the same time give good noise performance at the expected load capacitance of about 30 pF. A number of different front ends, implemented in two test chips, have been investigated [9] in Zürich (A. Vollhardt) and Heidelberg in order to optimise for these somewhat contradictory requirements. The finally selected front end was measured to have a fast enough response, with a rise time of below 20 ns and a remainder of less than 30% of the amplitude 25 ns after the maximum, together with an ENC noise of $450\,e^- + 47\,e^- / \mathrm{pF}$. This should allow the operation of a 22 cm long ladder at an acceptable S/N ratio of about 13.

8.5 Detector boxes

The silicon sensors have to be operated at a temperature of about -5°C, in order to minimise additional noise from radiation-induced leakage currents. Efficient cooling of the sensors is thus an important parameter in the design of detector mechanics. Since the detector boxes are completely located inside the acceptance of the spectrometer, the amount of material must be minimised everywhere. F. Lehner plays a leading role in the design of the detector box and the choice and development of low-mass materials for its components.

Within a detector box, all silicon ladders will be individually mounted onto a common cooling plate, as indicated in Fig. 8.4. The cooling plate will be constructed from either beryllium or a light-weight carbon-carbon composite. It will carry alignment pins for precise positioning of the ladders and will be kept at typically -10°C. Liquid C_6F_{14}, running through a cooling pipe attached to the plate, will be used as cooling agent.

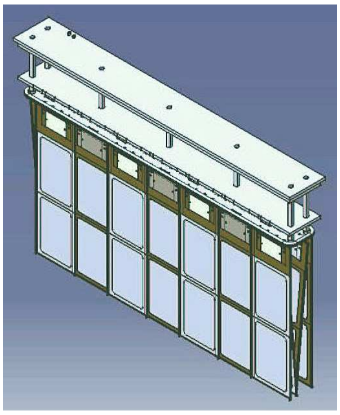

Figure 8.4: *A detector box. The housing is not shown.*

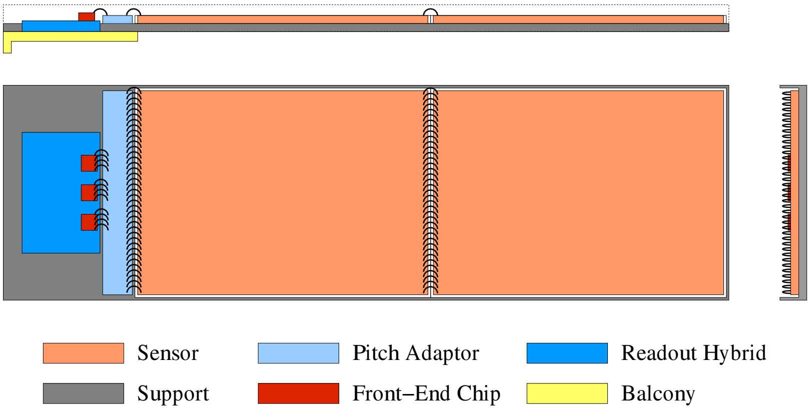

Figure 8.5: *Sketch of a 2-sensor ladder.*

Detector ladders will be assembled on a U-shaped carbon-fibre support, as sketched in Fig. 8.5. This support frame provides mechanical stiffness to the ladder and will be composed of a highly thermal conductive fibre in order to remove the heat generated by leakage currents in the sensors. The support frame will be attached to a cooling balcony from either beryllium or a metal matrix composite material being custom developed in cooperation with the swiss federal institute EMPA/Thun. This balcony will provide the mechanical and thermal contact to the cooling plate. The read-out hybrid will be directly attached to this cooling balcony and will not be in direct thermal contact with the carbon support frame. This construction avoids possible heat flow from the hybrid to the sensors.

The detector box will be enclosed in a housing from thermally insulating polyurethane foam, covered with a thin aluminium foil to provide electrical insulation.

First prototypes of detector box and ladder mechanics have been produced and their thermal and mechanical properties are currently being investigated in Zürich and Lausanne, respectively.

8.6 Outlook

Within the framework of a general re-optimisation of the LHCb detector that aims at a significant reduction the amount of material in front of the calorimeters, a reduction of the number of tracking stations from nine to four is currently being discussed. Studies of tracking algorithms for the new layout are under way and show promising results. M. Needham, who has made significant contributions to the development of the LHCb tracking code, has recently joined the Zürich group and will play an important role in further optimisation studies.

The reduction of the number of tracking stations would allow the possibility to construct the first tracking station, in between the interaction point and the magnet, completely from silicon. The overall size and cost of the silicon tracker would then remain approximately unchanged. The main motivation for this upgrade would be to use information from this station in the Level-1 trigger decision.

A technical design report for the silicon inner tracker is going to be submitted by the end of this year. The construction of the detector is foreseen to take about 18 months and will be scheduled such that the detector can be installed and fully commissioned before the startup of LHC.

References

[1] LHCb technical proposal, CERN/LHCC 998-4

[2] O.Steinkamp, Layout of a Cross-Shaped Inner Tracker, LHCb-2001-114

[3] F.Lehner *et al.*, Description and Characterization of Inner Tracker Silicon Prototype Sensors, LHCb-2001-036

[4] C.Bauer *et al.*, Test Beam Results on Inner Tracker Silicon Prototype Sensors, LHCb-2001-135

[5] http://wwwasic.kip.uni-heidelberg.de/ trunk/projects/Helix/

[6] C.Bauer *et al.*, Nucl.Instr.and Meth. A 418 (1998) 65-79, LHCb-2001-046

[7] N.v.Bakel *et al.*, The BEETLE Reference Manual, Version 1.0, LHCb-2001-046

[8] T.Glebe *et al.*, First Measurements on Inner Tracker Silicon Prototype Sensors Using the BEETLE v1.1 Readout Chip, LHCb-2002-018

[9] D.Baumeister *et al.*, LHCb note in preparation

9 A Silicon Detector for the DØ Experiment at the Tevatron

Frank Lehner

in collaboration with:
the DØ Run IIb silicon detector group: CINVESTAS, Mexico City, Mexico, Fermi National Accelerator Laboratory, Batavia, USA; Kansas State University, Manhattan, USA; Moscow State University, Russia; State University of New York at Stony Brook, New York, USA; University of Illinois, Chicago, USA; University of Washington, Seattle, USA.

The full DØ collaboration consists of 79 institutes from the countries Argentina, Brazil, China, Czech Republic, Colombia, Ecuador, France, Germany, India, Korea, Mexico, Netherlands, Poland, Russia, Sweden, United Kingdom, United States of America and Vietnam.

(DØ Collaboration)

The Run IIa phase of the Tevatron $p\bar{p}$ collider at Fermilab, USA, has started in 2001. It offers an outstanding research programme [1] in high energy physics over the next three years for both of the experiments CDF and DØ which are operational at the Tevatron. Because of the tantalising physics prospects a higher integrated luminosity will bring, Fermilab extends the running of the Tevatron collider, called Run IIb, which could deliver a total integrated luminosity of 15 fb^{-1} in the years 2004-2007. To optimise its physics capability for the future run, the existing silicon detector of the DØ experiment is being replaced [2]. This replacement is even necessary, since the present silicon vertex detector would not survive the harsh radiation environment of Run IIb [3]. The new silicon device will be the centrepiece detector to perform the rich physics programme, which is highlighted by a significant chance of a Higgs boson discovery, if its mass is below 115 GeV [4].

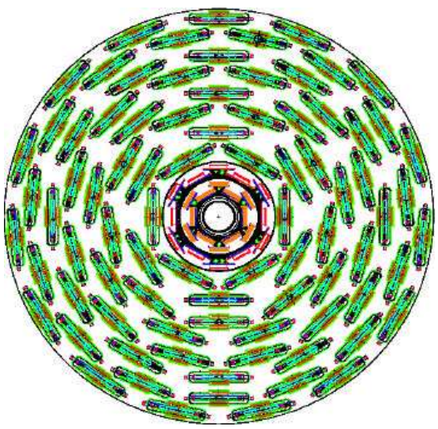

Figure 9.1: *End view of the DØ 6-layer silicon device.*

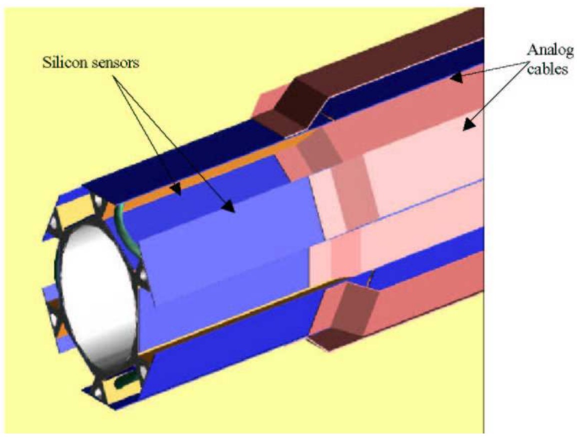

Figure 9.2: *The innermost silicon layer close to the beam pipe. The analog cable routing the silicon signals to the hybrid is also shown.*

The main requirements for the silicon detector are efficient and reliable tracking, precise vertex measurements and radiation hardness in a very harsh charged hadron radiation environment of up to 15 MRad. All of these goals will be met with the designed 6-layer single sided silicon device segmented in two barrels around the beam pipe and covering a pseudo-rapidity range of $|\eta| \leq 2.5$. Fig. 9.1 shows an axial view of the Run IIb silicon tracker. The track lever arm of the detector between the innermost silicon layer and the outermost one will be 150 mm. The outer layers are constructed of 60 μm readout pitch silicon and provide hits essential for improved pattern recognition in a high occupancy environment. In addition, two inner layers 0/1, constructed with 50/58 μm readout pitch silicon sensors with intermediate strips at 25/29 μm, provide precise coordinate measurements essential for good secondary vertex separation and excellent impact parameter resolution in the $r - \varphi$ plane.

Based on this design a total of 2200 single sided silicon sensors in 6"-wafer technology will be used, giving more than 950,000 readout channels. The prototyping, testing and assembly of the silicon detector has to happen on a rather short time scale. However, we can build on our experience gained during the construction of the Run IIa silicon detector [5] and simpler fabrication and assembly methods should result in a much more efficient construction and testing cycle.

The inner two layers have a 12-fold crenellated geometry and will be mounted on a separate carbon fibre lined, carbon foam support structure. Figure 9.2 shows a drawing of the innermost layer. Due to the lack of space and severe cooling requirements, this layer has off-board electronics. The analog signals are transmitted through up to 420 mm long cables, wire-bonded to the silicon sensors, to a hybrid where the signals will be digitised and sent to the data acquisition system. Keeping the hybrid mass out of the detector active area region helps in reducing photon conversions. The design and operation of a long low-mass analog cable with very fine pitch is non-trivial concerning pick up noise and fabrication issues [6]. In collaboration with the Swiss company Dyconex [7] we have started to develop several cable prototypes based on different design layouts.

References

[1] *First Run IIa results from CDF and DØ* , talks presented by S. Donati (CDF) and A. Juste (DØ) at the XXXVIIth Rencontres de Moriond, Moriond, France, March 17-24, 2002.

[2] The DØ Run IIb silicon detector collaboration: *DØ Run IIb silicon detector upgrade, technical design report*, http://d0server1.fnal.gov/projects/run2b/Silicon/www/smt2b/smt2b.html.

[3] SuYong Choi and Frank Lehner: *What do we know about the radiation damage in silicon detectors for Run II*, internal DØ publication, DØ -note 3803.

[4] Higgs physics at Run IIb, proceedings of the Run IIb workshop at Fermilab. *http://fnth37.fnal.gov/run2.html* and M. Carena, S. Mrenna and C. Wagner, Phys Rev. D62, 055008(2000).

[5] F. Lehner (representing the DØ collaboration): *The status of the DØ silicon tracker upgrade project*, proceedings of the 8th International Workshop on Vertex Detectors, Texel, The Netherlands, June 20-25, 1999, Nucl.Instrum.Meth.A447:9-14, 2000.

[6] K. Hanagaki, Frank Lehner and A. Nomerotski: *The layer 0 analog flex cable for the Run IIb silicon upgrade*, internal DØ publication, to be submitted.

[7] Dyconex advanced circuit technologies, Zurich, Switzerland.

10 Particle Physics with CMS

C. Amsler, A. Dorokhov, R. Kaufmann‡, K. Prokofiev, H. Pruys,
C. Regenfus, P. Robmann, T. Speer, and S. Steiner

in collaboration with:
ETH-Zürich, Paul Scherrer Institut (PSI), Universität Basel and the CMS Collaboration.

(CMS Collaboration)

‡ Now at CSEM, Switzerland

10.1 Introduction

We participate in the CMS experiment at the Large Hadron Collider (LHC) where we shall concentrate on physics involving the b-quark, e.g. b-quark production associated with the formation of Higgs bosons, t-quark decays, spectroscopy of B mesons and CP violation in B decays. For a low mass Higgs, below about 135 GeV/^{2}, the dominant decay mode is $H^0 \to b\bar{b}$. The tagging of b-jets is also essential for the detection of the top quark as, V_{tb} being essentially one, the top quark decays nearly exclusively to W^+b. The study of the rare decays $t \to W^+d$ and $t \to W^+s$ gives a direct measurement of the CKM matrix elements V_{td} and V_{ts} and hence, in case unitarity is violated, leads to physics beyond the Standard Model. Also, searches for flavor changing neutral currents in rare B-decays, like B_d or B_s to $\mu^+\mu^-$, are forbidden at the tree level, but may occur at higher orders and therefore allow to test the Standard Model and to probe its extensions at low energy.

The most interesting events at LHC will therefore contain one or several b-jets originating from the decay of B mesons, with typical mean free paths of a few mm. To allow for efficient tagging of B mesons among the large background of light quark and gluon jets, the detection system has to follow particles towards the primary vertex. In fact, our pixel detector, the detector closest to the interaction point, will be located only 4 cm from the beam-beam interaction point. The extremely high particle flux near the primary vertex ($\sim$ 1000 particles every 25 ns, see Fig.10.1) requires the innermost tracking layers to be composed of pixel devices delivering 3D coordinates with high resolution and no ambiguity. Furthermore, the radiation dose to the nearest detector will approach 10^6 Gy (corresponding to 6×10^{14} hadrons /cm^2) after 10 years of LHC operation (Fig.10.2). This is about 10^6 more than for detectors developed earlier for space research.

Our group joined the CMS collaboration in 1995. During the following years we contributed [1, 2, 3] to the development of the pixel detector, the specifications of which are given in the Technical Design Report [4]. We are also responsible for the design and delivery of the mechanical support structure and the service tubes that will transfer the power, the signals and the coolant to the detector. We are participating in the reconstruction and physics simulation software involving the charged particle tracker. In 2000/2001 we initiated a study of various designs for pixel sensors [5] (which will be briefly discussed below) and, recently, we embarked on tests of the readout chips for the pixel sensors.

10.2 The pixel sensors

The CMS pixel detector consists of three cylindrical layers, 53 cm long, with radii of 4.3, 7.1 and 11 cm (Fig. 10.3, and Table 10.1). The barrel layers containing some 3×10^7 silicon pixels

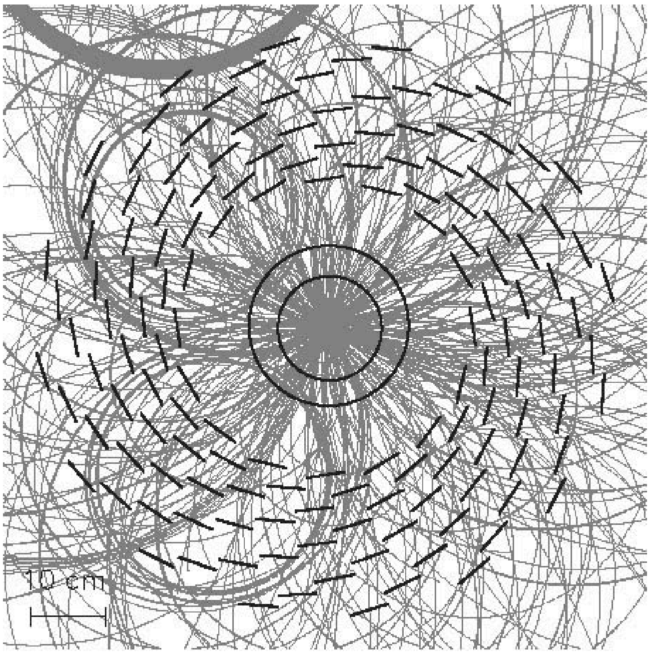

Figure 10.1: *Events of interest will have to be filtered from events with on average 18 superimposed interactions occurring during the same bunch crossing. Shown is a simulated Higgs decay $H \to Z^0 Z^0 \to 2(\mu^+\mu^-)$. The circles indicate the two innermost pixel layers, the circle segments represent the microstrip silicon tracker.*

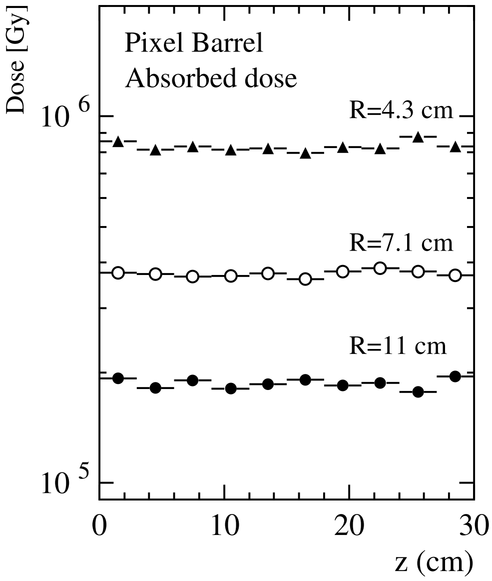

Figure 10.2: *Expected dose absorbed by the CMS pixel barrel in the three layers (radii R), as a function of coordinate along the beam axis (for 10 years of LHC operation).*

will be provided by the ETH-PSI-Basel-Zürich collaboration while the forward/backward wheels will be supplied by the U.S. participants. The pixel modules consist of thin, segmented sensor plates with highly integrated readout chips connected by the indium bump bonding technique (Fig.10.4). A sensor plate contains 53 × 52 pixels, each with an area of 150×150 μm^2 and a thickness of 200 μm. The analog signals are read out to determine the coordinates more accurately, using charge sharing between adjacent pixels in the strong magnetic field of CMS.

The bulk of the sensor is n-material and the implants are n^+. The negative bias voltage is applied to the backside and hence the readout signal is generated by electrons.

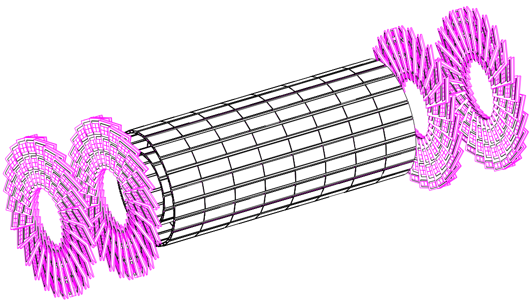

Figure 10.3: *Perspective view of the CMS pixel detector.*

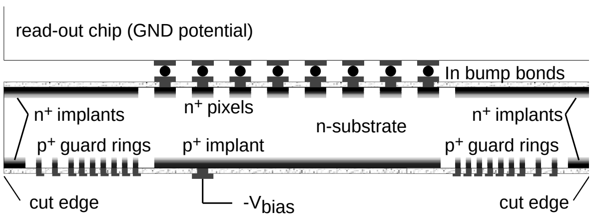

Figure 10.4: *Design of a sensor plate connected to the readout chip. The bias voltage is applied to the backside.*

Table 10.1: *Number of channels and rates at the design luminosity of* $10^{34}\,cm^{-2}s^{-1}$.

	Barrel (r)			End cap (z)	
Layer	4 cm	7 cm	11 cm	33 cm	47 cm
Number of chips	2340	2840	5888	1080	1080
Number of pixels	6.35×10^6	10.6×10^6	16.2×10^6	3.0×10^6	3.0×10^6
Area	0.15 m^2	0.25 m^2	0.38 m^2	0.07m^2	0.07 m^2
Pixel hit rate	24.0 kHz	10.3 kHz	6.9 kHz	lower	

The depletion layer grows from the backside (p^+ layer) and reaches the n^+ implants at full depletion (typically 150 V and up to several 100 V for irradiated devices). However, after irradiation, type inversion occurs (due to displacements of atoms in the lattice) and hence the depletion layer grows from the n^+ side. The guard rings ensure a smooth decrease of the bias potential over the edge so that the high field region does not reach the n^+ side which is at ground potential with the readout chip. For n^+ implants in n-material the pixels have to be isolated from one another. This is usually done with one or several narrow p^+-rings around each pixel (the so-called p-stop rings). To avoid excessive charging of a floating pixel (one with poor indium connection to the chip), leading to local discharges and momentary failures of whole pixel clusters, the resistance between pixels should remain finite. A narrow resistive path between the pixels would prevent the pixels from charging up. This is accomplished by small openings in the p-rings which lead to atoll-like structures. Figure 10.5 shows our favorite design for the elementary sensor cell.

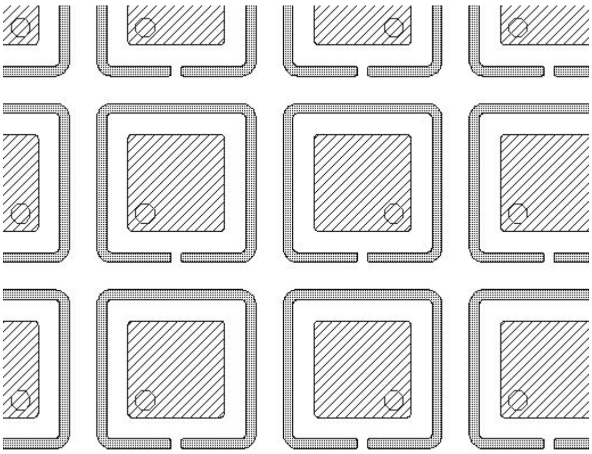

Figure 10.5: *Sensor design with one p-stop ring surrounding the pixels. The sizes of the* n^+*-implants and the spacings are typically 75* μm *and 10* μm*, respectively.*

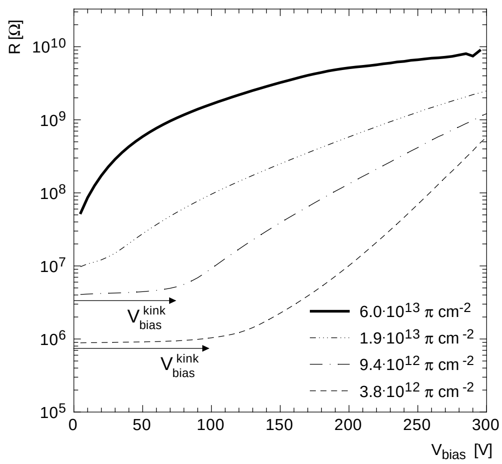

Figure 10.6: *Interpixel resistance as a function of bias voltage, for various particle fluxes. The kink in the bias voltage vanishes when type inversion occurs.*

During 2001 we performed many tests on the sensor designs that were submitted to SINTEF (Oslo) and CSEM (Neuchâtel) [5]. A sample of 16 layouts, including various p-stop ring geometries and guard rings, were produced on 24 wafers with different resistivities. We inspected the planarity of the delivered devices, performed leakage current and $C-V$ measurements with a probe station, and determined from the depletion voltage the doping concentration (donor concentration in the bulk, $2\times\,10^{12}$ cm^{-3}). In the implants the concentration was determined to be $n^+ = 10^{18}$ cm^{-3}. The interpixel resistance was found to be typically a few MΩ, depending on the p-stop ring design.

Some of the devices were then irradiated with protons at the ROSE facility at CERN, and with pions at PSI. We determined the radiation dose at which type inversion occurs: after type inversion there is no flat interpixel resistance regime as a function of bias voltage, as there is no undepleted zone between the implants (the depletion layer grows from the n^+ side). For CSEM (SINTEF) devices type inversion occurs at a dose of 2.1×10^{13} (3.6×10^{13}) hadrons cm^{-2} (the expected radiation dose is 6×10^{14} after 10 years of LHC operation). The resistance is shown in Fig.10.6 for several irradiation doses. One finds that the interpixel resistance rises dramatically with dose, reaching several GΩ at full irradiation. Nonetheless, a beam test with an irradiated bump-bonded sensor showed a satisfactory behaviour without stochastic discharges in spite of this very high resistance.

We also measured the pixel capacitance (25.8 ± 1.8 fF, in good agreement with calculations) between a pixel and its neighbours and the backplane, by connecting many pixels in parallel. This result is very important for readout noise considerations.

From these and other R &D investigations [5] we conclude that the pixel detector envisaged in the proposal [4] is feasible. In 2002 we will investigate oxygen enriched sensors, for which the radiation hardness is increased due to the reduced acceptor concentration in n-type silicon [6].

10.3 Tests of the readout chip

Figure 10.7 explains the operation of the pixel readout chip (developed at PSI). The pixels are grouped in double columns, with a common bus to a double column periphery which controls the chip. The chips are produced in the radiation hard DMILL SOI (silicon on insulator) technology. Each pixel has its pixel unit cell (PUC), which consists of an analog and a digital block. It is equipped with a comparator allowing individually adjustable thresholds. Whenever a PUC detects a signal above threshold it stores the analog signal in a capacitor and notifies the double column periphery, which copies a time stamp into memory and requests a readout. A readout token is then sent through the chip and all double columns with hits are read out.

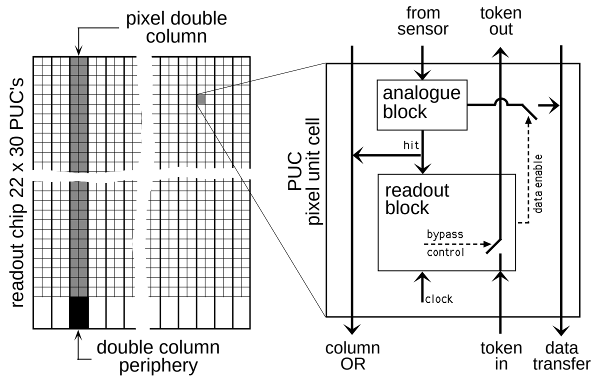

Figure 10.7: *Schematic of the PSI34 readout chip.*

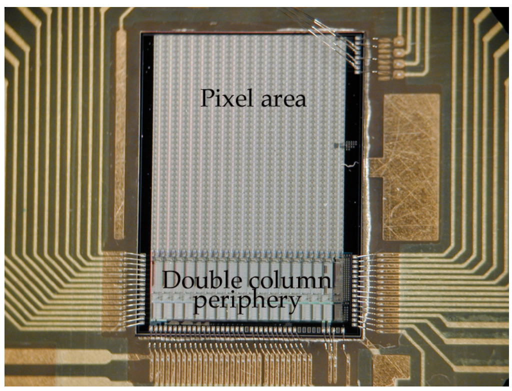

Figure 10.8: *Readout chip (version DM-PSI41) bonded to a test printed circuit board.*

Each pixel is hit at an average rate of 10 kHz, and the information (address and collected charge) has to be stored for 3.2 ms in the front end part of the pixel readout electronics (Fig.10.8), until it is read out or discarded by the external readout electronics. The front end part of the electronics consists of the following parts: readout chip (ROC), line drivers, $\mathrm{I}^2\mathrm{C}$

interface for controlling, token bit manager chip (TBM). Each readout chip reads out 2756 pixels (53 columns × 52 rows), and 16 readout chips are controlled by one token bit manager chip. The read out chip contains analog preamplifiers, shapers and discriminators, column periphery, readout buffers/amplifiers.

The analog preamplifier is made of two integrating amplifiers and one differentiating stage. Last year a preliminary version of the readout chip (DM-PSI41) was tested in our lab. Several parameters were optimised to get acceptable gain, peaking time and power dissipation. The minimum power consumption was determined as a function of gain and peaking time by varying the supply voltages to the amplifiers. It is typically 25 μW per channel.

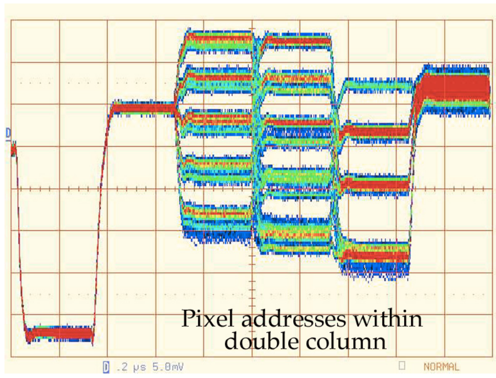

Figure 10.9: *Output signals from the readout chip for a single hit pixel (left) and for 80 superimposed signals from different pixels of the same double column (right). The six time bins encode the address and the charge collected by the pixel (see text).*

We also tested the digital part of the readout chip DM-PSI41 with a digital pattern generator DG2020 and a PCI digital I/O card. Because of the expected huge data rates at LHC (32 Gb/s), a 5-level logic is used instead of binary logic. For each hit pixel, the readout chip produces a signal (shown in Fig.10.9), which is divided into six bins. The first two bins encode the double column address and the next three encode the pixel address within the double column. With five levels a total of $5^5 = 3125$ pixel addresses can be encoded by one readout chip. The sixth bin represents the analog signal from the pixel.

10.4 Simulation and reconstruction software

The Zürich group has taken major responsibilities in the development of the reconstruction software. Charged particles usually leave between 8 and 15 hits in the tracker (pixel and silicon detectors), depending on rapidity. The challenge is to reliably find tracks in a reasonable amount of time in a high rate environment (see the typical event of Fig.10.1 above), where low luminosity events will feature around 5000 hits and high luminosity events ten times more. Combinatorial problems can thus be severe.

Figure 10.10 shows the new cms121 layout of the silicon tracker. We discovered that the transverse momentum resolution of high-p_t single muon tracks deteriorated significantly (Fig.10.11) when the microstrip gas chambers (cms118 layout) were replaced by the current all-silicon configuration. We could attribute this deterioration to the removal of one layer, reducing the average track length by 10 cm, to the gap between the outer barrel and the endcap detectors, and to a degradation of the resolution in the last rings of the disks.

A possible improvement is to reduce the average pitch of the sensors in the 7th (last) ring of the endcap disks from 156 to 104 μm. The effect on mass resolution was studied for the

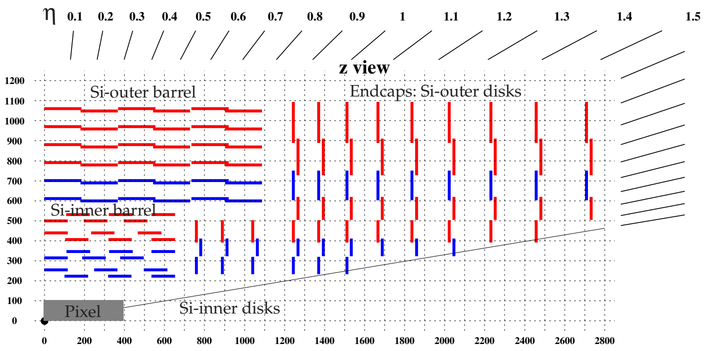

Figure 10.10: *The current cms121 all-silicon layout of the tracker; red, single-sided, blue double-sided readout. The parameter η denotes the pseudorapidity.*

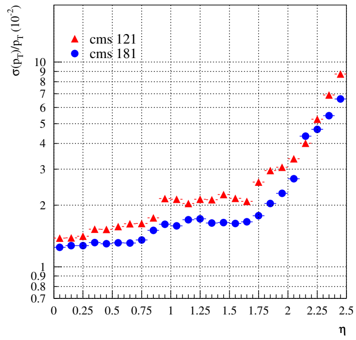

Figure 10.11: *p_t-Resolution for muons with p_t=100 GeV/c versus pseudorapidity η for the cms118 and cms121 configurations.*

decay $H \to Z^0Z^0 \to 2(\mu^+\mu^-)$. No improvement was observed since muons from Higgs decay are emitted with relatively low transverse momenta (below 50 GeV/c), where the resolution is dominated by multiple scattering. On the other hand, improvements on the mass resolution are expected for higher mass objects ($\sim$ 400 GeV) for which the decay momentum spectrum is harder. These states are, however, not expected to be narrow.

We also studied the effect of an increase of the pitch of the sensors of the first two Outer Barrel layers from 122 to 133 μm which would lower the number of readout chips by 2160 units. In this case b and τ jets were used in the simulation. The modification which affects only hits in the middle of the tracks turned out to have little effect on the momentum resolution. Since the track reconstruction efficiency remained essentially unchanged the pitch will be increased in these layers to reduce costs.

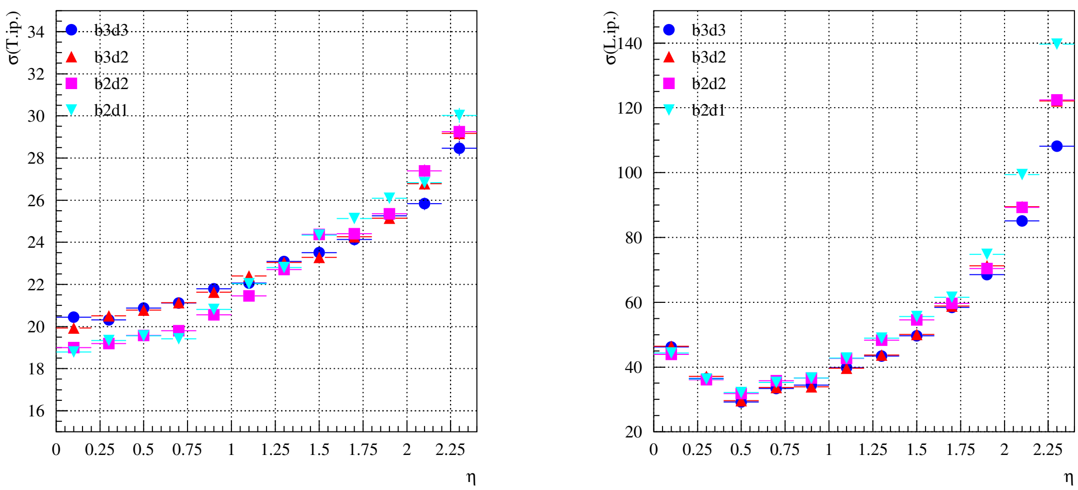

Figure 10.12: *Resolution of the transverse (left) and longitudinal (right) impact parameter (in μm) as a function of the pseudo-rapidity η for different configurations and 10 GeV/c muons.*

We studied several alternatives for the number of pixel layers which were discussed at a workshop in December 2001. The resolution on transverse momentum depends slightly on the radius of the innermost layer, as it is mostly determined by the total length of the track. The resolution on the azimuthal angle ϕ in the barrel improves slightly with the number of layers, but the resolution on the polar angle improves significantly, both in the barrel and in the endcaps. At high momentum the resolution on the transverse impact parameter (Fig. 10.12, left) improves with the number of barrel layers, but shows no significant dependence on the number of disks. However, at low momentum, the resolution is best with two barrel layers, due to the reduction of material thickness. The resolution on the longitudinal impact parameter (Fig. 10.12, right) shows little dependence on the number of barrel layers but improves dramatically with the number of endcap disks. No dramatic change was observed, the layout with the largest number of layers offering the best performance. The pixel system will therefore consist of three barrel layers and two pairs of endcap disks.

We also studied the detection efficiency as a function of LHC bunch length. At injection the length of the longitudinal beam overlap is about 11 cm (FWHM). From experience with $\bar{p}p$ collisions at the SPS collider this length will increase to 18 cm (FWHM) after 10 hours of coasting beams. To estimate the coverage in $\eta - \phi$ of each layer as a function of vertex position, muons with a transverse momentum of 100 GeV/c were generated with a uniform $\eta - \phi$ distribution and a vertex z-coordinate between between -30 and 30 cm. The coverage of the barrel pixel layers is fortunately not sensitive to the vertex position. The inefficiency is 2.9% in each layer (Fig.10.13, left), resulting mainly from the longitudinal gaps between the pixel modules, see Fig.10.13 (right). The coverage of the forward disks is, as expected, strongly dependent on the vertex position, and the total inefficiency is about 2%, mainly due to the radial gaps between the pixel modules.

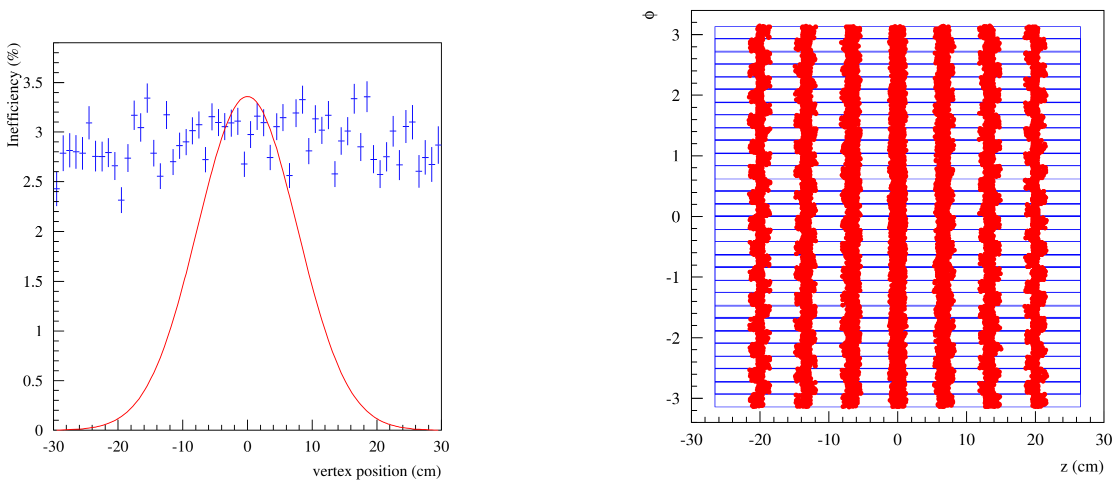

Figure 10.13: *Left: inefficiency as a function of vertex position for the second barrel pixel layer (crosses) and expected distribution of collision points after 10 hours of coasting beams (curve); right: $\phi - z$ view of the detector modules showing the missing hits in the second barrel pixel layer.*

In 2002 we will complete the optimisations of the tracker geometry and tackle the vertex reconstruction. Our aim is to study and implement robust secondary vertex fit procedures, which are not sensitive to tracks that have a small probability to emerge from the secondary vertex.

References

[1] V. Dubacher, *Test of a Silicon Pixel Detector with 50 GeV Pions*, Universität Zürich (1996); R. Kaufmann, *Performance of a Silicon Pixel Detector in a Magnetic Field*, Universität Zürich (1997); M. Glättli, *Untersuchung von Silizium-Pixeldetektoren mit einem Silizium-Mikrostreifen-Strahlteleskop*, Universität Zürich (1998).

[2] G. Bolla *et al.*, Nucl. Instr. Meth. in Phys. Research **A** 461 (2001) 182.

[3] B. Henrich, R. Kaufmann, Nucl. Instr. Meth. in Phys. Research **A** 304 (2002) 304.

[4] The Tracker Project, Technical Design Report, CERN LHCC 98-6, CMS TDR 5 (1998).

[5] R. Kaufmann, PhD thesis, Universität Zürich (2001).

[6] M. Moll, E. Fretwurst, G. Lindström, Nucl. Instr. Meth. in Phys, Res. **A** 439 (2000) 282.

11 Superconductivity and Magnetism

D. Di Castro (since February 2002), H. Keller, R. Khasanov,
S. Kohout (since September 2001), M. Mali, P. Morf (till Mai 2001),
R. Renggli (till Mai 2001), J. Roos, A. Schilling (till October 2001),
Ph. Schneider (till Mai 2001), A. Shengelaya, G.M. Zhao (till June 2001),
V.A. Ivanshin (visiting scientist), E. Kirov (visiting scientist),
B. Kochelaev (visiting scientist), T. Schneider (Titularprofessor),
and K.A. Müller (Honorarprofessor)

in collaboration with:
ETH Zürich (M. Angst, K. Conder, J. Karpinski), Paul Scherrer Institute (E. Morenzoni), IBM Rüschlikon Research Laboratory (J.G. Bednorz), University of Birmingham (E.M. Forgan), University of St. Andrews (S.L. Lee), University of Rome (A. Bianconi), Kazan State University (A. Dooglav, M.V. Eremin, B.I. Kochelaev), University of Belgrade (I.M. Savić), Institute of Low Temperature and Structure Research, Polish Academy of Sciences, Wroclaw (P.W. Klamut), Institute of Physics, Polish Academy of Sciences, Warsaw (A. Wisniewski), University of Tokyo (K. Kishio and T. Sasagawa), Northern Illinois University, DeKalb (B. Dabrowski), University of Maryland (R. L. Greene, T. Venkatesan, D. J. Kang, W. Prellier, M. Rajeswari), University of Berkeley (R.A. Fisher and N.E. Phillips), Los Alamos National Laboratory (M. Hundley, A. Lacerda), Argonne National Laboratory (U. Welp, W.K. Kwok, R.J. Olsson, G.W. Crabtree).

11.1 Introduction

In the last year we have continued our investigations on the fundamental physical properties of non-conventional (cuprates and MgB_2) and conventional superconductors, manganites and other related perovskite systems. One central research topic involves detailed oxygen isotope ($^{16}O/^{18}O$) effect (OIE) studies on various physical quantities (critical temperature, in-plane penetration depth, resistivity, thermoelectric power, specific heat) in manganites and cuprates in order to investigate the role of the electron-phonon interaction in the basic physics of these systems. In another project, we have continued our studies of vortex matter in strongly layered superconductors (static vortex structure and vortex motion), that we have started several years ago. A great advantage of our approach is the combined application of complementary experimental techniques, such as muon-spin rotation (μSR), nuclear magnetic resonance (NMR), nuclear quadrupole resonance (NQR), electron paramagnetic resonance (EPR), together with bulk SQUID and torque magnetometry, resistivity, and thermal measurements. The scientific goal of our research is to gain new insight on the fundamental physical processes involved in cuprate superconductors and related systems.

11.2 Studies of oxygen isotope effects

11.2.1 Oxygen isotope effect in manganites

Although a consensus is reached that strong electron-phonon coupling plays an essential role in the basic physics of the colossal magnetoresistive manganites, the very nature of charge carriers in the ferromagnetic states at low temperatures has not been understood. One theory [1] shows that the nature of charge carriers is polaronic even in the low-temperature metallic state, while others [2, 3] believe that polaronic effects are not important.

In order to provide clear evidence for the 'metallic' polaronic liquid in the low temperature ferromagnetic state, it is essential to study the isotope effects on the low-temperature kinetic and thermodynamic properties. These properties are dominated by the impurity and electron-electron scatterings, so the only source of the isotope effect might be the polaron mass dependence on the lattice ion mass. For example, replacing ^{16}O with ^{18}O will increase the polaron mass, leading to the changes in the residual resistivity, and in other kinetic and thermodynamic properties.

We thus studied the isotope effects on the residual resistivity ρ_o, the thermoelectric power S and the electronic specific heat C_{el} both experimentally and theoretically [4]. In the low-temperature ferromagnetic state, the intrinsic resistivity of the manganite thin films shows a strong dependence on the oxygen isotope mass. The residual resistivity of the films increases by 15(3)% upon replacing ^{16}O with ^{18}O. In contrast, the thermoelectric power is nearly independent of the oxygen isotope mass. The observed large isotope effect on the resistivity and negligible effect on the thermoelectric power are in quantitative agreement with our theory based on a novel polaronic Fermi liquid [4]. Furthermore, we have also found that C_{el} does not have a significant isotope dependence [5], in agreement with theory [4]. Therefore, our theoretical and experimental studies of the isotope effects on the kinetic and thermodynamic properties provide strong evidence for the polaronic Fermi-liquid in the low-temperature ferromagnetic state of doped manganites.

11.2.2 Oxygen isotope effects in cuprates

a) Oxygen isotope effect on the magnetic penetration depth in underdoped $Y_{1-x}Pr_xBa_2Cu_3O_{7-\delta}$

There is increasing evidence that a strong electron-phonon coupling is present in cuprate superconductors, which may lead to the formation of polarons (bare charge carriers accompanied by local lattice distortions) [6, 7]. One way to test this hypothesis is to demonstrate that the effective mass of the supercarriers m^* depends on the mass M of the lattice atoms. This is in contrast to conventional BCS superconductors, where m^* is independent of M. For cuprate superconductors (clean limit) the in-plane penetration depth λ_{ab} is given by $\lambda_{ab}^{-2}(0) \propto n_s/m^*_{ab}$, where n_s is the superconducting charge carrier density, and m^*_{ab} is the in-plane effective mass of the superconducting charge carriers. This implies that the OIE on $\lambda_{ab}^{-2}(0)$ is due to a shift in n_s and/or m^*_{ab}, according to the relation:

$$\Delta\lambda_{ab}^{-2}(0)/\lambda_{ab}^{-2}(0) = \Delta n_s/n_s - \Delta m^*_{ab}/m^*_{ab}. \tag{11.1}$$

Therefore a possible mass dependence of m^*_{ab} can be tested by investigating the isotope effect on λ_{ab}, provided that the contribution of n_s to the total isotope shift is known.

The muon-spin rotation (μSR) technique is a powerful method to determine directly the magnetic penetration depth in type-II superconductors. In a powder sample the magnetic penetration depth λ can be extracted from the superconducting part of the muon-spin depolarisation rate $\sigma_{sc}(T) \propto 1/\lambda^2(T)$, which probes the second moment $\langle \Delta B^2\rangle^{1/2}$ of the local magnetic field distribution $p(B)$ in the mixed state [8]. For the highly anisotropic layered cuprate superconductors the simple relation $\sigma_{sc}(T) \propto 1/\lambda^2_{ab}(T) \propto n_s/m^*_{ab}$ holds [8].

We performed a detailed investigation of the OIE on the in-plane penetration depth $\lambda_{ab}(0)$ in underdoped $Y_{1-x}Pr_xBa_2Cu_3O_{7-\delta}$ ($x = 0.3$ and 0.4) by means of μSR [9]. For both concentrations x a pronounced OIE on T_c as well on $\lambda_{ab}^{-2}(0)$ was observed. The corresponding results for $x = 0.4$ are displayed in Fig. 11.1. The relative isotope shifts on $\lambda_{ab}^{-2}(0)$ were found to be $\Delta\lambda_{ab}^{-2}(0)/\lambda_{ab}^{-2}(0) = -5(2)\%$ for $x = 0.3$ and $-9(2)\%$ for $x = 0.4$. These results are in excellent agreement with recent results of our group obtained for underdoped $La_{2-x}Sr_xCuO_4$ by means of torque magnetometry [10]. According to Eq (11.1) the observed $\Delta\lambda_{ab}^{-2}(0)/\lambda_{ab}^{-2}(0)$ is due to a shift of n_s and/or m^*_{ab}. For $La_{2-x}Sr_xCuO_4$ several independent experiments

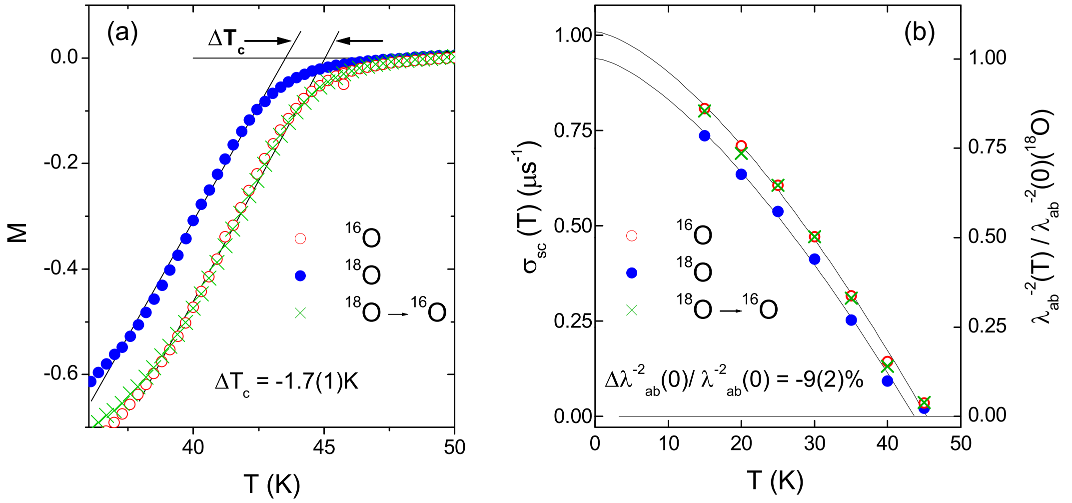

Figure 11.1: *(a) Low-field (1 mT, field-cooled) magnetisation curves (normalised at 10K) near* T_c *for* $Y_{0.6}Pr_{0.4}Ba_2Cu_3O_{7-\delta}$*. (b) Temperature dependence of the depolarization rate* σ_{sc} *of* $Y_{0.6}Pr_{0.4}Ba_2Cu_3O_{7-\delta}$ *measured in a field of 200 mT after field-cooling the sample from the normal state. The solid lines correspond to fits to the power law:* $\sigma_{sc}(T)/\sigma_{sc}(0) = 1-(T/T_c)^n$.

[10, 11, 12] have shown that the change of n_s during the exchange procedure must be *negligibly small*. The same arguments also apply for the $Y_{1-x}Pr_xBa_2Cu_3O_{7-\delta}$ system [9]. This implies that the observed change in $\lambda_{ab}^{-2}(0)$ is mainly due to the OIE on the in-plane effective mass m^*_{ab} with $\Delta m^*_{ab}/m^*_{ab} \simeq 5(2)$ % and 9(2) % for $x = 0.3$ and $x = 0.4$, respectively.

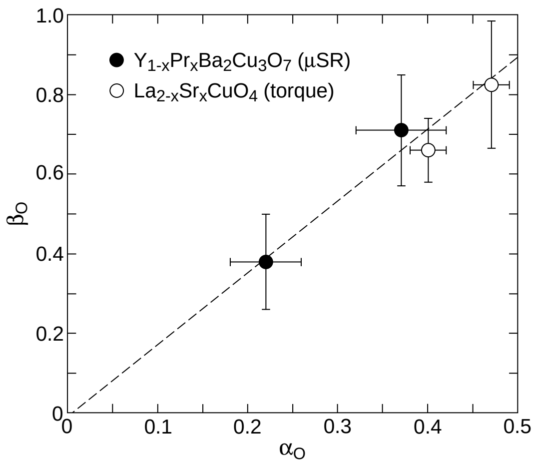

Figure 11.2: *Plot of the OIE exponent* β_O *versus the OIE exponent* α_O *for* $Y_{1-x}Pr_xBa_2Cu_3O_{7-\delta}$ *(x = 0.3 and 0.4) and* $La_{2-x}Sr_xCuO_4$ *(x = 0.080 and 0.086) from [10]. The dashed line represents a best fit to the empirical relation* $\beta_O = A\cdot\alpha_O+B$ *with* $A = 1.8(4)$ *and* $B = -0.01(12)$.

In Fig. 11.2 the OIE exponent β_O of $\lambda_{ab}^{-2}(0)$ is plotted versus the OIE exponent α_O of T_c for $Y_{1-x}Pr_xBa_2Cu_3O_{7-\delta}$, where $\beta_O = -d\ln\lambda_{ab}^{-2}(0)/d\ln M_O$ and $\alpha_O = -d\ln T_c/d\ln M_O$. For comparison the recent magnetic torque results of underdoped $La_{2-x}Sr_xCuO_4$ [10] are also included. Evidently β_O and α_O are proportional to each other with $\beta_O/\alpha_O \simeq 1.8(4)$. This empirical relation appears to be generic for various families of cuprate superconductors.

In conclusion, our OIE studies imply that the effective supercarrier mass m^*_{ab} in underdoped $Y_{1-x}Pr_xBa_2Cu_3O_{7-\delta}$ depends on the oxygen mass of the lattice atoms, which is not expected for a conventional phonon-mediated BCS superconductor. To our knowledge there are only two theoretical models of high-temperature superconductivity, which predict an OIE on the effective carrier mass, namely, a bipolaronic model of Alexandrov and Mott [6] and a nonadiabatic superconductivity model proposed by Grimaldi, Cappelluti and Pietronero [13].

b) Low-energy μSR investigation of the oxygen isotope effect on the magnetic penetration depth of $YBa_2Cu_3O_{7-\delta}$

At present the novel low-energy (LE) μSR technique recently developed at PSI [14] is the most direct method to determine the magnetic penetration depth λ in a superconductor. It allows to measure directly the magnetic field profile beneath the surface of a superconductor in the Meissner state, with a depth resolution of a few nanometers [15]. It is well known, that for superconductors in the clean limit, a magnetic field B_0 applied parallel to the surface of a semi-infinite slab decays with depth z according to the exponential law: $B(z) = B_0 \exp(-z/\lambda_{ab})$.

We performed LE μSR studies of the OIE on the in-plane magnetic penetration depth λ_{ab} in a c-axis oriented $YBa_2Cu_3O_{7-\delta}$ film in the Meissner state. During the experiments the magnetic field $B_0 = 9.5$ mT was applied parallel to the surface of the 600 nm thick $YBa_2Cu_3O_{7-\delta}$ film after zero-field cooling the film to 5 K from the normal state. In this geometry, currents flowing in the ab-planes determine the magnetic field profile along the c-axis inside the film. LE muons were implanted at depths ranging from 40 to 150 nm by varying the energy of the incident muons from 5 to 30 keV. Fig. 11.3 shows the measured magnetic field profile in the Meissner state of the $YBa_2Cu_3O_{7-\delta}$ thin film for ^{16}O and ^{18}O samples. It is evident that the magnetic field inside the film decays stronger for the ^{16}O sample than for the ^{18}O one, implying that λ_{ab} is smaller for ^{16}O than for ^{18}O. The relative oxygen-isotope shifts extracted from these preliminary data were found to be $\Delta\lambda_{ab}/\lambda_{ab} = 0.025(10)$ and $0.029(15)$ at $T = 4$ K and 30 K, respectively. This result clearly indicates that lattice effects play an essential role also in optimally doped cuprate superconductors, in contrast to the general belief. These effects have to be considered in any successful theory of high-temperature superconductivity.

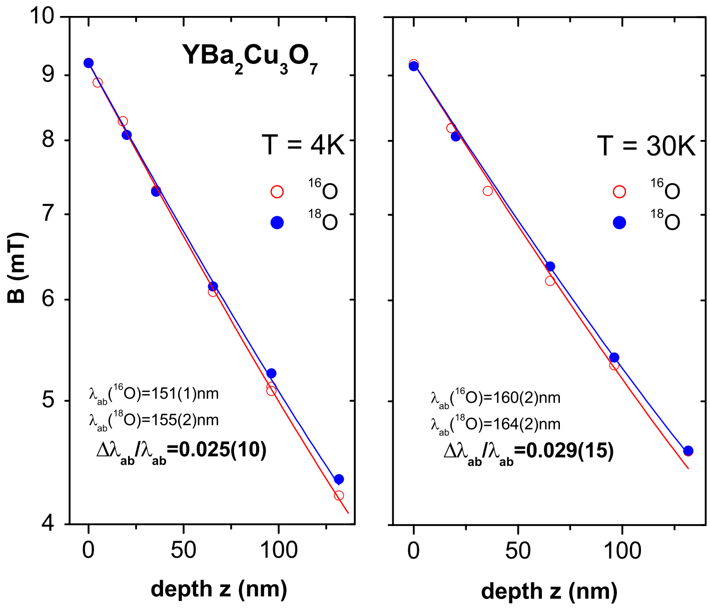

Figure 11.3: *Magnetic field profile $B(z)$ in a 600 nm thick c-axis oriented $YBa_2Cu_3O_{7-\delta}$ film in the Meissner state near the surface for ^{16}O and ^{18}O at two different temperatures. Solid curves represent fits to the theoretical expression given in the text.*

c) Antiferromagnetic transition

It is well known that the parent compounds of the cuprate superconductors exhibit long-range 3D antiferromagnetic (AF) order, which is rapidly destroyed as holes are doped into the CuO_2 planes. However, short-range 2D AF correlations survive well into the superconducting region of the phase diagram. There is also increasing evidence that a strong electron-phonon coupling is present in cuprates [16] which may lead to the formation of polarons (bare charge carriers accompanied by local lattice distortions) [6]. On the other hand, little is known about the influence of the electron-phonon interaction on magnetism in cuprates. Conventional theories of magnetism neglect atomic vibrations; the atoms are generally considered as infinitely heavy and static in theoretical descriptions of magnetic phenomena, so there should be no isotope effect on magnetism. However, if charge carriers are polaronic, i.e., nuclear and electronic motions are no longer decoupled (breakdown of the Born-Oppenheimer approximation), one might expect isotope effects on magnetic properties. The question is whether such an isotope effect exists in the cuprates.

To answer this question we previously studied the OIE on low-temperature magnetism in $La_{2-x}Sr_xCuO_4$ ($x = 0.03$, 0.05) using the zero-field μSR technique [17]. In these samples a so-called cluster spin glass magnetic state is present below the spin glass freezing temperature T_g. We observed that T_g is isotope dependent: $T_g = 8.60(2)$ K and 8.80(2) K for the ^{16}O and ^{18}O sample, respectively. This results in a OIE exponent for the spin glass freezing temperature $\alpha_{T_g} = -d\ln T_g/d\ln M = -\,0.19(1)$. It is important to show that this novel isotope effect is generic and also exists in other cuprate families.

This time we have studied the OIE on magnetism in $Y_{0.2}Pr_{0.8}Ba_2Cu_3O_{7-\delta}$. It is known that Pr doping in $YBa_2Cu_3O_{7-\delta}$ suppresses superconductivity, and long-range antiferromagnetic order is induced [18]. The μSR experiments were performed at the Paul Scherrer Institute in Villigen, Switzerland, using essentially 100% spin-polarized positive "surface muons". The pair of samples with different oxygen isotopes ^{16}O and ^{18}O were measured under the same experimental conditions.

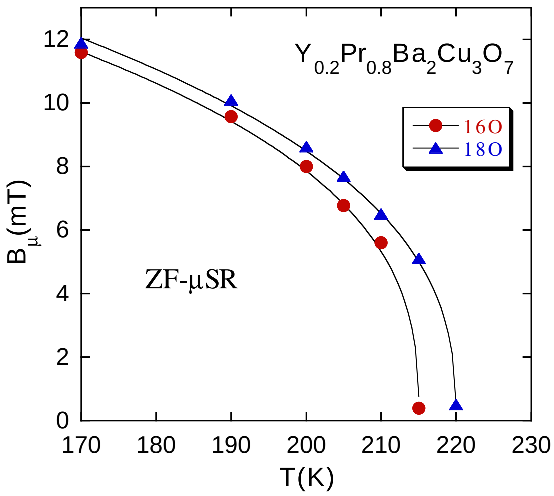

Figure 11.4: *Temperature dependence of the internal magnetic field B_μ at the muon site for the ^{16}O and ^{18}O samples of $Y_{0.2}Pr_{0.8}Ba_2Cu_3O_{7-\delta}$. Solid lines represent fitted curves to the power law $B_\mu(T) = B_\mu(0)(1 - T/T_N)^n$.*

At low temperatures in all studied samples we observed damped oscillations due to muon-spin precession in local magnetic fields. A clear oscillation observed in ZF-μSR spectra implies that the muons sense a well defined internal magnetic field, in agreement with previous μSR measurements [18]. Fig. 11.4 shows the internal magnetic field B_μ for the two oxygen isotope (^{16}O and ^{18}O) samples as a function of temperature. One can see that the antiferromagnetic transition temperature T_N is isotope dependent. T_N of the ^{18}O sample is 5 K higher than that of the ^{16}O sample, yielding an oxygen isotope exponent $\alpha_{T_N} = -d\ln T_N/d\ln M = -\,0.19(1)$. It is remarkable that the values of the isotope exponents α_{T_g} in $La_{2-x}Sr_xCuO_4$ and α_{T_N} in $Y_{0.2}Pr_{0.8}Ba_2Cu_3O_{7-\delta}$ are the same. Moreover, our results imply that the isotope effect on magnetism is a generic phenomenon in cuprate systems. This novel isotope effect clearly demonstrates that the lattice vibrations strongly affect magnetism in cuprates which may be explained by taking into account the polaronic nature of the charge carriers.

11.3 Studies of MgB_2

The recent discovery of superconductivity in MgB_2 by Nagamatsu *et al.* [19] has lead in our group to a number of investigations with the aim to understand the intrinsic properties of this structurally layered and thus highly anisotropic compound. Its transition temperature of 39 K is on the limit expected theoretically for BCS, phonon mediated superconductivity, and its superconducting properties are rather unusual.

11.3.1 NMR investigations

So far, NMR studies of MgB_2 were performed by using the ^{11}B nuclei as microscopic probes and there are no experimental data concerning the NMR quantities at the Mg site in MgB_2, although theoretical predictions based on *ab initio* local density approximation (LDA) calculations exist for Mg Knight shift, spin-lattice relaxation, $1/T_1$, and electric field gradient (EFG) [20, 21].

The only NMR active ^{25}Mg isotope has a small magnetic moment and low natural abundance and consequently the ^{25}Mg NMR signals are weak even in high magnetic fields. Despite this handicap we were able to investigate NMR of the naturally abundant ^{25}Mg in powder samples of MgB_2. We measured the temperature dependence of Knight shift, spin-lattice relaxation time, and quadrupole coupling frequency of ^{25}Mg in MgB_2 [22]. Figure 11.5 shows a ^{25}Mg powder NMR spectrum at room temperature and the temperature independent Knight shift, K_c, in normal conducting MgB_2 powder grains with the c axis parallel to the applied magnetic field. From our results for the linearly temperature dependent spin-lattice relax-

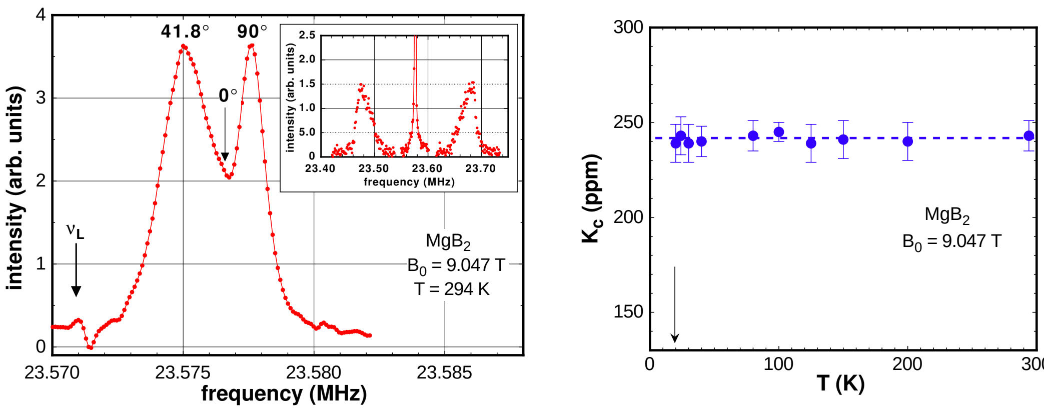

Figure 11.5: *Left:* ^{25}Mg *central line of* MgB_2 *powder spectrum measured at* $T = 294$ *K in a magnetic field* $B_0 = 9.047$ *T. Insert:* ^{25}Mg *first satellites' singularities of* MgB_2 *powder spectrum measured at* $T = 294$ *K in a magnetic field* $B_0 = 9.047$ *T. Right: Temperature dependence of the* ^{25}Mg *Knight shift,* K_c*, in normal conducting* MgB_2 *powder grains with c* $\parallel B_0$*. The shift is with respect to the* ^{25}Mg *resonance in a water solution of* $MgCl_2$ *at room temperature. The dashed line represents the weighted average of* K_c*. The arrow marks the transition temperature of* MgB_2 *powder grains with* $c \perp B_0 = 9.047$ *T.*

ation time, T_1, the Korringa ratio can be formed. We get experimentally $(K^2T_1T)/S \approx 0.95$, where $S = (\gamma_e/\gamma_n)^2(h/8\pi^2k_B) = 7.0323 \times 10^{-5}$ sK for ^{25}Mg, with γ_e and γ_n the gyromagnetic ratios for electron and nucleus, respectively. This value is very close to the ideal value of unity for s-electrons. This result is a confirmation that the Fermi-contact interaction is the dominant mechanism responsible for relaxation and Knight shift at the Mg site.

Comparing our experimental results with the theoretical predictions [20, 21], we find for all three Mg NMR quantities an excellent agreement. Since all calculations were done by state of the art LDA methods the good agreement between calculated and measured NMR quantities confirms the LDA as a good approximation for MgB_2.

11.3.2 Micro-torque measurements

In a collaboration with M. Angst and J. Karpinski (Laboratorium für Festkörperphysik, ETH Zürich) high quality single crystals of MgB_2 ($T_c \approx 38 - 39$ K, $\Delta T_c \leq 0.5$ K) were used in an investigation of the upper critical field of this novel superconductor with torque magnetometry [23]. As shown in Fig. 11.6 $H_{c2}^{\|c}$ is very low (2.5 T at the temperature of

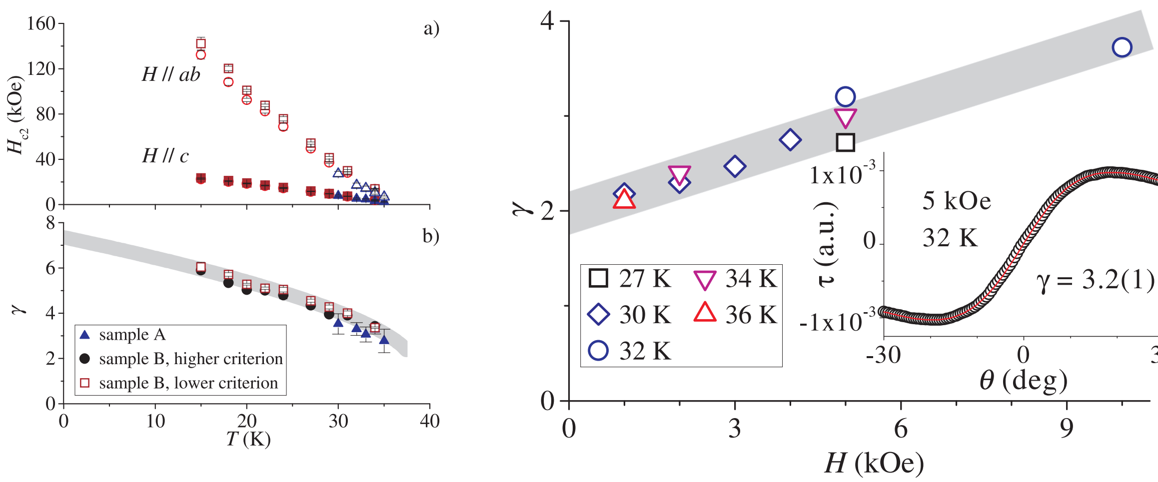

Figure 11.6: *Left side: Upper critical field H_{c2} (a) and H_{c2} anisotropy γ (b) vs temperature. Right side: Anisotropy γ as a function of field, inset shows the fitting of torque vs angle data.*

15 K) and saturates with decreasing temperature, while $H_{c2}^{\|ab}$ increases at low temperatures up to about 14 T at 15 K. The upper critical field anisotropy γ was found to be temperature dependent (decreasing from $\gamma \simeq 6$ at 15 K to 2.8 at 35 K). The anisotropy deduced from reversible torque data near T_c is also field dependent (increasing roughly linearly from $\gamma \simeq 2$ in zero field to 3.7 in 10 kOe). Such results imply a breakdown of standard anisotropic Ginzburg-Landau theory with a temperature and field independent effective mass anisotropy. A quantitative explanation of the measured $\gamma(T)$ has to take into account both the wave-vector dependence of the band effective mass tensor and the anisotropic electron-phonon coupling. The latter can lead to an anisotropic energy gap (or two gaps), which can result in a temperature dependent anisotropy of the upper critical field.

11.4 Vortex-matter studies

11.4.1 Possible phase transitions in the mixed state of 2H-$NbSe_2$ and $LuNi_2B_2C$

Various experiments on the type-II superconductor *2H*-$NbSe_2$ have suggested that a phase transition from an ordered to a disordered vortex phase below the upper critical field H_{c2} may take place [24]. However, no calorimetric evidence for such a phase transition has been reported so far. Corresponding features in heat capacity are indeed expected to be extremely small when compared to the total heat capacity of the material. We have therefore done a series of 140 high-resolution heat-capacity measurements on a 19 mg *2H*-$NbSe_2$ single crystal with a critical temperature $T_c = 7.2$ K, that was also characterised by detailed magnetisation measurements (in collaboration with G. Ravikumar, Forschungszentrum Karlsruhe). In all these experiments, we have not found any features in the heat capacity that would support the scenario of a vortex-related thermodynamic phase transition. However, since the transition is expected to occur in the magnetically irreversible region of the H-T diagram, we may expect metastable vortex states, and thermodynamic equilibrium may be difficult to achieve [24].

A rich magnetic phase diagram has been discovered by neutron-scattering experiments in the borocarbide compound $LuNi_2B_2C$, where a transition from a cubic to a hexagonal vortex phase takes place [25]. This transition is most likely of second order [26]. We have studied a $LuNi_2B_2C$ single crystal with $T_c = 16.6$ K (in collaboration with P. Canfield and V. Kogan, Iowa State University) that was taken from the same batch as the samples that have been used for the neutron-scattering experiments. Again, no significant discontinuities suggesting a thermodynamic phase transition within the vortex state could be detected. As in the case of *2H*-$NbSe_2$, the corresponding solid vortex phases are subject to pinning and irreversibility, which may make a measurement in thermodynamic equilibrium impossible.

We have therefore adapted a technique, that has been developed earlier at the University of Zürich, to accelerate thermodynamic equilibrium in the vortex state by applying an external transverse ac field [27, 28]. The corresponding heat-capacity cell has been constructed and tested, but has not yet been used to continue the investigations on *2H*-$NbSe_2$ and $LuNi_2B_2C$.

11.4.2 ^{63}Cu NMR linewidth in $YBa_2Cu_3O_7$

We have studied in detail thermodynamic quantities (magnetisation and heat capacity) in connection with the first-order melting of the vortex lattice in $YBa_2Cu_3O_7$ [29, 30, 31, 32]. However, these investigations did not allow us to draw any conclusions about microscopic properties of the vortex arrangement. It is known from neutron-scattering experiments [33] that above the first-order transition (i.e., in the vortex fluid state), no static spatial order exists on a time scale of the order of seconds. Moreover, muon-spin rotation experiments on $Bi_2Sr_2CaCu_2O_8$ have shown that no hexagonal order is present in the respective fluid phase on a time scale of microseconds [34].

NMR experiments would be, in principle, of great advantage to study the local magnetic-field distribution in the mixed state of type-II superconductors because the method is relatively simple and inexpensive compared to other techniques. Early measurements of the ^{89}Y NMR linewidth on $YBa_2Cu_4O_8$ powders, however, have not revealed any distinct signatures that could be clearly related to a phase transition between vortex phases [35]. We have therefore performed a linewidth measurement of the plane ^{63}Cu NMR central line on a $YBa_2Cu_3O_7$ single crystal that has been previously characterised by magnetisation and specific-heat measurements [29]. The NMR linewidth experiment is sensitive to spatial magnetic-field distributions that vary on a time scale of μs and longer, and thus can serve as a tool to distinguish between static and dynamic vortex phases.

The NMR measurements have been done on an untwinned $YBa_2Cu_3O_7$ single crystal in an external magnetic field $\mu_0 H = 9$ T parallel to the c-axis. The linewidth $\Delta\nu_{1/2}$ decreases monotonically with increasing temperature T in the vortex solid phase, but dramatically drops by 15% within 3 K at $T_m \approx 77$ K (see Fig. 11.7), the melting temperature of the vortex lattice as determined by calorimetric measurements. This motional narrowing-effect is a clear indication for a transition from a static, ordered vortex phase to a fluid-like phase with no static order on the time scale of the measurement. It is interesting to note that there is a further small but discontinuous decrease in $\Delta\nu_{1/2}$ by 2% within the fluid phase (i.e., around $T = 81$ K), that has no counterpart in our specific-heat data. Above 83 K, and particularly at $T_c(\mu_0 H = 9$ T$) \approx 86$ K, no further anomalies in $\Delta\nu_{1/2}$ could be detected.

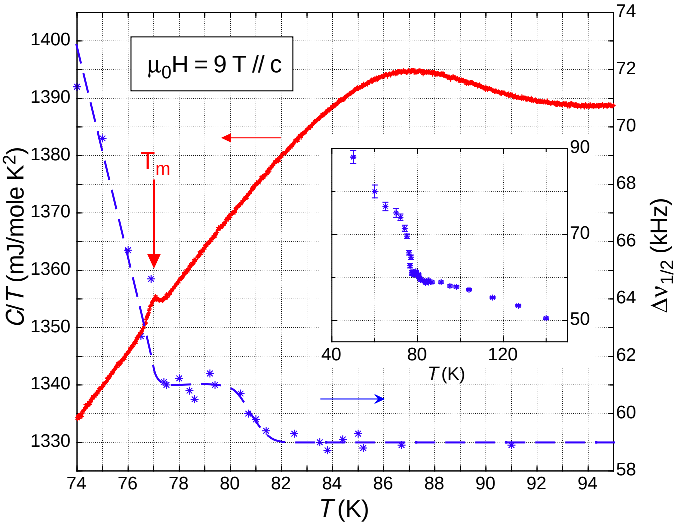

Figure 11.7: ^{63}*Cu NMR half line-width* $\Delta\nu_{1/2}$ *and reduced specific heat* C/T *of* $YBa_2Cu_3O_7$ *in* $\mu_0 H =$ *9 T parallel to the c-axis.* $\Delta\nu_{1/2}$ *drops by 15% at the vortex-lattice melting temperature* $T_m \approx$ *77 K, where* C/T *shows a sharp first-order like peak.*

The NMR investigations suggest that the local magnetic-field distribution changes discontinuously even within the fluid vortex phase of $YBa_2Cu_3O_7$, indicating the presence of several possible fluid vortex phases. Although we could not confirm a corresponding phase transition between such phases by specific-heat measurements in $\mu_0 H = 9$ T, there is calorimetric evidence that beyond the upper critical point (i.e., above $\mu_0 H = 12$ T where the liquefaction of the vortex lattice is continuous), several fluid vortex phases may exist [36] (collaboration with UC Berkeley, U.S.A., and Argonne National Laboratory, U.S.A.). The corresponding phase boundary is deep in the magnetically reversible region and well above the temperatures, where the solid-to-fluid transition is expected to take place. Both the magnitude and the sign of the observed discontinuities in specific heat ($\Delta C/T \approx +1$ mJ/MolK^2) raise puzzling questions concerning the symmetry of the corresponding phases [36] and the number of thermodynamic degrees of freedom involved in the phase transition [37].

11.4.3 Vortex motion in type-II superconductors probed by μSR

It is well known that when a transport current is flowing in a type-II superconductor in the mixed state, the vortex lattice may be depinned from the pinning centers and may move freely due to the Lorentz force [38]. The μSR technique is an ideal tool to investigate vortex motion on a microscopic scale by investigating the local magnetic flux distribution $p(B)$ in the presence of a transport current. The first μSR experiment on vortex motion in a high-temperature superconductor was performed by our group several years ago on a ceramic sample of $YBa_2Cu_3O_{7-\delta}$ [39].

Recently, we were able to observe vortex motion in a conventional type II superconductor by means of μSR. The experiments were carried out at ISIS (Rutherford Appleton Laboratory, U.K.) which provides a pulsed muon beam with longitudinal polarisation. The sample was a polycrystalline $Pb_{0.8}In_{0.2}$ alloy with dimensions of 20 x 30 x 1 mm^3. It was mounted at 45^o relative to the muon beam direction, and the magnetic field (0.03mT) was applied perpendicular to the incoming muon momentum. Transport currents (up to 80A) were applied along the largest dimension of the sample and at right angles to the magnetic field and the muon beam direction, giving rise to vortex motion (see Fig. 11.8).

Figure 11.9 shows a series of local magnetic field distributions $p(B)$ (determined from

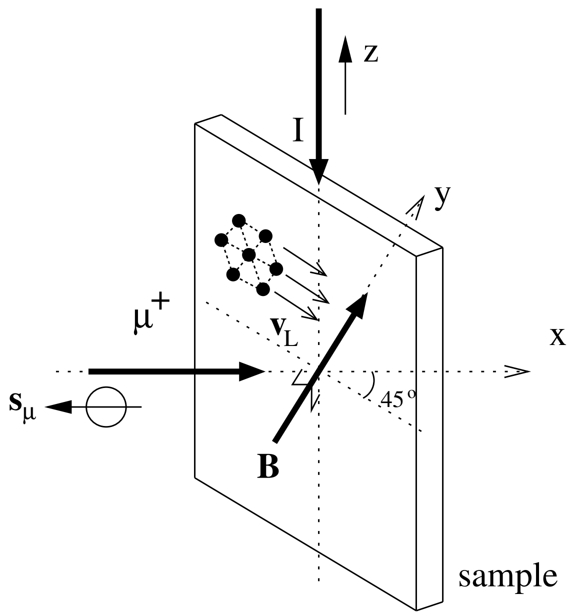

Figure 11.8: *Schematic diagram of the experimental setup used for the μSR experiments to detect vortex motion.*

the μSR time spectra using a maximum entropy algorithm) for various transport currents, ranging from 0 to 80A. It can be seen that as the vortices move faster, $p(B)$ becomes narrower due to motional narrowing, i.e. muons experience an effective magnetic field closer to the average field. At the highest current (high vortex velocity) the magnetic field inhomogeneity in the mixed state is almost completely averaged out, and $p(B)$ tends to have the form of a delta function [40]. More detailed experiments are in progress.

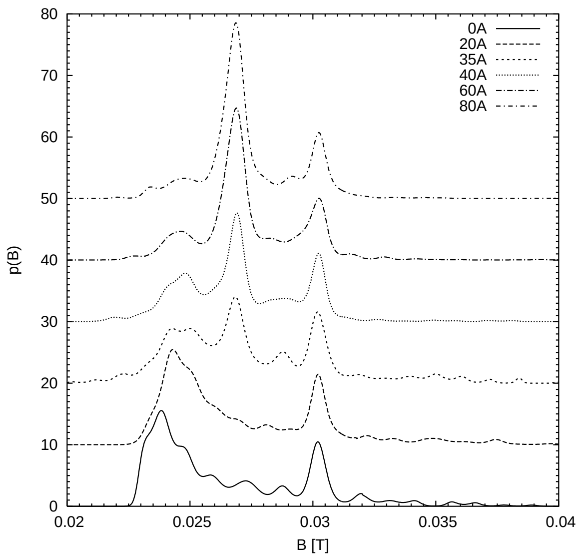

Figure 11.9: *Vortex motion in a polycrystalline $Pb_{0.8}In_{0.2}$ alloy. The μSR lineshapes $p(B)$ were obtained in a magnetic field of 0.03 mT at 4.2 K for various applied currents, ranging from 0 to 80 A. The peak at approximately 0.03 mT arises from muons stopping in the sample holder and cryostat windows.*

11.5 Charge effects investigated by magnetic resonance techniques

11.5.1 EPR studies of $SrTiO_3$

Materials showing reversible resistive switching are attractive for today's semiconductor technology with its wide interest in nonvolatile random-access memories (RAM). Recently researchers at IBM Rüschlikon found very interesting phenomena of resistive switching with a memory effect in transition metal doped thin films of $SrTiO_3$ [41]. They observed that positive or negative voltage pulses can induce resistivity changes of thin films up to six orders of magnitude. The switching time is shorter than 100 ns. Once a low resistivity state has been achieved it persists without external power for months, demonstrating the feasibility of nonvolatile memory elements. Recently this effect was observed also in single crystals of Cr-doped $SrTiO_3$ [42]. This indicates that the effect has a bulk character and is not restricted to the surface. Up to now the physical mechanism responsible for the resistive switching is not known. However, it is clear that the Cr ion and its different valence states play a crucial role. Electron Paramagnetic Resonance (EPR) has been intensively used to study the electronic character of transition metal ions in $SrTiO_3$ [43]. Therefore, we decided to study Cr-doped $SrTiO_3$ using EPR. In a first step two different $SrTiO_3$:Cr single crystals were measured: one with reduced oxygen content and another one as received. The Cr content was 0.2 at. %. It was found that in the crystals as received the majority of Cr ions are in the 5+ valence state. However, a significant amount of Cr^{3+} is also seen in the EPR spectra. On the other hand, in reduced crystals only Cr^{3+} centers were observed with no evidence of the presence of Cr^{5+} ions. These preliminary results show that using EPR it is possible to microscopically characterise different charge states of Cr in $SrTiO_3$. The next step would be to perform EPR experiments on the samples which show the resistive switching effect. To do this a special sample holder will be developed which allows to apply an electric field on the $SrTiO_3$ crystals directly in the resonance cavity. This will enable to study this interesting effect *in situ* and possibly clarify its microscopic mechanism.

11.5.2 Lutetium NQR in $(Y_{1-x}Lu_x)Ba_2Cu_4O_8$

In previous NMR/NQR investigations of $YBa_2Cu_4O_8$ we found that spin-lattice relaxation of Cu and O is not only driven by magnetic fluctuations, but also significantly by charge fluctuations. Due to the site symmetry the effect of antiferromagnetic spin fluctuations cancels at the Y site. In this sense the Y site represents an ideal location where only the effect of possible charge fluctuations could be detected. Unfortunately the Y nucleus (nuclear spin $I = 1/2$) has no electric quadrupole moment necessary for the detection of charge fluctuations.

One way to overcome this handicap is to replace Y by another trivalent ion of a rare earth element with a nuclear electric quadrupole moment (nuclear spin $I \geq 1$). The coupling of the rare earth nuclear quadrupole moment to the electric field gradient at the nuclear site can then be directly observed in a NQR experiment. In order to avoid disturbing magnetic hyperfine interaction with an on-site electron spin the rare earth element should have a closed outermost shell. Moreover, a large nuclear quadruple moment is of advantage to obtain a strong nuclear quadrupole interaction. The Lutetium isotope ^{175}Lu (nuclear spin 7/2) is the best candidate. Like Y its oxidation state is +3 and it has a large nuclear quadrupole moment $Q = 5.68 \cdot 10^{-24}\mathrm{cm}^2$ and a high natural abundance of 97.4 %.

In collaboration with S. M. Kazakov and J. Karpinski (Laboratorium für Festkörperphysik, ETH Zürich), who synthesised $(Y_{1-x}Lu_x)Ba_2Cu_4O_8$ samples with various compositions x, an extensive search for ^{175}Lu NQR was performed in the framework of a diploma thesis [44]. In case of a nuclear spin 7/2 three NQR lines exist. Up to now, in our study of $(Y_{0.8}Lu_{0.2})Ba_2Cu_4O_8$ and $(Y_{0.7}Lu_{0.3})Ba_2Cu_4O_8$ performed at 90 K two of the three Lutetium NQR lines were detected at 39 and 42.5 MHz, respectively. Knowledge of these two frequencies allows an estimation of the electric field gradient asymmetry parameter and of the third line's frequency. The third line is expected to be at 3.5 MHz or 17 MHz, a frequency range to be covered in the ongoing investigation.

References

[1] A.S. Alexandrov and A.M. Bratkovsky, Phys. Rev. Lett. **82**, 141 (1999).

[2] A.J. Millis, P.B. Littlewood, and B.I. Shraiman, Phys. Rev. Lett. **74**, 5144 (1995).

[3] A. Moreo, S. Yunoki, and E. Dagotto, Science **283**, 2034 (1998).

[4] A.S. Alexandrov *et al.*, Phys. Rev. B **64**, R140404 (2001).

[5] V.N. Smolyaninova *et al.*, Phys. Rev. B **65**, 104419 (2002).

[6] A.S. Alexandrov and N.F. Mott, Int. J. Mod. Phys. **8**, 2075 (1994).

[7] K.A. Müller, Physica C **341-348**, 11 (2000).

[8] P. Zimmermann *et al.*, Phys. Rev. B **52**, 541 (1995).

[9] R. Khasanov *et al.*, cond-mat/0201165 (2002).

[10] J. Hofer *et al.*, Phys. Rev. Lett. **84**, 4192 (2000).

[11] G.M. Zhao *et al.*, J. Phys.: Condens. Matter **10**, 9055 (1998).

[12] G.M. Zhao *et al.*, Nature (London) **385**, 236 (1997).

[13] C. Grimaldi, E. Cappelluti, and L. Pietronero, Europhys. Lett. **42**, 667 (1998).

[14] E. Morenzoni *et al.*, J. Appl. Phys. **81**, 3340 (1997).

[15] T.J. Jackson *et al.*, Phys. Rev. Lett. **84**, 4958 (2000).

[16] Proc. Int. Workshop on *Anharmonic Properties of High- T_c Cuprates* edited by D. Mihailovic, G. Ruani, E. Kaldis, and K. A. Müller) 118-146 (World Scientific, Singapore, 1994).

[17] A. Shengelaya *et al.*, Phys. Rev. Lett. **83**, 5142 (1999).

[18] D.W. Cooke *et al.*, Phys. Rev. B **41**, 4801 (1990).

[19] J. Nagamatsu *et al.*, Nature **410**, 63 (2001).

[20] Eva Pavarini and I.I. Mazin, Phys. Rev. B **64**, 140504 (2001).

[21] A.V. Tsvyashchenko *et al.*, Solid State Commun. **119**, 153 (2001).

[22] M. Mali, J. Roos, A. Shengelaya, and H. Keller, Phys. Rev. **65**, 100518(R) (2002).

[23] M. Angst *et al.*, cond-mat/0112166 (Phys. Rev. Lett., in press).

[24] G. Ravikumar *et al.*, Phys. Rev. B **63**, 024505 (2000).

[25] M.R. Eskildsen *et al.*, Phys. Rev. Lett. **86**, 5148 (2001).

[26] V.G. Kogan *et al.*, Phys. Rev. B **55**, R8693 (1997).

[27] M. Willemin *et al.*, Phys. Rev. B **58**, R5940 (1998).

[28] N. Avraham *et al.*, Nature **411**, 451 (2001).

[29] A. Schilling *et al.*, Phys. Rev. B **58**, 11157 (1998).

[30] M. Willemin *et al.*, Phys. Rev. Lett. **81**, 4236 (1998).

[31] A. Schilling *et al.,* Phys. Rev. B **61**, 3592 (2000).

[32] A. Schilling *et al.*, Phys. Rev. B **65**, 054505 (2002).

[33] C.M. Aegerter *et al.*, Phys. Rev. B **57**, 14511 (1998).

[34] S.L. Lee *et al.*, Phys. Rev. Lett. **71**, 862 (1993).

[35] M. Corti *et al.*, Phys. Rev. B **54**, 9469 (1996).

[36] F. Bouquet *et al.*, Nature **411**, 448 (2001).

[37] A. Schilling *et al.*, Phys. Rev. Lett. **76**, 4833 (1997).

[38] P.G. de Gennes, *Superconductivity of metals and alloys*, (Addison-Wesley, Massachusetts, 1989).

[39] P. Zimmermann *et al.*, Hyperfine Interactions **63**, 33 (1990).

[40] J.M. Delrieu, J. Phys. F: Metal Phys. **3**, 893 (1973).

[41] A. Beck *et al.*, Appl. Phys. Lett. **77**, 139 (2000).

[42] Y. Watanabe *et al.*, Appl. Phys. Lett. **78**, 3738 (2001).

[43] K.A. Müller *et al.*, Solid State Commun. **85**, 381 (1993).

[44] Philipp Schneider, Diploma thesis, Physik-Institut, Universität Zürich, 2001.

12 Surface Physics

T. Greber, M. Hengsberger, J. Wider, H. J. Neff, W. Auwärter, F. Baumberger, M. Hoesch, M. Muntwiler, I. Matsuda, R. Karrer, M. Barry, W. Deichmann, J. Osterwalder

Artificial nanostructures, exemplified e.g. by ultrathin films, quantum wires or quantum dots, are of enormous scientific and technological interest. Their electronic and magnetic properties are dominated by size- and shape dependent quantum effects and can thus be tailored to fulfill any particular need. Their diameter in at least one dimension does not exceed a few atomic layers, and therefore they consist to a large extent of interfaces and surfaces. In the surface physics laboratory we prepare clean surfaces, ultrathin films and nanostructures under ultrahigh vacuum (UHV) conditions and characterize their surface and interface structures at atomic resolution. Their electronic and magnetic properties are studied in detail. In order to measure the geometric arrangement of the atoms within the first few monolayers of the surface we apply predominantly electron-based techniques such as x-ray photoelectron diffraction (XPD), medium-energy electron diffraction (MEED), low-energy electron diffraction (LEED), and more recently also scanning-tunneling and atomic force microscopy (STM/AFM). Angle-resolved UV photoelectron spectroscopy (ARUPS) gives us a detailed picture of the electronic band structure of such systems. Specifically, our experimental setup permits to directly map sections through the Fermi surface, which describes the electronic degrees of freedom relevant for transport properties, magnetic interactions and phase transitions. An important asset of such experiments is that the same probe (photoemission) gives us structural, electronic and magnetic information, and we can therefore study the interplay between these different degrees of freedom on the same sample.

Over the past year we have continued our work on the following systems:
Vicinal Cu(111) surfaces expose (111)-oriented terraces separated by a roughly regular array of monoatomic steps, therefore they represent lateral nanostructures that can be easily prepared. We have studied the behaviour of the two-dimensional electron gas formed by a surface state in this well-defined and tunable potential energy landscape. In particular, we observed that the repulsive energy barriers represented by the clean steps are replaced by attractive potential wells when the steps are decorated with adsorbed carbon monoxide molecules (see Section 12.1). Moreover, in a collaboration with groups from the Technical University of Berlin and from Kansas State University, a solely optical technique was found to be sensitive to the detailed geometry of the steps (Section 12.2). As a photon-in photon-out technique, reflection anisotropy spectroscopy (RAS) is very attractive because it allows one to characterize microscopic surface properties under much less stringent conditions than the usual electron-based techniques that require UHV.

The quality and the electronic character of the interfaces are very important in metal-insulator heterojunctions, especially for magnetic devices based on junctions in which the tunneling barrier depends on the electron spin. A system which we continued to study thoroughly is the Ni(111) surface covered with one monolayer of hexagonal boron nitride (h-BN). In a collaboration with the Technical University of Vienna, it could be established by density functional theory that the magnetic moment per nickel atom is reduced at the interface, and based on the photoemission data a new reduction mechanism could be proposed (Section 12.3). An attempt to grow a regular array of linear metal-insulator-metal nanostructures based on a vicinal Ni(111) surface failed (Section 12.4). This study illustrates important pitfalls in materials science on the nanoscale.

In this last year we have also begun to investigate metal-semiconductor systems that form self-organizing nanostructures. When annealed at high temperature, the deposition of monolayer quantities of Cu on Si(111) leads to a discommensurate structure where a two-dimensional metallic copper-silicide layer is organized in more or less regular 20 Å-size domains. In Section 12.5 it is described how the conduction electrons respond to this nanostructuring. On the same Si(111) surface, gold atoms can form linear chains. Our investigation of the electronic states near the Fermi energy reveals that these chains produce a one-dimensional surface state, but that this state does not cross the Fermi energy, i.e. these chains are not metallic wires (Section 12.6). A third metal-semiconductor interface, namely lead on Ge(111), has caught our attention because it exhibits a surface phase transition. In a collaboration with Tohoku University we have applied a promising new technique for measuring surface bond geometries inside this interface (Section 12.7).

Concurrent with these ongoing system-oriented studies, significant progress has been made in two projects related to the development of new experimental techniques:

The construction of our new spectrometer for spin-polarized Fermi surface mapping, which is designed to go eventually to the Surface and Interface Spectroscopy beamline of the Swiss Light Source (SLS), has been completed. First test experiments on a magnetized Ni(111) sample were highly successful (see Section 12.8). This experiment will permit the spin-resolved measurement of Fermi surfaces in magnetic nanostructures.

Our picosecond time-resolved electron diffraction experiment is now close to completion, with the ongoing implementation of the laser pulse amplifier that will deliver enough energy per pulse to produce significant transient temperature rises for each individual pulse (Section 12.9). The pulsed low-energy electron gun that has been designed and tested last year will be used for the first picosecond time-resolved LEED experiments revealing ultrafast structural changes at surfaces.

The near-node photoelectron holography spectrometer has been moved to the Surface and Interface Microscopy (SIM) beamline of the SLS where it will be used for studying adsorption geometries of biomolecules by direct holographic reconstruction. The group's activities at the Advanced Photoemission (APE) beamline at the ELETTRA synchrotron in Trieste, Italy, have been very limited during this past year due to continuing delays in the commissioning of the beam optics.

We have continued our collaboration with the surface chemistry group of Prof. J. R. Huber of the Physical Chemistry Department (P. Willmott, H. Spillmann) who have developed unique thin film preparation capabilities using pulsed reactive crossed-beam laser ablation. They have grown single crystalline films of zirconium carbonitrides (ZrC_xN_{1-x}) with the aim of correlating the hardness of these materials with their electronic structure as a function of the composition parameter x.

12.1 Tailoring confining barriers for surface states: CO/vicinal Cu(111)

in collaboration with B. Delley, Solid State Theory Group, Paul–Scherrer–Institut, Villigen, Switzerland

The clean Cu(111) surface supports a free electron like Shockley–type surface state, with a maximum binding energy of ~ 0.4eV at $\bar{\Gamma}$. This state arises as a consequence of the broken translational symmetry in the normal direction at the crystal surface. Its wave functions propagate parallel to the surface with a Fermi wave length of $\lambda_F \sim 3$nm. They fall off exponentially both towards the vacuum and towards the bulk and are thus quasi two-dimensional (2D). Monoatomic steps on an otherwise flat surface are known to act as repulsive potential barriers for surface state electrons [1]. Hörmandinger *et al.* showed that periodic arrays of steps, as present on a vicinal surface, are well described by a 1D model with rectangular potential barriers [2]. The superlattice leads to an enhanced effective mass perpendicular to the steps, causing the elliptic Fermi surface contour observed on Cu(332) [3].

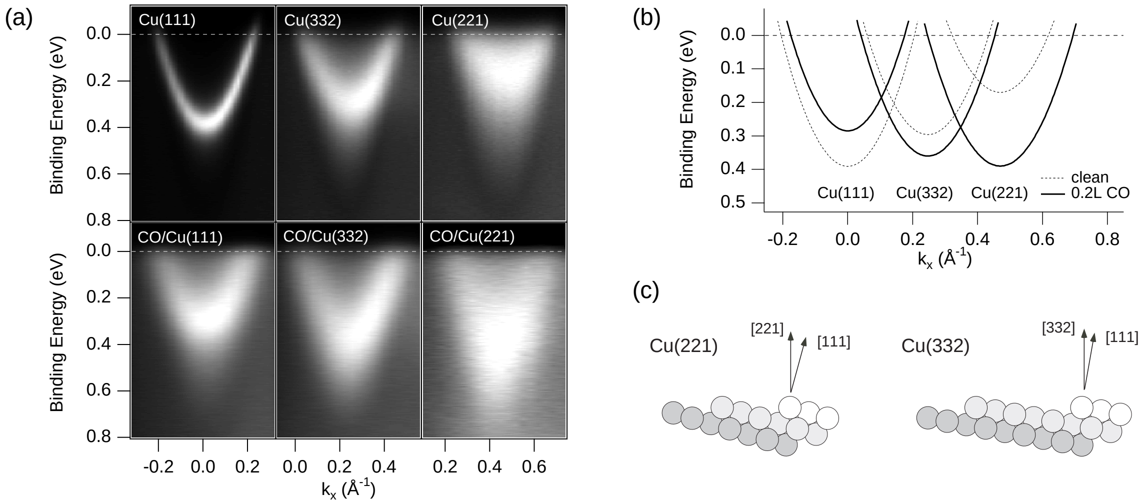

Figure 12.1: *(a) Measured photoemission dispersion plots (He Iα excitation), showing parabolic dispersion of the Shockley surface state on Cu(111) and two vicinal surfaces with and without CO adsorption (0.2L). (b) Compilation of the dispersion relations found on the clean (dotted lines) and CO-adsorbed (solid lines) surfaces, obtained from fitting the data shown in (a). (c) Hard sphere models of the two vicinal surfaces.*

We have investigated the change of the step potential after decoration with carbon monoxide. The CO molecules preferentially adsorb on top of the step atoms, and different ordered structures where steps sites are consecutively filled up to 0.75ML were observed by STM [4]. Photoemission dispersion plots for the clean and step decorated surfaces are shown in Fig. 12.1.

The energy shift ΔE of the band bottom in going from the flat (111) surface to the vicinal surfaces changes the sign with the adsorption of CO. In a 1D model, ΔE is given to first order by $\Delta E = U_0 a/\ell$, where $U_0 a$ is the integrated step potential and ℓ the terrace length. We thus conclude that the step potentials change the sign from being repulsive on the bare surfaces to attractive on the step decorated surfaces. Density functional calculations reveal that this effect is due to the very local change of the electrostatic potential at the adsorption site.

12.2 Reflection anisotropy spectroscopy (RAS) on vicinal Cu(111) surfaces

in collaboration with Th. Herrmann, N. Esser, W. Richter, Institut für Festkörperphysik, TU Berlin, Germany, and A. Kara, T. Rahman, Physics Department, Kansas State University, Manhattan U.S.A.

It is a main perspective of condensed matter research to link the microscopic electronic structure of surfaces with their macroscopic properties such as e.g. electrical resistance or hardness. Optical phenomena are governed by microscopic as well as macroscopic properties and are therefore a useful pilar for this bridge. In this context we performed reflection anisotropy spectroscopy (RAS) measurements on vicinal Cu(111) surfaces. The bulk contribution to the normal incidence reflectivity of a cubic crystal does not depend on the azimuthal orientation of the polarization vector. Therefore any anisotropy in reflection must stem from an anisotropy in the surface. This makes RAS an optical method that is sensitive to the topmost atomic layers [5].

In Fig. 12.2b) the RA spectra for two vicinal surfaces with the two different step geometries (A and B type) are shown. The two types of steps can clearly be distinguished by RAS. The maximum difference between the two surfaces occurs at a photon energy of 4.2 eV. The reflection anisotropy is defined as $A = 2(R_{||} - R_{\perp})/(R_{||} + R_{\perp})$ where $R_{||}$ and $R_{\perp}$

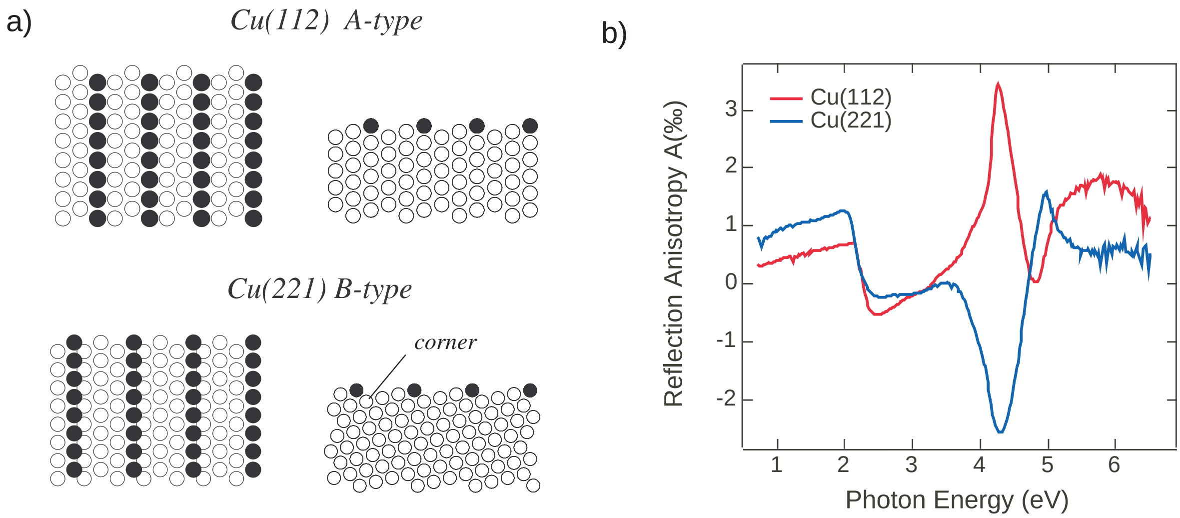

Figure 12.2: *Reflection anisotropy from Cu(112) and Cu (221). In a) the two vicinal surfaces are shown in a top and in a side view, where it becomes clear that the A type steps of Cu(112) consist of (001) facets, while the B type steps of Cu(221) are (111) facets. b) RA spectra in the photon energy range between 0.8 and 6.5 eV. The anisotropy A is largest at 4.2 eV and changes its sign in going from A to B type steps.*

are the amplitudes of the reflected light with polarization parallel or perpendicular to the steps. The maximum anisotropy is in the order of 3000 ppm. The penetration length of 4 eV (310 nm) light in copper is 18 nm or 86 layers. At a reflectivity of 33 % a single atom in the Cu(221) unit cell can therefore, in a simple atomic picture, contribute a maximum anisotropy of 0.8 %. There is one particular site in these vicinal surfaces that has a significantly different local environment: the corner atoms (see Fig. 12.2a)) have coordination numbers 10 or 11 in A and B type vicinals, respectively. Density functional calculations show that the corner atoms of A and B type steps have ellipsoidal charge density distributions with their long axis parallel or perpendicular to the steps. Within the model of Tarriba and Mochán [6] this may explain the dependence of the reflection anisotropy on the step geometry.

12.3 Reduction of the magnetic moment at the h-BN/Ni(111) interface

in collaboration with G. Grad and P. Blaha, Institut für Physikalische und Theoretische Chemie, TU Wien

Atomically sharp interfaces are a prerequisite for the realization of electronic and spintronic devices with ultimate performance. The single-layer system of hexagonal boron-nitride on nickel(111) is an ideal case for testing the concepts of spin-dependent electron scattering at interfaces. h-BN/Ni(111) is a perfect (1x1) commensurate interface, where the small lattice mismatch of 0.4% is compensated by a slight corrugation (0.1Å) of the h-BN layer [7]. The influence of h-BN on the Ni magnetic moments is investigated by means of photoemission and density functional theory (DFT) [8].

Figure 12.3a) shows He Iα excited photoemission spectra for Ni(111) and h-BN/Ni(111) in normal emission. The most prominent features upon formation of the h-BN layer are the BN related σ and π bands at 5.3 and 10.0 eV binding energy. The work function shifts by 1.8 eV from 5.3 eV to 3.5 eV. This signals that the h-BN layer acts as an electron donor to the nickel substrate. The DFT calculations for a single (free-standing) layer of h-BN indicate a charge transfer of 0.56 electrons from boron to nitrogen. In the case of h-BN on Ni(111) a

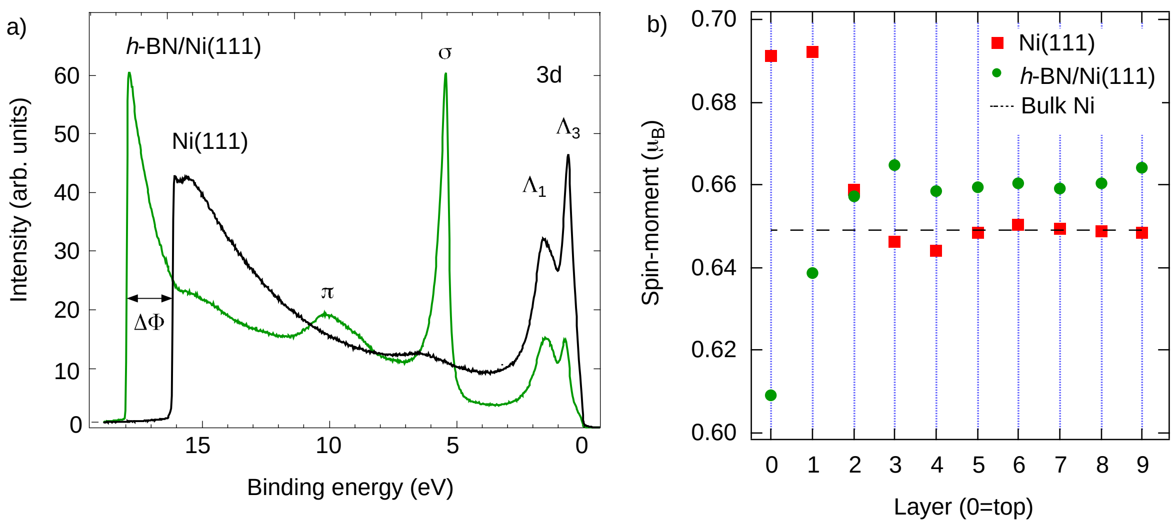

Figure 12.3: *a) Normal emission UP-spectra from Ni(111) and h-BN/Ni(111). b) Layer-resolved magnetic moment of Ni(111) and h-BN/Ni(111) as determined from DFT slab calculations.*

charge of 0.59 electrons on nitrogen and -0.65 e^- on boron is found. Therefore the net charge transfer to the substrate is 0.06 electrons per unit cell. Within an electrostatic picture where a charge separation length of 1Å is assumed this yields a work function shift of 2 eV which has the same sign and order of magnitude as the observation. The charge transfer is reflected as well in the energy down-shift of the Λ_3 d-band by 0.1 eV to 0.65 eV. In a rigid-band picture this shift is explained by charge transfer into empty bands of the substrate. This charge is mainly transferred into the minority Ni d-band since its density of states is much larger than that of the sp-bands. A decrease of the magnetic moment per Ni atom in the h-BN/Ni(111) interface is the consequence. Slab calculations support this picture and give a more precise, layer-dependent view of the magnetic moment near the interface. In Figure 12.3b) the layer-resolved spin moment, i.e. the difference of spin-up and spin-down charges inside atomic spheres of $R_{MT} = 2.3a_o$ are shown. For Ni(111) we find a bulk magnetic moment of $0.65\mu_B$ and the surface enhancement of the magnetic moment is 6%. The large 19 layer calculations do furthermore indicate Friedel type oscillations in the magnetic moment with an amplitude of less than 0.5% and a wavelength in the order of 3 to 4 layer spacings. For the case of h-BN/Ni(111) the magnetic moment in the top layer is reduced by $0.08\mu_B$ with respect to the Ni(111) top layer. The reduction of the magnetic moment induced by a charge transfer into unoccupied minority d-band states describes a mechanism that is qualitatively different from the hybridisation mechanism of Tersoff and Falicov [9].

12.4 Self-Organized 1D Nanostructures on Stepped Boron Nitride Films

On a flat Ni(111) surface *h*-BN can be grown as a compact commensurate monoatomic layer [10, 11]. With a second metallic phase grown on top of the *h*-BN, a well-defined model system for the study of metal-insulator-metal interfaces was prepared and investigated experimentally [12]. While it is known that on stepped metal surfaces one-dimensional atomic

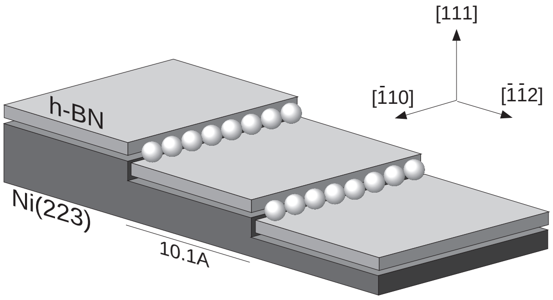

Figure 12.4: *Idealized model of a one-dimensional quantum wire on a stepped h-BN/Ni substrate.*

structures ("quantum wires") can be grown with elementary molecular beam epitaxy [13], this "step-decoration" growth mode has not yet been reported for a three-phase system like metal/*h*-BN/Ni. Our intention was to produce a sample close to the idealized model illustrated in Fig. 12.4 with the same methods and to examine its electronic structure. As substrate a nickel single-crystal cut along a (223) face is chosen. This surface ideally consists of 10.1 Å (4 2/3 atomic rows) wide (111) terraces separated by monoatomic steps. On this substrate a *h*-BN layer was expected to follow the steps of the substrate and allow step-decoration with a metal, e.g. copper or cobalt. Established preparation techniques (Ar ion sputtering, annealing of the substrate, catalytic growth of *h*-BN under borazine exposure, and molecular beam epitaxy with Cu) were applied until either a partial stage or completion of the Cu/*h*-BN/Ni(223) layered structure was reached. The prepared structures were characterized with regard to long-range step order (LEED) and *h*-BN film quality (XPS, UPS). As it was reported by Rokuta *et al.* for *h*-BN/Ni(755) [14], the surface strongly facets. The most

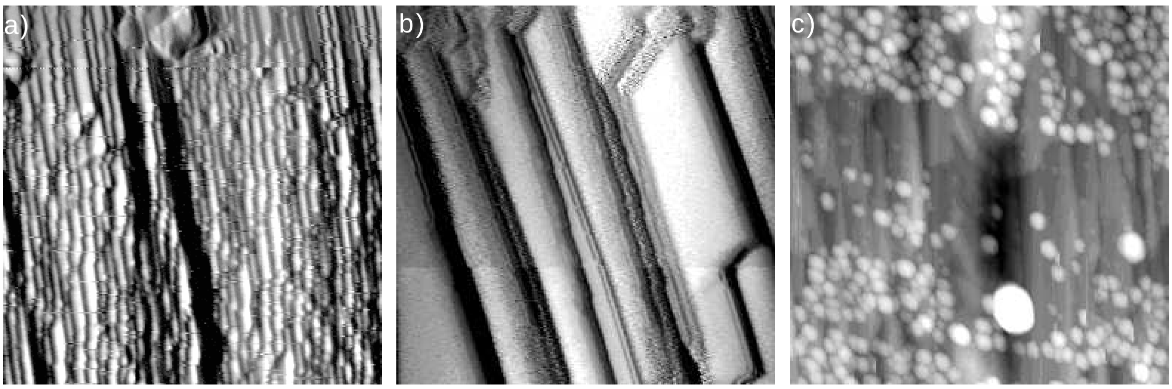

400 Å × 400 Å   400 Å × 400 Å   1000 Å × 1000 Å

Figure 12.5: *STM measurements of different samples: (a) The vicinal Ni(223) surface shows narrow terraces with an average width of 10.7 Å. (b) After h-BN film growth terraces are up to 70 Å wide and separated in height by several atomic layers. (c) In the Cu/h-BN/Ni(223) image the wide BN/Ni terraces are visible in the background. The bright disks represent Cu islands, their apparent shape (height ≈ 8 Å (4 layers), width ≈ 35 Å) is a convolution with the STM tip.*

striking results were obtained with STM: Although a fairly good Ni(223) vicinal substrate with narrow terraces could be prepared (Fig.12.5a), the terraces become much larger and the steps significantly higher during h-BN film growth (Fig.12.5b). Furthermore, the terrace width distribution gets much broader, and non-(111) facets show up.

The real situation with Cu evaporated onto h-BN/Ni(223) is shown in Fig.12.5c: The Cu atoms aggregate to islands which are located in the terrace centers rather than close to step edges. Their coordinates are correlated with the steps but they do not connect, and thus do not form the desired one-dimensional nanostructures. The tendency of the h-BN/Ni(223) system to step bunching, and the preferred growth of Cu islands on the terraces rather than at the steps, are currently not understood.

12.5 The Fermi surface of a discommensurate surface layer

The growth of copper on Si(111) has attracted a lot of academic and technological attention as a highly relevant metal-on-semiconductor interface. Maybe the most intriguing issue is the well-defined and stable interface layer formed during elevated-temperature growth. This layer exhibits a (5.55×5.55) periodicity that is not commensurate with the Si(111) substrate. A recent structure model was brought forward by Zegenhagen *et al.* [15] and is depicted in Fig. 12.6a). The main elements of this model are (i) an in-plane lattice constant of the Cu_2Si layer that is expanded by 10 % relative to the underlying substrate, (ii) a rotation of $\pm 3°$ of the silicide lattice relative to the Si(111) lattice, and (iii) the formation of a more or less regular pattern of silicide domains with about 20 Å diameter bounded by a dislocation network. The local geometry within this two-dimensional silicide layer has recently been confirmed by photoelectron diffraction experiments of our group [16].

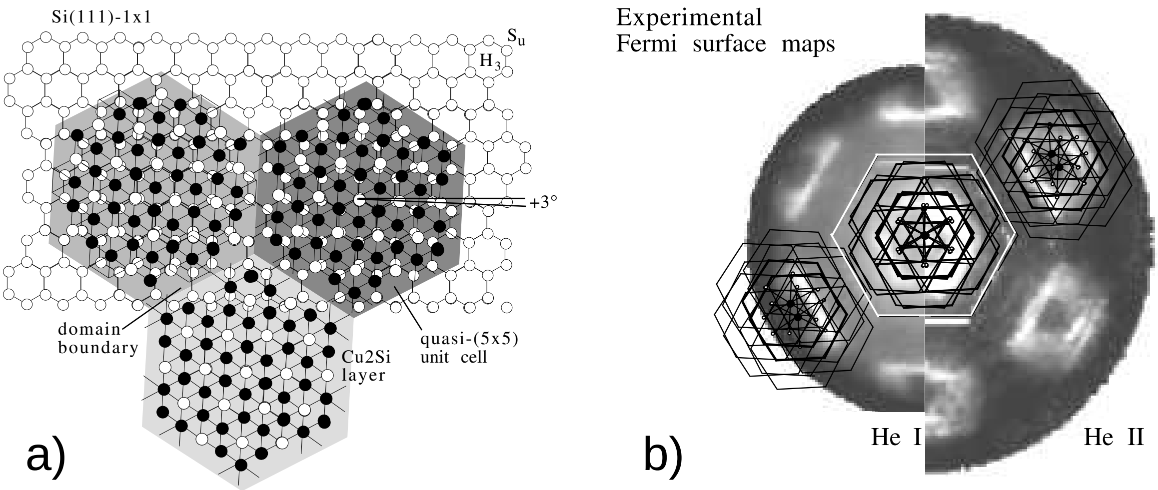

Figure 12.6: *a) Schematic representation of the structural model for the discommensurate quasi-5x5 Cu/Si(111) layer. b) Overlay of the schematic Fermi surface pattern, containing all the structural elements of the model depicted in a), on the measured Fermi surface data measured by He I and He II excitation. The two experimental intensity maps have been brought to matching k-vector scales.*

In early photoemission experiments [17] we realized that this silicide layer is metallic, so we engaged in a detailed study of how this unusual discommensurate structure is reflected in the electronic structure and specifically in the Fermi surface. Fig. 12.6b) shows photoemission Fermi surface maps taken with He I and with He II radiation at photon energies of 21.2 eV and 40.8 eV, respectively. The data show sharp contours that suggest a hexagonal Fermi surface spanning half the linear dimensions of the Si(111) (1×1) surface Brillouin zone. In addition, umklapp Fermi surface contours are seen, originating from electrons that have scattered off the regular network of discommensuration lines. The positions of these umklapp contours are consistent with all aspects of the Zegenhagen model described above, as is demonstrated by the overlay of the schematic Fermi surface contours that have been symmetry-expanded according to the structure model. This study thus gives a further confirmation of its correctness, and it demonstrates that the electrons in this metallic silicide layer have a coherence length - at room temperature - long enough to sample the full complexity of the discommensurate structure.

12.6 Fermi-surface and band mapping study of the Si(111)5x2-Au surface

Low-dimensional, especially one-dimensional (1D), structures induced by metal adsorption on semiconductor surfaces have attracted a considerable interest. They exhibit very in-

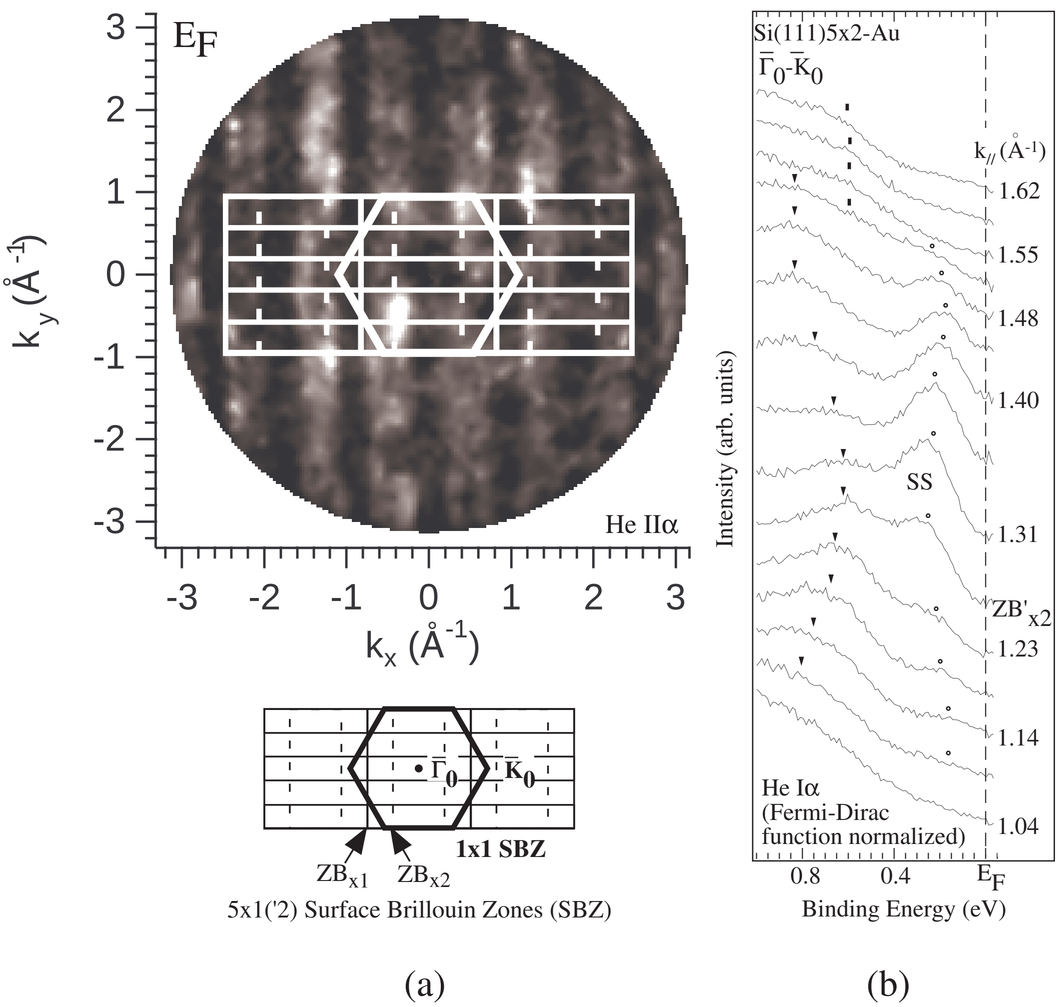

Figure 12.7: *(a) He IIα excited photoemission Fermi surface map and (b) He Iα excited ARPE spectra (normalized by the Fermi-Dirac distribution) from a single-domain Si(111)5x2-Au surface. The surface Brillouin zones and high symmetry points are indicated. The Au chains run along the horizontal (x) direction.*

triguing electronic properties due to increased interactions and subsequent correlations as a result of the electron confinement. Even though 1D *metallic* systems represent maybe the most interesting case, only few among the numerous varieties of the low-dimensional metal/semiconductor structures studied so far were reported to exhibit metallicity [19, 20]. The Si(111)5x2-Au surface is one such example according to a recent angle-resolved photoemission spectroscopy (ARPES) study [21]. However, the ARPES data were taken with low energy resolution and the electronic structure near the Fermi level is still not well established [21]. More recently, a "pseudo-gap" of 300 meV at the Fermi level has been reported [22], raising again the question of the metallic character of the observed Au chains.

We have carried out detailed Fermi surface and band mapping measurements with high-resolution ARPES. The goal of this project was to study the electronic structure of the (single-domain) Si(111)5x2-Au surface near the Fermi level, which governs the thermodynamical properties, and to map directly the Fermi surface, which has not been investigated so far. Fig. 12.7(a) shows the resulting Fermi surface contours obtained with He IIα excitation with the 5x1(2) surface Brillouin zones (SBZ) superimposed. One can observe perfectly straight 1D features along the zone boundaries of $SBZ_{5\times2}$. At first glance, the result seems to confirm the previous proposal of a quasi-1D metal. However, through a detailed analysis of the spectra, we find that the apparent Fermi surface can be attributed to a broadening of ARPES signals from a 1D surface state just below the Fermi level. Figure 12.7(b) shows the Fermi-Dirac normalized ARPE spectra taken with He Iα photons. These data reveal that the 1D surface state (SS) that is responsible for the observed Fermi surface contours in Fig. 12.7(a) is *not* crossing the Fermi level. Thus, contrary to the previous understanding, the Si(111)5x2-Au surface is found to be non-metallic but semiconducting with 1D surface states just below the Fermi level, maybe due to a periodic lattice distortion within the Au chains. The present results are expected to contribute to our understanding of instabilities in low-dimensional systems.

12.7 Correlated Thermal Diffuse Scattering (CTDS) from Pb/Ge(111)

in collaboration with T. Abukawa and S. Kono, Research Institute for Scientific Measurements, Tohoku University, Sendai, Japan

Correlated Thermal Diffuse Scattering (CTDS) is a new structural tool for the detection of surface bonds, recently introduced and developed by a group at Tohoku University [23]. The Fourier transform of oscillations in the three dimensional (multiple-energy) diffraction pattern of medium-energy electrons reveals the surface Patterson function, i.e. bond lengths and bond angles within the surface layers. The Patterson function is derived directly from the experimental data, i.e. without assuming a model structure. Although the experimental setup is very similar for CTDS and low-energy electron diffraction (LEED), the two methods are complementary. LEED probes the *surface periodicities* whereas CTDS reveals information on the *local geometries* within the unit cell. The loss of surface sensitivity due to higher electron energies used for CTDS can partly be regained by chosing grazing incidence and/or excidence of the electrons. By chosing the appropriate scattering geometry, a specific bond direction can be emphasized in the Patterson function. We want to use this method for studying structural changes within the surface when a temperature dependent phase transition is crossed.

An example of CTDS measurements from the Pb/Ge(111) surface is shown in Fig. 12.8. At a coverage of 1/3 monolayer, this system exhibits an interesting phase transition around 250 K that has been associated with the formation of a surface charge density wave [24]. Interesting surface bonds are the tetrahedral Ge-Ge bond (yellow in Fig. 12.8a)) and the Ge-

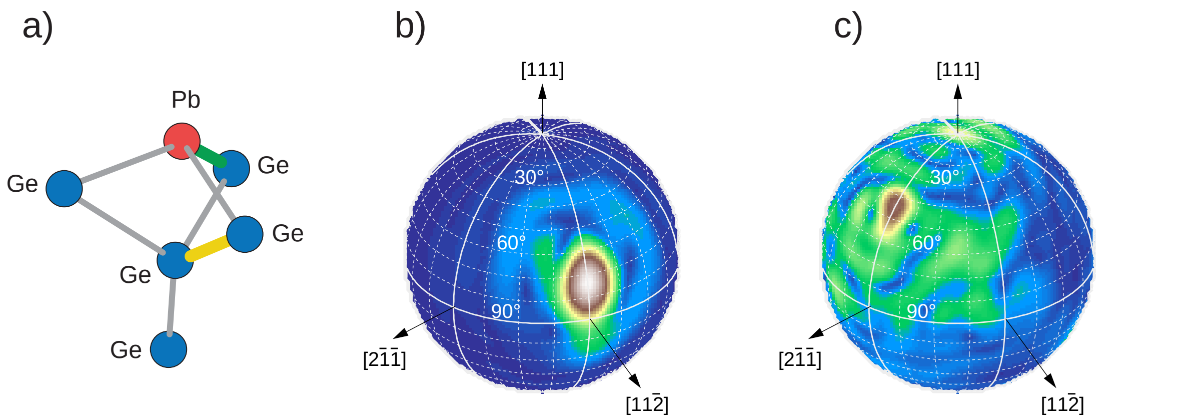

Figure 12.8: *CTDS measurements of the Pb/Ge(111)-$\sqrt{3}\alpha$-surface. a) Bonding geometry of the Pb/Ge surface. Pb atoms occupy T_4 sites above the truncated Ge lattice. The Ge-Ge tetrahedral bond and the Ge-Pb adatom bond are highlighted in yellow and green, respectively. b) Shell with radius 2.45 Å through the Patterson function displaying the Ge-Ge tetrahedral bond. c) Shell with radius 3.05 Å displaying the Ge-Pb adatom bond.*

Pb adatom bond determined by the adsorption geometry of the Pb adatom on the Ge surface (green in Fig. 12.8a)). Cuts through the experimental Patterson function (Figs. 12.8b) and c)) demonstrate that both surface bonds are clearly resolved. The elongation of the peaks along [111] can be explained by the relaxation of the surface which leads to a “distortion” of the surface bonds. The experimental Patterson function displays the superposition of the variety of these distorted bonds. The accuracy of the CTDS method is 0.1 Å and 1° in bond length and bond angle, respectively.

12.8 First experiments with COPHEE

in collaboration with V.N. Petrov, St. Petersburg Technical University, Russia

First experiments have been performed with COPHEE, the COmplete PHotoEmission Experiment on the Ni(111) surface. The COPHEE instrument is a high resolution photoelectron spectrometer with spin resolution, which has been taken into operation in 2001. The principle of operation is shown in Fig. 12.9. Photoelectrons emitted by VUV radiation from a sample are angle and energy selected by an electron lens and a hemispherical energy analyzer. The beam is then transported into one of two Mott detectors, which analyze the spin polarization [25]. A symmetric two-way deflector switches the beam periodically ($\approx$ 1 Hz) between the two Mott detectors to allow quasi simultaneous data collection. Each of the Mott polarimeters has two pairs of energy-selective detectors which count the electrons that are elastically backscattered at 50 keV from a gold foil, and therefore analyses two components of the polarization vector transverse to the incoming beam axis. In an electrostatic beam transport system the spin remains fixed in space and the two orthogonally arranged polarimeters cover all three axes and thus allow the complete measurement of the spin polarization vector. In a Fermi-surface mapping experiment using photoemission with a fixed light source and detector, the angular distribution of photoelectrons above the sample surface is measured by rotating the sample about two axes to cover all emission angles. In a magnetized sample, also the magnetization axis sweeps the whole hemisphere and therefore a three-dimensional

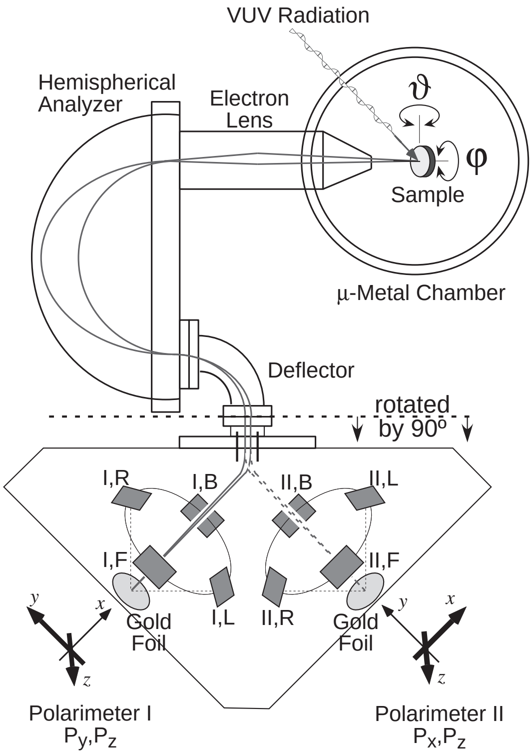

Figure 12.9: *Schematic view of COPHEE. Electrons photoemitted from a sample by UV radiation are energy- and angle-selected by an electrostatic analyzer and detected in two orthogonal Mott polarimeters. In an electrostatic beam deflection system the spin direction is conserved and polarimeter I measures the polarization components P_y and P_z, while polarimeter II measures P_x and P_z. The beam is switched between the two to allow quasi-simultaneous data collection. The polarimeter system is shown rotated by 90° for graphical clarity.*

polarimeter is necessary. In this sense COPHEE merits its ambitious name, because it measures all degrees of freedom of the photoelectron in the sample coordinates, *i.e.* the energy, momentum and spin.

12.8.1 Spin-resolved Fermi-surface mapping on Ni(111)

For the first experiments a newly developed magnetizable Ni(111) sample in a picture frame geometry was used. Because the Ni sample forms a closed loop, a sizable remnant in-plane magnetization can be achieved and stray fields are reduced. First the magnetization direction was determined directly by measuring the spin polarization vector of secondary electrons in normal emission upon excitation with UV light from a helium lamp. These electrons are polarized ($P \simeq 8\%$ for a fully magnetized sample [26]) through spin dependent scattering processes in the sample with the direction of polarization along the magnetization axis. The degree of magnetization of our sample was estimated to be 15 to 25 %. For further information see [27].

The Fermi-surface of nickel features sheets due to minority d-bands and a large sp-band electron surface. On the Ni(111) surface, a pair of spin-split sp-bands is seen around the $[\bar{1}\bar{1}2]$ azimuth with a pair of d-bands near by. In this geometry the two Mott detectors measure the spin-polarisation almost equivalently and a direct cross checking is possible. Fig. 12.10 shows spin-resolved photoemission data. The spin-character of the band is clearly revealed through the sign of the Mott detector asymmetry. The two asymmetry curves were measured quasi-simultaneously by 2 Hz switching between the two detectors. They fall precisely on top of each other.

12.9 Time-resolved electron diffraction

This project aims at the study of atom dynamics on solid surfaces near phase transitions. In the vicinity of the critical temperature T_c fluctuations in the order parameter are expected

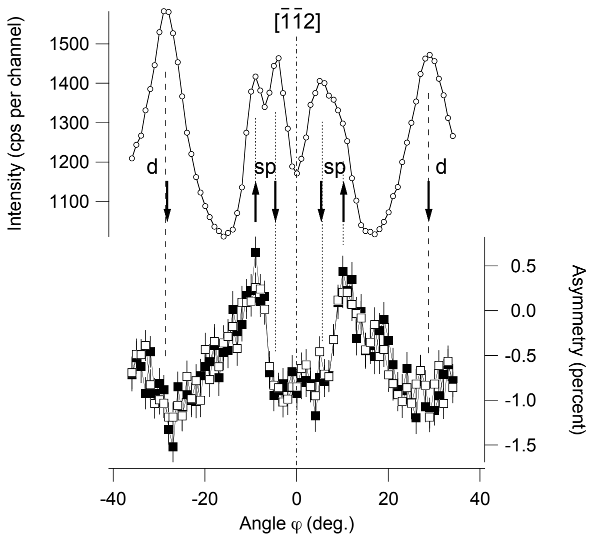

Figure 12.10: *Spin-resolved photoemission data from Ni(111) excited with HeIα radiation ($h\nu$ = 21.2 eV). The upper part shows the photoelectron intensity and the lower part the measured asymmetry as a function of the azimuthal emission angle ϕ near grazing emission. Black arrows mark the known assignment of the peaks to (minority) d-bands and spin-split sp-bands. Scattering asymmetries from two Mott detectors (polarization component P_z) are shown by black and white squares.*

to occur, which should be reflected in the structural arrangement of the surface atoms. Two electron diffraction methods have been adopted allowing the appropriate parameter (local or long-range order) to be measured:

At medium kinetic energy (typ. 1 keV), broad oscillations appear in the diffuse background of the diffraction pattern, from which the local environment of the surface atoms can be extracted by numerial Fourier transform (Correlated Thermal Diffuse Scattering, CTDS, see section 12.7).

At low energy, (typ. 100 eV) the long-range periodicity of the surface is probed (Low-Energy-Electron Diffraction, LEED).

The necessary equipment has been developed and thoroughly tested in 2001. In particular, a 5 picosecond pulsed gun for low-energy electrons, which was built recently in our group [28] (see Annual Report 2000/2001), has been shown to provide bunches of electrons coherent enough for allowing diffraction patterns to be recorded [29].

Real-time measurements on a picosecond time scale will be effectuated in a pump-probe setup (see Fig 12.11): A train of 800 nm photon pulses from a laser oscillator is split into two, one of the branches being guided via a delay stage to the vacuum chamber and focused onto the sample (pump pulse). The sample, held below and close to T_c by use of a cryostat, is transiently heated above T_c by absorbing the light pulse and crosses again the phase transition during the subsequent cooldown. The photoelectron pulse, produced in the electron gun by frequency-doubled photons from the second branch, probes the surface structure at a certain time after the pump pulse. Using the delay stage this retardation can be varied, allowing the structural evolution after the pump pulse to be followed as a function of delay time.

The realization of this ambitious project, which has been in its final design stage in 2001, is in progress now and will be finished in spring 2002 : The laser system will be upgraded by a pulse amplifier, which will provide enough energy per pulse to obtain a significant temperature rise of a few tens of degree Kelvin in the sample surface area seen by the probing electrons. As a consequence a larger optical table top had to be ordered, and the new optical setup had to be planned. Moreover, since one single experiment will run over up to 30 hours, data acquisition and experiment control are automated. The hardware, necessary to pilot delay stage and CCD camera and to record all crucial experimental parameters like, e.g., sample temperature and laser power, was installed and tested. The software is currently being developed using Visual Basic language on a remote personal computer.

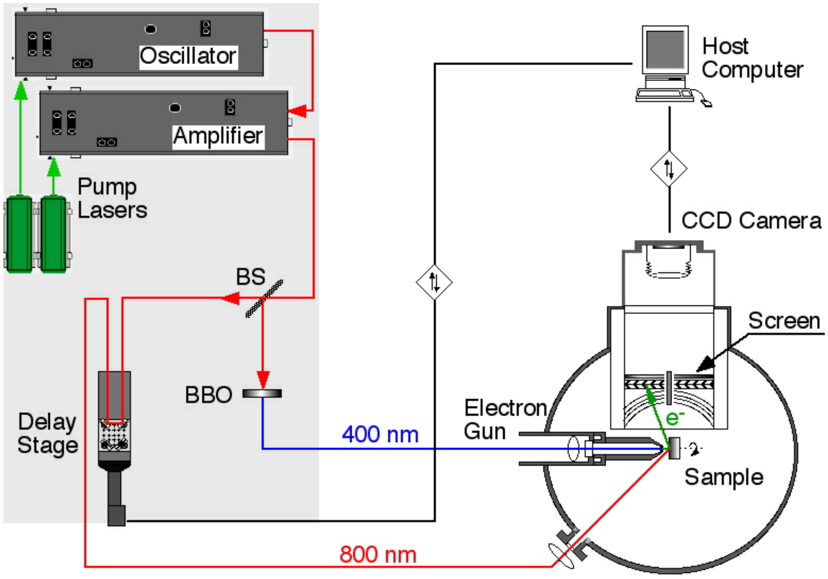

Figure 12.11: *Schematic view of the final experimental setup: Pulses from the laser oscillator are amplified and split (BS) into two branches; one branch (800 nm) leads via a delay stage to the vacuum chamber and is focused onto the sample; photons of the second branch are frequency doubled in a BBO crystal and used to produce photoelectrons in the electron gun. Electrons backreflected from the sample are amplified and detected on a fluorescent screen. The diffraction patterns are recorded by using a CCD camera coupled to a host computer.*

References

[1] M.F. Crommie, C.P. Lutz and D. M. Eigler, Science **262**, 218 (1993).

[2] G. Hörmandinger and J.B. Pendry, Phys. Rev. B **50**, 18607 (1994).

[3] F. Baumberger, T. Greber, and J. Osterwalder, Phys. Rev. B, **64**, 195411 (2001).

[4] G. Meyer, B. Neu, K.H. Rieder, Chem. Phys. Lett. **240**, 379 (1995).

[5] D.E. Aspnes, J.P. Harbison, A.A. Stunda and L.T. Florez, Phys. Rev. Lett. **59**, 1687 (1987).

[6] J. Tarriba and Luis Mochán, Phys. Rev. B **46**, 12902 (1992).

[7] W. Auwärter, T. J. Kreutz, T. Greber and J. Osterwalder, Surf. Sci. **429**, 229 (1999).

[8] P. Blaha, K. Schwarz and J. Luiz, WIEN 97, TU Vienna, 1997, Updated UNIX version of the Wien code as published by P. Blaha, K. Schwarz P. Sorantin, S. B. Tickey in Comput. Phys. Commun. **59**, 399 (1990).

[9] J. Tersoff and L.M. Falicov, Phys. Rev. B **26**,6186 (1982).

[10] Y. Gamou, M. Terai, A. Nagashima, and C. Oshima, Sci. Rep. RITU **A44**, 211 (1997).

[11] W. Auwärter, T. J. Kreutz, T. Greber, and J. Osterwalder, Surf. Sci. **429**, 229 (1999).

[12] W. Auwärter, M. Muntwiler, T. Greber, and J. Osterwalder, Surf. Sci., in press (2002).

[13] F. J. Himpsel, T. Jung, and J. E. Ortega, Surf. Rev. Lett. **4**, 371 (1997).

[14] E. Rokuta, Y. Hasegawa, A. Itoh, K. Yamashita, T. Tanaka, S. Otani, C. Oshima, Surf. Sci. **427-428**, 97 (1999).

[15] J. Zegenhagen, P. F. Lyman, M. Böhringer, M. J. Bedzyk, Phys. Status Solidi B **204**, 587 (1997).

[16] M. De Santis, M. Muntwiler, J. Osterwalder, G. Rossi, F. Sirotti, A. Stuck, L. Schlapbach, Surf. Sci. **477**, 179 (2001).

[17] M. De Santis, A. Stuck, J. Osterwalder, F. Sirotti, G. Rossi, Vuoto **21**, 200 (1991).

[18] H.-J. Neff, I. Matsuda, M. Hengsberger, F. Baumberger, T. Greber, J. Osterwalder, Phys. Rev. B **64**, 235415 (2001).

[19] P. Segovia, D. Purdie, M. Hengsberger, and Y. Baer, Nature (London) **402**, 504 (1999).

[20] H.W. Yeom, S. Takeda, E. Rotenberg, I. Matsuda, K. Horikoshi, J. Schaefer, C.M. Lee, S.D. Kevan, T. Ohta, T. Nagao, and S. Hasegawa, Phys. Rev. Lett. **82**, 4898 (1999).

[21] I.R. Collins, J.T. Moran, P.T. Andrews, R. Cosso, J.D. O'Mahony, J.F. McGilp, and G. Margaritondo, Surf. Sci. **325**, 45 (1995).

[22] K.N. Altmann, J.N. Crain, A. Kirakosian, J.-L. Lin, D.Y. Petrovykh, and F.J. Himpsel, Phys. Rev. B **64**, 035406 (2001).

[23] T. Abukawa, C.M. Wei, T. Hanano, and S. Kono, Phys. Rev. Lett. **86**, 335 (1999).

[24] J. M. Carpinelli, H. H. Weitering, E. W. Plummer, R. Stumpf, Nature (London) **381**, 398 (1996).

[25] V. N. Petrov, M. Landolt, M. S. Galaktionov, B. V. Yushenkov, Rev. Sci. Instrum. **68**, 4385 (1997).

[26] M. Landolt *Spin Polarized Secondary Electron Emission from Ferromagnets* in *Polarized Electrons in Surface Science*, ed. R. Feder, World Scientific, Singapore 1985.

[27] M. Hoesch, T. Greber, V. N. Petrov, M. Muntwiler, M. Hengsberger, W. Auwärter, J. Osterwalder, J. Electron Spectrosc. Relat. Phenom., in press (2002).

[28] R. Karrer, *Bau einer Elektronenkanone für zeitaufgelöste Beugung mit langsamen Elektronen*, Diplomarbeit, Universität Zürich, 2000.

[29] R. Karrer, H.J. Neff, M. Hengsberger, T. Greber, and J. Osterwalder, Rev. Sci. Instrum. **72**, 4404 (2001).

13 Physics of Biological Systems

Tatiana Latychevskaja (since December 2001), Cornel Andreoli, Graham Cross (since September 2001), Markus Drechsler (since December 2001), Conrad Escher, Hiroshi Okamoto (since February 2002) and Hans-Werner Fink

13.1 Overview

Since January 18th 2002, a new laboratory building (see Fig.13.1), designed with a special emphasis for carrying out sensitive experiments with coherent low energy electron wave fronts, has become available. Currently, the group works on the following five projects:

- Manipulation of individual DNA molecules in the liquid phase (C. Escher, since February 2001)
- Fermion-statistics (G. Cross, since September 2001)
- Online hologram reconstruction (T. Latychevskaja, since December 2001)
- Methods for preparing individual bio-molecules (M. Drechsler, since December 2001)
- Low temperature LEEPS Microscopy (H. Okamoto, since February 2002)

The overall motivation of all our efforts is to develop methods and tools to gain insight into the structural and electronic properties of individual molecules that is not accessible by other techniques. Apart from these microcopy aspects, we are also interested in using biological molecules as materials to design functional devices. Those functions must not necessarily be related to the natural purpose of these biological systems. A precondition for achieving this is to be able to interface single molecules with appropriate structures, to direct them to defined locations on such a device and to electrically contact them. Eventually, an "automatic" assembly of more complex structures in envisioned by taking advantage of the recognition capabilities that nature provides for biological species.

Figure 13.1: *At left, a view of the new laboratory building is shown. At right, the Low Energy Electron Point Source (LEEPS) microscope, mounted on a vibration damping stage, is shown. A total of four such platforms are available inside the new building. They are embedded in three orthogonal Helmholtz coil pairs used for compensating the local magnetic field to protect the coherence of our low energy electrons.*

We employ optical fluorescent microscopy techniques combined with mechanical manipulation and local electric fields to direct single molecules at will in the liquid phase. Micromachining tools, in collaboration with Clondiag Chip Technologies, are used to fabricate appropriate structures on which the scenario should take place. Conventional electron microcopy allows us to characterise and modify the devices. Coherent low energy electrons are finally employed to characterise the fragile molecules without damaging them. High contrast holographic imaging and in-situ manipulation provides us presently with structural and electronic information on the nanometer-scale. Once routine operation in the new laboratory environment has been established, the resolution limit should move towards the sub-nanometer-scale. In the following an overview about the present status of the individual projects is given.

13.2 Manipulating individual DNA molecules in the liquid phase

By employing video fluorescent microscopy techniques, Conrad Escher [1] succeeded to observe the dynamics of individual DNA molecules in liquid solution. Electric fields were used to stretch out individual DNA molecules, an example of which is shown in Fig.13.2. Alternating electric fields, localised on a device to micrometer dimensions, were used to at-

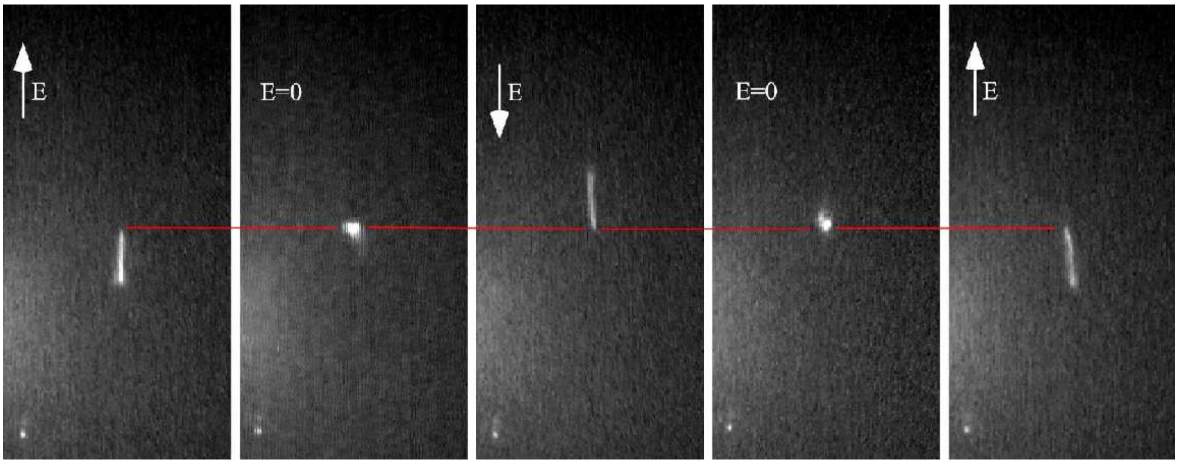

Figure 13.2: *DNA stretching experiment in a liquid film. The 17-micron long molecule is anchored at one end to the substrate. Under ordinary thermal conditions, the Brownian agitation of the solvent leads to a random coil structure of the DNA that corresponds to the minimum of the free energy. This random coil structure, assumed by minimising the entropy of the system, can be transformed into a linear chain structure by applying an external electric field.*

tract the molecules to the high field regions. We consider this ability of controlled in vivo motion of single molecules as an important first step towards interfacing bio-molecules with silicon structures. Future experiments will be carried out using a device that has recently been fabricated for us by Clondiag Chip Technologies in Jena. It is a two-terminal microchip device with an integrated liquid chamber. It has been designed in such a way as to be compatible with both, optical fluorescent microcopy and electron holography.

13.3 Fermion statistics

Besides the more technical and application oriented aspects of our electron point source, an ensemble of free electrons with an unprecedented high phase space density is of interest of

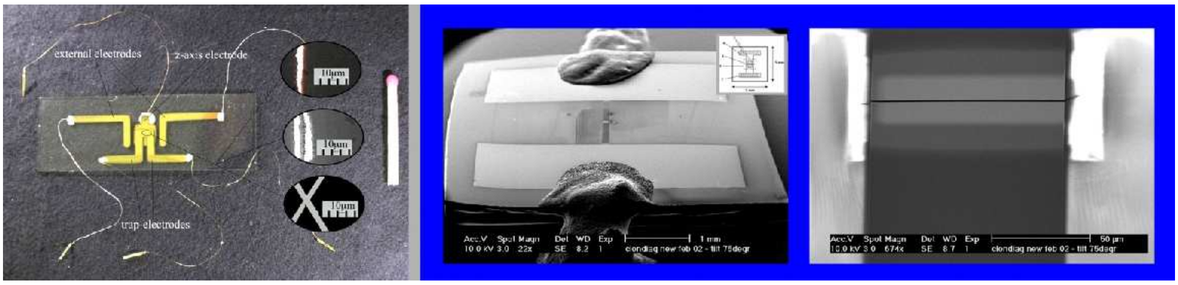

Figure 13.3: *Left: "Home-made" simple device for manipulating DNA molecules in liquids [1]. Right: Integrated chip structure, fabricated by Clondiag Chip Technologies.*

its own right in as much as it provides us with the possibility to observe interference effects of higher order. All electron interference effects observed so far, including our holograms, are brought about by a single electron at a time: "loosely speaking", this implies that an electron interferes with itself. In a high-density ensemble of electrons in a vacuum, they should however feel each others presence and their fermion character must show up. Since we are in the unique situation to create such beams, we shall try to explore their statistics by carrying out cross correlation experiments within a pulsed coherent electron beam.

13.4 Numerical reconstruction of electron holograms

Our involvement in the "National Center of Competence Research for Nanoscale Science" in collaboration with the Bio-Chemistry Institute of the University of Zurich is focused on exploring the potential of holography with low energy electrons for the structure determination of individual bio-molecules. A vital aspect of this endeavour is the ability to be able to reconstruct the high-resolution holographic information on-line. In December 2001 we have started a project aiming at a fast numerical hologram reconstruction routine. This work is done in close collaboration with CNRS researchers in Marseille.

13.5 Preparing individual bio-molecules for holography studies

In the same context, namely that of structural biology, an effort was initiated to prepare individual bio-molecules in such a way that they can be exposed to our coherent electron wave front without being attached to a substrate. As a first approach to this problem we are currently investigating the preparation of freestanding bacteria phages that could later serve as a template by assembling the proteins of interest to the elongated protein-shell of the virus.

13.6 Low temperature LEEPS microscopy

Once all system related aspects to optimise the coherence of our point source and the detection ability for the electron holograms are in place, the intrinsic thermal fluctuations of the molecules become resolution limiting. To minimise those, the construction of a liquid helium cooled LEEPS microscope has been started in February 2002. Ultimate 3-dimensional resolution in molecular imaging is one aspect of this effort. Another one is related to interesting low temperature physics problems, like the dynamics of single electron effects in nanometer-sized objects. Those should directly be accessible with such a new tool.

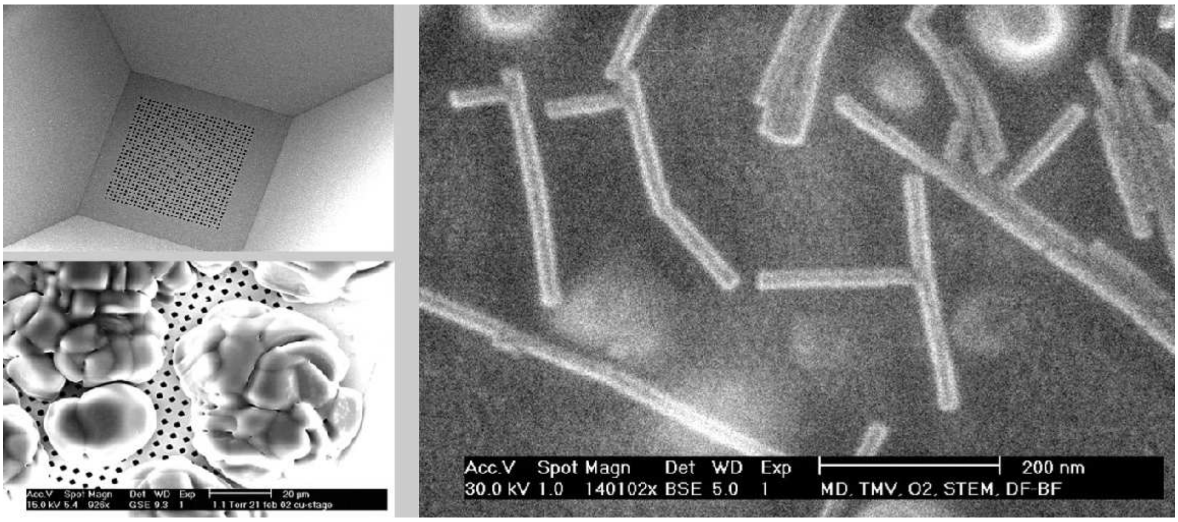

Figure 13.4: *Preliminary experiments, carried out in our environmental scanning electron microscope for controlling various preparation steps for single bio-molecules. Left: Formation of water droplets while cooling down a silicon microstructure. Right: Viruses deposited on a perforated film observed in the scanning transmission mode.*

References

[1] Conrad Escher, *Manipulating $\lambda-DNA$ molecules in aqueous solution*, Diploma Thesis Zurich University (2001), unpublished.

14 Computer Assisted Physics

C. Bersier (since May 01), P. F. Meier, E. Olbrich,
S. Pliberšek (until Sept. 01), S. Renold, J. Schneider (until Aug. 01) and Y. Shen

In this report, we want to concentrate on the following research topics:

- Interpretation of the properties of high temperature superconductivity materials using spin-polarised theoretical methods.

  We selectively report on the differences of electric field gradients derived from first-principles and point-ion calculations (14.1.1), on the calculation of the microscopic structure of $YBa_2Cu_3O_7$, in particular the study of electric field gradients and hyperfine couplings (14.1.2), and on an investigation of the differences in the electronic structures of La_2CuO_4 and $Sr_2CuO_2Cl_2$ (14.1.3).

- Non-linear dynamical study with particular reference to time series analysis of electroencephalograms.

  This involves collaboration with two groups of the Medical Faculty and we jointly present results of time series analysis of epilepsy EEG.

14.1 Electronic structure of high-T$_c$ materials

14.1.1 Electric field gradients from first-principles and point-ion calculations

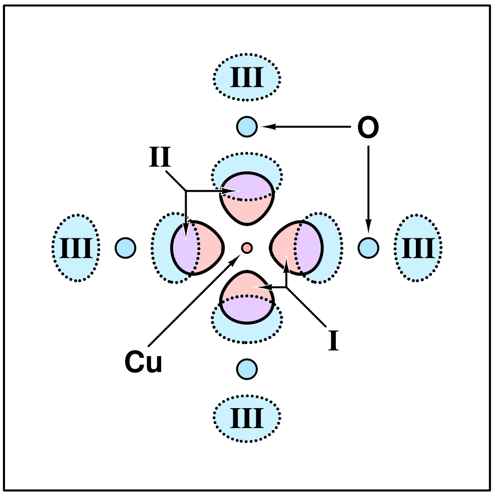

Figure 14.1: *Schematic illustration of the contributions I to III to electron densities for a molecular orbital in a CuO_4 cluster. In the centre there is a Cu atom which is surrounded by four neighbouring O atoms. To simplify matters we have drawn only the regions I of the central Cu d-electrons circumscribed by solid curves, the regions III of the oxygen p-electrons circumscribed by dotted curves, and the overlap regions II of d- and p-electrons.*

Point-ion models have been extensively used to determine "hole numbers" at copper and oxygen sites in high-temperature superconducting cuprate compounds from measured nuclear quadrupole frequencies. We embarked on a project to assess the reliability of point-ion models to predict electric field gradients accurately and also to test the validity of the implicit assumption that the values can be calculated from the "holes" rather than the total electronic structure. The latter assumption was readily shown to have a very limited range of applicability.

First-principles cluster calculations using basis sets centred on the nuclei enabled us to determine the charge and spin density distribution in the CuO_2-plane. We analysed in detail the contributions to the electric field gradients and the magnetic hyperfine couplings. In particular we partitioned the contributions into regions I, II, and III (see Fig. 14.1). The regional partition I comprises all contributions from on-site basis functions (the given example illustrates the electron density attributed to the atomic $3d$ wave functions). Contributions arising from both on-site ($3d$) and off site (oxygen $2p$) basis functions belong to region II. Region III contains no reference to the on-site basis functions.

This partitioning scheme was chosen in an attempt to find a correlation with the most commonly used point-ion model, the Sternheimer equation: $V_{ii} = (1-R)V_{ii}^{local} + (1-\gamma)V_{ii}^{lattice}$ which depends on the two parameters R and γ. Our most optimistic objective was to find expressions for these parameters, which would improve our understanding of them, but although estimates of the R parameter were encouraging the method used to obtain the γ parameter indicated that the two parameters may not be independent. The problem seems to stem from the covalently bonded nature of the CuO_2-planes in these structures which severely questions using the Sternheimer equation for such crystals, since its derivation is heavily reliant on the application of perturbation theory to predominantly ionic structures. Furthermore it was shown that the complementary contributions of electrons and holes in an isolated ion cannot be applied to estimates of electric field gradients at copper and oxygen nuclei in cuprates. For more details, see Ref. [1].

14.1.2 First-principles calculation of electric field gradients and hyperfine couplings in $YBa_2Cu_3O_7$

$YBa_2Cu_3O_7$ is a high temperature superconducting material which has a lower symmetry than La_2CuO_4 which has been studied before. The local electronic structure of $YBa_2Cu_3O_7$ was calculated using first-principles cluster methods. Several clusters of differing size, embedded in an appropriate background potential, were investigated. The electric field gradients at the copper and oxygen sites were determined and compared to previous theoretical calculations and experiments. Spin polarised calculations with different spin multiplicities have enabled a detailed study of the spin density distribution to be made and a simultaneous determination of magnetic hyperfine coupling parameters. The contributions from on-site and transferred hyperfine fields have been disentangled. The mechanism of the spin transfer from the two neighbouring Cu^{2+}-ions to the oxygen is illustrated in Fig. 14.2 where the difference $D(\vec{r})$

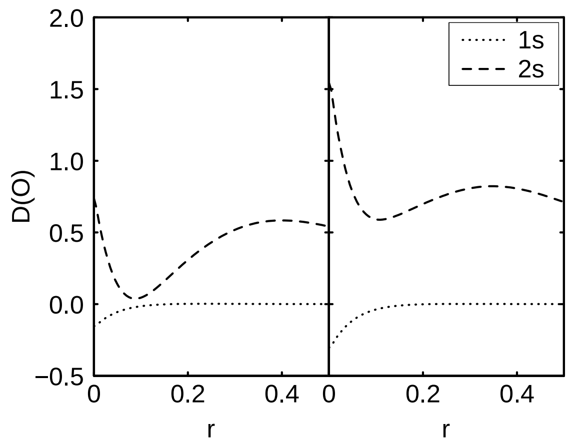

Figure 14.2: *Radial dependence (along bond direction in units of a_B) of D (in a_B^{-3}) subdivided into contributions from MOs with mainly 1s and 2s AO character at a planar oxygen nucleus for the small cluster $CuO_5/Cu_5Y_{12}Ba_{12}$ with one Cu^{2+} neighbour (left panel) and for the large cluster $Cu_5O_{21}/Cu_{13}Y_{12}Ba_{12}$ with two Cu^{2+} neighbours (right panel).*

between spin-up, $|\psi^{\uparrow}|^2$, and spin-down, $|\psi^{\downarrow}|^2$, densities, around the oxygen nucleus is shown. In the left panel of Fig. 14.2, the spin density transferred from a single copper ion is shown, subdivided into contributions of mainly $1s$ and $2s$ character around the oxygen. On the right panel, the oxygen is surrounded by two nearest neighbour copper ions. The value of the contact term at ($r = 0$) is now $D = 1.56$ which corresponds to twice the value in the left panel.

A detailed analysis (see Ref. [2]) has shown that the transferred spin densities at the oxygen essentially are due to nearest neighbour copper ions only with marginal influence of ions further away. This implies that the variant temperature dependencies of the planar copper and oxygen NMR spin-lattice relaxation rates are only compatible with commensurate anti-ferromagnetic correlations.

Furthermore, the theoretical hyperfine parameters have been compared with those derived from experimental data. It was found that the on-site hyperfine field A^c at the copper nucleus perpendicular to the CuO_2-plane is not cancelled by $4B$, the field transferred from the four nearest neighbour ions. Such an incidental correlation, however, is required to explain the observed temperature independence of the Cu magnetic shift with field parallel to the c-axis.

14.1.3 La_2CuO_4 versus $Sr_2CuO_2Cl_2$, similarities and differences in electronic structure

The structural and magnetic properties of $Sr_2CuO_2Cl_2$ are almost identical to the ones in La_2CuO_4 except: (i) the La_2CuO_4 crystal structure shows a phase transition from tetragonal to orthorhombic while the substance with chlorine at the apex positions remains tetragonal; (ii) La_2CuO_4 can easily be doped and becomes superconducting, while $Sr_2CuO_2Cl_2$ can only be doped with difficulty. Since we had already studied the electronic structure of La_2CuO_4 in detail we embarked on a similar project to investigate $Sr_2CuO_2Cl_2$. Effectively we are studying the changes introduced by replacing the axial oxygen ions in La_2CuO_4 with chlorine ions, the strontium counter ions simply maintaining the correct charge balance, in an attempt to rationalise the differences qualitatively. So far two clusters have been investigated: (a) a small octahedral-like cluster, CuO_4Cl_2 and (b) the cluster $Cu_5O_{16}Cl_{10}$ made up of effectively five CuO_4Cl_2 octahedra (see Fig. 14.3.).

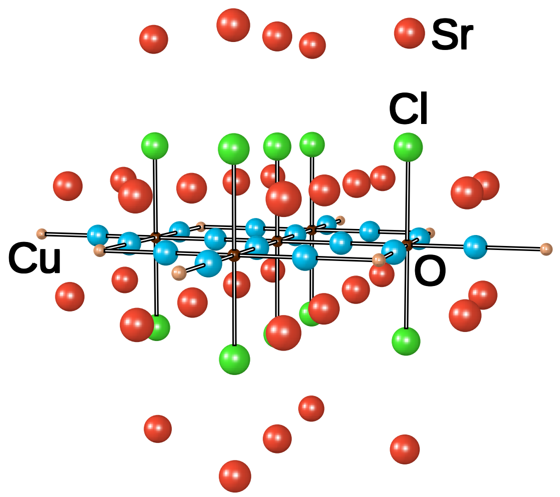

Figure 14.3: *The $Cu_5O_{16}Cl_{10}$ cluster with 5 Cu (black) and 16 O atoms in the CuO_2 plane and 10 apical Cl atoms. These atoms have been provided with basis sets. In addition 34 Sr^{2+} atoms and 8 Cu^{2+} atoms are represented with pseudopotentials.*

Since spin-polarised calculations have been carried out the spin-up molecular spin-polarised orbital (MSO) energies are distinct from the spin-down MSO energies. In Fig. 14.4 the calculated orbitals with energies in an interval of 7 eV below the Fermi energy are plotted with solid bars for spin-up MSOs and dotted bars for spin-down MSOs. The highest occupied MSO (HOMO) is an anti-bonding orbital predominantly between Cu $3d_{x^2-y^2}$ and the four planar O $2p_\sigma$ AOs, probably best interpreted as non-bonding or at most weakly anti-bonding.

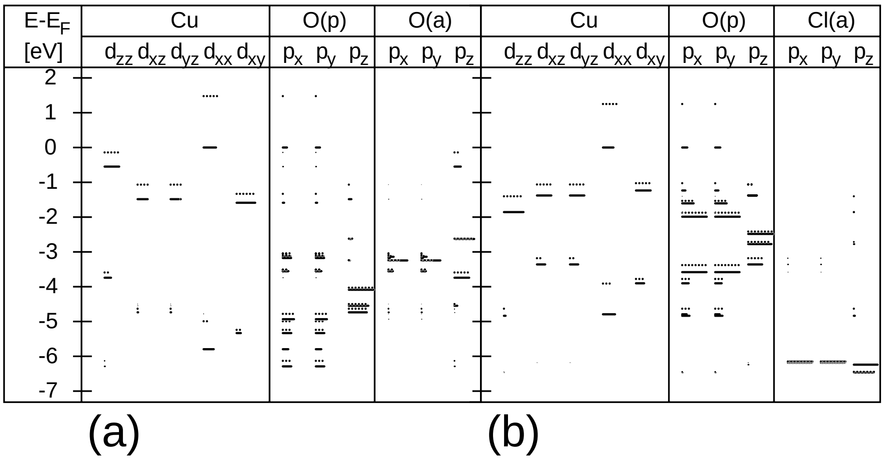

Figure 14.4: *Energies of the highest occupied MSOs in (a) the CuO_6/Cu_4La_{10}-cluster and (b) in the CuO_4Cl_2/Cu_4Sr_{10}-cluster with contributions of the individual AOs. The length of the bar is proportional to the square of the expansion coefficient of the MSO into the corresponding AOs. Spin-up (spin-down) orbitals are denoted by solid (dotted) bars.*

This is occupied by a spin-up electron but the corresponding spin-down anti-bonding MSO (1.3 eV higher) is unoccupied and is referred to as the lowest unoccupied MSO (LUMO). Also in Fig. 14.4 the composition of each MSO in terms of the more important atomic orbitals is indicated.

Just below these MSOs are MSOs which are interpreted to be the anti-bonding combinations of the Cu $3d_{3\mathrm{z}^2-\mathrm{r}^2}$ and apical O $2p_\mathrm{z}$ orbitals. These are followed at energies around -1.5 eV by MSOs that can be formed as anti-bonding combinations with the three other Cu 3d AOs, thought to be effectively non-bonding. Deeper in energy, between -2.6 and -4.4 eV, are the MSOs that are composed of oxygens only without contributions from Cu. They comprise the $2p_\mathrm{z}$ AOs of the planar oxygens and the $2p_\mathrm{x}$ and $2p_\mathrm{y}$ of the apex oxygens. The MSOs at lower energies are bonding combinations between the Cu $3d$ and the O $2p$ AOs.

The $3d_{3\mathrm{z}^2-\mathrm{r}^2}$ orbital participates at slightly lower orbital energies than the $d_{x^2-y^2}$ orbital in La_2CuO_4 as expected for the crystal field of a distorted octahedron extended along the z-axis. The corresponding $3d_{3z^2-r^2}$ orbital in the $Sr_2CuO_4Cl_2$ compound is lowered significantly in energy, even below the $3d_{xy}$, $3d_{yz}$ and $3d_{xz}$ orbital energies, which is characteristic of a square planar complex. The chlorine ions are so far removed that their influence on the crystal field is now relatively small. This may account for the observation that this crystal behaves like a ‘perfect’ two-dimensional anti-ferromagnet. This is to be contrasted with the occupied orbitals of the La compound which involve the $3d_{3\mathrm{z}^2-\mathrm{r}^2}$ orbital as well as the apical oxygen orbitals. The planar anti-ferromagnetic behaviour is clearly disturbed by this extra delocalisation in the z-direction.

14.2 Time series analysis of epilepsy EEG

Our research on nonlinear time series analysis of electroencephalograms (EEG) is continuing, a project which is conducted in collaboration with the institute of pharmacology and toxicology and the neurological clinic. Our studies have concentrated on two main aspects: (i) developing a general dynamical model of the EEG and, from the results of an EEG analysis, (ii) understanding the processes of sleep and epilepsy and how they interact.

Our investigations were focused on non-linearity in the intracranial EEG of patients suffering from epilepsy. We addressed both the temporal evolution of non-linearity in course of sleep and the spatial distribution of non-linearity in the brain. Non-linearity can be analysed by comparing the dimensional complexity (DC) of the original EEG data with those of surrogate data, which show the same linear properties as the original data but are otherwise random. The null-hypothesis that EEG signals could be generated by linear processes can be rejected with 95% probability, if the measure for significance of surrogate data test S, which is defined by

$$S = \frac{|\langle DC^{\mathrm{surr}}\rangle - DC|}{\sigma(DC^{\mathrm{surr}})},$$

is larger than the threshold value two.

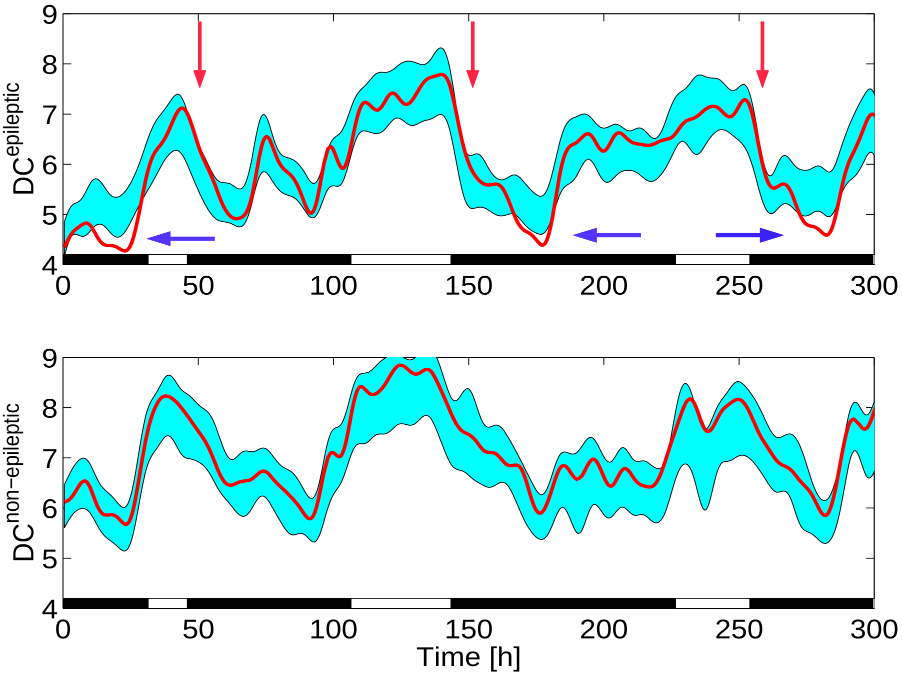

Figure 14.5: *Time courses of dimensional complexity DC for the intracranial sleep EEG of one epilepsy patient (for details see text).*
Upper panel: The DC-values for the original EEG channel derived from the epileptic hemisphere are represented by the red curve (steepest descents are marked by red arrows), whereas those for surrogate data are displayed by the cyan shaded area corresponding to $\langle DC^{surr}\rangle \pm 2 \times \sigma(DC^{surr})$. *The blue arrows point out prominent non-linearity.*
Lower panel: as for the upper panel but for the EEG channel from the healthy hemisphere.
At the bottom of each panel, a white bar indicates the occurrence of REM sleep.

In Fig. 14.5 we compare the time courses of the DC (red curves) for two intracranial EEG channels of one patient. One EEG is derived from the epileptic hemisphere (upper panel) and the other one from the healthy hemisphere (lower panel). To detect non-linearity in both EEG channels, the DC-values for the surrogate data are also displayed in terms of the blue area corresponding to $\langle DC^{\mathrm{surr}}\rangle \pm 2 \times \sigma(DC^{\mathrm{surr}})$. Firstly, we observe that the cyclic changes of DC-values for both channels coincide to a large extent with the alternation of non-REM and REM sleep cycles. This means that the DC-values of intracranial EEG can reflect sleep intensity in the same way as those of scalp EEG. However, the DC-values of the channel in the epileptic area decrease steeper during the transition from REM sleep to non-REM sleep than in the non-epileptic hemisphere shown in the lower panel. This is emphasised in Fig. 14.5 by the red arrows and can be explained by the occurrence of the abnormal slow-wave activity in the epileptic channel. Secondly, it is seen that for the epileptic channel the DC-curve of the original data deviates from the shaded area during three short episodes within non-REM sleep, which are denoted by the blue arrows in Fig. 14.5. Note that this deviation indicates prominent non-linearity. Since these non-linear signatures are observed only in the epileptic channel, we conclude that they reflect the epileptic activity only. Furthermore, we find that non-linearity emerges not in REM sleep but in the central part of non-REM sleep, where the DC-value reaches its minimum. Therefore, we suggest that sleep processes can promote epileptic activity.

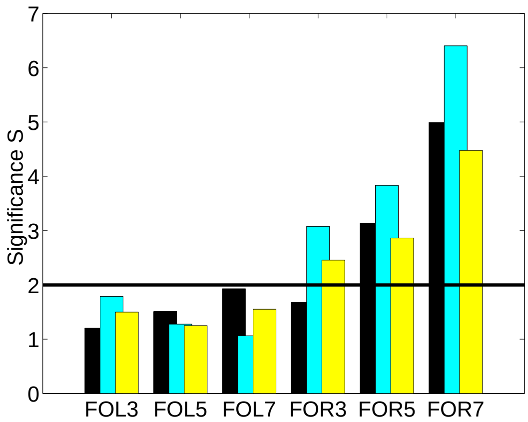

Figure 14.6: *The degree of nonlinearity for intracranial EEG recordings from a patient with temporal lobe epilepsy. Six bipolar derivations are shown: three from the left and three from the right. The different bars correspond to different recording conditions: sleep (black and turquoise) and awake (yellow). The horizontal line denotes the threshold alue $S = 2$ (for details see text).*

Now we turn our attention to the spatial distribution of non-linearity in the brain of patients suffering from epilepsy. The significance of surrogate data test S was used for quantifying non-linearity. Three intracranial recordings of one patient were analysed. For each recording we chose 6 artifact-free channels, three of them from the epileptic hemisphere (FOR3, FOR5 and FOR7) and the other three from the healthy hemisphere (FOL3, FOL5 and FOL7). The mean value of the S for each of these channels is displayed in Fig. 14.6. Firstly, we see that prominent non-linearity, i.e. the S-value larger than the threshold value two, occurs only in the channels from the epileptic hemisphere. Secondly, the S-values decrease gradually from FOR7 to FOR3 within the epileptic hemisphere. Since it is known that for this patient the epileptic focus is nearest to channel FOR7, we conclude that the degree of non-linearity in an EEG channel decreases with the increasing distance between the epileptic focus and the electrode from which this channel was derived. In summary, the degree of non-linearity we have used can describe epileptic activity in the intracranial EEG recording quantitatively.

References

[1] Electric field gradients from first-principles and point-ion calculations
E. P. Stoll, T. A. Claxton, and P. F. Meier
Phys. Rev. B, **65**, 064532-12 (2002)

[2] First-Principles Calculation of Electric Field Gradients and Hyperfine Couplings in $YBa_2Cu_3O_7$
S. Renold, S. Pliberšek, E. P. Stoll, T. A. Claxton, and P. F. Meier
Eur. Phys. J. B, **23**, 3-15 (2001)

15 Mechanical Workshop

B. Schmid, K. Bösiger, M. Schaffner (since 8/01), Y. Steiger (apprentice until 7/01),
P. Treier, B. Wachter, B. Zaugg (retired 11/01 - left us after 27 years),
R. Caro (apprentice, since 8/01) and A. Rochat (apprentice)

Last year the workshop was again fully occupied manufacturing numerous components for the different research projects presented in this report. A small part of the shop activity was also devoted to orders from outside consisting in special designs, modifications and small series. This work is charged and provides some income. More than 30 institutes made use of the metal/technical material supply stores maintained by us[3].

In April 2001 we helped install the new 5 layer cylindrical wire chamber (CIP) in H1. Pictures are shown in Fig.6.2. Below we show a selection of our contributions to the following three projects:

- CMS pixel detector (Sec.10) and LHCb inner tracking detector (Sec.8): different test setups and prototypes were manufactured.

Figure 15.1: *Picures from the CMS pixel project:*
a) support structure
b) service tube prototype
c) test setup for the laser welding of the cooling tubes
d) a welding seam under the microscope
e) different pure aluminum parts which have to be laser welded

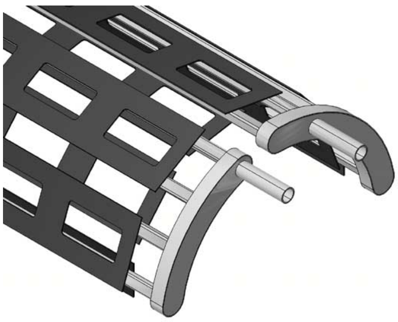
a)


b)

c)


d)
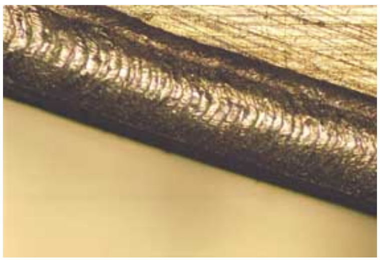

e)


- Surface physics group: For the spin-resolved photoelectron spectrometer COPHEE (see Sec.12.8) an electrostatic beam transport system was manufactured, which guides the electrons from the energy analyzer to the two Mott detectors. The system consists of a set of aluminum electrodes, spherical deflection elements and cylindrical lens parts, separated by macor insulators for use in ultrahigh vacuum. A two-way switch with parallel deflection plates and a symmetric end-deflector allows the beam to be sent to either of the two Mott detectors. The vacuum envelope consists of several welded stainless steel chambers. A special stainless steel chamber encloses the switch and the large entrance optics of the Mott detectors. It was cut from a single 231 kg block of steel (final mass $\approx$ 50 kg).

[3]For a catalogue see http://www.physik.unizh.ch/groups/werkstatt/ dienstleistung.html

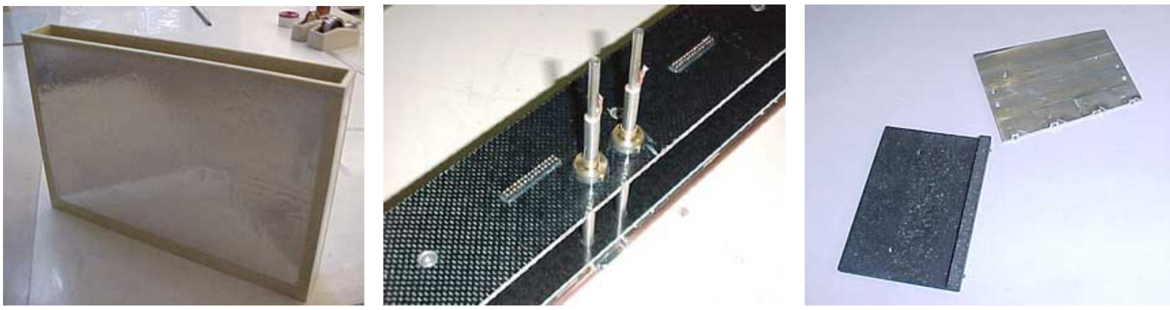

a) b) c)

Figure 15.2: *the LHCb inner tracker:*
a) polyurethane isolating detector box
b) box cover with electrical connectors and cooling tubes
c) cooling parts made of aluminum and foam-impregnated carbon fibre
d) silicon detectors with temperature sensors
e) complete test setup

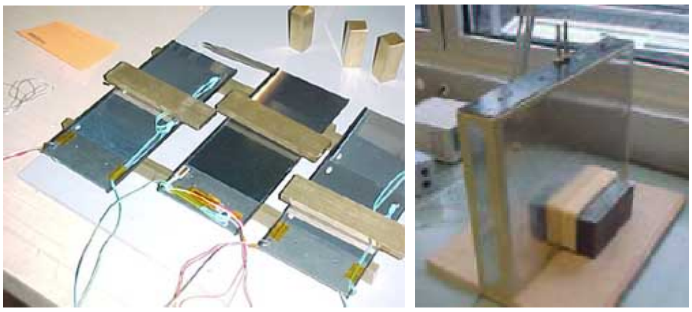

d) e)

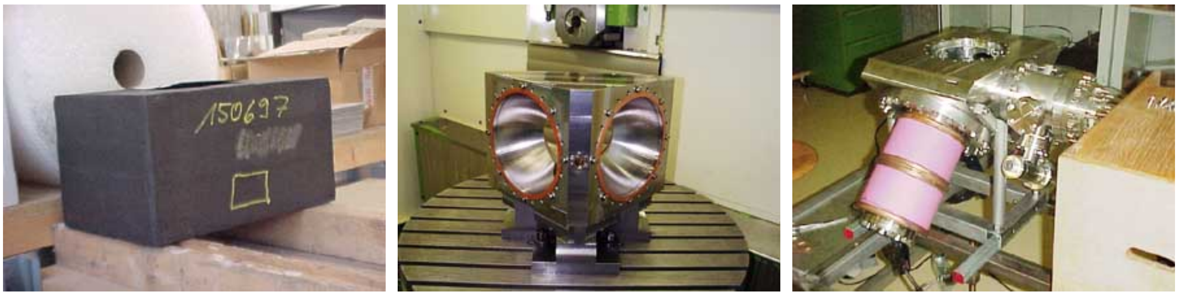

a) b) c)

Figure 15.3: *the COPHEE project.*
a) forged steel block used for the beam chamber (weight 231 kg)
b) resulting chamber (weight 50 kg)
c) beam chamber during assembly
d) view inside the 90 ° deflection part of the beam transport system
e) aluminum electrodes for the beam transport system with 45 ° switch

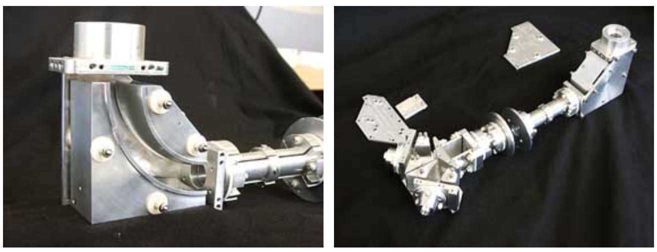

d) e)

- Artificial Intelligence Laboratory, Department of Computer Science (this work was done by the apprentices): The "Whirling Arm" will be used at the Artificial Intelligence Lab as an experimental tool for research on insect vision. It can be looked at as a "flight-simulator for insect eyes": An artificial insect eye (camera or specially constructed compound eye) is mounted on the Whirling Arm and is then subjected to fast and complex movements in space that can (to some degree) mimic the actual situation encountered by the head of a flying insect. One goal of these studies is to better understand how the specific features of insect eyes (e.g., its sensor morphology) relate to the visual input the animal encounters during its flight and how this can facilitate flight control. Since insects - like the housefly - can navigate very fast the Whirling Arm has to be able to produce very fast reactions too. Consequently it was designed for a minimum of inertia for each of its three rotational degrees of freedom while at the same time providing enough motor power for fast accelerations.

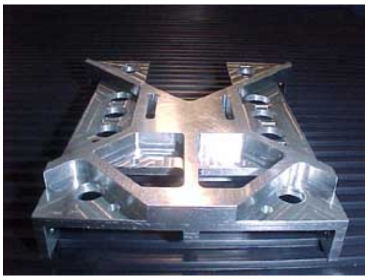

a)

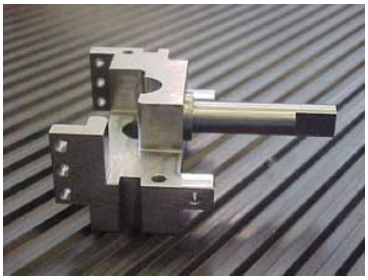

b)

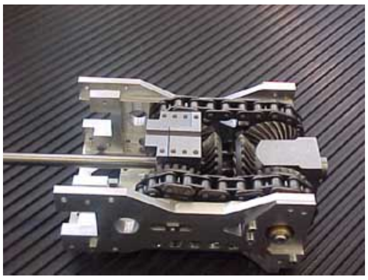

c)

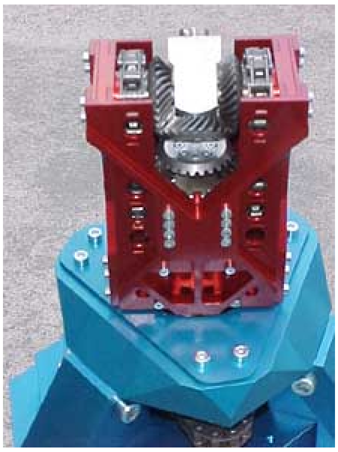

d)

e)

Figure 15.4: *the whirling arm project:*
a) reinforced side piece of the moving part milled out off aluminum
b) another single piece illustrating the complex processing
c) look inside the moving head showing the complicated transmission
d) detail of the assembled moving head
e) the completed "Whirling Arm" with support frame and motors

16 Electronics Workshop

W. Fässler, H.P. Meyer, P. Soland, K. Szeker

The electronics workshop was occupied with repair and service work for various research groups at the institute and at some other institutes of our university. In addition we like to mention the following two major activities:

- NMR spectrometer (Group Keller and Prof. emeritus D. Brinkmann): In collaboration with the National Institute for Research and Development of Isotopic and Molecular Technologies (NRDIIMT, 65-103 Donath St., 3400 Cluj-Napoca, Romania) an NMR spectrometer is developed within the framework of the SNF-scope 2000-2003 program (project Nr. 7 IP 062580). We assist in the design work and construction of the high frequency electronics.

- H1 CIP upgrade project (Group Straumann, Truöl, see Sec.6): we manufactured a test board for the readout chip, several interface cards and a low voltage power supply.

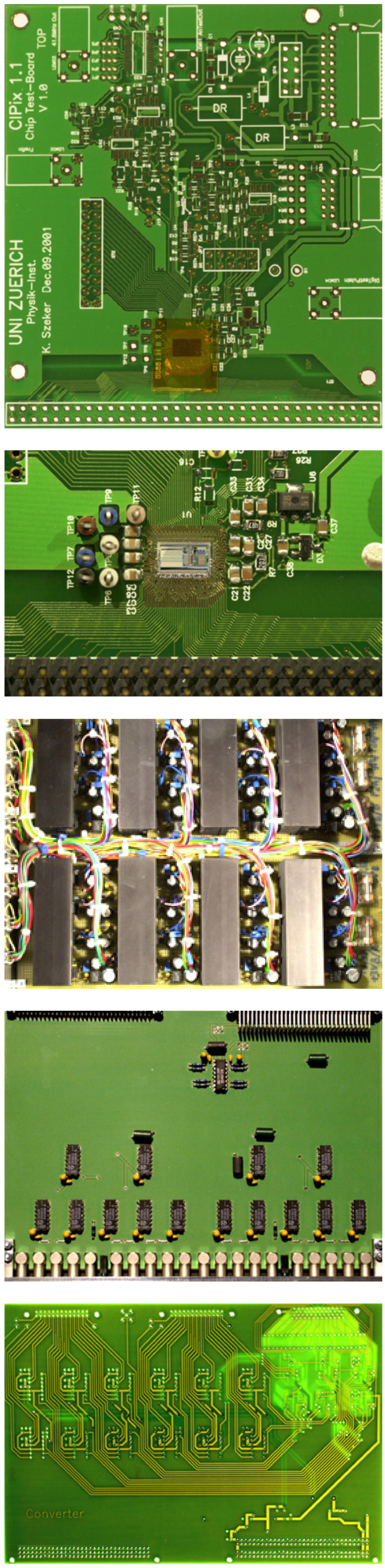

a)
b)
c)
d)
e)

Figure 16.1:
a) testboard for the CIPix readout chip
b) enlarged view of the testboard with the wire bonded CIPix readout chip in the center
c) low voltage power supply
d) STC fanout card
e) SCSI converter card

17 Publications

17.1 Research group of Prof. C. Amsler

Articles

- Study of f_0 decays into four neutral pions
  A. Abele et al. (Crystal Barrel Collaboration)
  Eur. Phys. Journal C 19 (2001) 667
- 4π-decays of scalar and vector mesons
  A. Abele et al. (Crystal Barrel Collaboration)
  Eur. Phys. Journal C 21 (2001) 261
- Branching ratios for $\bar{p}p$ annihilation at rest into two-body final states
  A. Abele et al. (Crystal Barrel Collaboration)
  Nucl. Phys A 679 (2001) 563
- A High Resolution Search for the Tensor Glueball Candidate $\xi(2230)$
  C. Amsler et al. (Crystal Barrel Collaboration)
  Phys. Lett. B 520 (2001) 175
- Proton-antiproton annihilation at 900 MeV/c into $\pi^0\pi^0\pi^0$, $\pi^0\pi^0\eta$ and $\pi^0\eta\eta$
  C. Amsler et al. (Crystal Barrel Collaboration)
  Eur. Phys. J. C 23 (2002) 29
- Design and test of pixel sensors for the CMS experiment
  G. Bolla et al.
  Nucl. Instr. Meth. in Physics Research A 461 (2001) 182
- Lorentz-angle in irradiated silicon
  B. Henrich, R. Kaufmann
  Nucl. Instr. Meth. in Physics Research A 477 (2002) 304
- Antihydrogen Production and Precision Spectroscopy with ATHENA / AD1
  C. Amsler et al. (ATHENA Collaboration)
  "The Hydrogen Atom, Precision Physics of Simple Atomic Systems", ed. S.G. Karshenboim et al., Springer Lecture Notes in Physics, Berlin 2001, p. 469-488
- Proton-antiproton annihilation into $\pi^0\pi^0\pi^0$, $\pi^0\pi^0\eta$ and $\pi^0\eta\eta$ at 900 MeV/c
  C. Amsler
  Proc. of the Int. Workshop XXIX on Gross Properties of Nuclei and Nuclear Excitations, Hirschegg, ed. H. Feldmeier et al., GSI Pub. 2001, p. 18
- The ATHENA Antihydrogen Detector
  C. Amsler
  Proc. Int. Conf. on High Energy Physics, Budapest, Journal of High Energy Physics PRHEP-hep2001 (2001) 174
- New Results in Proton-Antiproton Annihilation and the Status of Glueballs
  C. Amsler
  Proc. Int. Conf. on High Energy Physics, Budapest, Journal of High Energy Physics PRHEP-hep2001 (2001) 270
- Detection of Antihydrogen with a Si-μ-strip and CsI-Crystal Detector at Cryogenic Temperature
  C. Regenfus
  Proc. of the XXXth Int. Conf. on High Energy Physics, Osaka, ed. C.S. Lim and T. Yamanaka, World Scientific (2001) 1225

Articles in press

- A high resolution silicon beam telescope
  C. Amsler et al.
  Nucl. Instr. Meth. in Physics Research A 480 (2002) 499
- Temperature dependence of pure CsI: scintillation light yield and decay time
  C. Amsler et al.
  Nucl. Instr. Meth. in Physics Research A 480 (2002) 492
- Meson Resonances in Proton-Antiproton Annihilation
  C. Amsler
  Proc. Int. Conf. on the Structure and Interactions of the Photon (PHOTON 2001), Ascona, World Scientific, 2001
- Comment on "Protonium annihilation into $\pi^0\pi^0$ at rest in a liquid hydrogen target"
  C. Amsler et al. (Crystal Barrel Collaboration)
  Phys. Rev. D (2002)
- Sub MeV Particle Detection and Identification in the MUNU Detector
  M. Avenier et al.
  Nucl. Instr. Meth. in Physics Research A (2002)
- Non-$q\bar{q}$ mesons
  C. Amsler
  Eur. Phys. Journal (2002)
- The $\eta(1440)$, $f_1(1420)$, and $f_1(1510)$
  M. Aguilar/Benitez, C. Amsler and A. Masoni
  Eur. Phys. Journal (2002)
- Producing Slow Antihydrogen for a Test of CPT Symmetry with ATHENA
  M.C. Fujiwara et al. (ATHENA Collaboration)
  Preprint nucl-ex/0202020
  Journal of Hyperfine Interactions (2002)
- Design, construction and performance of the cryogenic antihydrogen detector for ATHENA
  C. Regenfus
  Proc. 10th Int. Workshop on vertex detectors (VERTEX 2001), Brunnen, Switzerland, 2001

Diploma and PhD theses

- Development of Radiation Hard Pixel Sensors for the CMS Experiment
  R. Kaufmann
  Dissertation, Universität Zürich, 2001
- Temperature Dependence of Pure CsI between 77 K and 165 K and the Performance of Wavelength Shifters
  D. Grögler
  Diplomarbeit, Universität Zürich, 2001

Invited Lectures

- C. Amsler
  Contributed talk, Int. Conf. on High Energy Physics, Budapest, 13.7.01
  "The ATHENA Antihydrogen Detector"

- C. Amsler
  Contributed talk, Int. Conf. on High Energy Physics, Budapest, 13.7.01
  "New Results in Proton-Antiproton Annihilation and the Status of Glueballs"
- C. Amsler
  Invited talk, Int. Conf. on the Structure and Interactions of the Photon (PHOTON 2001), Ascona, 6.9.01
  "Meson resonances in $\bar{p}p$ annihilation"
- N. Madsen
  Contributed talk, 3rd Euroconf. on Atomic Physics at Accelerators (APAC01), Aarhus, 10.9.01
  "Vertical blow up in a low current, stored, laser-cooled ion beam"
- C. Regenfus
  10th Int. Workshop on vertex detectors (VERTEX 2001), Brunnen, 24.9.01
  "Design, construction and performance of the cryogenic antihydrogen detector for ATHENA"
- C. Regenfus
  Seminar, ETHZ, 20.11.01
  "Detection of antihydrogen in the ATHENA experiment with a cold Si-microstrip and a pure CsI detector"

ATHENA Collaboration (2002):
M. Amoretti, C. Amsler, G. Bendiscioli, G. Bonomi, A. Bouchta, P. Bowe, C. Carraro, M. Charlton, M. Collier, M. Doser, V. Filippini, A. Fontana, M.C. Fujiwara, R. Funakoshi, P. Genova, A. Glauser, J. Hangst, R.S. Hayano, H. Higaki, M.H. Holzscheiter, O. Iannarelli, L. Jorgensen, D. Kleppner, V. Lagomarsino, R. Landua, C. Lenz Cesar, D. Lindelf, E. Lodi-Rizzini, M. Macri, N. Madsen, G. Manuzio, M. Marchesotti, P. Montagna, H. Pruys, C. Regenfus, P. Riedler, A. Rotondi, G. Rouleau, P. Salvini, G. Testera, D.P. van der Werf, A. Variola, T. Watson, T. Yamazaki, Y. Yamazaki

CRYSTAL BARREL Collaboration (2001):
C. Amsler, C.A. Baker, B.M. Barnett, C.J. Batty, M. Benayoun, A. Berdoz, P. Blüm, K. Braune, T. Case, K.M. Crowe, M. Doser, W. Dünnweber, D. Engelhardt, M.A. Faessler, P. Giarritta, R.P. Haddock, F.H. Heinsius, M. Heinzelmann, N.P. Hessey, P. Hidas, D. Jamnik, H. Kalinowsk, B. Kämmle, P. Kammel, J. Kisiel, E. Klempt, H. Koch, M. Kunze, U. Kurilla, M. Lakata, R. Landua, H. Matthäy, C.A. Meyer, F. Meyer-Wildhagen, L. Montanet, R. Ouared, K. Peters, B. Pick, M. Ratajczak, C. Regenfus, W. Roethel, U. Strohbusch, M. Suffert, J.S. Suh, U. Thoma, I. Uman, S. Wallis-Plachner, D. Walther, U. Wiedner, K. Wittmack, Č. Zupančič.

17.2 Research group of Prof. H. Keller

Articles

- The phase diagram of high-T_c superconductors in the presence of dynamic stripes
  A. Bussmann-Holder, A.R. Bishop, H. Büttner, T. Egami, R. Micnas, and K.A. Müller
  J. Phys.: Condens. Matter **13**, L545-L551 (2001)
- Isotope effects in underdoped cuprate superconductors: A quantum critical phenomenon
  T. Schneider and H. Keller
  Phys. Rev. Lett. **86**, 4899-4902 (2001)

- An unusual phase transition to a second liquid vortex phase in the superconductor $YBa_2Cu_3O_{7-\delta}$
  F. Bouquet, C. Marcenat, E. Steep, R. Calemczuk, W.K. Kwok, U. Welp, G.W. Crabtree, R.A. Fisher, N.E. Phillips, and A. Schilling
  Nature **411**, 448-451 (2001)
- Influence of Sr substitution on the structure, charge distribution and critical temperature of $Y(Ba_{1-x}Sr_x)_2Cu_4O_8$ single crystals
  J. Karpinski, S. Kazakov, M. Angst, A. Miranov, M. Mali, and J. Roos
  Phys. Rev. B **64**, 094518-1-12 (2001)
- Tilting mode relaxation in the electron paramagnetic resonance of isotope substituted $La_{2-x}Sr_xCuO_4$: Mn^{2+}
  A. Shengelaya, H. Keller, K.A. Müller, B.I. Kochelaev, and K. Conder
  Phys. Rev. B **63**, 144513-1-9 (2001)
- Magnetic properties of $RuSr_2RECu_2O_8$ (RE = Gd, Eu) and $Ru_{1-x}Sr_2GdCu_{2+x}O_{8-y}$ superconductors
  P.W. Klamut, B. Dabrowski, S.M. Mini, M. Maxwell, S. Kolesnik, J. Mais, A. Shengelaya, R. Khasanov, I. Savic, H. Keller, T. Graber, J. Gebhardt, P.J. Viccaro, and Y. Xiao
  Physica C **364-365**, 313-319 (2001)
- Bulk experimental evidence of half-metallic ferromagnetism in doped manganites
  Guo-meng Zhao, H. Keller, W. Prellier, and D.J. Kang
  Phys. Rev. B **63**, 172411-1-4 (2001)
- Isotope effects and possible pairing mechanism in optimally doped cuprate superconductors
  Guo-meng Zhao, V. Kirtikar, and D.E. Morris
  Phys. Rev. B (Rapid Communications) **63**, 220506-1-4 (2001)
- Evidence for novel polaronic Fermi-liquid in doped manganites
  A.S. Alexandrov, Guo-meng Zhao, H. Keller, B. Lorenz, Y.S. Wang, and C.W. Chu
  Phys. Rev. B (Rapid Communications) **64**, 140404-1-7 (2001)
- Identification of the bulk pairing symmetry in high-temperature superconductors: Evidence for an extended s wave with eight line nodes
  Guo-meng Zhao
  Phys. Rev. B **64**, 024503-1-10 (2001)
- Unconventional isotope effects in the high-temperature cuprate superconductors
  Guo-meng Zhao, H. Keller, and K. Conder
  J. Physics: Condens. Matter **13**, R569 - R587 (2001)
- The attainable superconducting T_c in a model of phase coherence by percolating
  D. Mihailovic, V.V. Kabanov, and K.A. Müller
  Europhys. Lett. **57**, 254-259 (2002)
- Vortex-lattice melting in untwinned $YBa_2Cu_3O_{7-\delta}$ for $H \perp c$
  A. Schilling, U. Welp, W.K. Kwok, and G.W. Crabtree
  Phys. Rev. B **65** 054505-1-7 (2002)
- ^{25}Mg NMR study of the MgB_2 superconductor
  M. Mali, J. Roos, A. Shengelaya, and H. Keller
  Phys. Rev. B (Rapid Communications) **65**, 100518-1-4 (2002)

Articles in press

- On the macroscopic *s*- and *d*-wave symmetry in cuprate superconductors
  K.A. Müller
  Philosophical Magazine
- High-temperature superconductors: Results and relations
  K.A. Müller
  Applied Physics A
- Implantation studies of keV positive muons in thin metallic films
  E. Morenzoni, H. Glöckler, T. Prokscha, R. Khasanov, H. Luetkens, M. Birke, E.M. Forgan, Ch. Niedermayer, and M. Pleines
  Nuclear Instruments and Methods B
- Oxygen isotope effect of the plane-copper NQR frequency in $YBa_2Cu_4O_8$
  M. Mali, J. Roos, H. Keller, J. Karpinski, and K. Conder
  Phys. Rev. B
- EPR of rare-earth-ions in the underdoped YBaCuO-compound
  V.A. Ivanshin, M.R. Gafurov, I.N. Kurkin, M.P. Rodionova, and H. Keller
  The Physics of Metals and Metallography
- Temperature and field dependence of the anisotropy of MgB_2
  M. Angst, R. Puzniak, A. Wisniewski, J. Jun, S.M. Kazakov, J. Karpinski, J. Roos, and H. Keller
  Phys. Rev. Lett.

Diploma and PhD theses

- Aufbau eines Differential-Thermoanalyse Kalorimeters für tiefe Temperaturen
  Peter Morf
  Diplomarbeit, Physik-Institut, Universität Zürich, 2001
- Reare-earth ion size dependencies of oxygen isotope effects on the charge ordering and superconducting transition temperatures in single-layer cuprates
  Roland Renggli
  Diploma thesis, Physik-Institut, Universität Zürich, 2001
- Search for Lutetium NQR in $Y_{1-x}Lu_xBa_2Cu_4O_8$ compounds
  Philipp Schneider
  Diploma thesis, Physik-Institut, Universität Zürich, 2001

Conference reports

- EPR studies in $La_{1-x}Sr_xMnO_3$. Experiment and theory
  V.A. Ivanshin, M.V. Eremin, R.M. Eremina, H.-A. Krug von Nidda, T. Kurz, A. Loidl, and H. Keller
  Specialized Colloque Ampere "ESR and Solid State NMR in High Magnetic Fields", Stuttgart, Germany, July 22-26, 2001
- Oxygen-isotope effect on the in-plane penetration depth in underdoped $Y_{1-x}Pr_xBa_2Cu_3O_{7-\delta}$ as revealed by muon-spin rotation
  R. Khasanov, A. Shengelaya, E. Morenzoni, I.M. Savic, K. Conder, and H. Keller
  2001 Swiss Workshop on Materials with Novel Electronic Properties, Les Diablerets, Switzerland, October 1-3, 2001

- Oxygen isotope ($^{16}O/^{18}O$) effect on stripe formation and structural phase transitions in LaSrCuO compounds
  M. Mali, R. Renggli, J. Roos, A. Schilling, Guo-meng Zhao, K. Conder, and H. Keller
  2001 Swiss Workshop on Materials with Novel Electronic Properties, Les Diablerets, Switzerland, October 1-3, 2001
- Oxygen isotope ($^{16}O/^{18}O$) effect of the spin-pseudogap in $YBa_2Cu_4O_8$
  M. Mali, J. Roos, H. Keller, K. Conder, and J. Karpinski
  2001 Swiss Workshop on Materials with Novel Electronic Properties, Les Diablerets, Switzerland, October 1-3, 2001
- Oxygen isotope effect of the plane-copper NQR frequency in $YBa_2Cu_4O_8$
  M. Mali, J. Roos, H. Keller, J. Karpinski, and K. Conder
  Annual meeeting of the Swiss Physical Society, Lausanne, Switzerland, February 28-March 3, 2002
- Microtorque magnetometry on $YBa_2Cu_4O_8$
  S. Kohout, J. Roos, H. Keller, and J. Karpinski
  Annual meeeting of the Swiss Physical Society, Lausanne, Switzerland, February 28-March 3, 2002

Invited Lectures

- H. Keller
  Probing high-temperature superconductivity with muons
  Meson Science Laboratory, Institute of Material Structure Science, High Energy Accelerator Research Organization (KEK)
  Tsukuba, Ibaraki, Japan, September 11, 2001
- H. Keller
  Unconventional isotope effects in high-temperature cuprate superconductors and magnetoresistive doped manganites
  Department of Applied Physics, University of Tokyo, Japan, September 14, 2001
- H. Keller
  Probing high-temperature superconductivity with muons
  Department of Advanced Materials Sciences, University of Tokyo, Japan, September 21, 2001
- H. Keller
  Unconventional isotope effects in high-temperature cuprate superconductors
  The Institute of Physical and Chemical Research (RIKEN), Wako, Saitama, Japan, September 22, 2001
- H. Keller
  Unconventional isotope effects in high-temperature cuprate superconductors
  Department of Physics, Graduate School of Science, Kyoto University, Japan, September 25, 2001
- H. Keller
  Investigation of microscopic magnetic properties of high-temperature superconductors and magnetic systems with positive muons
  The 8th Workshop on Oxide Electronics
  Osaka University, Japan, September 27 - 28, 2001

- H. Keller
  Unconventional isotope effects in high-temperature cuprate superconductors
  Department of Physics, Faculty of Science, Kochi University, Japan, October 5, 2001
- H. Keller
  Unconventional isotope effects in high-temperature cuprate superconductors
  Department of Physics, Faculty of Engineering, Tokushima University, Japan, October 12, 2001
- H. Keller
  Unconventional isotope effects in high-temperature cuprate superconductors and magnetoresistive doped manganites
  10 Lectures as guest professor
  Department of Physics, Faculty of Engineering, Tokushima University, Japan, October 1 -12, 2001
- H. Keller
  Investigation of microscopic magnetic properties of high-temperature superconductors and magnetic systems with positive muons
  MRS 2001 Fall Meeting Boston
  Boston, USA, November 26 - 30, 2001
- A. Schilling
  Specific heat of $YBa_2Cu_3O_7$ near $H//ab$ and in low magnetic fields
  Critical Properties of Vortex Matter
  Loen, Norway, June 21 - 24, 2001

17.3 Research group of Prof. P. F. Meier

Articles

- Analysis of NMR data on cuprate superconductors based on calculated hyperfine coupling energies
  P. F. Meier
  Physica C 364-365 (2001) 411

- First-Principles Calculation of Electric Field Gradients and Hyperfine Couplings in $YBa_2Cu_3O_7$
  S. Renold, S. Pliberšek, E. P. Stoll, T. A. Claxton, and P. F. Meier
  Eur. Phys. J. B 23 (2001) 3

- Electric field gradients from first-principles and point-ion calculations
  E. P. Stoll, T. A. Claxton, and P. F. Meier
  Phys. Rev. B 65 (2002) 064532

- Parallel random number generator for inexpensive configurable hardware cells
  J. Ackermann, U. Tangen, B. Bödekker, J. Breyer, E. Stoll, and J. S. McCaskill
  Computer Physics Communications 140 (2001) 293

- An efficient algorithm to determine fractal dimensions of point sets
  R. M. Füchslin, Y. Shen, P. F. Meier
  Phys. Lett. A 285 (2001) 69

Diploma and PhD theses

- First-principles investigations of electronic, magnetic and structural properties of high-temperature superconductors
  S. Pliberšek
  PhD-thesis, University of Zurich (2001)

17.4 Research group of Prof. J. Osterwalder

Articles

- Surface states on clean and adsorbate-covered metal surfaces
  J. Osterwalder, T. Greber, J. Kröger, J. Wider, H.-J. Neff, F. Baumberger
  M. Hoesch, W. Auwärter, R. Fasel, P. Aebi
  in *Physics of Low Dimensional Systems*, J. L. Morán-López, ed.
  (Kluwer Academic / Plenum Publishers, 2001), p.245-255
- Influence of an atomic grating on a magnetic Fermi surface
  T. Greber, W. Auwärter, J. Osterwalder
  in *Physics of Low Dimensional Systems*, J. L. Morán-López, ed.
  (Kluwer Academic / Plenum Publishers, 2001), p.411-417
- Electronic and atomic structure of the Cu/Si(111) 'quasi-5x5' overlayer
  M. De Santis, M. Muntwiler, J. Osterwalder, G. Rossi, F. Sirotti, A. Stuck,
  L. Schlapbach
  Surf. Sci. 477 (2001) 179-190
- Coexisting inequivalent orientations of C_{60} on Ag(001)
  C. Cepek, R. Fasel, M. Sancrotti, T. Greber, J. Osterwalder
  Phys. Rev. B 63 (2001) 125406-1-5
- Correlation effects and magnetism in 3d transition metals
  J. Osterwalder
  J. Electron Spectrosc. Relat. Phenom. 117-118 (2001) 71-88
- Temperature-dependent Fermi gap opening in the c(6x2)-C_{60}/Ag(001) two-dimensional superstructure
  C. Cepek, I. Vobornik, A. Goldoni, E. Magnano, G. Selvaggi, J. Kröger, G. Panaccione,
  G. Rossi, M. Sancrotti
  Phys. Rev. Lett. 86 (2001) 3001-3004
- Probing the electronic states of band ferromagnets with photoemission
  T. Greber
  in *Band Ferromagnetism - Ground-State and Finite-Temperature Phenomena*, K. Baberschke, M. Donath, W. Nolting, eds.
  Springer Lecture Notes in Physics 580 (2001), p. 94-110
- Fermi surfaces of the two-dimensional surface states on vicinal Cu(111)
  F. Baumberger, T. Greber, J. Osterwalder
  Phys. Rev. B 64 (2001) 195411-1-8
- Orientation of chiral heptahelicene $C_{30}H_{18}$ on copper surfaces: an x-ray photoelectron diffraction study
  R. Fasel, A. Cossy, K.-H. Ernst, F. Baumberger, T. Greber, J. Osterwalder
  J. Chem. Phys. 115 (2001) 1020-1027

- Design of a miniature picosecond low-energy electron gun for time-resolved scattering experiments
  R. Karrer, H. Neff, M. Hengsberger, T. Greber, J. Osterwalder
  Rev. Sci. Instrum. 72 (2001) 4404-4407
- Exploiting the photoelectron source wave with near-node photoelectron holography
  T. Greber
  J. Phys.: Condens. Matter 13 (2001) 10561-10576
- Räumliche Bilder von Atomen
  J. Wider, T. Greber
  Neue Zürcher Zeitung, Nr. 112 (2001) 75
- Imaging atom sites with near-node photoelectron holography
  T. Greber, J. Wider, A. Verdini, A. Morgante, J. Osterwalder
  Euro Phys. News 32 (2001) 172-175
- High-resolution photoemission study of the discommensurate (5.55x5.55) Cu/Si(111) surface layer
  H.-J. Neff, I. Matsuda, M. Hengsberger, F. Baumberger, T. Greber, J. Osterwalder
  Phys. Rev. B 64 (2001) 235415-1-9
- Binding and ordering of C_{60} on Pd(110): investigations at the local and mesoscopic scale
  J. Weckesser, C. Cepek, R. Fasel, J. V. Barth, F. Baumberger, T. Greber, K. Kern
  J. Chem. Phys. 115 (2001) 9001-9009

Articles in press

- The Fermi surface in a magnetic metal-insulator interface
  T. Greber, W. Auwärter, M. Hoesch, G. Grad, P. Blaha, J. Osterwalder
  Surf. Rev. Lett. (2002)
- Reduction of the magnetic moment at the h-BN/Ni(111) interface
  T. Greber, W. Auwärter, G. Grad, P. Blaha, J. Osterwalder
  Proceedings of the *Conference on Atomic Level Characterization (ALC'01)*, Nara, Japan (2002)
- Spin-polarized Fermi surface mapping
  M. Hoesch, T. Greber, V. N. Petrov, M. Muntwiler, M. Hengsberger, W. Auwärter, J. Osterwalder
  J. Electron Spectrosc. Relat. Phenom. (2002)
- Co on h-BN/Ni(111): from island to island-chain formation and Co intercalation
  W. Auwärter, M. Muntwiler, T. Greber, J. Osterwalder
  Surf. Sci. (2002)

Diploma and PhD Theses

- Applications and Developments in x-ray photoelectron diffraction: oxygen on rhodium and near-node photoelectron holography experiments
  Joachim Wider
  Ph. D. Thesis, Physik-Institut, Universität Zürich, 2001
- Electronic and structural aspects of metal on semiconductor surfaces and development of a time-resolved surface-structure probe
  Hansjörg Neff
  Ph. D. Thesis, Physik-Institut, Universität Zürich, 2001

Contributed conference presentations

- Surface state bands on vicinal Cu
  F. Baumberger, M. Hengsberger (Poster)
  Workshop on *Two-dimensional conductivity in surface states and monolayers*, Bad Honnef, Germany, 5.3.01
- L-gap surface states on vicinal Cu(111)
  T. Greber
  American Physical Society March Meeting, Seattle,USA, 15.3.01
- Atomically resolved three-dimensional images from surfaces
  J. Wider
  American Physical Society March Meeting, Seattle,USA, 15.3.01
- Electronic structure study of the Si(111) (5.55x5.55)-Cu surface by the Fermi surface mapping method
  I. Matsuda
  Japanese Physical Society Meeting, Tokyo, Japan, 27.3.01
- Design and testing of a picosecond low-energy electron gun
  R. Karrer
  SPG Jahrestagung, EMPA Dübendorf, 3.5.01
- Characterizing interfaces within nanostructures
  T. Greber
  SPG Jahrestagung, EMPA Dübendorf, 3.5.01
- Co on $h-BN/Ni(111)$: from island to island-chain formation and Co intercalation
  W. Auwärter (Poster)
  Scanning Tunneling Microscopy Conference (STM'01), Vancouver, Canada, 16.7.01
- Design of a complete photoemission experiment
  M. Hoesch, M. Muntwiler, M. Hengsberger, T. Greber, J. Osterwalder (Poster)
  8th International Conference on *Vacuum Ultraviolet Radiation Physics* (VUV-XIII), Trieste, Italy, 24.7.01
- Electronic structure of the Si(001) (5x3.2)-Au surface
  I. Matsuda
  8th International Conference on *Vacuum Ultraviolet Radiation Physics* (VUV-XIII), Trieste, Italy, 25.7.01

Invited Lectures

- T. Greber
  Probing the dissociation of O_2 and N_2O on alkali metal surfaces with exoemission
  Physical Chemistry Seminar, UCSD, San Diego, USA, 20.3.01
- T. Greber
  Über die Benutzung von Photoelektronenwellen: von Vorwärtsstreuung bis zu Holographie mit atomarer Auflösung
  Seminar am Institut für Experimentalphysik, TU Wien, 8.5.01
- T. Greber
  Angle-scanned photoemission: from x-ray photoelectron diffraction (XPD) to near-node photoelectron holography and Fermi surface mapping
  Seminar am MPI Stuttgart, 9.5.01

- M. Hoesch
  COPHEE, the complete photoemission experiment
  Journée photoémission de spin, LURE, Orsay, France, 18.5.01
- T. Greber
  Untersuchung der magnetischen Tunnelbarriere $h{-}BN/Ni(111)$ mittels winkelaufgelöster Photoemission
  Seminar im SFB *Grenzflächenbestimmte Materialien*, Universität des Saarlandes, Saarbrücken, 29.5.01
- J. Wider
  Anwendungen und Entwicklungen in der Photoelektronenbeugung
  Festkörperphysik-Seminar, ETH Zürich, 3.7.01
- F. Baumberger
  Surface electronic structure of vicinal Cu(111): step-induced one-dimensional states and step-modified two-dimensional states
  Workshop on Stepped Surfaces, Universität Erlangen-Nürnberg, 25.7.01
- T. Greber
  k-resolved one- and two-photon photoemission around the Fermi level
  8th International Conference on *Vacuum Ultraviolet Radiation Physics* (VUV-XIII), Trieste, Italy, 26.7.01
- I. Matsuda
  Electronic structure of the nano-structures (monolayer, quantum film, quantum wire) formed by noble metals on Si surfaces
  Seminar am Institut de Physique, Université de Fribourg, 21.8.01
- J. Osterwalder
  Interface and manybody effects in the electronic structure of Ni and Co: photoemission results
  Seminar am MPI für Mikrostrukturforschung, Halle, Germany, 23.10.01
- M. Hoesch
  Spin-polarized Fermi surface mapping
  Experimental Science Discussion (XSD), SLS, PSI, 24.10.01
- T. Greber
  Untersuchung mikroskopischer Prozesse mit Elektronen
  Physik-Kolloquium, TU München, 25.10.01
- T. Greber
  Exploring the Fermi surface of a magnetic metal-insulator interface with angle-resolved photoemission
  Physics Seminar, Tokyo University,Japan, 6.11.01
- T. Greber
  Metal adsorption and intercalation on $h - BN/Ni(111)$
  Physics Seminar, Waseda University, Tokyo, Japan, 8.11.01
- T. Greber
  Investigations on a ferromagnetic, atomically sharp interface: $h - BN$ on Ni(111)
  International Conference on *Atomic Level Characterization*, Nara, Japan, 12.11.01
- T. Greber
  L'exploration de la durée des processus microscopiques et - und was können wir darüber mit Elektronen lernen
  Physik-Kolloquium, Université de Fribourg, 26.11.01

- T. Greber
  Untersuchungen der Elektronenbewegung an einer spintronischen Grenzfläche
  Physik-Kolloquium, Universität Kiel, 8.1.02
- T. Greber
  From 2π x-ray photoelectron diffraction to near-node photoelectron holography
  Journée des surfaces et interfaces, Toulouse, France, 1.2.02

17.5 Research group of Prof. U. Straumann (for H1 publications see group of Prof. P. Truöl, Sec. 17.6)

Articles

- A triple GEM detector with two-dimensional readout
  M. Ziegler, P. Sievers, U. Straumann
  NIM **A** 471 (2001) 260-263
- Study of CP-Violating Asymmetries in $B^0 \longrightarrow \pi^+\pi^-, K^+\pi^-$ Decays.
  B. Aubert et al., Phys. Rev. D 65 (2002) 051502
- Direct CP Violation Searches in Charmless Hadronic B Meson Decays.
  B. Aubert et al., Phys. Rev. D 65 (2002) 051101
- Measurement of the Branching Fractions for $\psi(2S) \longrightarrow e^+e^-$ and $\psi(2S) \longrightarrow \mu^+\mu^-$.
  B. Aubert et al., Phys. Rev. D 65 (2002) 031101
- Measurement of Branching Fractions for Exclusive B Decays to Charmonium Final States.
  B. Aubert et al., Phys. Rev. D 65 (2002) 032001
- Search for the Decay $B^0 \longrightarrow \gamma\gamma$.
  B. Aubert et al., Phys. Rev. Lett. 87 (2001) 241803
- Measurement of the $B \longrightarrow J/\psi K^*(892)$ Decay Amplitudes.
  B. Aubert et al., Phys. Rev. Lett. 87 (2001) 241801
- Measurements of the Branching Fractions of Exclusive Charmless B Meson Decays with η' or ω Mesons.
  B. Aubert et al., Phys. Rev. Lett. 87 (2001) 221802
- Measurement of the B^0 and B^+ Meson Lifetimes with Fully Reconstructed Hadronic Final States.
  B. Aubert et al., Phys. Rev. Lett. 87 (2001) 201803
- Measurement of J/ψ Production in Continuum e^+e^- Annihilations near $\sqrt{s} = 10.6$ GeV.
  B. Aubert et al., Phys. Rev. Lett. 87 (2001) 162002
- Measurement of Branching Fractions and Search for CP-Violating Charge Asymmetries in Charmless Two-Body B Decays into Pions and Kaons.
  B. Aubert et al., Phys. Rev. Lett. 87 (2001) 151802
- Measurement of the Decays $B \longrightarrow \pi K$ and $B \longrightarrow \pi K^*$.
  B. Aubert et al., Phys. Rev. Lett. 87 (2001) 151801
- Observation of CP Violation in the B^0 Meson System.
  B. Aubert et al., Phys. Rev. Lett. 87 (2001) 091801
- Measurement of CP-Violating Asymmetries in B^0 Decays to CP Eigenstates.
  B. Aubert et al., Phys. Rev. Lett. 86 (2001) 2515
- Search for R-parity violating supersymmetry in dimuon and four-jets channel
  V. M. Abazov *et al.*, hep-ex/0111053

- Search for leptoquark pairs decaying to nu nu + jets in p anti-p collisions at s**(1/2) = 1.8-TeV,
  V. M. Abazov *et al.*, hep-ex/0111047
- The inclusive jet cross-section in p anti-p collisions at s**(1/2) = 1.8-TeV using the k(T) algorithm
  V. M. Abazov *et al.*, Phys. Lett. B **525** (2002) 211
- Subjet multiplicity of gluon and quark jets reconstructed with the k(T) algorithm in p anti-p collisions
  V. M. Abazov *et al.*, Phys. Rev. D **65** (2002) 052008
- A search for the scalar top quark in p anti-p collisions at s**(1/2) = 1.8-TeV
  V. M. Abazov *et al.*, hep-ex/0108018
- Measurement of the ratio of differential cross sections for W and Z boson production as a function of transverse momentum in p anti-p collisions at s**(1/2) = 1.8-TeV
  V. M. Abazov *et al.*, Phys. Lett. B **517** (2001) 299
- A study of multiple jet production at transverse energy near 20-GeV
  V. M. Abazov *et al.*, hep-ex/0106072
- Search for leptoquark pairs decaying to nu nu + jets in p anti-p collisions at s**(1/2) = 1.8-TeV
  V. M. Abazov *et al.*, hep-ex/0106065.
- Search for single top quark production at D0 using neural networks
  V. M. Abazov *et al.*, Phys. Lett. B **517** (2001) 282
- Search for new physics using QUAERO: A general interface to D0 event data
  V. M. Abazov *et al.*, Phys. Rev. Lett. **87** (2001) 231801
- The inclusive jet cross section in p anti-p collisions at s**(1/2) = 1.8-TeV using the k(T) algorithm
  V. M. Abazov *et al.*, hep-ex/0106032
- The ratio of the isolated photon cross sections at s**(1/2) = 630-GeV and 1800-GeV
  V. M. Abazov *et al.*, Phys. Rev. Lett. **87** (2001) 251805
- Improved D0 W boson mass determination
  V. M. Abazov *et al.*, hep-ex/0106018
- Search for first-generation scalar and vector leptoquarks
  V. M. Abazov *et al.*, Phys. Rev. D **64** (2001) 092004
- Search for heavy particles decaying into electron positron pairs in p anti-p collisions
  V. M. Abazov *et al.*, Phys. Rev. Lett. **87** (2001) 061802, Int. J. Mod. Phys. A **16S1B** (2001) 866
- Direct search for charged Higgs bosons in decays of top quarks
  V. M. Abazov *et al.*, hep-ex/0102039
- A quasi-model-independent search for new high p(T) physics at D0
  B. Abbott *et al.*, Phys. Rev. Lett. **86** (2001) 3712

Articles in press

- Compact Frontend-Electronics and Bidirectional 3.3 Gbps Optical Datalink for Fast Proportional Chamber Readout
  S. Lüders, R. Baldinger, D. Baumeister, K. Bösiger, R. Eichler, M. Feuerstack-Raible, C. Grab, S. Löchner, B. Meier, B.A. Schmid, U. Stange, S. Steiner, U. Straumann, S.

Streuli, K. Szeker, and P. Truöl
hep-ex 0107064
Nuclear Instruments and Methods in Physics Research **A**

LHCb and D0 notes

- Test Beam Results on Inner Tracker Silicon Prototype Sensors
  C.Bauer, T.Glebe, A.Ludwig, V.Pugatch, F.Sanchez, M.Schmelling (MPI für Kernphysik, Heidelberg)
  F.Lehner, P.Sievers, O.Steinkamp, U.Straumann, A.Vollhardt, M.Ziegler (Universität Zürich)
  LHCb public note 2001-135, November 2001
- Investigations of the thermal properties of the LHCb Inner Tracker silicon ladders by infinite element analysis
  Jacek Beloki (Institute for Nuclear Physics, Cracow)
  F.Lehner (Universität Zürich)
  LHCb public note 2001-128, October 2001
- Characterization of Inner Tracker silicon Prototype Sensors Using a 106 Ru-source and a 1083 nm Laser System
  C.Bauer, T.Glebe, V.Pugatch, M.Schmelling, B.Schwingenheuer (MPI für Kernphysik Heidelberg)
  P.Sievers (Universität Zürich)
  LHCb internal note 2001-121, September 2001
- First results from LHCb inner tracker performance studies using new digitization software
  A.Polouektov, O.Steinkamp, U.Straumann
  LHCb internal note 2001-118, September 2001
- Revised z positions for tracking stations
  O.Steinkamp
  LHCb internal note 2001-115, September 2001
- Layout of a cross-shaped inner tracker
  O.Steinkamp
  LHCb internal note 2001-114, September 2001
- Description and Characterization of Inner Tracker Silicon Prototype Sensors
  F.Lehner, P.Sievers, O.Steinkamp, U.Straumann, M.Ziegler (Universität Zürich)
  V.Pugatch (MPI für Kernphysik Heidelberg)
  LHCb public note 2001-036, April 2001
- First irradiation of Inner Tracker Prototype Sensors
  V.Pugatch, F.Sanchez, M.Schmelling (MPI für Kernphysik)
  P.Sievers, O.Steinkamp (Universität Zürich)
  LHCb internal note 2001-035, March 2001
- The construction and performance of the 6-chip silicon ladders for the DZERO silicon main tracker
  F. Lehner
  D0-note-003846, March 2001
- Leakage currents and noise expectations for Run2b
  F. Lehner
  D0-note-003844, March 2001

Conference reports

- Quality Assurance for the D0 silicon detector
  Frank Lehner
  1^{st} Workshop on Quality Assurance Issues in Silicon Detectors
  May 17-18, 2001, CERN, Geneva, Switzerland
- The LHcb Silicon Inner Tracker
  P. Sievers
  5th International Conference on Large Scale Applications and Radiation Hardness of Semiconductor Detectors
  Firenze, July 04-06, 2001.
  LHCb public note 2001-108, submitted to Nucl. Intr. and Meth. Research, A
- The D0 silicon microstrip tracker
  Frank Lehner
  10th International Workshop on Vertex Detectors 'Vertex 2001'
  September 23-28, Brunnen, Switzerland
- CDF/D0 Run2b upgrade silicon projects
  Frank Lehner
  10th International Workshop on Vertex Detectors 'Vertex 2001'
  September 23-28, Brunnen, Switzerland
- The LHCb Silicon Inner Tracker
  U. Straumann
  10th International Workshop on Vertex Detectors 'Vertex 2001'
  September 23-28, Brunnen, Switzerland,

Invited Lectures

- Status of the LHCb experiment
  U. Straumann
  9th International Symposium on Heavy Flavor Physics
  Sept. 10-13, 2001, Caltech, Pasadena, Ca.
  Proceedings in press.
- St. Schlamminger
  The Zürich Big G Experiment from the Comparators Point of View,
  METAS (Swiss Federal Office of Metrology and Accreditation), December 4, 2001.
- St. Schlamminger
  Determination of the Gravitational Constant
  Open User Meeting, Paul Scherrer Institut (PSI), Villigen, January 8, 2002.
- St. Schlamminger
  Determination of the Gravitational Constant Using a Beam Balance
  Nuclear Physics Laboratory, University of Washington, Seattle, January 29, 2002.
- St. Schlamminger
  Determination of the Gravitational Constant Using a Beam Balance
  University of California, Irvine, January 31, 2002.
- The H1 Experiment at HERA
  U. Straumann
  Frühjahrstagung der Schweiz. Physikalischen Gesellschaft
  Lausanne, 28. Feburar 2002

- The Silicon Inner Tracker for LHCb
  O. Steinkamp
  8th international conference on instrumentation for colliding beam physics
  Novosibirsk, Feb. 28 - Mar. 6, 2002
  LHCb public note 2002-019
  submitted to Elsevier Science to be published in NIM

Diploma and PhD Theses

- Development of a triple GEM detector for the LHCb experiment
  Marcus Ziegler
  Dissertation, Physik-institut, Universität Zürich, Januar 2002

17.6 Research group of Prof. P. Truöl (incl. H1 publications of group Prof. U. Straumann)

Articles

- Di-jet Production in Charged and Neutral Current e^+p Interactions at High Q^2
  H1-Collaboration**, C. Adloff *et al.*
  DESY 00 – 143, hep-ex 0010016
  The European Physical Journal **C19** (2001), 429 - 440
- Measurement and QCD Analysis of Jet Cross Sections in Deep-Inelastic Positron-Proton Collisions at $\sqrt{s}$ of 300 GeV
  H1-Collaboration**, C. Adloff *et al.*
  DESY 00 – 145, hep-ex 0010054
  The European Physical Journal **C19** (2001), 289 - 311
- Diffractive Jet-Production in Deep-Inelastic e^+p Collisions at HERA
  H1-Collaboration**, C. Adloff *et al.*
  DESY 00 – 174, hep-ex 0012051
  The European Physical Journal **C20** (2001), 29 - 49
- Deep-Inelastic Inclusive ep Scattering at Low x and a Determination of α_s
  H1-Collaboration**, C. Adloff *et al.*
  DESY 00 – 181, hep-ex 0012053
  The European Physical Journal **C21** (2001), 33 - 61
- Measurement of Neutral and Charged Current Cross Sections in Electron-proton Collisions at High Q^2 at HERA
  H1-Collaboration**, C. Adloff *et al.*
  DESY 00 – 187, hep-ex 0012052
  The European Physical Journal **C19** (2001), 269 - 288
- A Large Acceptance, High Resolution Detector for Rare K^+-decay Experiments
  E865-Collaboration†, R. Appel *et al.*
  Nuclear Instruments and Methods in Physics Research **A479** (2002), 340 - 406
- Searches at HERA for Squarks in R-Parity Violating Supersymmetry
  H1-Collaboration**, C. Adloff *et al.*
  DESY 01 – 021, hep-ex 0102050
  The European Physical Journal **C20** (2001), 639 - 657

- A New Measurement of K^+_{e4} Decay and the $s-$Wave $\pi\pi$ Scattering Length
E865-Collaboration†, S. Pislak *et al.*
hep-ex 0106071
Physical Review Letters **87** (2001), 221801-1 - 221801-4
- Photoproduction with a Leading Proton at HERA
H1-Collaboration**, C. Adloff *et al.*
DESY 01 – 062, hep-ex 0106070
Nuclear Physics **B619** (2001), 3 - 21
- Three-Jet Production in Deep-Inelastic Scattering at HERA
H1-Collaboration**, C. Adloff *et al.*
DESY 01 – 073, hep-ex 0106078
Physics Letters **B515** (2001), 17 - 29
- First Measurement of the Cross Section for Deeply Virtual Compton Scattering
H1-Collaboration**, C. Adloff *et al.*
DESY 01 – 093, hep-ex 0107005
Physics Letters **B517** (2001), 47 -58
- Measurement of Open Beauty Production at HERA
H1-Collaboration**, C. Adloff *et al.*
Physics Letters **B518** (2001), 331 - 332; erratum to Physics Letters **B467** (1999), 156 - 164
- A Search for Leptoquark Bosons in e^-p Collisions at HERA
H1-Collaboration**, C. Adloff *et al.*
DESY 01 – 094, hep-ex 0107038
Physics Letters **B523** (2001), 234 - 242
- On the Rise of the Proton Structure Function F_2 towards Low x
H1-Collaboration**, C. Adloff *et al.*
DESY 01 – 104, hep-ex 0108035
Physics Letters **B520** (2001), 183 - 190
- Measurement of $D^{*\pm}$-Meson Production and F_2^c in Deep-Inelastic Scattering at HERA
H1-Collaboration**, C. Adloff *et al.*
DESY 01 – 100, hep-ex 0108039
Physics Letters **B528** (2002), 199 -215
- $D^{*\pm}$ Meson Production in Deep-Inelastic Diffractive Interactions at HERA
H1-Collaboration**, C. Adloff *et al.*
DESY 01 – 105, hep-ex 0108047
Physics Letters **B520** (2001), 191 - 203
- Muon Capture by ^{11}B and the Hyperfine Effect
V. Wiaux, R. Prieels, J. Deutsch, J. Govaerts, V. Brudanin, S. Egorov, C. Petitjean and P. Truöl
Physical Review **C65** (2002), 025503-1 - 025503-8
- Search for Excited Neutrinos at HERA
H1-Collaboration**, C. Adloff *et al.*
DESY 01 – 145, hep-ex 0110037
Physics Letters **B525** (2002), 9 - 16
- New Results on Rare and Forbidden Semileptonic K^+ Decays
P. Truöl
HQ2K, 5^{th} International Workshop on Heavy Quarks at Fixed Target, Centro Brasileiro

de Pesquisas Fisicas, Rio de Janeiro - Brazil, October 2000
hep-ex 0012012
Proc. eds. I. Bediaga, J. Miranda, and A. Reis, Frascati Physics Series Vol. XX (INFN Frascati 2001), p. 49 - 63

Articles in press

- Compact Frontend-Electronics and Bidirectional 3.3 Gbps Optical Datalink for Fast Proportional Chamber Readout
  S. Lüders, R. Baldinger, D. Baumeister, K. Bösiger, R. Eichler, M. Feuerstack-Raible, C. Grab, S. Löchner, B. Meier, B.A. Schmid, U. Stange, S. Steiner, U. Straumann, S. Streuli, K. Szeker, and P. Truöl
  hep-ex 0107064
  Nuclear Instruments and Methods in Physics Research **A** (2001)
- Measurement of Dijet Electroproduction at Small Jet Separation
  H1-Collaboration**, C. Adloff *et al.*
  DESY 01 – 178, hep-ex 0111006
  The European Physical Journal **C** (2002)
- Measurement of Dijet Cross Sections in Photoproduction at HERA
  H1-Collaboration**, C. Adloff *et al.*
  DESY 01 – 225, hep-ex 0201006
  The European Physical Journal **C** (2002)
- Studies of Aging and HV Breakdown Problems during Development and Operation of MSGC and GEM Detectors for the Inner Tracking System of HERA-B
  Y. Bagaturia, O. Baruth, H.B. Dreis, F. Eisele, I. Gorbunov, S. Gradl, W. Gradl, S. Hausmann, M. Hildebrandt, T. Hott, S. Keller, C. Krauss, B. Lomonosov, M. Negodaev, C. Richter, P. Robmann, B. Schmidt, U. Straumann, P. Truöl, S. Visbeck, T. Walter, C. Werner, U. Werthenbach, G. Zech, T. Zeuner, M. Ziegler
  hep-ex 0204011
  Nuclear Instruments and Methods in Physics Research **A** (2002)
- Physics with Low-Energy Muons at a Neutrino Factory Complex
  J. Aysto, A. Baldini, A. Blondel, A. de Gouvea, J.R. Ellis, W. Fetscher, G.F. Giudice, K. Jungmann, S. Lola, V. Palladino, K. Tobe, A. Vacchi, A. van der Schaaf, K. Zuber
  Report of the Stopped Muons Working Group for the ECFA - CERN study on Neutrino Factory and Muon Storage Rings at CERN; CERN-TH-2001-231 (Sept. 2001), hep-ph/0109217.
- Energy Flow and Rapidity Gaps between Jets in Photoproduction at HERA
  H1-Collaboration**, C. Adloff *et al.*
  DESY 02 – 023, hep-ex 0203011
  submitted to The European Physical Journal **C** (2002)
- A Measurement of the t dependence of the Helicity Strcuture of Diffractive ρ Meson Electroproduction at HERA
  H1-Collaboration**, C. Adloff *et al.*
  DESY 02 – 027, hep-ex/0203022
  submitted to Physics Letters **B** (2002)
- Experimental Study of the Radiative Decays $K^+ \to \mu^+\nu_\mu e^+e^-$ and $K^+ \to e^+\nu_e e^+e^-$
  E865-Collaboration†, A.A. Poblaguev *et al.*

hep-ex/0204006
submitted to Physical Review Letters (2002)

Invited lectures

- A. van der Schaaf
  Summary WG2, *Short-baseline Neutrino Physics and Rare Processes*
  Proc. Int. Workshop on Neutrino factories based on Muon Storage Rings (Nufact'01), Tsukuba, Japan (May 24-30 2001), to appear in Nucl.Instr.Meth.**A**
- A. van der Schaaf
  Searching for μ-e Conversion
  Seminar at ICEPP, University of Tokyo, May 31 2001
- A. van der Schaaf
  SINDRUM II
  Seminar at ETHZ, June 4 2001
- A. van der Schaaf
  Testing Lepton Flavor Conservation
  Proc. Int. Conf. on CP Violation (KAON 2001), Pisa, Italy, June 12 - 17 2001
- F. Sefkow
  Open beauty production
  Proc. Workshop on New Trends in HERA Physics 2001, Ringberg Castle, Tegernsee, Germany (June 2001); hep-ex/0109038.
- P. Truöl
  A new measurement of Ke4 decay and the s-wave $\pi\pi$ scattering length
  CERN, June 22, 2001
- A. van der Schaaf
  Report and Plans of the Slow Muons WG,
  ECFA Plenary Meeting, CERN, October 15-18 2001
- P. Truöl
  Neuere experimentelle Resultate des Experiments E865 in Brookhaven
  Institut für theoretische Physik, Universität Bern, January 15, 2002

Conference reports

- Open beauty production at HERA
  J. Kroseberg
  hep-ex/0108052, Proc. 9^{th} Int. Workshop on Deep Inelastic Scattering (DIS 2001), Bologna, Italy, 27 Apr - 1 May 2001
- The Gluon Distribution xg and the Strong Coupling Constant α_s from Inclusive DIS data by H1
  R. Wallny
  Proc. 9^{th} Int. Workshop on Deep-Inelastic Scattering (DIS2001), Bologna, Italy (May 2001)
- SINDRUM II
  A. van der Schaaf
  Proc. Int. Workshop on Neutrino factories based on Muon Storage Rings (Nufact'01), Tsukuba, Japan, May 24-30 2001

- Measurement and QCD interpretation of the deep inelastic ep scattering cross section by H1
  R. Wallny
  Proc. Int. Europhysics Conf. on High-Energy Physics (HEP 2001), Budapest, Hungary (July 2001), D. Horvath et. al. eds., The Journal of High-Energy Physics (JHEP, *http://jhep.sissa.it/*), Proc. Sec. PRHEP-hep2001/008
- A New Measurement of $K^+ \to \pi^+\pi^-e^+\nu_e$ (K_{e4}) Decay and the $\pi\pi$ s-wave Scattering Length
  P. Truöl
  Proc. Int. Europhysics Conf. on High-Energy Physics (HEP 2001), Budapest, Hungary (July 2001), D. Horvath et. al. eds., The Journal of High-Energy Physics (JHEP, *http://jhep.sissa.it/*), Proc. Sec. PRHEP-hep2001/175.
- Heavy quark production in deep-inelastic scattering
  F. Sefkow
  Proc. Int. Europhysics Conf. on High-Energy Physics (HEP 2001), Budapest, Hungary (July 2001), D. Horvath et. al. eds., The Journal of High-Energy Physics (JHEP, *http://jhep.sissa.it/*), Proc. Sec. PRHEP-hep2001/021, hep-ex/0110036.
- Search for muon - electron conversion on gold
  W. Bertl for the SINDRUM collaboration
  Proc. Int. Europhysics Conf. on High-Energy Physics (HEP 2001), Budapest, Hungary (July 2001), D. Horvath et. al. eds., The Journal of High-Energy Physics (JHEP, *http://jhep.sissa.it/*), Proc. Sec. PRHEP-hep2001/155.
- Aging Tests with GEM-MSGC
  M. Hildebrandt
  Proc. Int. Workshop on Aging Phenomena in Gaseous Detectors, DESY, Hamburg (October 2001), Nuclear Instruments and Methods in Physics Research **A**, in print
- Open Heavy Flavour Production at HERA
  J. Kroseberg
  Proc. Lake Louise Winter Institute on Fundamental Interactions, Lake Louise, Alberta, Canada (February 2002)
- Das Triggersystem der CIP Kammer bei H1
  M. Urban
  Frühjahrstagung der Deutschen Physikalischen Gesellschaft, Fachverband Teilchenphysik, Leipzig (May 2002)

PhD Theses

- Deep-Inelastic Inclusive ep Scattering at Low x and a Determination of α_s
  Rainer Wallny
  Ph.D Thesis, Physik-Institut, Universität Zürich, 2001

† E865-collaboration:

R. Appel[8,6], G.S. Atoyan[2,8], B. Bassaleck[5], D.R. Bergman[8], N. Cheung[6], S. Dhawan[8], H. Do[8], J. Egger[3], S. Eilerts[5], W.D. Herold[3], V.V. Isakov[2,8], H. Kaspar[3], D. Kraus[6], D. Lazarus[1], P. Lichard, J. Lowe[5], J. Lozano[8], H. Ma[1], W. Majid[8], S. Pislak[7,8], A.A. Poblaguev[2,8], P. Rehak[1], A. Sher[6], J.A. Thompson[6], P. Truöl[7,8], M.E. Zeller[8]

[3] Paul Scherrer Institut, Villigen
[7] Physik-Institut der Universität Zürich, Zürich

** H1-collaboration (status of February 2002, the actual author list may differ from paper to paper somewhat):

C. Adloff[33], V. Andreev[24], B. Andrieu[27], T. Anthonis[4], A. Astvatsatourov[35], A. Babaev[23], J. Bähr[35], P. Baranov[24], E. Barrelet[28], W. Bartel[10], S. Baumgartner[36], J. Becker[37], M. Beckingham[21], A. Beglarian[34], O. Behnke[13], C. Beier[14], A. Belousov[24], Ch. Berger[1], T. Berndt[14], J.C. Bizot[26], J. Böhme[10], V. Boudry[27], W. Braunschweig[1], V. Brisson[26], H.-B. Bröker[2], D.P. Brown[10], D. Bruncko[16], F.W. Büsser[11], A. Bunyatyan[12,34], A. Burrage[18], G. Buschhorn[25], L. Bystritskaya[23], A.J. Campbell[10], S. Caron[1], F. Cassol-Brunner[22], D. Clarke[5], C. Collard[4], J.G. Contreras[7,41], Y.R. Coppens[3], J.A. Coughlan[5], M.-C. Cousinou[22], B.E. Cox[21], G. Cozzika[9], J. Cvach[29], J.B. Dainton[18], W.D. Dau[15], K. Daum[33,39], M. Davidsson[20], B. Delcourt[26], N. Delerue[22], R. Demirchyan[34], A. De Roeck[10,43], E.A. De Wolf[4], C. Diaconu[22], J. Dingfelder[13], P. Dixon[19], V. Dodonov[12], J.D. Dowell[3], A. Droutskoi[23], A. Dubak[25], C. Duprel[2], G. Eckerlin[10], D. Eckstein[35], V. Efremenko[23], S. Egli[32], R. Eichler[36], F. Eisele[13], E. Eisenhandler[19], M. Ellerbrock[13], E. Elsen[10], M. Erdmann[10,40,e], W. Erdmann[36], P.J.W. Faulkner[3], L. Favart[4], A. Fedotov[23], R. Felst[10], J. Ferencei[10], S. Ferron[27], M. Fleischer[10], P. Fleischmann[10], Y.H. Fleming[3], G. Flügge[2], A. Fomenko[24], I. Foresti[37], J. Formánek[30], G. Franke[10], G. Frising[1], E. Gabathuler[18], K. Gabathuler[32], J. Garvey[3], J. Gassner[32], J. Gayler[10], R. Gerhards[10], C. Gerlich[13], S. Ghazaryan[4,34], L. Goerlich[6], N. Gogitidze[24], C. Grab[36], V. Grabski[34], H. Grässler[2], T. Greenshaw[18], G. Grindhammer[25], T. Hadig[13], D. Haidt[10], L. Hajduk[6], J. Haller[13], W.J. Haynes[5], B. Heinemann[18], G. Heinzelmann[11], R.C.W. Henderson[17], S. Hengstmann[37], H. Henschel[35], R. Heremans[4], G. Herrera[7,44], I. Herynek[29], M. Hildebrandt[37], M. Hilgers[36], K.H. Hiller[35], J. Hladký[29], P. Höting[2], D. Hoffmann[22], R. Horisberger[32], A. Hovhannisyan[34], S. Hurling[10], M. Ibbotson[21], Ç. İşsever[7], M. Jacquet[26], M. Jaffre[26], L. Janauschek[25], X. Janssen[4], V. Jemanov[11], L. Jönsson[20], C. Johnson[3], D.P. Johnson[4], M.A.S. Jones[18], H. Jung[20,10], D. Kant[19], M. Kapichine[8], M. Karlsson[20], O. Karschnick[11], F. Keil[14], N. Keller[37], J. Kennedy[18], I.R. Kenyon[3], C. Kiesling[25], P. Kjellberg[20], M. Klein[35], C. Kleinwort[10], T. Kluge[1], G. Knies[10], B. Koblitz[25], S.D. Kolya[21], V. Korbel[10], P. Kostka[35], S.K. Kotelnikov[24], R. Koutouev[12], A. Koutov[8], J. Kroseberg[37], K. Krüger[10], T. Kuhr[11], T. Kurča[16], D. Lamb[3], M.P.J. Landon[19], W. Lange[35], T. Laštovička[35,30], P. Laycock[18], E. Lebailly[26], A. Lebedev[24], B. Leißner[1], R. Lemrani[10], V. Lendermann[10], S. Levonian[10], B. List[36], E. Lobodzinska[10,6], B. Lobodzinski[6,10], A. Loginov[23], N. Loktionova[24], V. Lubimov[23], S. Lüders[37], D. Lüke[7,10], L. Lytkin[12], N. Malden[21], E. Malinovski[24], I. Malinovski[24], S. Mangano[36], R. Maraček[25], P. Marage[4], J. Marks[13], R. Marshall[21], H.-U. Martyn[1], J. Martyniak[6], S.J. Maxfield[18], D. Meer[36], A. Mehta[18], K. Meier[14], A.B. Meyer[11], H. Meyer[33], J. Meyer[10], P.-O. Meyer[2], S. Michine[24], S. Mikocki[6], D. Milstead[18], S. Mohrdieck[11], M.N. Mondragon[7], F. Moreau[27], A. Morozov[8], J.V. Morris[5], K. Müller[37], P. Murín[16,42], V. Nagovizin[23], B. Naroska[11], J. Naumann[7], Th. Naumann[35], G. Nellen[25], P.R. Newman[3], F. Niebergall[11], C. Niebuhr[10], O. Nix[14], G. Nowak[6], M. Nozicka[30], J.E. Olsson[10], D. Ozerov[23], V. Panassik[8], C. Pascaud[26], G.D. Patel[18], M. Peez[22], E. Perez[9], A. Petrukhin[35], J.P. Phillips[18], D. Pitzl[10], R. Pöschl[26], I. Potachnikova[12], B. Povh[12], G. Rädel[1], J. Rauschenberger[11], P. Reimer[29], B. Reisert[25], C. Risler[25], E. Rizvi[3], P. Robmann[37], R. Roosen[4], A. Rostovtsev[23], S. Rusakov[24], K. Rybicki[6], J. Samson[10], D.P.C. Sankey[5], S. Schätzel[13], J. Scheins[1], F.-P. Schilling[10], P. Schleper[10], D. Schmidt[33], D. Schmidt[10], S. Schmidt[25], S. Schmitt[10], M. Schneider[22], L. Schoeffel[9], A. Schöning[36], T. Schörner[25], V. Schröder[10], H.-C. Schultz-Coulon[7], C. Schwanenberger[10], K. Sedlák[29], F. Sefkow[37], V. Shekelyan[25], I. Sheviakov[24], L.N. Shtarkov[24], Y. Sirois[27], T. Sloan[17], P. Smirnov[24], Y. Soloviev[24], D. South[21], V. Spaskov[8], A. Specka[27], H. Spitzer[11], R. Stamen[7], B. Stella[31], J. Stiewe[14], I. Strauch[10], U. Straumann[37], S. Tchetchelnitski[23], G. Thompson[19], P.D. Thompson[3], F. Tomasz[14], D. Traynor[19], P. Truöl[37], G. Tsipolitis[10,38], I. Tsurin[35], J. Turnau[6], J.E. Turney[19], E. Tzamariudaki[25], S. Udluft[25], A. Uraev[23], M. Urban[37], A. Usik[24], S. Valkár[30], A. Valkárová[30], C. Vallée[22], P. Van Mechelen[4], A. Vargas Trevino[7], S. Vassiliev[8], Y. Vazdik[24], A. Vest[1], A. Vichnevski[8], K. Wacker[7], J. Wagner[10], R. Wallny[37], B. Waugh[21], G. Weber[11], D. Wegener[7], C. Werner[13], N. Werner[37], M. Wessels[1], G. White[17], S. Wiesand[33], T. Wilksen[10], M. Winde[35], G.-G. Winter[10], Ch. Wissing[7], M. Wobisch[10], E.-E. Woehrling[3], E. Wünsch[10], A.C. Wyatt[21], J. Žáček[30], J. Zálešák[30], Z. Zhang[26], A. Zhokin[23], F. Zomer[26], and M. zur Nedden[25]

[32] Paul Scherrer Institut, Villigen

[36] Institut für Teilchenphysik, ETH, Zürich
[37] Physik-Institut der Universität Zürich, Zürich